



# The 2<sup>nd</sup> IMAT

International Meeting on Advances in Thermo-Fluids

November 16-17, 2009

Taman Safari, Indonesia

Department of Mechanical Engineering

**University of Indonesia**



---

# TABLE OF CONTENTS

Welcome ..... 10

Organizing Committee ..... 11

Program Summary ..... 12

List of Papers ..... 14

---

**Cascade Refrigeration System for Low-Temperature Application using CO<sub>2</sub>+Hydrocarbon Mixture as Alternative Refrigerant**

*Nasruddin, Darwin Rio Budi Syaka, M. Idrus Alhamid*

Refrigeration and Air-conditioning Laboratory, Department of Mechanical Engineering-Faculty of Engineering, University of Indonesia, Kampus UI Depok 16424

..... 14

---

**Experimental and Computational Study on Thermal Structure of a Separated Reattachment Flow under Heated Gas Injection**

*Harinaldi, Damora Rhakasywi, Sri Haryono*

Department of Mechanical Engineering Faculty of Engineering, University of Indonesia, Depok 16424

..... 18

---

**Development of Water Mist System for Pool Fire Extinguishment**

*Yulianto Sulistyo Nugroho, Donny Tigor Hamonangan and Ivan Santoso*

Department of Mechanical Engineering University of Indonesia, Kampus UI Depok 16424, INDONESIA

..... 23

---

**Preparation of Activated Carbon from Low Rank Coal with CO<sub>2</sub> Activation**

*Awaludin Martin, Bambang Suryawan, Muhammad Idrus Alhamid, Nasruddin*

Refrigeration and Air Conditioning Laboratory, Mechanical Engineering Department

Faculty of Engineering, University of Indonesia

..... 29

---

**Experimental Study of Characteristic and Performance of Non-Branded Thermoelectric Module**

*Zuryati Djafar, Nandy Putra, Raldi A. Koestoer*

Heat Transfer Laboratory, Mechanical Engineering Department, University of Indonesia, Kampus Baru UI, Depok, 16424- West Java-Indonesia

..... 35

---

**Development Mathematical Modelling For Design and Analysis Proton Exchange Membrane Fuel Cell**

*Hariyotejo Pujowidodo<sup>a</sup>, Verina Januati Wargadalam<sup>b</sup>, Ahmad Indra Siswantara<sup>c</sup>*

<sup>a</sup>Centre for Thermodynamics, Engine and Propulsion System, Agency for Assessment and Application of Technology, Puspiptek Serpong Tangerang 15314

<sup>b</sup>Research and Development Centre for The Electricity and Renewable Energy Technology, Ministry of Energy and Mineral Resources Cipulir Jakarta

<sup>c</sup>Faculty Engineering, University of Indonesia, Depok 16424

..... 40

---

**Experimental Study and Correlation of Two-Phase Flow Evaporation Heat Transfer Coefficient of Propane in Intermittent, Stratified Wavy and Annular Flows**

*Agus S. Pamitran<sup>a</sup>, Jong-Taek Oh<sup>b</sup>*

<sup>a</sup>Department of Mechanical Engineering, University of Indonesia, Kampus Baru UI, Depok 16424, Indonesia

<sup>b</sup>Department of Refrigeration and Air-Conditioning Engineering, Chonnam National University, San 96-1, Dunduk-Dong, Yeosu, Chonnam 550-749, Republic of Korea

..... 52

---

**Solar-powered Adsorption Desalination cum Cooling: experiments and simulation**

*Professor Kim Choon Ng, Professor Kim Choon Ng*

Mechanical Engineering Dept., Mechanical Engineering Dept., National University of Singapore  
National University of Singapore

..... 60

---

**Glimpses of Solar Energy Research at the Faculty of Mechanical Engineering University of Technology Malaysia Skudai, Johor Bharu, Johor**

*Amer Nordin Darus*

Department of Thermofluids, Faculty of Mechanical Engineering, Universiti Teknologi Malaysia  
81300 Skudai, Johor Bharu

..... 65

---

**Experimental Study of Confined Biogas Pulse Detonation Combustion**

*Mazlan A. Wahid, Haffis Ujir, Khalid M. Saqr and Mohsin M. Sies*

High-Speed Reacting Flow Laboratory, Faculty of Mechanical Engineering, Universiti Teknologi  
Malaysia, 81310 Skudai, Johor – MALAYSIA

..... 71

---

**Transient Flow Effect due to Geometrical Characteristics of Pressure-Swirl Gasoline Direct Injection (GDI) Atomizers**

*Azhar Abdul Aziz, Mas Fawzi Ali, Zulkarnian Abdul Latiff*

Automotive Development Centre (ADC), Faculty of Mechanical Engineering, Universiti  
Teknologi Malaysia

..... 78

---

**Swirl Intensity Effect on Premixed Jet Flame**

*Mohd Heady Jalaluddin, Mohd Ibthisham Ardani, Mazlan A. Wahid*

Faculty of Mechanical Engineering, Department of Thermofluid, Universiti Teknologi Malaysia,  
UTM, Malaysia

..... 85



---

**Liquid Fuel Vaporization System**

*Mazlan Abdul Wahid, Mohsin Mohd Sies, Mohd Khairrul Mohd Suhaimi, Mohd Ayub Sulong*

Faculty of Mechanical Engineering, Universiti Teknologi Malaysia, 81310 UTM Skudai, Johor, Malaysia

..... 90

---

**Characteristics of Turbulent Whirling Flow in an Asymmetric Passage**

*Khalid M. Saqr<sup>a</sup>, Mohsin M. Sies<sup>a</sup>, Hossam S. Aly<sup>b</sup>, Mazlan Abdul Wahid<sup>a</sup>*

<sup>a</sup>High-Speed Reacting Flow Laboratory, Faculty of Mechanical Engineering, Universiti Teknologi Malaysia, 81310 Skudai, Johor, MALAYSIA

<sup>b</sup>F Department of Aeronautical Engineering, Faculty of Mechanical Engineering, Universiti Teknologi Malaysia, 81310 Skudai, Johor, MALAYSIA

..... 97

---

**Thermal Conversion of Biomass using Microwave Irradiation**

*Farid Nasir Ani, Arshad Adam Salema*

Faculty of Mechanical Engineering, Universiti Teknologi Malaysia, 81310 Skudai, Johor Bahru, Malaysia

..... 102

---

**A Study of Transient flow in a lid-driven square cavity**

*Nor Azwadi Che Sidik, Muhammad Ammar Nik Mu'tasim*

Faculty of Mechanical Engineering, Universiti Teknologi Malaysia, UTM Skudai, Johor, Malaysia

..... 110

---

**Efficient Mesh for Driven Square Cavity**

*Nor Azwadi Che Sidik, Fudhail Abdul Munir*

Faculty of Mechanical Engineering, Universiti Teknologi Malaysia, UTM Skudai, Johor, Malaysia

..... 115

---

**Study of Flow Behaviour in Triangular Cavity**

*Nor Azwadi Che Sidik, Fudhail Abdul Munir*

Faculty of Mechanical Engineering, Universiti Teknologi Malaysia, UTM Skudai, Johor, Malaysia

..... 121

---

**Design and Fabrication of a 200N Thrust Rocket Motor Based on  $\text{NH}_4\text{ClO}_4$  + Al + HTPB as Solid Propellant**

*Mastura Ab Wahid, Wan Khairuddin Wan Ali*

Department of Aeronautics, Faculty of Mechanical Engineering, Universiti Teknologi Malaysia, 81310 UTM Skudai, Johor, Malaysia

..... 130

---

**Development of Ammonium Perchlorate + Aluminium Base Solid Propellant**

*Norazila Othman, Wan Khairuddin Wan Ali*

Department of Aeronautics, Faculty of Mechanical Engineering, Universiti Teknologi Malaysia, 81310 UTM Skudai, Johor, Malaysia

..... 135

---

**Reduction of Time Consumption For Simulating Lid-Driven Cavity Flow Using Lattice Boltzmann Method (LBM)**

*H. M. Faizal, C. S. Nor Azwadi*

Faculty of Mechanical Engineering, Universiti Teknologi Malaysia, 81310 UTM Skudai, Johor, Malaysia

..... 139

---

**Preliminary Numerical Analysis on Helicopter Main-Rotor-Hub Assembly Wake**

*Iskandar Shah Ishak, Shuhaimi Mansor, Tholudin Mat Lazim and Muhammad Riza Abd Rahman*

Department of Aeronautical Engineering, Faculty of Mechanical Engineering, Universiti Teknologi Malaysia, 81300 Skudai, Johor, Malaysia

..... 144

---

**Virtual Investigation of Free Convection from Concentric Annulus Cylinder by the Finite Difference Lattice Boltzmann Method**

*O. Shahrul Azmi<sup>a</sup>, C. S. Nor Azwadi<sup>b</sup>*

<sup>a</sup>Faculty of Mechanical & Manufacturing Engineering, Department of Plant and Automotive, Universiti Tun Hussien Onn Malaysia (UTHM), 86400 Parit Raja, Batu Pahat Johor

<sup>b</sup>Faculty of Mechanical & Manufacturing Engineering, Department of Thermo-Fluid, Universiti Teknologi Malaysia (UTM), 81310 Skudai, Johor

..... 147

---

**Engineering Analysis on the Conceptual Design of Portable Hand Truck for Staircase**

*Muhamad Hasbullah Padzillah<sup>a</sup>, Idris Ishak<sup>b</sup>, Abdul Rahman Musa<sup>c</sup>*

<sup>a</sup>Department of Thermo-Fluids, Faculty of Mechanical Engineering, Universiti Teknologi Malaysia, 81310 Skudai, Johor, Malaysia

<sup>b</sup>Department of Design, Faculty of Mechanical Engineering, Universiti Teknologi Malaysia, 81310 Skudai, Johor, Malaysia

<sup>c</sup>Department of Applied-Mechanics, Faculty of Mechanical Engineering, Universiti Teknologi Malaysia, 81310 Skudai, Johor, Malaysia

..... 155

---

**Numerical Analysis of Helicopter Tail Shake Phenomenon: A Preliminary Investigation**

*Iskandar Shah Ishak, Shuhaimi Mansor, Tholudin Mat Lazim, Muhammad Riza Abd Rahman*

Department of Aeronautical Engineering, Faculty of Mechanical Engineering, Universiti Teknologi Malaysia, 81310 UTM Skudai, Johor, Malaysia

..... 161

---

**Study on Characteristics of Briquettes Contain Different Mixing Ratio of EFB Fibre and Mesocarp Fibre**

*H. M. Faizal, Z. A. Latiff, Mazlan A. Wahid, Darus A. N.*

Faculty of Mechanical Engineering, Universiti Teknologi Malaysia, 81310 UTM Skudai

..... 168

---

**The Effect of Underneath Wavy Surface to the Flow Structure Downstream of a Bluff Body**

*Jamaluddin Md Sheriff, Asral, Kahar Osman, Muhamad Hasbullah Padzillah*

Faculty of Mechanical Engineering, Universiti Teknologi Malaysia, 81310 UTM Skudai Malaysia

..... 173

---

**Computational Fluid Dynamics Simulation of Stenosis Effect in Upper Human Airways**

*Zuhairi Sulaiman, Nasrul Hadi Johari, Kahar Osman*

Faculty of Mechanical Engineering, University of Technology Malaysia, 81310 Skudai, Johor, Malaysia

..... 183

---

**Study on Characteristics of Briquettes Contain Different Mixing Ratio of EFB Fibre and Mesocarp Fibre**

*H. M. Faizal, Z. A. Latiff, Mazlan A. Wahid, Darus A. N.*

Faculty of Mechanical Engineering, Universiti Teknologi Malaysia, 81310 UTM Skudai

..... 188

---

**The Flow Modeling of Aneurysm under Physical and Physiological Condition**

*Ishkrizat Taib<sup>1</sup>, Kahar Osman<sup>2</sup>, Mohammed Rafiq Abd Kadir<sup>3</sup>*

<sup>1</sup>Faculty of Mechanical and Manufacturing Engineering, Universiti Tun Hussein Onn Malaysia,

<sup>2</sup>Faculty of Mechanical Engineering, Universiti Teknologi Malaysia

..... 193

---

**Experimental Evaluation of the Effect of Taper Die on Lubricant Performance**

*Syahrullail, S., Teh, S.C., Najib, Y.M.*

Faculty of Mechanical Engineering, Universiti Teknologi Malaysia, 81310 UTM, Skudai, Johor, Malaysia

..... 198

---

**Unsteady Flow Analysis for Trachea and Main Bronchi for Various Reynolds Number**

*Mohd Zamani Ngali, Kahar Osman*

Faculty of Mechanical Engineering, Universiti Teknologi Malaysia, 81310, Skudai, Johor, Malaysia

..... 202

---

**Thermally-Induced Strain in FCBGA Microelectronics Package Subjected to Transient Temperature Loading**

*Nazri Bin Kamsah, Nurul Nadiah Bt Mohd Top*

Faculty of Mechanical Engineering, Universiti Teknologi Malaysia, 81310 Skudai, Johor, Malaysia

..... 209

---

**A Review – Thermal Load Analysis of Passenger Compartment**

*Haslinda Mohamed Kamar, Mohd Yusoff Senawi*

Department of Thermo-Fluids, Faculty of Mechanical Engineering, Universiti Teknologi Malaysia, 81310 Skudai, Johor Bahru, Malaysia

..... 213



---

**Utilization of Waste Cooking Oil as Diesel Fuel and Improvement in Combustion and Emission**

*Wira Jazair, Mohd Norhisyam*

Faculty of Mechanical Engineering, Universiti Teknologi Malaysia, 81310 UTM Skudai, Johor, Malaysia

..... 219

---

# WELCOME

It is our pleasure to welcome you, for the Second IMAT 2009, International Meeting on Advances in Thermo-Fluids, to Taman Safari Bogor, Indonesia. The Second IMAT 2009 is organized by Department of Mechanical Engineering, University of Indonesia.

This conference is a follow-up of the First IMAT 2008 organized by Universiti Teknologi Malaysia. The increased concerns about new technological innovations and solutions on thermo-fluids recently, the conference will bring the aims of the First IMAT become stronger. This would bring together academics, research scientists, and students from Universitas Indonesia (UI), National University of Singapore (NUS) and Universiti Teknologi Malaysia (UTM) to foster discussion and exchange ideas, experiences, challenges, solutions, new methods and techniques, and future research lines in the fields of Fluid Mechanics, Heat Transfer, Thermodynamics, Advance Fluid Mechanics and Advance Thermal Engineering. In this light, the Conference covers areas of research that are prerequisite for advancing thermo-fluids technology to improve performance.

We wish to provide the most pleasurable time in meeting all participant to talk and discuss about new researches and applications related to thermal and fluids engineering, and give an opportunity for the communication and cooperation between the researchers.

On behalf of the organizing committee, we invite you to our Second IMAT to be held at Taman Safari Bogor in November 2009.

## ORGANIZING COMMITTEE

The 2<sup>nd</sup> IMAT 2009 is organized by Department of Mechanical Engineering, Faculty of Engineering, University of Indonesia.

Kampus UI, Depok 16424, Indonesia

Phone : +62 21 727 0032

Fax : +62 21 727 0033

Email : [imat@eng.ui.ac.id](mailto:imat@eng.ui.ac.id)

### Advisory Committee

Prof. Dr. Ir. Bambang Sugiarto, M.Eng (Dean of Engineering Faculty)

Dr. Ir. Harinaldi, M.Eng (Head of Mechanical Engineering Department)

### Organizing Committee

Chairperson : Agus S. Pamitran, ST, M.Eng., Ph.D.

Email : [pamitran@eng.ui.ac.id](mailto:pamitran@eng.ui.ac.id)

Secretariat : M. Yulianto, MT

Email : [muhamad\\_yulianto@yahoo.com](mailto:muhamad_yulianto@yahoo.com)

### Board of Reviewers

Dr. M. Idrus Alhamid (UI)

Dr.-Ing. Nasruddin, M.Eng (UI)

Prof. Dr. Azhar Abdul Aziz (UTM)

Dr. Mazlan Abdul Wahid (UTM)

Prof. Dr. M.N.A. Hawlader (NUS)

Prof. Dr. Kim Choon Ng (NUS)

Prof. Dr. Ir. Bambang Suryawan, MT (UI)

Prof. Dr. Ir. I Made Kartika, Dipl-Ing (UI)

Prof. Dr. Ir. Raldi Artono Koestoer (UI)

Prof. Dr. Ir. Yanuar MSc. MEng (UI)

Prof. Dr. Ir. Budiarmo, MSc (UI)

Prof. Dr. Ir. Yulianto Sulistyono Nugroho, MSc (UI)

Dr.-Ing. Ir. Nandy Putra (UI)

# PROGRAM SUMMARY

## Day 1 : 16 November 2009

- 08.30 Registration
- 09.00 Opening ceremony (Prof. Dr. Bambang Sugiarto, Dean of Faculty of Engineering, Universitas Indonesia)
- 09.30 **Oral Presentation 1**  
Cascade Refrigeration System for Low-Temperature Application using CO<sub>2</sub>/Hydrocarbon Mixture as Alternative Refrigerant.  
*Dr. Ir. Nasruddin MSc., Universitas Indonesia*
- 09.50 **Oral Presentation 2**  
Glimpses of Solar Energy Research at the Faculty of Mechanical Engineering  
University of Technology Malaysia Skudai, Johor Bharu, Johor  
*Prof. Amer Nordin Darus MSc., Universiti Teknologi Malaysia*
- 10.10 **Oral Presentation 3**  
Experimental Study of Confined Biogas Pulse Detonation Combustion  
*Dr. Mazlan A. Wahid MSc., Universiti Teknologi Malaysia*
- 10.30 **Tea Break and Poster Session**
- 11.00 **Oral Presentation 4**  
Computational and Experimental Study on Thermal Structure of a Separated Reattachment Flow Under Heated Gas Injection.  
*Dr. Ir. Harinaldi MEng., Universitas Indonesia*



- 11.20      **Oral Presentation 5**  
Progress in Adsorption Desalination and Cooling  
*Prof. Dr. K. C. Ng, National University of Singapore*
- 11.40      **Oral Presentation 6**  
The Storage of Methane using Sorption Method.  
*Loh WS and Kazi, National University of Singapore*
- 12.00      **Lunch and Poster Session**
- 13.00      **Safari Tour and Attractions**
- 18.00      **Dinner Buffet**
- 20.00      **Social Program and Snack**

**Day 2 : 17 November 2009**

- 07.00      Breakfast
- 09.30      **Oral Presentation 7**  
Development of Water Mist System for Pool Fire Extinguishment.  
*Prof. Dr. Ir. Yulianto S. Nugroho MSc., Universitas Indonesia*
- 09.50      **Oral Presentation 8**  
Transient Flow Effect due to Geometrical Characteristics of  
Pressure-Swirl  
Gasoline Direct Injection (GDI) Atomizers  
*Prof. Dr. Azhar Abdul Aziz MEng., Universiti Teknologi Malaysia*
- 10.10      **Oral Presentation 9**  
Desalination Using Solar Energy, Ambient Energy and Waste Heat  
*Prof. Dr. M N A Hawlader and Zakaria M. A., National University of  
Singapore*
- 10.30      Closing Ceremony and Awards.
- 11.00      **Lunch**
- 12.00      **Visiting Universitas Indonesia**

# Cascade Refrigeration System for Low-Temperature Application using CO<sub>2</sub>+Hydrocarbon Mixture as Alternative Refrigerant

Nasruddin, Darwin Rio Budi Syaka, M. Idrus Alhamid

*Refrigeration and Air-conditioning Laboratory  
Department of Mechanical Engineering-Faculty of Engineering  
University of Indonesia  
Kampus UI Depok 16424,  
nasruddin@eng.ui.ac.id*

## ABSTRACT

This study was undertaken to obtain experimental data of R-744+R-290 mixture as an alternative refrigerants for the low temperature stage cascade refrigeration system using the R-13 compressor. Cascade system with compressor R-13 in LS can perform a good result for R-744+R-290 mixture. The performance of the system depends on the R-744+R-290 composition. The increasing mass fraction of CO<sub>2</sub> in the system will cause the higher discharge pressure at the LS compressor. This will increase the evaporating temperature. The composition of R-744+R-290 (70g : 30g) could reach temperature around -80°C more stable than the R-744 pure.

## Keywords

*cascade, refrigerant, mixture, CO<sub>2</sub>, low temperature*

## 1. INTRODUCTION

For more than 50 years, CFCs were considered to be the “perfect refrigerants” for their good properties being stable, non-flammable, low toxicity, and inexpensive to produce. Since the Montreal Protocol, the production and consumption of CFCs and of other ozone depleting chemicals has been almost phased out in most industrialized countries.

There are however, only a small number of alternative refrigerants that can be considered for the low temperature application range, between -40°C to -70°C. Refrigerants R13 and R503 were possible refrigerants for this range but their future

use had been capped because of their contribution to the ozone depletion. Possible replacements such as R23, R116 and their derivatives, R508A and R508B have limited value because of their contribution to the greenhouse effect (Schön, 1998).

Kim (2007) and Baolian Niu. (2007) propose a new binary mixture of R744 and R290 as an alternative natural refrigerant to R13. Experimental studies for this mixture and R13 were performed on a cascade refrigeration system only with modification to capillary in low-temperature circuit. COP and refrigeration capacity of this binary mixture were higher than those of R13, at the same time, condensing pressure, evaporating pressure, compression ratio, and discharge temperature were also higher than that of R13 when the high- temperature circuit of cascade refrigeration system was kept invariable.

On the other hand, a mixture of carbon dioxide with ethane (R170) creates near azeotropic mixture, which blends perfectly in the two phase region. This mixture creates low temperature glides compared with that of R744/R290 (Nasruddin et al, 2009).

However, R744/R290 (71/29) is considered as a promising alternative refrigerant to R13 when the evaporator temperature is higher than 201 K. Additionally, this zeotropic binary mixture are not perfectly mixed in the new refrigerant, the binary mixture, this refrigerant generate temperature glide (temperature different between the beginning and end of phase change process) up to 20 K, which will makes a problem in the heat

exchangers. This high temperature glide will affect heat transfer performance in the condenser as well as evaporator.

This study was undertaken to obtain experimental data of R744+R290 mixture as a alternative refrigerants and compared with pure R744 as single fluid in low-temperature system (LS) and using R290 as refrigerant in high-temperature system (HS) and equipped with manual expansion valves.

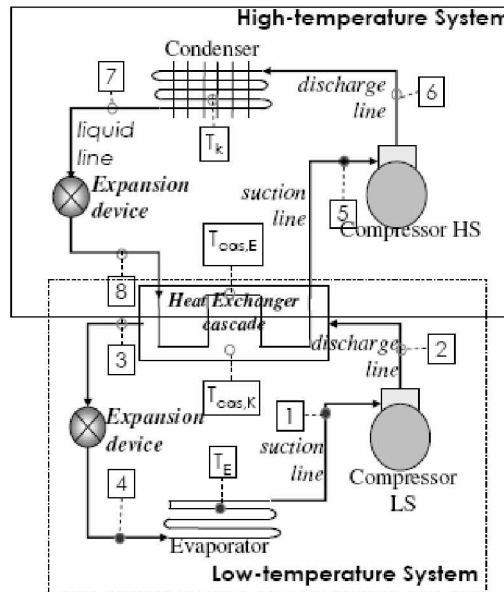
## 2. EXPERIMENTAL APPARATUS, PROCEDURE, AND MATERIALS

### 2.1 Experimental Apparatus

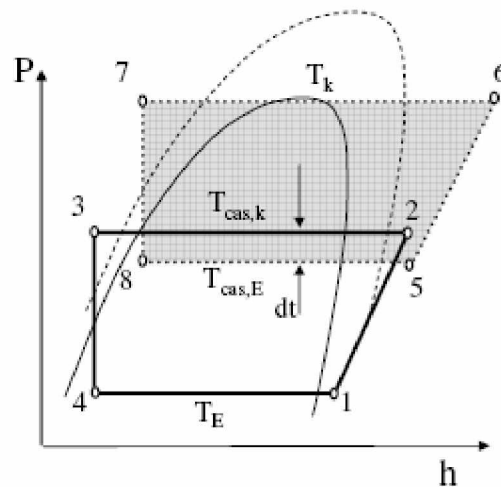
The schematic of experimental apparatus of the cascade system is shown in Fig. 1. It consists of two main systems which are low-temperature system (LS) and high-temperature system (HS). In every system has four main components such as compressor, condenser, expansion device and evaporator. Some accessories are also used in the system such as oil separator, accumulator, filter dryer. In the cascade system, one heat exchanger is used together in HS and LS. The evaporator of HS is functioned as the condenser of the LS. The type of this heat exchanger is tube-tube with 60 cm length and 2.4 in outer diameter.

The compressor for HS is a Tecumseh hermetic type which actually designed for R22 and will be used also for R290 with the capacity 1 hp. The LS compressor is hermetic compressor which has 1 hp capacity and designed actually for R13 or R23 for low temperature system. The type of the expansion valve is manual expansion valve from Sporlan with adjustment range 0.17 bar – 6.21 bar. The adjustment can be done with a screw at the top of the valve.

The experimental parameters measured for this experiment are also shown in figure 1. The temperatures at some points are measured with thermocouples and some pressure gauges are located in the system.



(a)



(b)

Figure 1: (a).Schematic of Experimental of The cascade System (b). p-h Diagram of Cascade System

### 2.2 Experimental Procedure and materials

Before running of the experiment, whole of the system must be evacuated by using vacuum pump

and run for leak-testing. After assuring there is no leak in the system, refrigerant is charged to the HS and LS. For HS, the system will be charged with R290 with the constant composition and charged refrigerant around 250g. Meanwhile for LS the mass of charged refrigerant mixture of the R290 and R744 are Table 1.

Table 1. The composition of charged refrigerant mass of R290/R744

Composition	R290	R744
I	0 g	100 g
II	30 g	70 g

#### 4. RESULTS AND DISCUSSION

The experimental results for the first run using 100% CO<sub>2</sub> in the low-temperature system is shown in Figure 2. It is shown that the temperature profiles as function of running time. The experiment has run for 6 hours at different measurement locations. The discharge temperature of the HS-compressor tends to increase as the highest temperature of the system. The evaporator temperature drops significantly after 25 minutes into around -40°C and steady for 6 hours. The evaporator of LS can reach around -80°C for the last 3 hours but not stable. It could be caused by the solid-ice forming in the LS and also at the compressor discharge temperature in LS.

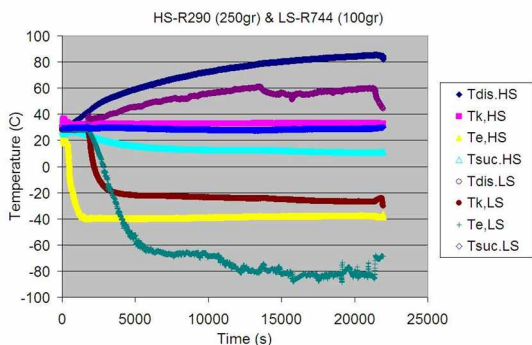


Figure 2 : Temperature profile of R-744 in LS 100 g and R-290 in HS

The effect of mixing of CO<sub>2</sub> with natural hydrocarbon refrigerant R-290 is shown in Figure 3. Generally the temperatures in the system are more stable than pure CO<sub>2</sub> for 4 h running test. It could be concluded that the effect of mixing of

CO<sub>2</sub> and propane not only can reduce its flammability but also could stabilize temperature in the system especially in LS-evaporator.

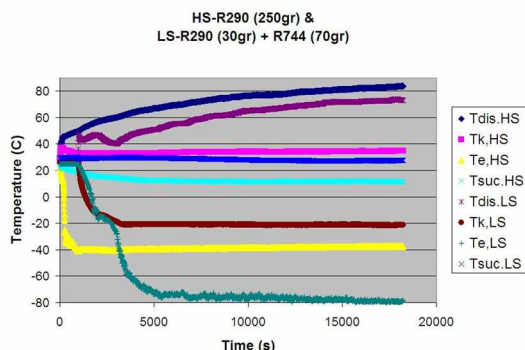


Figure 3 : Temperature profile of R-744+R-290 in LS (70 g + 30 g) and R-290 in HS

#### 5. CONCLUSION

The cascade system with compressor R-13 in LS can perform a good result for R-290+R-744 mixture. Hopefully the performance will be better if the compressor is designed for R13 or R23 for low temperature application. The performance of the system depends on the R-290+R-744 composition. The increasing mass fraction of CO<sub>2</sub> in the system tend to cause the higher discharge temperature at the LS compressor. This will increase the evaporating temperature.

The mixture of R-290+R-744 has some advantages such as to decrease the flammability of refrigerant in compare to pure R-290 and lower pressure of the discharge pressure in compare to pure R-744, and the most important effect to environmental protection.

#### ACKNOWLEDGMENTS

The authors would like to thank University of Indonesia for supporting this research activity by RUUI.

#### REFERENCES

[1] Schön P, 1998, New Refrigerants and the Environment, *The 1998 Business Meeting*, UK Controlled Environment Users' Group Minutes



- [1] Kim, J.H., Cho, J.M., Lee, I.H., Lee, J.S., and Kim, M.S, 2007, Circulation concentration of CO<sub>2</sub>/propane mixtures and the effect of their charge on the cooling performance in an air-conditioning system International Journal of Refrigeration Volume 30, pp. 43~49.
- [2] Boulian, N, Yufeng, Z. 2006, Experimental Study of the Refrigeration Cycle Performance for R744/R290 Mixtures, International Jurnal Of Refrigeration, 30(2007):37-42
- [3] Lee, T.S., Liu, C.H. and Chen, T.W., 2006, Thermodynamic analysis of optimal condensing temperature of cascade-condenser in CO<sub>2</sub>/NH<sub>3</sub> cascade refrigeration systems International Journal of Refrigeration Volume 29, pp. 1100~1108.
- [4] Nasruddin, D. Rahmat, L. Rahadiyan, 2009, "Utilization of CO<sub>2</sub>/Ethane Mixture as a New Alternative of Eco-Friendly Refrigerant for Low Temperature Applications". *ICSERA 2009*, UI Depok, Indonesia.

## EXPERIMENTAL AND COMPUTATIONAL STUDY ON THERMAL STRUCTURE OF A SEPARATED REATTACHEMENT FLOW UNDER HEATED GAS INJECTION

**Harinaldi , Damora Rhakasywi, Sri Haryono**

Department of Mechanical Engineering Faculty of Engineering  
University of Indonesia, Depok 16424  
Tel : (021) 7270011 ext 51. Fax : (021) 7270077  
E- mail : harinald@eng.ui.ac.id

### ABSTRACTS

*Flow channel with sudden expansion produces a separated flow so that causing a recirculation flow. This investigation is revealing the alteration of the thermal structure within the flow field due to a heated gas penetration. Main focus is placed on the influence of the ratio of specific momentum injection ( $I=0.1$  and  $I=0.5$ ), the injection location of heated gas ( $l_f=2H$  and  $l_f=4H$ ) and the variation of injection temperature ( $T_i=100^{\circ}C$  and  $T_i=300^{\circ}C$ ) The investigation was done computationally using finite volume method as well as experimentally in a closed loop flow channel with a backward-facing step flow configuration. Numerical solution models turbulence used were  $k$ -epsilon standard model and RNG  $k$ -epsilon. The numerical model was then validated by the experimental results. This model works on 2-D and 3-D Reynolds average Navier-Stokes (RANS) equations. From the results of thermal structure obtained, it can be suggested that increasing the the ratio of specific momentum injection supports more effective thermal mixing except to the narrow region around area injection. More significant results are obtained in the region of shear layer and area downstream of the injection.*

**Keywords:** *separated flow, heated gas injection,  $k$ -epsilon model standard, RNG  $k$ -epsilon, numerical model*

### 1. INTRODUCTION

Reattaching separated flow plays a vital importance in many aspects of engineering equipments, for example in heat exchanger, chemistry reactor and energy system, as well as in many combustor configurations. Especially in application of a combustor this kind of flow field is frequently used to stabilization flame. In a condition of a high speed flow, a reattaching separated flow provides a certain area for flame holding, where the turbulence of flow highly supports the mixing between fuel and air. In this case the velocity field speed plays important role in the growth of flammable mixture. Fuel injection into the area of recirculation in a reattaching-separated flow such as from the bottom wall of a backward facing step is one of methods that can be applied. It is then realized that to get an efficient combustor device needs a comprehensive understanding of chemistry and mixing process between fuels which inseminating and air around.

A certain approach to this problem shows that the difficulties arise because of complex viscous-inviscid

interaction within the flow structure. Many methods suggest empirical estimation of pressure distribution at separated stream area and some successfulness have been obtained in supersonic flow [1]. Flow patterns after backward facing step without mass addition have been checked for several aspects of turbulence transport such as the characteristic of heat transfer [2]. Along with the development of turbulence flow theories and the progress in flow diagnostic technology as well as progress in computational fluid dynamics, the research direction moves to the effort to get much more understanding on the mechanism to modify turbulence structure with excitation external so that the nature of transport turbulence which support fast transport properties (momentum, heat and mass) can be controlled.

Until about decade of 90<sup>th</sup>, most research were still oriented on the fundamental characterization of recirculation flow which formed by various stream geometry in external flow and also internal flow configuration without existence of external excitation. The main focus was on the elucidation of various features of fluid dynamics found in a recirculation flow. Entering era of millennium some pioneer research on the influence of external excitation was started such as works of Yang and Tsai [3] by using secondary fluid injection from the bottom wall of a channel flow which have step contour in the upstream. Their results show the some remarkable alteration of the flow structure which influenced a significant change of heat transfer coefficient in the flow channel.

In a research which focus on the mechanism of convective mass transfer on mixing process by turbulence in a backward facing step Harinaldi et al. [4] indicated that mixing process between air stream and injected gas very intensively occurred within the region from three to five height of step in streamwise direction. The mixing intensity also influenced by the ratio specific momentum of gas injection to free air stream. The research also showed that gas injection can control the level of turbulence in the field with growth resistance mechanism to the coherent structure in the shear layer. Meanwhile, a computational work was

reported using Large Eddy Simulation (LES) and statistical turbulence closures to study unsteadiness effect of external excitation with a slot jet with angle 45° relative to streamwise direction [5].

## 2. EXPERIMENTAL WORK

### 2.1 Apparatus Set-up

Experimental work of the current investigation was conducted in an airflow channel as shown in Fig. 1. The main air was supplied from a centrifugal blower with adjustable flow rate. Prior to the test section, the air stream passed through a wind tunnel consists of a diffuser, flow straightener, and nozzle. A slot with 1 mm width providing 2D jet injection was installed at the base wall of the test section with a backward facing step configuration. The test section had dimension of 80 mm x 80 mm rectangular cross-section upstream of the step. The step height (H) is 20 mm, with total length 337 mm. The air from a compressor was heated with a coil-type heater before being supplied to the test section. A hot wire anemometer with accuracy of 0.01 m/s was installed in the nozzle exit to measure the velocity of free stream which entered the test section. The thermal structure was investigated by temperature measurement of the flow field using a digital thermometer (FLUKE 50S) with K-type thermocouple probe having measurement range of 0 -1250 °C and measurement accuracy ± 0.1%. The probe was installed in a manual traverse system allowing three dimensional movements with accuracy of 0.1 mm.

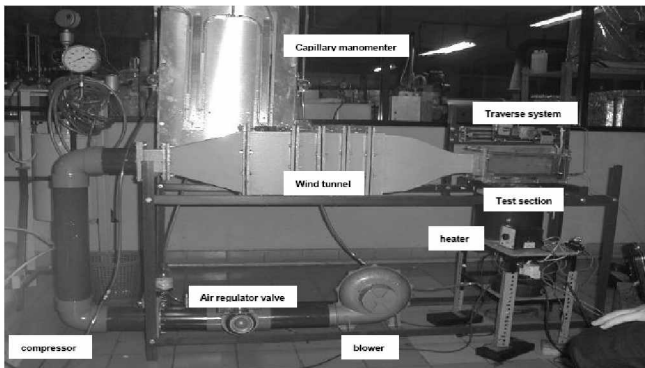


Fig 1. Experimental Setup

### 2.2 Experimental Parameters

In the experiment, the adjustments of blower speed and injection temperature are to get the designated ratio of specific momentum of injection. The ratio of specific momentum of injection is defined as follow:

$$I = \frac{\rho_i v_i^2}{\rho_0 v_0^2} \quad (1)$$

where  $I$  = specific ratio momentum injection,  $v_i$  = injection gas speed (m/s),  $v_0$  = main air flow speed (m/s),  $\rho_0$  = density main air flow (kg/m<sup>3</sup>),  $\rho_i$  = density gas injection (kg/m<sup>3</sup>).

Tables 1 show the details of the parameter's values in current experimental works for both type of injection geometry.

Table 1. Variation of condition for slot jet injection

Injection distance ( $I_p$ )	Specific ratio momentum injection ( $I$ )	Main air flow speed ( $v_0$ )	Injection gas speed ( $v_i$ )
		Main air flow temperature ( $t_0$ )	Injection temperature ( $t_{inj}$ )
2H = 40 mm 4H = 80 mm	0,1	14,1 m/s dan 30°C 13,2 m/s dan 30°C	4,95 m/s dan 100°C 5,74 m/s dan 300°C
	0,5	6,5 m/s dan 30°C 6,5 m/s dan 30°C	5,1 m/s dan 100°C 6,32 m/s dan 300°C

## 3. COMPUTATIONAL APPROACH

### 3.1 Computational domain

Figure 2 shows the computational domain being studied. Computational study used finite volume solver Fluent 6.2 to solve flow and temperature fields. Figure 3 presents mesh type. The mesh type for slot injection was developed by tri pave method which projects a mesh in form of trilateral of equal and unequal size.

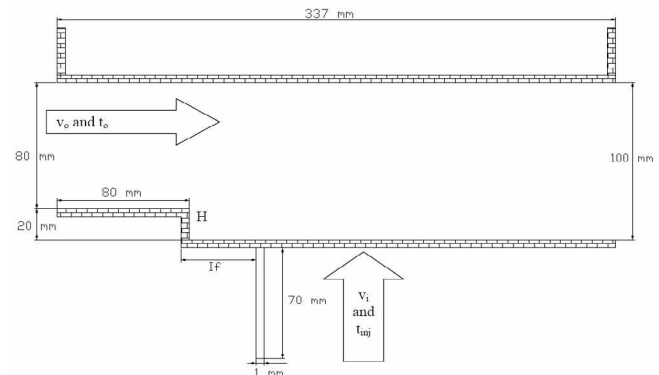


Fig. 2. Computational domain backward facing step flow

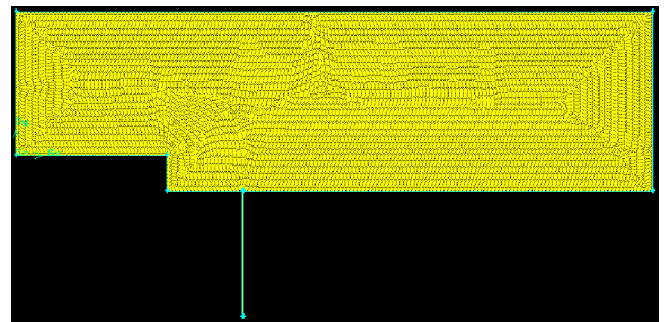


Fig.3. Tri pave type meshing for slot injection

### 3.2 Transport Equations for the standard k-ε model

The turbulence kinetic energy,  $k$ , and its rate dissipation,  $\epsilon$ , are obtained from the following transport equations:

$$\frac{\partial}{\partial t}(\rho k) + \frac{\partial}{\partial x_i}(\rho k u_i) = \frac{\partial}{\partial x_j} \left[ \left( \mu + \frac{\mu_t}{\sigma_k} \right) \frac{\partial k}{\partial x_j} \right] + G_k + G_b - \rho \epsilon - Y_M + S_k \quad (2)$$

and

$$\frac{\partial}{\partial t}(\rho\varepsilon) + \frac{\partial}{\partial x_i}(\rho\varepsilon u_i) = \frac{\partial}{\partial x_j} \left[ \left( \mu + \frac{\mu_t}{\sigma_\varepsilon} \right) \frac{\partial \varepsilon}{\partial x_j} \right] + C_{1\varepsilon} \frac{\varepsilon}{k} (G_k + C_{3\varepsilon} G_b) - C_{2\varepsilon} \rho \frac{\varepsilon^2}{k} + S_\varepsilon \quad (3)$$

In these equations,  $G_k$  represents the generation of turbulence kinetic energy due to the mean velocity gradients.  $G_b$  is the generation of turbulence kinetic energy due to buoyancy.  $Y_M$  represents the contribution of the fluctuating dilatation in compressible turbulence to the overall dissipation rate,  $C_{1\varepsilon}$ ,  $C_{2\varepsilon}$ , and  $C_{3\varepsilon}$  are constants.  $\sigma_k$  and  $\sigma_\varepsilon$  are the turbulent Prandtl numbers for  $k$  and  $\varepsilon$ , respectively.  $S_k$  and  $S_\varepsilon$  are user-defined source terms.

### 3.3 Transport Equations for the RNG k-ε model

$$\frac{\partial}{\partial t}(\rho k) + \frac{\partial}{\partial x_i}(\rho k u_i) = \frac{\partial}{\partial x_j} \left( \alpha k \mu_{eff} \frac{\partial k}{\partial x_j} \right) + G_k + G_b - \rho\varepsilon - Y_M + S_k \quad (4)$$

and

$$\frac{\partial}{\partial t}(\rho\varepsilon) + \frac{\partial}{\partial x_i}(\rho\varepsilon u_i) = \frac{\partial}{\partial x_j} \left( \alpha_\varepsilon \mu_{eff} \frac{\partial \varepsilon}{\partial x_j} \right) + C_{1\varepsilon} \frac{\varepsilon}{k} (G_k + C_{3\varepsilon} G_b) - C_{2\varepsilon} \rho \frac{\varepsilon^2}{k} - R\varepsilon + S_\varepsilon \quad (5)$$

For RNG k-ε model was also considered to its characteristics of:

- (i) having additional value at fast dissipation equation which can improve accuracy for blocked stream
- (ii) Rotation effect of turbulence also considered so that improve the accuracy for flow rotation.
- (iii) providing analytical formula for the number of Prandtl turbulent, while standard k-ε model using constant value of Prandtl number.
- (iv) providing formula for low Reynolds number flow.

## 4. RESULTS

Selected results are presented to describe important characteristics of thermal structures of the flow field.

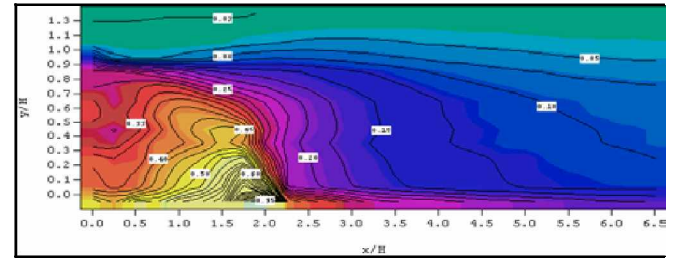
### 4.1 Measurement of Thermal Field

In order to enable comparing the thermal structure between some different injection conditions regardless the temperature magnitude, a normalized temperature [ $T^*$ ] is introduced and defined as follow:

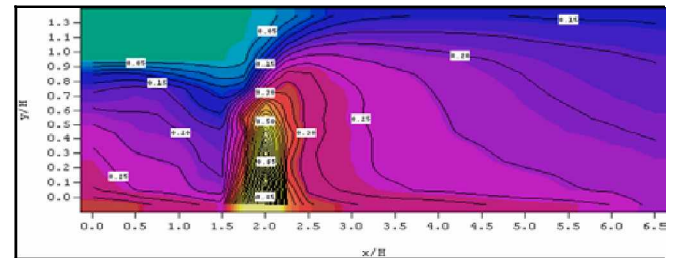
$$T^* = \frac{\bar{T} - T_0}{T_{inj} - T_0} \quad (6)$$

Two-dimensional contour of the normalized temperature field for several injection conditions are

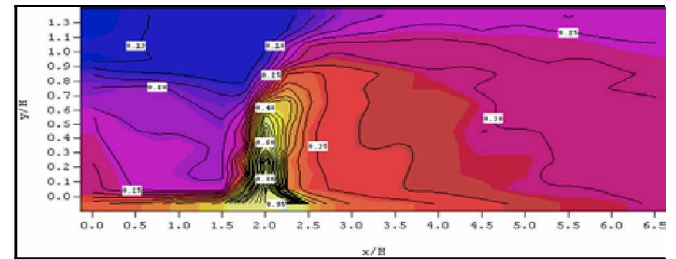
presented in Figs. 4(a)-(d). The figures show some remarkable differences of the thermal structure with regard to the heated gas spread due to variations of parameter of interest. The spatial density of contour lines suggests that the temperature gradient show some different tendency of heat transfer rate to certain direction. Further analysis is presented in the discussion section.



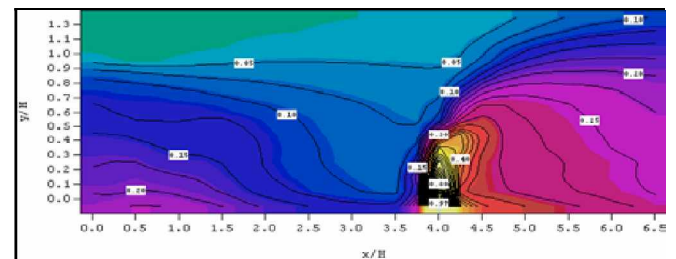
(a)  $l_f/H = 2; I = 0.1; T_{inj} = 100 \text{ }^\circ\text{C}$



(b)  $l_f/H = 2; I = 0.1; T_{inj} = 300 \text{ }^\circ\text{C}$



(c)  $l_f/H = 2; I = 0.5; T_{inj} = 100 \text{ }^\circ\text{C}$



(d)  $l_f/H = 4; I = 0.1; T_{inj} = 300 \text{ }^\circ\text{C}$

Fig.4 Contours of Mean Normalized Temperature ( $T^*$ ) for four different conditions of injection

### 4.2 Computational Results of Temperature Distribution

Some computational results showing the temperature distribution of the flow field are presented in Fig. 5 (a) and (b). The computational condition for Fig. 5(a) corresponds to the experimental condition previously shows in Fig. 4(a), meanwhile condition in Fig 5(b) corresponds to condition in Fig. 4(d). In general, it can be said that these results show a sufficient agreement between the thermal structures



developed by the numerical simulation to that obtained from experimental measurement. Both approaches show that the temperature distribution indicates similar thermal development with respect to the direction of temperature growth due to the heated gas injection.

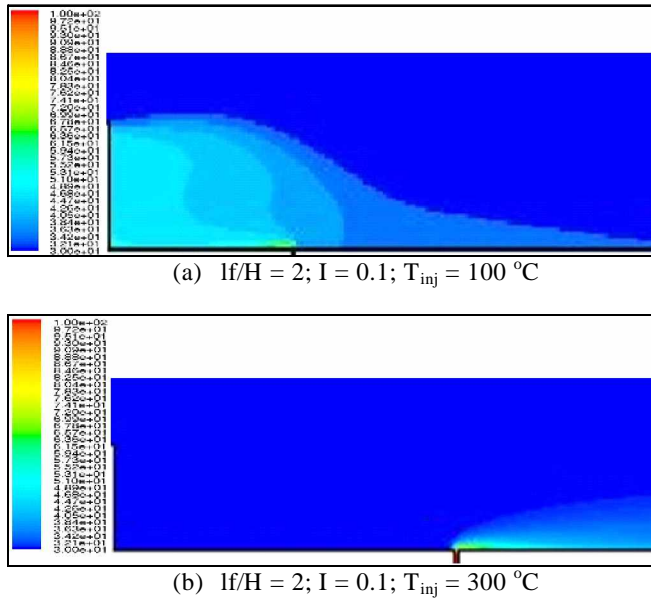


Fig.5 Temperature distribution in the flow field for some selective result of computational works

Figures 5 and 6 show the computational results of the characteristics of temperature distribution due to slot gas injection of heated gas located at  $2H$  (40 mm) and  $4H$  (80 mm) from step edge.

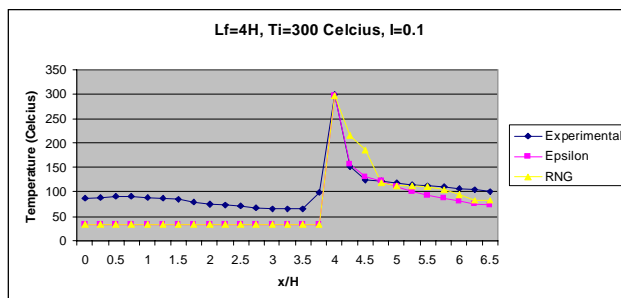


Fig.6 Temperature distribution in the flow field for some selective result of computational works

Meanwhile, Fig. 6 shows the comparison of experimental results with computational solution of transport equation with standard k- $\epsilon$  and RNG k- $\epsilon$  models at a representative condition of  $l_f/H = 4$ ,  $I = 0.1$  and  $T_{inj} = 300\text{ }^{\circ}\text{C}$ . The figure show that upstream of the injection, the computational solution gives a very good agreement for both turbulence models as both results collapse into single curve. However, the experimental measurement show higher temperature values than the numerical solution. It is

predicted that the flow field upstream the injection is dominated by a recirculation flow with low velocities. Meanwhile in the experimental condition, it can not be avoided that the bottom wall received to some extent a heating from the jet channel so that the conductive heat transfer give a remarkable influence to the thermal structure at this upstream region. On the other hand, in the down stream region of injection it seems that the standard k- $\epsilon$  model gives better prediction to the temperature distribution up to one step height ( $H$ ) distance from the injection point. Further downstream, the RNG k- $\epsilon$  shows better prediction.

## 5. DISCUSSIONS

### 5.1 Effect of Specific Momentum Ratio of Injection

Comparing Fig. 4(a) with 4(c), it can be understood that injection with higher specific momentum ratio ( $I = 0.5$ ) causes steeper temperature gradient as soon as heated injected flow enters the recirculation flow region, especially in the stream wise direction, suggested by denser contour lines. The jet of heated flow also penetrates deeper up to the shear layer indicated by high temperature in the region. Furthermore, with lower  $I$ , higher temperature distributions are seen in the upstream region from the injection point, and oppositely with higher  $I$  they are seen in the down stream direction.

From the mixing point of view, the previous report [6] has suggested that the jet of low specific momentum of injection grows with a spatially wavy trajectory and temporally oscillates toward upstream and down stream direction in the recirculation zone. The trajectory fluctuation causes less effective mixing compare to the turbulence mixing so that although rate of heat transfer is considerably high, the homogeneity of the mixing is relatively poor. This is indicated by high temperature gradient in the region near injection point. When the specific momentum ratio of injection is increased, the hot jet has the capability to penetrate vertically deeper into the shear layer where the shear turbulence dominates the region. Here the mixing of hot air jet and cold airflow from the free stream also supported by the intermingling mechanism of large scale coherent structures present in shear-mixing layer [7] which move convectively toward downstream direction. As a result more homogenous mixing can be obtained with the tendency to grow to the downstream of injection.

### 5.2 Effect of Temperature of the Injected Air

The effect of changing initial injection temperature can be figured out by carefully comparing Fig. 2(a) and (b). In the region near injection point, the stream wise temperature gradient remarkably increases as the initial temperature increases. With higher initial temperature,  $T_{inj} = 300\text{ }^{\circ}\text{C}$ , hot air injected from  $l_f/H = 2$  distributes more similarly toward upstream and downstream of injection point, compare to the case of lower initial injection temperature,  $T_{inj} = 100\text{ }^{\circ}\text{C}$ . Although not shown in Fig. 2, this tendency can be observed in both cases of specific momentum ratio of injection ( $I = 0.1$  and  $0.5$ ). However, for injection from  $l_f/H = 4$  such as described in Fig. 2 (d), the heated flow seems to be directed toward downstream of injection as the initial injection temperature is increased. The increase of temperature gradient especially in the stream wise direction is considered

due to the effect of viscosity increase of the injected air as the initial temperature of injection is increased. Therefore, hotter airflow is more capable to overcome the hydrodynamics disturbances from the recirculation flow due its increased inertia. Another effect that can be observed is that the hot injected jet gives blocking effect to the main free stream that enhanced the entrainment of cold flow into the recirculation region upstream of the injection point. This is indicated by the decrease of mean temperature in the upstream of injection point.

### 5.3 Effect of Location of Injection

The effect of shifting injection location to the alteration of temperature field can be analyzed by comparing Fig. 4(b) with 4(d). In general, it can be said that the distribution patterns of heated flow can be attributed to the hydrodynamics ability of the injected air to pierce through the shear layer. When the injection location is close to the reattachment point,  $l_f/H = 4$ , within most of recirculation zone a relative lower temperature gradients are observed compare to that of injection near the step at  $l_f/H = 2$ . Injecting heated airflow from  $l_f/H = 4$  also extends the high temperature region within the recirculation zone for every combination of parameters. The alterations of the field structures is considered to be attributed to two factors, i.e. the penetration capability of the injected heated gas to the shear layer and the relative influence of the free stream over the injection flow. When the heated air flow is injected from  $l_f/H = 4$ , the relative influence of the cold shear flow and free stream over the injected hot jet flow is enhanced and eventually the temperature gradient is suppressed. However, if the specific momentum ratio of injection is high, the domination of the shear flow and the free stream over the injected flow decreases and at a certain specific momentum ratio of injection, the injected flow will start to overcome the influence of shear flow and the free stream. When this occurs more amount of heated mass will distribute toward downstream of injection point, and the alteration of thermal structure will be more obvious in the downstream region. Furthermore, it can also be figured out that the shift of injection location approaching the reattachment point causes the cold recirculation flow mixed with hot injected flow better in the recirculation zone since the turbulence intensity is higher and the effect of shear mixing layer is more pronounced.

## 6. CONCLUSION

The behaviors of a recirculation flow over a sudden expansion behind a backward-facing step under the influence of heated gas injection has been studied comprehensively by experimental and computational approaches focusing on the thermal structures with regard to the mixing process between low temperature-free stream flow and high temperature-injected flow. Some important aspects can be concluded as follows:

- (1) An increase of specific momentum ratio of injection will influence the mixing effectiveness. In the region near injection point, the effectiveness of mixing will decrease while in the shear layer region and downstream region it will increase. However, injection in the location far from

the step, there rises a disadvantage since more heated injected flow penetrates through shear layer, carried away by the free stream and does not mix with the recirculation flow

- (2) When the initial temperature of injection is increased, the mixing take place more effectively in the downstream direction of injection, meanwhile in the region near injection point it will less effective
- (3) The shift of injection location approaching the reattachment point causes the cold recirculation flow mixed with hot injected flow better in the recirculation zone since the turbulence intensity is higher and the effect of shear mixing layer is more pronounced

## ACKNOWLEDGMENT

This work was supported within the DRPM-UI program of the University of Indonesia (project number S2/2009/I/3435).

## REFERENCES

- [1] Eaton, J.K., Johnstone, J.P., *A Review of Research on Subsonic Turbulent Flow Reattachment*, AIAA Journal, Vol.19, No.9, 1981, pp.1093-1099.
- [2] Armaly, B.F., Durst, F., Pereira, J.C.F., and Schonung, B., Experimental and theoretical investigation of backward-facing step flow, *J. Fluid Mechanics*, 127, 1983, pp. 473-496.
- [3] Yang, J.T and Tsai, C.H., 1996 " High temperature heat transfer of separated flow over a sudden expansion with base mass injection," *Int. J. Heat and Mass Transfer*, 39, pp.2293-2301.
- [4] Harinaldi, Ueda, T. and Mizomoto, M., dalam S. Dost, H. Struchtrup and I. Dincer (Eds., 2002, *Progress in Transport Phenomena*, Elsevier, Paris, pp.93-98).
- [5] Dejoan A., Jang, Y.J and Leschziner, M.A, 2005, "Comparative LES and Unsteady RANS Computations for a Periodically-Perturbed Separated Flow Over a Backward-Facing Step", *Trans. ASME, J. Fluid Eng.* 127, pp.872-878.
- [6] Harinaldi, Ueda, T., Mizomoto, M., "Laser Sheet Imaging of a Recirculation zone of a Backward Facing-step Flow with Gas Injection", *J.Chemical Engineering of Japan (International Edition)*, 34(3),.351-359 (2001)
- [7] Harinaldi, Ueda, T., Mizomoto, M.; "Effect of Slot Gas Injection to the Flow Field and Coherent Structure Characteristics of a Backstep Flow", *International Journal of Heat and Mass Transfer*, 44(14), 2711-2726 (2001)

# Development of Water Mist System for Pool Fire Extinguishment

Yulianto Sulisty Nugroho, Donny Tigor Hamonangan and Ivan Santoso

*Department of Mechanical Engineering University of Indonesia  
Kampus UI Depok 16424, INDONESIA  
Ph. +62 21 7270032, Fax. +62 21 7270033,  
E-mail: yulianto.nugroho@ui.ac.id*

## ABSTRACT

A new experimental set-up was designed to study experimentally the effect of operating parameter on the effectiveness of water mist fire suppression. Fine water mist driven by nitrogen through a nozzles system was used to suppress and extinguish fires from pool of gasoline at 5 and 8cm diameters. The spray characteristics of the mist was characterized under a constant pressure of 7 bar and various nozzle inclination angles of 30o to 60o. Flame temperature and extinction time are used as a measure of mist effectiveness. In general, the results show that the inclination angle and height of the nozzle play key roles in extinguishing performance of water mist system. Nevertheless, the flame size can be reduced by setting the mist envelope slightly above the pool surface. A flattened flame due to fire plume buoyancy being overcome by downward flow of mist was not identified in the present work.

### Keywords

*water mist system, pool fire, and nozzle configuration.*

## 1. INTRODUCTION

As the leading area of world economic growth for the last two decades, many Asian countries enjoy higher rate of economic development. Especially in urban areas of Asia, the spiraling land prices have been responded by the construction of tall buildings for multi purposes. In competitive situations, element of allurements and glamour would come into the fore, playing significant roles in the design concept of a tall building. With the introduction of new, synthetic materials throughout the tall buildings, the hazards have become much more widespread, and the risks to life and property are now much greater [1].

Fire in buildings and industrial facilities cause human suffering and materials losses. The economic cost from building fires and other cost of fire relevant to fire safety programs such as incremental building costs and the cost of fire services and insurance is estimated to reach up to 1% of the gross domestic product (GDP) of many industrialized nations [2]. The loss figure from fires in Asia is within a comparable range or higher, since one must also count the destructions resulted from natural fires. The general public is becoming increasingly aware of the problems and the risks, and there is now a perceived need to deal with fire safety in a more organized fashion in which engineering solutions are introduced at an early stage, either to prevent the outbreak of fire, or to mitigate its effects to an extent that the losses are small, and considered "acceptable" in the circumstances. Despite the great loss from fire related accidents in urban areas of Asia, effort to build the capacity of personnel in fire safety areas is limited, and mainly focused in the area of fire fighting techniques. In recent years, due to progress in fire safety technology, economic and social reasons, many countries are shifting their building codes from prescriptive-based to performance-based [1,2]. As consequences, this development requires a great need for better fire safety technology for existing and newly developed buildings and industries.

Deploying an effective fire suppression system is an important aspect of the fire safety design of a modern building and industrial premises. Drawbacks on the use of excessive amount of water in a sprinkler system, and a ban on the use of ozone depleting Halon 1301 would make research on finding an alternative protection system for fire control become a necessity [3].



arresting combustion. Water mist can also block the thermal radiation and pre-wet other combustibles in the neighbourhood to reduce their temperature and delay the ignition. Moreover, the use of a small amount of water with small-sized droplets is advantageous in situations where water can damage equipment [4-7]. However, there is no general design method for water mist fire protection systems has been well established, despite some water mist an attractive alternative for fire control.

The good design of a water mist system requires a detailed investigation of fundamental mechanisms of fire suppression based on the interaction between fire plumes and water sprays and water discharge conditions, i.e. droplet size, flow rate or injection pressure, spray momentum, etc. The design of such systems is complicated by the wide range of physical and design parameters which must be taken into account, so full-scale fire tests are often the main design method. Therefore, it is clear that specific and systematic investigations on the actions of mists for fires can usefully direct the progression of a design.

The general ideas of the physics behind the water mist pool fire extinguishment can be found in recent literatures [3-7]. More recent studies, by the author of opposed fine water sprays interacting with small-scale liquid gasoline pool fire, have revealed some interesting results. For instance, a strong enhancement of fire due to the spray has been observed [7]. In addition, the extinguishment time of pool fire is greatly affected by the pressure of water mist. This work follows on from these previous investigations. The fire source is a gasoline pool fire with a pan of 5 and 8 cm diameter and fine water spray is injected to form a side flow to the flame in an open environment. Nozzle inclination angle and distance from the nozzle to the fuel pan are selected as the major experimental parameters.

## 2. EXPERIMENTAL APPARATUS AND PROCEDURE

Experiments were performed with a small-scale liquid gasoline pool fire. The configuration of the apparatus is given in Fig. 1.

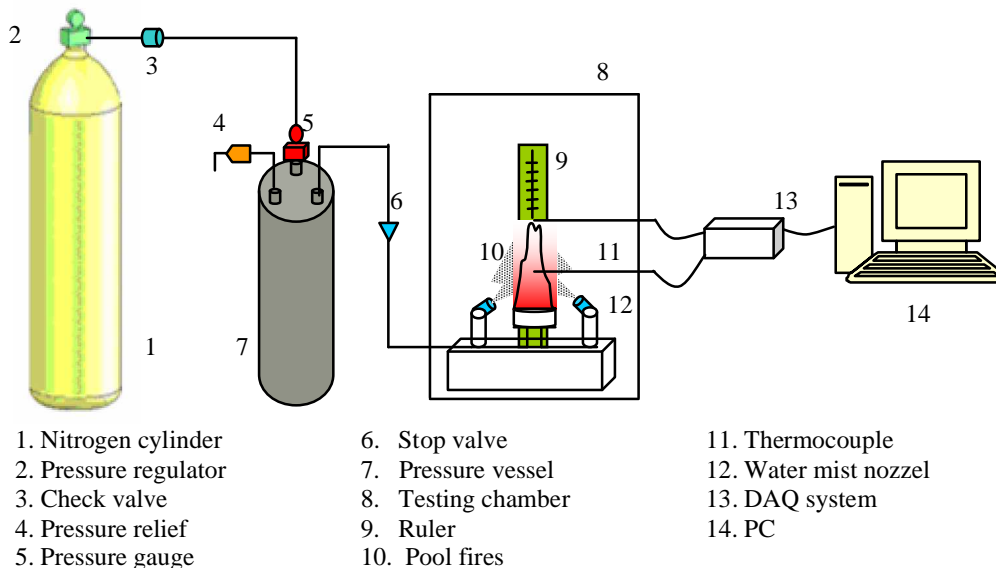


Figure 1 Experimental set-up.

The gasoline was contained in a circular steel pan with a diameter of 5 to 8 cm. The pool was mounted on a steel stand 40 cm above the ground. Four sideward-directed solid cone nozzles with a

single orifice were positioned on a square steel frame. The square steel frame can be moved vertically to adjust the level of the nozzle to the fuel pan. The pool and the nozzle were centered

inside a testing chamber with a black color background. Water was pressurized by a high pressure nitrogen gas cylinder, and injected through the nozzle via a stop valve to control onset of injection. For each test, the pan was filled to 1 cm below the pan lip with fresh fuel. Then, the fire was allowed to burn for at least 20s to ensure quasi-steady burning before the water injection. The flame height was measured using a ruler. Two K type thermocouples were placed at the centre line of the circular pan at 5 and 10 cm above the pool surface. In a typical run, important data such as flame temperatures, and suppression time were recorded via a data logging system linked to a computer. The interaction of pool fires and water mist spray were recorded using a digital video camera.

Design parameters for the water mist system requires information on injection pressure and the corresponding discharge rate for the nozzle system. In addition, the spray angle and the distance from the nozzle to the fuel pan are also governing parameters which can control the interaction between the water spray and the flame. The effective water flux of the nozzle can be defined by the amount of water flow that reaches the fuel pan from the nozzle discharges under non-combustion conditions. In this work, the spray characteristics and the mass flux density of the water mist was measured using 121 sponge blocks of 3cm x 3cm size. Spread and mass flux density are important characteristics of water mist spray for fire extinguishing purposes. Mass flux density was measured at a pressure of 7 bar pressure with several variations in spray angles of 30°, 45°, and 60° and three height variations of 0 cm, 2 cm and 4 cm above the pan lip.

### 3. RESULTS AND DISCUSSION

#### 3.1 Water mist characteristics

Water drops generated by the nozzle were very fine with diameters lower than 200  $\mu$ m. The spray angle of the individual nozzle was about 85 degrees and not changed with an increase in discharge pressure. A typical shape of mass flux density is shown in Figure 2. In general, a bell shape distribution was notified. The peaks were due to the interaction areas of individual nozzle producing higher mass flux. The average mass flux density for the arrangement of 7 bar, 60° nozzle angle, and measured at 4 cm below the nozzles is 1.53  $\text{mg}\cdot\text{cm}^{-2}\cdot\text{s}^{-1}$ . Figure 3 shows the

average mass flux density measured at various conditions of nozzle inclination and height.

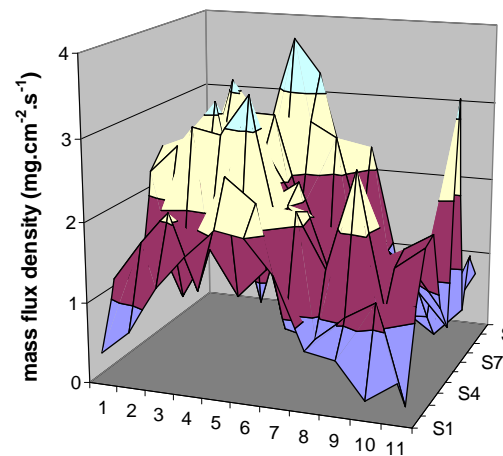


Figure. 2 Distribution of mass flux density at 7 bar, 60° nozzle angle, and measured at 4 cm below the nozzles. The average mass flux density is 1.53  $\text{mg}\cdot\text{cm}^{-2}\cdot\text{s}^{-1}$ .

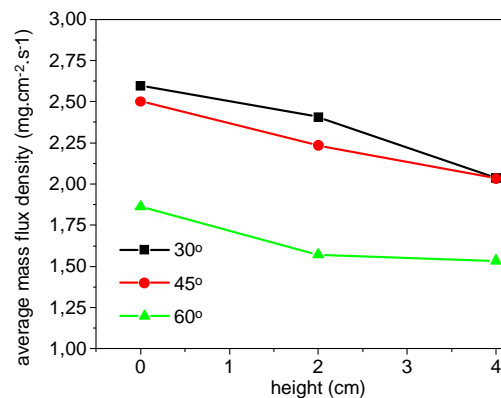


Figure 3 Effects of nozzle inclination and height on mass flux density.

#### 3.2 Performance of water mist system

On the basis of the average mass flux density found, only the 30° of nozzle inclination was tested for pool fire extinguishment. It is found that water mist systems extinguished the gasoline pool fires very effectively without substantial fire flare-up and burning oil being splashed outside the pan. As observed in the experiments, with the discharge of water mist, the flame inside the water mist envelop was extinguished quickly by flame

quenching and oxygen dilution. Figure 4 shows variation of temperatures measured above the pool surface at two different locations of thermocouple with time. Once the water mist discharge was activated, the temperatures inside the coverage areas of the mist were quickly dropped as fine water drops cooled the flame. Figure 5 shows the sequences of fire extinguishment. The figure clearly shows there is no flattened flame due to fire plume buoyancy being overcome by downward flow of mist. In fact the flame size was reduced by covering the fire inside the mist envelope.

The length of a flame is a significant indicator of the hazard posed by the flame. Flame length directly relates to flame heat transfer and the propensity of the flame to impact surrounding objects. As a plume of hot gases rises above a flame, the temperature, velocity, and width of the plume changes as the plume mixes with its surroundings. The size and temperature of the flame are important in estimating the ignition of adjacent combustibles. This work clearly shows that the flame geometry is affected by the pool sizes. As a consequence, the period of flame cooling and extinction are longer for larger pool diameter and nozzle height (Figure 6).

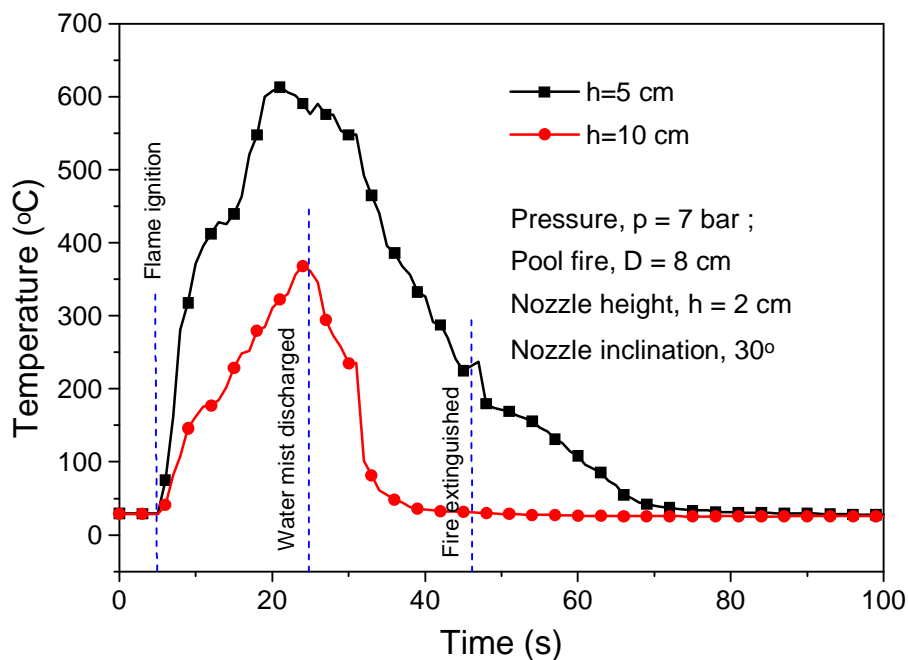


Figure 4 Variation of temperatures above pool surface with time.

#### 4. CONCLUSIONS

Flame geometry is greatly affected by the pool sizes. Flame cooling is the dominant extinguishing mechanisms of water mist for pool fires. It requires that the employed water mist systems shall have sufficient spray coverage, water mass flux, and spray momentum. The water mist systems using four sideward-directed solid cone nozzles developed in the current work were

effective in extinguishing pool fire with various diameters. The extinguishing performance was greatly affected by nozzle inclination and its height from the pan lip. In general, the flame size was reduced by covering the fire inside the mist envelope without generating a flattened flame due to fire plume buoyancy being overcome by downward flow of mist.

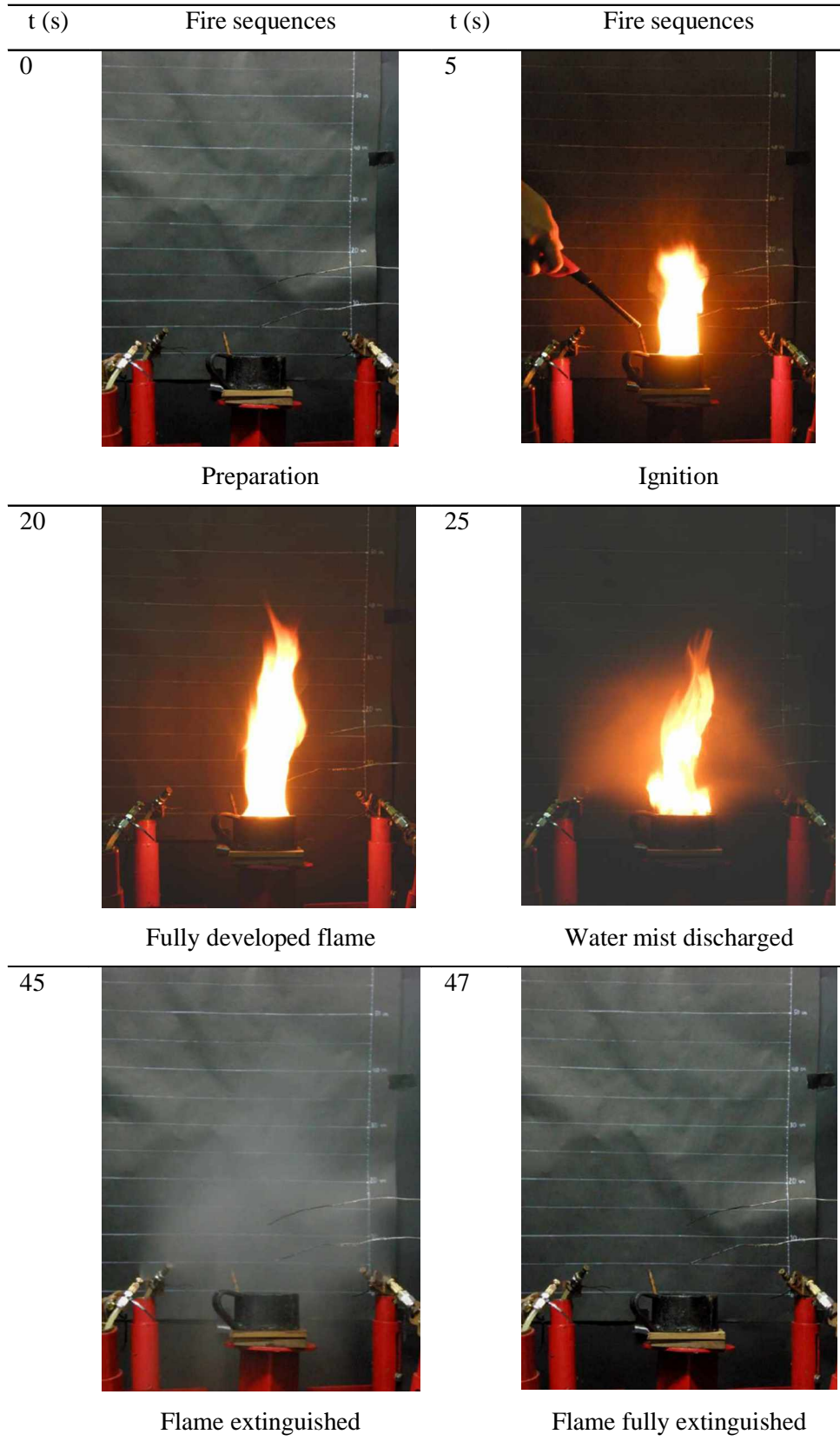


Figure 5 Sequences of fire extinguishment using water mist system.

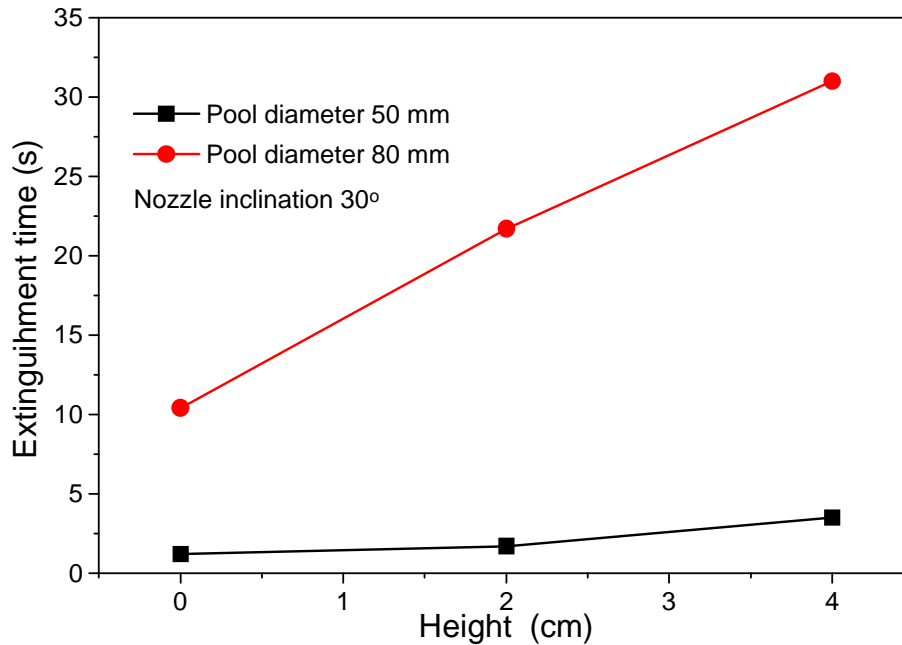


Figure 6 Extinguishment times of pool fires

## ACKNOWLEDGEMENT

Dr. Y.S. Nugroho would like to thank the financial support from the Directorate for Research and Public Services University of Indonesia (DRPM UI) and Directorate General of Higher Education (DP2M), Ministry of National Education Republic of Indonesia.

## REFERENCES

- [1] A.M. Hasofer, V.R. Beck, I.D. Bennetts, Risk Analysis in Building Fire Safety Engineering, Elsevier Butterworth-Heinemann, 2007.
- [2] Rasbach, D.J., Ramachandran, G., Kandola, B., Watts, J.M., and Law, M., Evaluation of Fire Safety, Wiley, 2004.
- [3] Liu, Z, Carpenter, D., dan Kim, A.K. (2005), Application of Water Mist to Extinguish Large Oil Pool Fires for Industrial Oil Cooker Protection, 8th International Symposium on Fire Safety Science, Beijing, China, pp. 1-12.
- [4] Kim, M.B., Jang, Y.J., and Yoon, M., Extinction Limit of a Pool Fire with a Water Mist, Fire Safety Journal 28 (1997) 295-306.
- [5] Mawhinney, J.R and Gerard G. Back III, Water Mist Fire Suppression Systems, Chapter 14 The SFPE Handbook of Fire Protection Engineering, 3rd Edition, 2002, pp. 4-311-4-337.
- [6] Wighus, R., Aune, P., and Brandt, A.W., Water Mist versus Sprinklers and Gas Fire Suppression Systems –Differences and Similarities, International Water Mist Conference, Amsterdam, The Netherlands 10 - 12 April 2002.
- [7] Nugroho, Y.S., Fajarudin, K., Wahyulianto, D., dan Harinaldi, Pengembangan Sistem Kabut Air Bertekanan Rendah untuk Pemadaman Pool Fire, Seminar Nasional Tahunan Teknik Mesin SNTTM-VI Banda Aceh Nanggroe Darussalam Univ Syiah Kuala 20-22 Nop 2007, ISBN 979-97726-8-0.

# Preparation of Activated Carbon from Low Rank Coal with CO<sub>2</sub> activation

Awaludin Martin, Bambang Suryawan, Muhammad Idrus Alhamid, Nasruddin

Refrigeration and Air Conditioning Laboratory, Mechanical Engineering Department  
Faculty of Engineering-University of Indonesia  
awaludin\_martin@yahoo.com

## ABSTRACT

The aim of this research is to produce activated carbon from Indonesian low rank coal. Activated carbon producing basically involve the following step; raw material preparation, carbonization and activation by physical or chemical method and for this research were use physical activation methods. Beside carbonization process (by N<sub>2</sub> gas) up to temperature 950°C, in this research carbonization with O<sub>2</sub> also were use up to temperature 300°C by variation time of process up to 360 minute. Physical activation method were use in this research by CO<sub>2</sub> as activating agent up to temperature 950°C by variation time of process up to 360 minute. Surface condition of activated carbon is known by Scanning Electron Micrograph (SEM) and iodine number was use to known quality of activated carbon. The result of this research is the maximum of burn off and iodine number are 71,88% and 589,10 g/kg.

Keyword: coal, activated carbon, burn off, Iodine number

## INTRODUCTION

Activated carbon consumption is continuously being increased because they are used in important areas such as waste, drinkable water treatments, atmospheric pollution control, poisonous gas separation, solvent recovery etc (Marsh, Harry and Francisco Rodriguez-Reinoso, 2006). Almost any carbonaceous material can be converted into activated carbon such as wood, nut shell, coconut shell, coal etc (Marsh, Harry and Francisco Rodriguez-Reinoso, 2006)

Activated carbon is the most widely used sorbent, surface area of activated carbon up to 4000 m<sup>2</sup>/g (Yang, Ralph. T, 2003) thus activated carbon can adsorb an adsorbate in high capacity.

Beside surface area, other parameters to know activated carbon quality is iodine number. Iodine number is defined as the amount of iodine (in milligrams) adsorbed by powdered carbon (per gram) from 0.02 N iodine aqueous solution (ASTM D4607-94) (Yang, Ralph. T, 2003). Iodine number is a simple testing to find activated carbon quality and iodine number has been roughly correlated to the surface area of pores >10<sup>3</sup> diameter (Yang, Ralph. T, 2003).

In this research, low rank coal were used as starting material to producing activated carbon. The modern manufacturing processes to produce activated carbon basically involve the following steps: raw material preparation, low-temperature carbonization, and physical or chemical activation (Yang, Ralph. T, 2003). In this research beside carbonization process (by N<sub>2</sub> as inert gas) up to temperature 950°C, oxidation process also done ( by variation of O<sub>2</sub> flowing) up to temperature 300°C with variation time of process up to 360 minute. Physical activation with CO<sub>2</sub> as activating agent were done up to temperature 950°C with variation time of process up to 360 minute.

## EXPERIMENT SECTION

**Coal Characteristics.** Low rank coal were use as the starting material and the analysis of coal as shown below:

q	Inherent Moisture	: 5,59 %
q	Ash Content	: 17,96 %
q	Volatile Matter	: 34,51 %
q	Fixed Carbon	: 41,94 %
q	Total Sulphur	: 1,74 %

Certificate of Sampling and Analysis, 2007, PT. Superintending Company of Indonesia (Sucofindo)

**Experimentation of Prosedure.** The as-received coals were crushed and sieved to a particle size of 2-10 mm before being treated. The production of activated carbons by a



physical activation technique was completed in an vertical autoclave activation reactor with a furnace. There are three variation process heat treatment to produced activated carbon. The processing to produce activated carbons were as follows:

1. Carbonization; Pyrolysis of fresh coals were performed in a furnace under a stream of High purity of N<sub>2</sub> at ± 40 cm<sup>3</sup>/minute as inert gas. The samples were heated from room temperature to maximum heat treatment temperatures in 600°C for 1 hour. Following the carbonization process, the char samples were gasified, also in the furnace, in a stream of CO<sub>2</sub> at ± 40 cm<sup>3</sup>/minute. The samples were heated from room temperature to maximum heat treatment temperatures in 600°C, 700°C, and 750°C for 1 hour. Scheme of this procedure as shown in figure 1a.

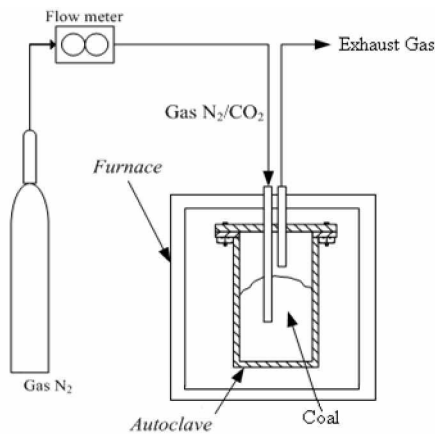


Figure 1a: Scheme of activated carbon; Carbonization and activation

2. Carbonization; Pyrolysis of fresh coals were performed in a furnace under a stream of High purity of N<sub>2</sub> at ± 80 cm<sup>3</sup>/minute as inert gas. The samples were heated from room temperature to maximum heat treatment temperatures in 900 °C for 1 hour. Following the carbonization process, the char samples were gasified, also in the furnace, in a stream of CO<sub>2</sub> at ± 80 cm<sup>3</sup>/minute. The samples were heated from room temperature to maximum heat treatment temperatures in 950°C for 3 hour.
3. Carbonization or Oxidation; Pyrolysis of fresh coals were performed in a furnace under a stream of High purity of O<sub>2</sub> at variation of gas flow. The samples were heated from room temperature to

maximum heat treatment temperatures in 300 °C for 1, 3 and 6 hour. Following the carbonization process, the char samples were gasified, also in the furnace, in a stream of CO<sub>2</sub> at ±80, 100 and 150 cm<sup>3</sup>/minute. The samples were heated from room temperature to maximum heat treatment temperatures in 950 °C for 1, 3 and 6 hour. Scheme of this procedure as shown in figure 1b.

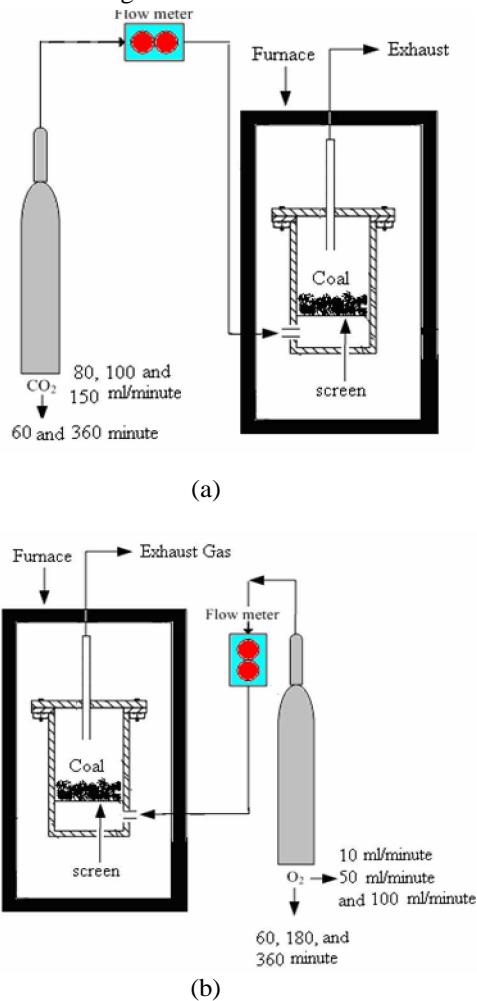


Figure 1b: Scheme of activated carbon; Carbonization or Oxidation Process with O<sub>2</sub> (a) and Activation Process (b)

After the above process activated carbon were crushed and sieved to a particle size of 10 x 20 mesh.

**Activated Carbon Characterization.** Scanning Electron Micrograph to show surface condition were done in Jakarta and Iodine number test were done in Bogor



**RESULT AND DISCUSSION**

In this work the result for three processing to produce activated carbon were compared.

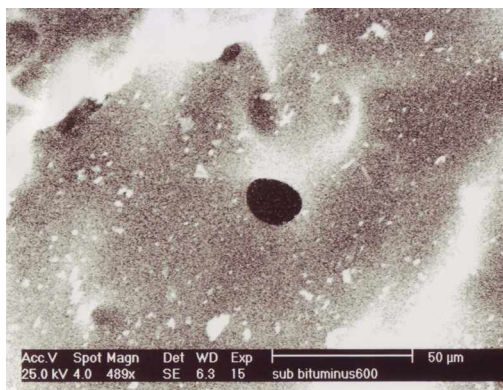
**First Procedure**

Table 1 describe the effect of temperature activation process on amount presentage of unsure in activated carbon, its impurity unsure still in activated carbon. First procedure is not resulting the optimum activated carbon yet, the maksimum unsure of carbon in activated carbon only 48,53%. The major unsure in activated carbon is carbon and is present to the extent of 85 to 95%. In addition, activated carbons contain other elements such as hydrogen, nitrogen, sulfur and oxigen (Bansal R.C. et al., 2005).

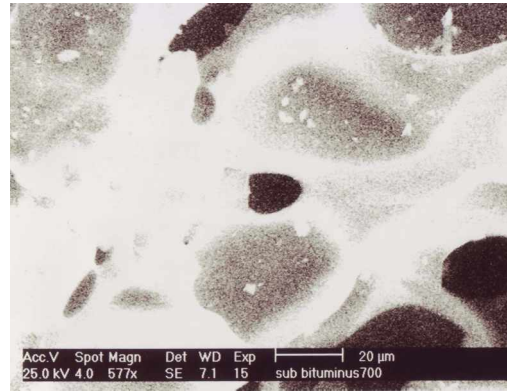
Tabel 1. First layer unsure of Activated Carbon

Temp. Process	Unsure			
	Carbon (%)	Oxigen (%)	Sulphur (%)	Ferro (%)
600 °C	47,89	29,44	22,67	-
700 °C	24,74	8,15	5	62,11
750 °C	48,53	4,4	1,73	45,35

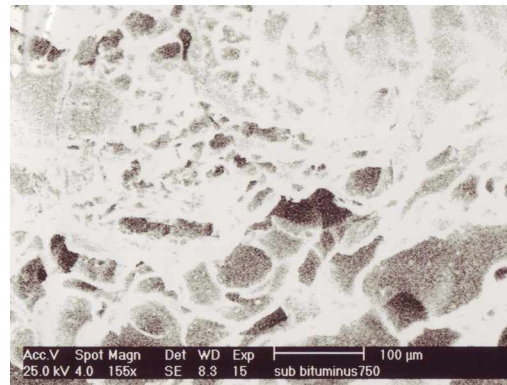
It can be seen in figure 2 that the macropore from activated carbon were performed but almost all the surface still covered with impurity unsure and from table 1 the impurity unsure are oxigen, sulphur and ferro.



(a)



(b)



(c)

Figure 2: Activated carbon from first procedure at 600°C (a), 700°C (b), dan 750°C (c)

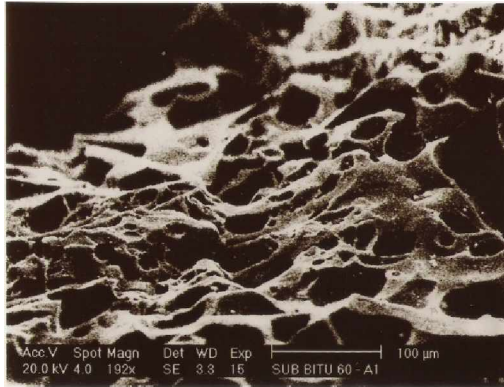
**Second Procedure**

Table 2 describe the effect of activation time on amount of carbon, longer activation time result in higher amount of carbon.

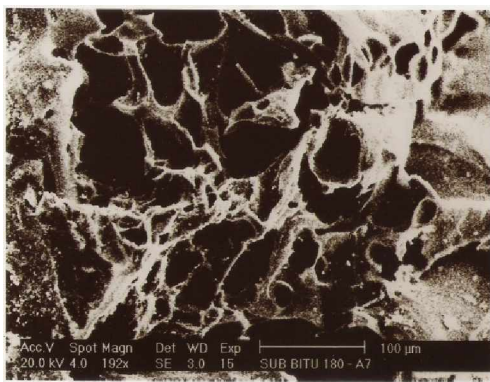
Tabel 2 First layer unsure of Activated Carbon at second Procedure

Time of Activation Process	Unsure			
	Carbon (%)	Oxigen (%)	Sulphur (%)	Ferro (%)
60 minute	75,22	9,33	7,57	7,88
180 minute	88,19	7,47	4,34	-

It can be seen in figure 3, the macropore from activated carbon were performed but almost all the surface still covered with impurity unsure and from table 2 the impurity unsure are oxigen, sulphur and ferro.



(a)



(b)

Figure 3. Activated Carbon; carbonization at 900°C and activation temperature 950°C with variation time of process activation 1 hour (a) and 3 hour (b) (Alhamid. M.I. et al., 2008)

Figure 4 describe the effect of activation time on burn-off and surface area. It can be seen from figure 4, in general longer activation time result in higher burn-off and surface area. This result was consistent with Marsh, Harry et al., 2006, that activation process influence of mass flow rate of activating agent and activation time.

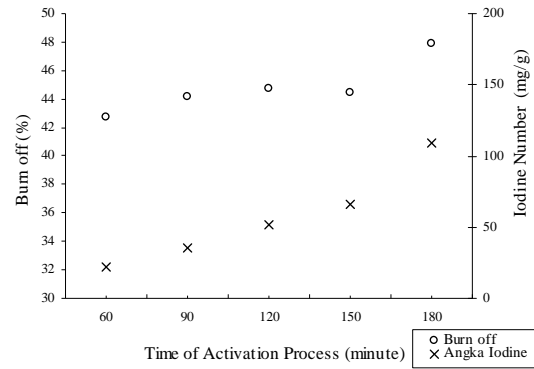


Figure 4. Weight loss or burn off and Iodine Number during activation process with heat treatment temperature 950°C

### Third Procedure

Beside influences of heat rate, mass flow rate of activating agent, activating agent, equipment and activation time, activation process also influence with ratio oxygen and carbon in raw material (Teng, Hsisheng et al., 1996).

In this procedure, carbinozation with N<sub>2</sub> as inert gas at first and second procedure were changes with O<sub>2</sub> up to temperatur 300°C. The aim of this procedure are to increasing oxygen unsure at the raw material. Activation process were done with CO<sub>2</sub> as activating agent up to temperature 950°C by variation of CO<sub>2</sub> flow and time of process.

Figure 5 describe the effect of stream of O<sub>2</sub> and time of process on burn-off. It can be seen from figure 5, in general longer carbonization time and bigger of steram of O<sub>2</sub> resulting in higher burn-off. This result is consistent with Teng, Hsisheng et al., 1996, that ratio of oxygen and carbon in the coal is ones of factor to improving quality of activated carbon product.

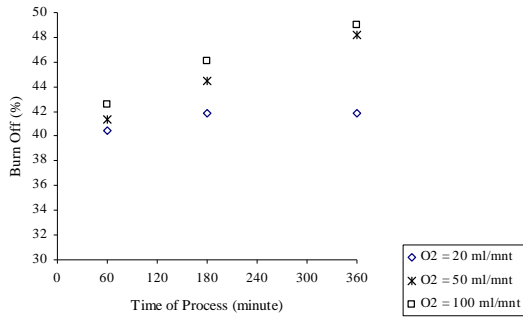


Figure 5. Weight loss or burn off during Oxidation process with heat treatment temperature 300°C by variation of O<sub>2</sub> flow 20, 50, and 100 ml/minute and for 1 hour activation process

Figure 6 describe the effect of time of process activation on burn-off and iodine number. It can be seen from figure 6, in general longer activation time resulting in higher burn-off and iodine number.

Coal were carbonized by 100 ml/minute O<sub>2</sub> up to 300°C for 6 hour, Following the carbonization process, the char samples were gasified, also in the furnace, in a stream of CO<sub>2</sub> at ± 80 cm<sup>3</sup>/minute up to 950°C with variation time of process are 1, 3, and 6 hour. The

maksimum burn off and iodine number in this process are 60,44% and 497,9 mg/g.

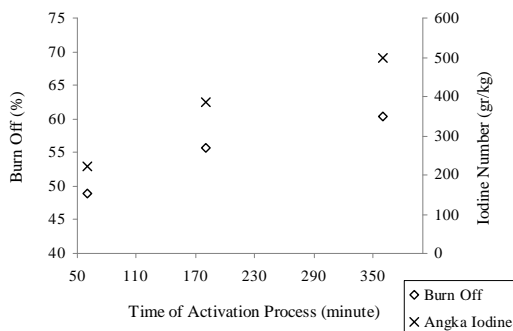
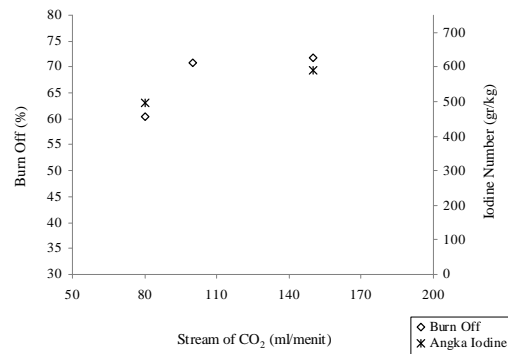


Figure 6. Weight loss and Iodine Number during activation process with heat treatment temperature 950°C

Figure 7 describe the effect of stream of CO<sub>2</sub> on burn-off and iodine number. It can be seen from figure 7, in general bigger stream of CO<sub>2</sub> resulting in higher burn-off and iodine number.

Coal were carbonized by 100 ml/minute O<sub>2</sub> up to 300°C for 6 hour, Following the carbonization process, the char samples were gasified, also in the furnace, in a stream of CO<sub>2</sub> at ± 80, 100, and 150 cm<sup>3</sup>/minute up to 950°C for 6 hour. The maksimum burn off and iodine number in this process are 71,88% and 589,1mg/g.



Gambar 7. Weight loss and Iodine Number during activation process with heat treatment temperature 950°C during activation process

The of result of the third procedure was consistent with Marsh, Harry et al., 2006, that activated carbon producing influence of mass flow rate of activating agent, temperature of process and activation time.

CONCLUSION

1. Activated carbon were produced from low rank coal with carbonization

- and activation process with variation of temperature, stream of Nitrogen, Oxygen and carbon dioxide, time of oxidation and activation process.
2. Producing of activated carbon was influences with mass flow rate of activating agent, Heat treatment temperature and activation time of process also ratio oxygen and carbon in raw material
  3. Weight losses or burn off is similiar with iodine number, increasing weight loss will increasing iodine number thus the surface area will be larger too
  4. The maximum weight loss or burn off and iodine number of activated carbon in this research is 71,88% and 589,10 g/kg by carbonization (by O<sub>2</sub> stream ±100 ml/minute for 6 hour) and activation process (by CO<sub>2</sub> stream ±150 ml/minute for 6 hour).

- [6] Teng, Hsisheng, Jui-An Ho, Yung-Fu Hsu, and Chien-To Hsieh, 1996, *Preparation of Activated Carbons from Bituminous Coals with CO<sub>2</sub> Activation*. 1. *Effects of Oxygen Content in Raw Coals*, *Ind. Eng. Chem. Res.*, 35 (11), 4043 -4049, American Chemical Society
- [7] Yang, Ralph. T, 2003, *Adsorbents: Fundamentals and Applications*, John wiley and Sons Inc, New Jersey.

#### REFERENCE

- [1] Alhamid, M. Idrus d, Bambang Suryawan, Nasruddin, Awaludin Martin, Sehat Abdi, Characterization of Activated Carbon as Adsorbent From Riau Coal by Physical Activatin Method, The First International Meeting on Advances in Thermo-fluids, Universiti Teknologi Malaysia, Malaysia, 26th August 2008
- [2] Bansal, Roop Chand & Meenakshi Goyal, 2005, *Activated Carbon Adsorption*, Taylor & Francis Group, USA
- [3] Certificate of Sampling and Analysis, 2007, PT. Superintending Company of Indonesia
- [4] Marsh, H. & Rodriguez-Reinoso, F. 2006, *Activated Carbon*, Elsevier Ltd, Oxford UK.
- [5] Rouquerol, Jean, François Rouquerol, Kenneth Sing, 1998 *Absorption By Powders And Porous Solids*, Elsevier



## Experimental Study of Characteristic and Performance of Non-Branded Thermoelectric Module

Zuryati Djafar, Nandy Putra, Raldi A. Koestoer

Heat Transfer Laboratory, Mechanical Engineering Department, University of Indonesia  
Kampus Baru UI, Depok, 16424- West Java-Indonesia

Phone: +62-081355026518, Fax: 021-7270033, email: [ydjafar@yahoo.com](mailto:ydjafar@yahoo.com)

Correspondence: [Nandyputra@eng.ui.ac.id](mailto:Nandyputra@eng.ui.ac.id)

### Abstract

Thermoelectric modules is thermoelement devices that can take advantage to convert heat into electric energy. As an electrical energy generating system, these elements are not noisy, easy to maintain and relatively small dimension, light and friendly to the environment because it does not produce pollution. The aim of this research is to evaluate and to determine characteristic of thermoelectric module as a non-branded (not accompanied by brand and specifications) thermoelectric generator system. The method is carried out in this research is to drain the fluid (hot water) from a Circulating Thermostatic Bath into a water block; the thermoelectric module is inset between water block and a heatsink-fan. The results show that a Thermoelectric module on the 4 temperature conditions of the CTB temperature 35 °C, 40° C, 45 °C and 50 °C can provide a temperature difference of 5.4°C, 7.6°C, 11.7°C and 14.8°C with output power obtained are 3.07W, 19.02W, 42.8W and 65.13W respectively.

**Keywords:** characteristic, non branded, thermoelectric module, circulating thermostatic bath, water block, output power

### I. INTRODUCTION

Thermoelectric generator modules work on the principle of work of Seebeck effect [1], the effect occurs when there are two different materials connected in a circuit is closed and the second connection maintained at different temperatures the electrical current will flow in the circuit, and when one wire decided then connected with a galvanometer, it will show the voltage difference of the two ends. So that the difference in temperature can cause the voltage difference that produces electromotive force.

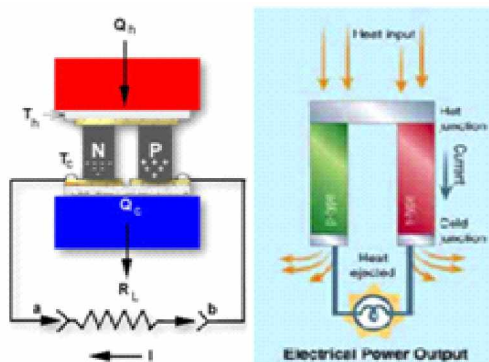


Figure 1. Mechanism of Seebeck Effect Principles [2]

Source: Melcor Industries, ([www.melcor.com](http://www.melcor.com))

Thermoelectric modules are typically measuring 40mm x 40mm or smaller and have more or less thick, 4 mm. Age of a Thermoelectric Module in accordance with industry standards is approximately 100000-200000 hours and more than 20 years when used as a coolant and the amount and the appropriate voltage characteristics of each module [3].

In the Thermoelectric planning, both for its use as a cooling system and using Thermoelectric generator module, there are 3 parameters that must be considered are: Q = heat load to be moved (watts); Tc = temperature of cold surface of the module (°C); Th = temperature of hot side surface of the module (°C). Heat Load is the total number of heat that must be removed by Thermoelectric modules from the object to be cooled / heat to the environment is taken [4].

A Thermoelectric modules can be characterized by comparing the maximum performance with a hot junction temperature. Parameters on a mutual interdependence. Electric power applied to Thermoelectric modules are:

$$P_{in} = V \times I$$

Where: P<sub>in</sub> is Electrical power (Watt); V is line voltage (Volt); I is Current Electricity (Ampere) Currently there are many Thermoelectric modules on the market. Thermoelectric modules are freely

Therefore deemed necessary to conduct the test specifications so that they can actually know capabilities that can be produced from these Thermoelectric modules. From the characteristics, the buyer can know the actual characteristics, as desired. Does economic considerations or the quality that will be used.

## II. RESEARCH METHOD

Therefore, in this study was conducted to determine the characteristics of Thermoelectric modules are non-branded.

Accordance with the purpose of the study to be conducted to determine the characteristics of non-branded Thermoelectric modules (modules without specification), then this research made a test installation as figure 2 below:

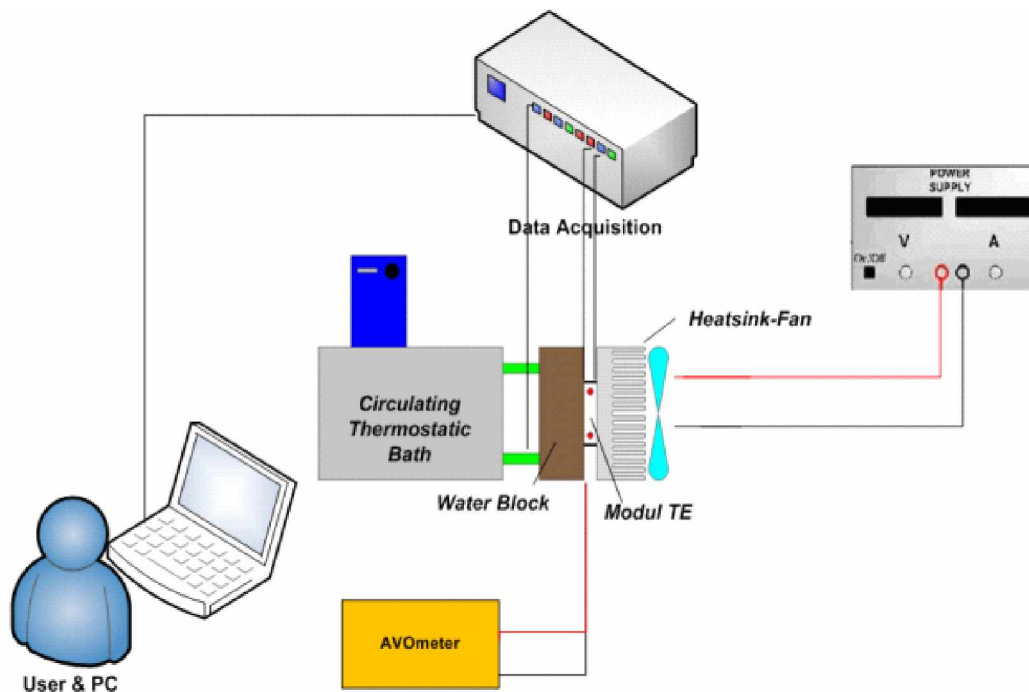


Figure 2. Testing Installation

### Mechanism of the Data Retrieval

Observations long test 1800 seconds (30 minutes) for each fluid temperature condition in the circulating Thermostatic Bath (CTB). Variation of fluid temperature conditions of the CTB are 35°C, 40°C, 45°C and 50°C.

Thermoelectric modules are placed between the water block and heatsink-fan, on both sides of the module (hot side and cold side) each placed a type K thermocouple wire, thermocouple is connected to the gauge ADAMtech special type of temperature measurement that is connected to the computer as a data acquisition. Another thermocouple wires placed in the water channel in and out of the water block. Two thermocouple wires in the fluid in the CTB and to the environment (ambient).

Temperature measurement data on the number 6 wire thermocouples were recorded directly in the form of a notepad file and can be read visually on the screen with the help of computer software that will be used Advantech. The data read is  $T_{hot}$  and Peltier elements  $T_{cold}$  side, fluid Temperatur of Water Block, Temperatur Circulating Thermostatic Bath (CTB), Current and voltage generated from the second junction of Thermoelectric module through the display reads AVOMeter used. Data of current, voltage and temperatures then is used to calculate the power output of a given and a large temperature difference on both sides of Thermoelectric modules.

## III. RESULT AND DISCUSSION

fluid temperature at the surface of the heat source side heat Thermoelectric modules.

**Table 1. Power Output at temperature difference ( $\Delta T$ ) for 4 temperatures condition of CTB**

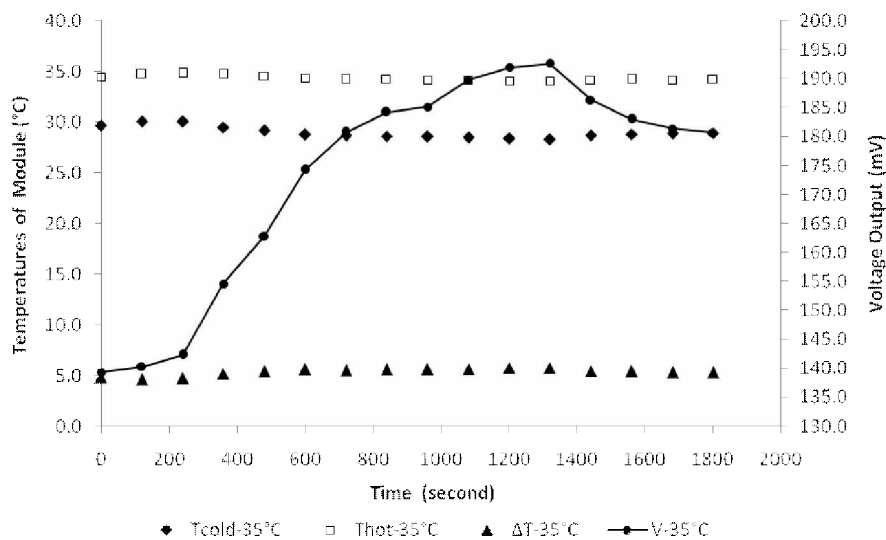
Temp CTB (°C)	Module 01		Module 02		Module 03	
	Power (watt)	$\Delta T$ (°C)	Power (watt)	$\Delta T$ (°C)	Power (watt)	$\Delta T$ (°C)
35	4.10	6.1	3.07	5.4	2.50	5.2
40	17.58	8.4	19.02	7.6	5.0	2.6
45	30.65	9.5	42.8	11.7	19.79	9.4
50	44.46	15.0	65.13	14.8		

Table 1 above shows the data measured in the temperature difference between hot and cold side of Thermoelectric modules, with output power obtained for each temperature condition of the CTB 35 ° C, 40 ° C, 45 ° C and 50°C.

The graph in Figure 1 describes the characteristics of No. 2 of Thermoelectric modules using heat source of hot fluid temperature conditions CTB at 35°C.

Hot side temperature Thermoelectric modules obtained around 34.3 ° C from the heat of hot fluid 35°C and cold side temperature can be maintained around 29.0°C so that the temperature difference is obtained for 5.4°C.

With temperature difference of about 5.4° C, the maximum voltage and the average voltage obtained from Thermoelectric modules are approximately 192mV and 173.1 mV with the current flows of about 16 mA so that the maximum output power and an average output power of 3.07 W and 2.8 W.



**Figure 1. Temperatures and Voltage output of Module Vs Time with heat source of fluid 35°C**

Figure 2 below, shows a somewhat different characteristics from the previous image, where the voltage is obtained, the initial maximum of 317 mV but decreases as the addition of a given measurement time and eventually looks voltage constant at 297 mV, while the average voltage of obtained approximately 303 mV with an electric

current that flows around 60 mA, so that the maximum power output and the average generated by 19.02 W and 18.2W. In Figure 2, the temperature difference obtained between the hot side temperature of 37.8°C and cold side temperature of 30.2°C Thermoelectric module is relatively constant 7.6 °C.



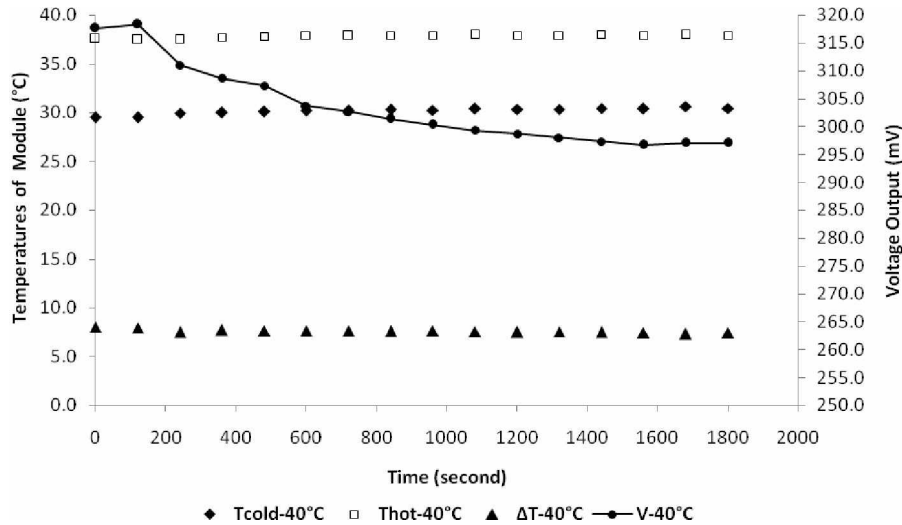


Figure 2. Temperatures and Voltage output of Module Vs Time with heat source of fluid 40°C

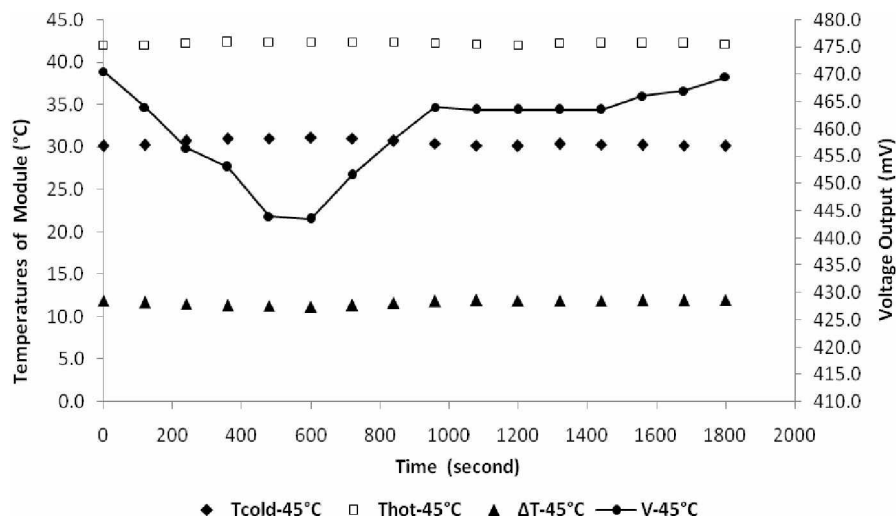


Figure 3. Temperatures and Voltage output of Module Vs Time with heat source of fluid 45°C

Thermoelectric module characteristics in Figure 3 shows that increasing of the temperature differences as increasing of fluid temperatures in the circulating Thermostatic Bath (CTB) as a source of heat. Temperature difference is obtained for 11.7°C with a temperature of hot and cold side of the module for 42.2°C and 30.5°C.

With increasing temperature difference obtained, voltage and power generated also showed improvement. Maximum and average voltage of 470.5 mV and 460.1 mV, while the maximum and the average output power of 42.8W and 41.9W with a large current flows of about 91 mA.

The higher temperature heat source fluid is given, the greater the temperature difference obtained. This has been shown in the three graphs obtained.

In Figure 4, also shown an increasing temperature difference between the two sides of the Thermoelectric module on the fluid temperature conditions in the CTB 50 ° C, i.e about 14.8°C with a temperature hot side and cold side of the Thermoelectric modules, are 46.6°C and 31.8°C. Maximum and average voltage are found about 581.5mV and 570.3 mV with current flowing around 112 mA, so the maximum and an

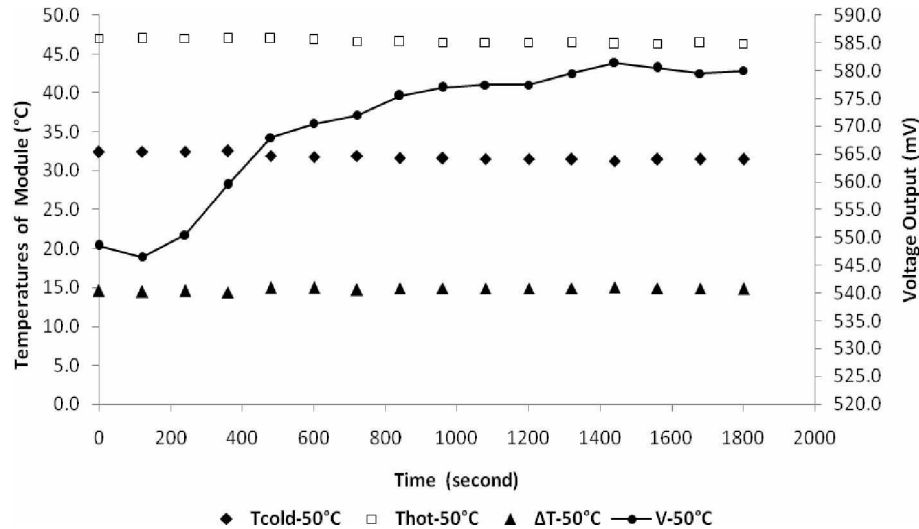


Figure 4. Temperatures and Voltage output of Module Vs Time with heat source of fluid 50°C

#### IV. CONCLUSION

The conclusion that can be obtained from testing the four temperatur conditions of the Circulating Thermostatic Bath (CTB) 35 °C, 40 °C, 45 °C and 50 °C with an interval of observation during 1800 seconds (30 minutes) are as follows:

- The higher temperature heat source fluid is provided (hot fluid), the greater the temperature difference obtained.
- The optimal temperature difference gives the output voltage, current and maximum output power.
- Improving the conditions of temperature of CTB 5°C, producing a large increase in voltage of 100 mV.
- The maximum output power obtained from the four variations of temperature conditions CTB 35 °C, 40 °C, 45 °C and 50°C, are 3.07W, 19.02W, 42.8W and 65.13W.

#### ACKNOWLEDMENT

This work was supported within the DRPM-UI program of the University of Indonesia (project number S3/2009/I/3625).

#### REFERENCES

- [1]. [www.melcor.com](http://www.melcor.com)
- [2]. Riffat, S.B, Ma .Xiaoli. 2003. *Thermoelectrics: a review of Present and Potential Applications*.

Applied Thermal Engineering 23 (2003) 913-935. Pergamon-Elsevier Science Ltd

- [3]. Nandy Putra, Axel Hidayat, 2006. *Pengembangan Alat Uji Kualitas dan Karakteristik Elemen Peltier*, Seminar Nasional Tahunan Teknik Mesin V, Universitas Indonesia, 21-23 November 2006, ISBN 979-977726-8-0.
- [4]. Anonymous. *Thermoelectric Handbook*. Accessed from [www.melcor.com](http://www.melcor.com), on October. 29. 2006.

# Development Mathematical Modelling For Design and Analysis Proton Exchange Membrane Fuel Cell

Hariyotejo Pujowidodo<sup>a</sup>, Verina Januati Wargadalam<sup>b</sup>,  
Ahmad Indra Siswantara<sup>c</sup>

<sup>a</sup>*Centre for Thermodynamics, Engine and Propulsion System*

*Agency for Assessment and Application of Technology*

*Puspiptek Serpong Tangerang 15314*

*Telp. (021) 7560539 Fax. (021) 7560538*

*E-mail : h\_pujowidodo@yahoo.co.id*

<sup>b</sup>*Research and Development Centre for The Electricity and Renewable Energy Technology*

*Ministry of Energy and Mineral Resources Cipulir Jakarta*

*Telp. (021) 7203530 Fax. (021) 7203525*

*E-mail : verinawargadalam@yahoo.com*

<sup>c</sup>*Faculty Engineering*

*University of Indonesia, Depok 16424*

*Tel : (021) 7270011 ext 51. Fax : (021) 7270077*

*E-mail : a\_indra@eng.ui.ac.id*

## Abstract

The study of mathematical modelling has been done for Proton Exchange Membrane Fuel Cell (PEMFC) using Computational Fluid Dynamics tools. The aim of this activity is to simulate the current density respected to reactant gas distribution in the parallel and serpentine electrode channels. The defined analysis domains are channel path and diffusion layer, with the boundary condition of operation pressure and mass flow rate. The obtaining result shows that using the relation current and species concentration, the serpentine channel model has bigger pressure drop flow than parallel. The bigger pressure drop would increase reactant gas distribution on the diffusion layer.

## 1. INTRODUCTION

### 1.1. Background and Objectives

Decreasing fossil fuel reserves as result of industrial and population development has lead to the new invention in the renewable energy. The others impact of this energy development are global climate change and air pollution resulting from fossil combustion process. One of the most versatile renewable energy, in the case of efficiency and environment friendly, is fuel cell technology. This technology uses hydrogen fuel to convert chemical potential energy into electrical energy through chemical reaction, called electrochemical. The application area begins from mini portable electrical device, automobile until power generating in industry. The

compactness and efficiently fuel consumption and energy conversion makes fuel cell as the future expectation energy for human life.

Recently fuel cell design and analysis development has much done through numerical and simulation model for study the reaction improvement. The basic principle of momentum, mass and energy transport being used to develop mathematical differential model in numerical solver. From result of modelling could be predicted pressure distribution, velocity, concentration and also reactant gas temperature which are useful in comprehending distribution characteristic of gas to electric current performance yielded.

## 1.2. Literature Review

### 1.2.1. PEMFC Technology

PEMFC or Proton Exchange Membrane Fuel Cell is a device of electrochemical energy converter through oxidation and reduction process at a compact electrolyte membrane. This reaction produces ionization of proton and electron which is conducted to pass electrolyte membrane and external payload yields water product in cathode side as a place of the happening of reduction reaction. Concisely the process in PEMFC is shown as follows:

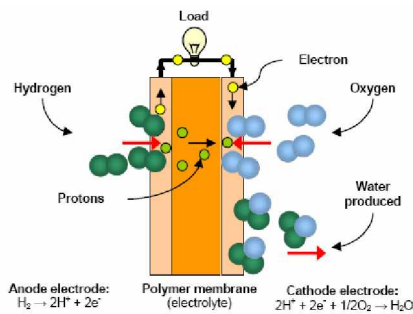
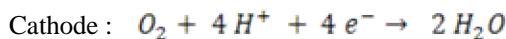
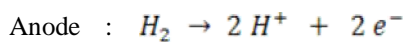


Figure 1. Fuel Cell Reaction Process<sup>[10]</sup>



### 1.2.2. Reaction Rate

Electrochemical reaction rate determined by activation energy limit for electron, to transfer from the electrolyte to electrode or vice versa. This reaction velocity depends on the yielded electron, named electric current. Current

density is current (electron or ion) per reaction surface area unit, the value determined by Faraday's law as follows:

$$i = nF j \quad (1-1)$$

Where:  $nF$  is transfer charge (electron/mol) and  $j$  is reactant flux (mol/s.m<sup>2</sup>)

In electrochemical reaction, oxidation and reduction occur on the anode and cathode with the following reaction:

Forward reaction (cathode):



Backward reaction (anode):



For equilibrium condition on the electrode, no external current flow, oxidation and reduction take place on the same rate:



And reactant species consumption on reaction surface is proportional to concentration according to relation:

Cathode:

$$j_f = k_f C_{ox} \quad (1-5)$$

Anode:

$$j_b = k_b C_{red} \quad (1-6)$$

$k_b$  and  $k_f$  are coefficient of reaction rate

The generated current is difference between forward current and backward current:

$$i = nF(k_f C_{ox} - k_b C_{red}) \quad (1-7)$$

### 1.2.3. Mathematical Description and Physical Conservation

Numerical solution for heat transfer, fluid flow and other related process started by arranging Governing Laws for physical process, which expressed in the form of mathematical, generally in the equation form of differential terms. Variable is generalizing by through a modelling

analysis of system with decision of quantitative conservation at one particular volume analysis model arranges (control volume). In a system physical of come near by simplification using discretization elements (dividing) and solving equation of continuity by entering variable limiting value physical of as limiting value numerical calculation.

### 1.2.4. Control Differential Equation

Decision of conservation utilized in building a mathematical modelling for fluid flow system is consisted:

- Fluid mass flow is constant.
- Momentum rate of change equal to number of fluid particle forces (Newton second's law).
- Energy change rate is total heat flow and work in at fluid particle (First Law of Thermodynamics)

### 1.2.5. Mass Conservation and Property Change Rate

In obtaining the mathematical differential equation for fluid mass flow, firstly writing down the equilibrium state of fluid element refers to velocity and cross area as follow:

Mass accumulation in fluid element = mass inflow netto

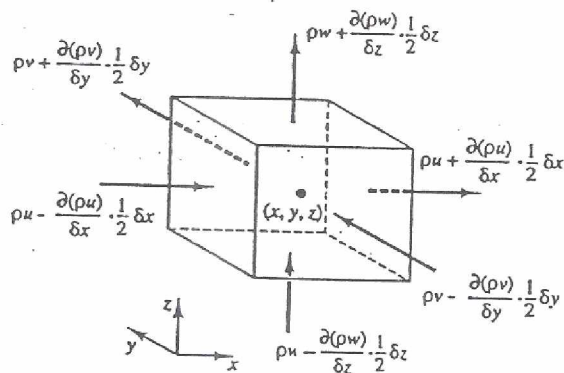


Figure 2. Fluid mass equilibrium

In vector notation form stated generally:

$$\frac{\partial \rho}{\partial t} + \text{div}(\rho \mathbf{u}) = 0 \quad (1-10)$$

Which is conservation for compressible fluid element 3 dimensional

Physical property change determined by convective term inward/outward (as result of existing flow).

For incompressible flow, the differential equation is:

$$\frac{\partial u}{\partial x} + \frac{\partial v}{\partial y} + \frac{\partial w}{\partial z} = 0 \quad (1-11)$$

In analyzing transformation of property in a numerical model for conservation of mass and momentum, every property influenced by variables of position (distance) and time. If property is calculated per mass unit is  $\Phi$ , hence total derivative determined through derivative total to distance and time as follows:

$$\frac{D\Phi}{Dt} = \frac{\partial \Phi}{\partial t} + \frac{\partial \Phi}{\partial x} \frac{\partial x}{\partial t} + \frac{\partial \Phi}{\partial y} \frac{\partial y}{\partial t} + \frac{\partial \Phi}{\partial z} \frac{\partial z}{\partial t} \quad (1-12)$$

$$\frac{D\Phi}{Dt} = \frac{\partial \Phi}{\partial t} + \frac{\partial \Phi}{\partial x} u + \frac{\partial \Phi}{\partial y} v + \frac{\partial \Phi}{\partial z} w = \frac{\partial \Phi}{\partial t} + \mathbf{u} \cdot \text{grad } \Phi \quad (1-13)$$

For property change rate per volume stated by :

$$\rho \frac{D\Phi}{Dt} = \rho \left( \frac{\partial \Phi}{\partial t} + \mathbf{u} \cdot \text{grad } \Phi \right) \quad (1-14)$$

Hence in the general form of mass conservation becoming :

$$\frac{\partial \rho \Phi}{\partial t} + \text{div}(\rho \Phi \mathbf{u}) = 0 \quad (1-15)$$

### 1.2.6. Momentum Conservation

Newton second's law states that momentum change rate equal to the resultant of acting forces that is:

Momentum accumulation in the direction of x, y and z are  $\rho \frac{Du}{Dt}$ ,  $\rho \frac{Dv}{Dt}$ ,  $\rho \frac{Dw}{Dt}$

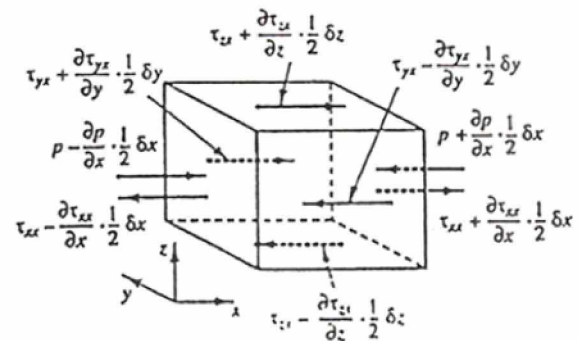


Figure 3. Force Equilibrium in x direction

By vanishing body force, and entering the momentum source rate per volume  $S_M$ , the momentum change rate becomes :

$$\rho \frac{Du}{Dt} = \frac{\partial(-p+\tau_{xx})}{\partial x} + \frac{\partial\tau_{yx}}{\partial y} + \frac{\partial\tau_{zx}}{\partial z} + S_{Mx} \quad (1-16)$$

$$\rho \frac{Dv}{Dt} = \frac{\partial\tau_{xy}}{\partial x} + \frac{\partial(-p+\tau_{yy})}{\partial y} + \frac{\partial\tau_{zy}}{\partial z} + S_{My} \quad (1-17)$$

$$\rho \frac{Dw}{Dt} = \frac{\partial\tau_{xz}}{\partial x} + \frac{\partial\tau_{yz}}{\partial y} + \frac{\partial(-p+\tau_{zz})}{\partial z} + S_{Mz} \quad (1-18)$$

### 1.2.7. Species Conservation

Within chemical reaction phenomena, the interaction among reactant species forms reaction product, analysis process of numerical system involving species fraction (mass) wherein species conservation governed by a mathematical differential equation as follows:

$$\frac{\partial}{\partial t}(\rho m_i) + \text{div}(\rho u m_i + J_i) = R_i \quad (1-19)$$

$\frac{\partial}{\partial t}(\rho m_i)$  is species mass change rate per volume and  $\rho u m_i$  term is species convection flux caused by flow field  $\rho u$ , whereas  $J_i$  indicates diffusion flux as a result from mass fraction gradient, which expressed in Fick's Law :

$$J_i = -\Gamma_1 \text{grad } m_i \quad (1-20)$$

$\Gamma_1$  is coefficient of diffusion, so if substituted becoming

$$\frac{\partial}{\partial t}(\rho m_i) + \text{div}(\rho u m_i) = \text{div}(\Gamma_1 \text{grad } m_i) + R_i \quad (1-21)$$

$R_i$  is generation rate of chemistry species per volume unit.

## 2. Developed Methods

### 2.1. Modelling

As modelling system in this study, takes formation area of discretization based on 2 dimension model and one part of passage channels, either parallel channel and turning one (serpentine). Secondly domain area system divided into region of electrode plate gas flow channels and gas diffusion layer as integration of arrangement of electrolyte membrane (MEA, Membrane Electrolyte Assembly). For the definition of process condition, it would be needed information such as temperature, pressure for

hydrodynamic simulation; material and reactant properties for mass transport.

Simplified process has been defined in model as follows:

- Steady state and membrane full humidified with ideal water and heat management
- Single phase water transport in diffusion layer and gas channel
- Low Reynold number, so flow is laminar
- Isothermal and pressure is inversely proportional to species volume
- Reactant governed by Ideal Gas Law

### 2.2. Implementation

Model simulation for reactant flow distribution in PEMFC was built with CFD tools software EFD. Computational domain generated using CAD model, consisted of channel paths and diffusion layer. The condition of operation and dimension given in the following table :

Table 1. Data of Simulation Model

Constraint Parameters	Boundary Condition/Value
Channel Distribution	Paralel dan Serpentine
Flow Modes	Internal flow
Simulation Modes	Steady flow
Fluid Modes	Hidrogen and Oksigen
Momentum Dimensional	2 D
Species Dimensional Modes	1 D
H <sub>2</sub> inflow (@ 1 A)	0,04 kg/h
O <sub>2</sub> inflow (@ 1 ampere)	0,02 kg/h
Static Pressure out	108.218 Pa (1 Psig)
Electrode Porosity	0,4
Diffusion Layer thickness	23 μm
Electrolyte membrane Area	50 cm <sup>2</sup> (73 mm x 73 mm)
Electrode Channel Depth	1 mm
H <sub>2</sub> mass fraction in and out	1 and 0
O <sub>2</sub> mass fraction in and out	1 and 0

### 2.3. Evaluation

In this section would be done the assessment of momentum and mass distribution, accordingly there are three parts of analysis such as:

#### 2.3.1. Computational Model

The aim of this step is to know approaching level that used in solid modelling, process criterion and calculation solving. Solid modelling was done by using integrated or



compatible Computer Aided Design. The importance thing of this stage is the exactly fluid domain bounded by electrode channel side. The working fluid in this simulation has the type of internal flow with steady state condition and using hydrogen and oxygen as reactant and oxidant. Particularly for mass transport, we have to define parameters such as porosity, permeability, thickness of diffusion material and also the relation drop pressure and mass flow. In this model it used the value of pressure as much as 200 Pa at the maximum mass flow.

### 2.3.2. Pressure Drop Calculation

To verify pressure distribution as result of simulation model, it is used the Darcy Weisbach correlation to calculate the pressure drop which depend on the roughness wall and the change of cross area or solid boundary.

$$\Delta P \dots = \dots f \frac{l}{d} \frac{v^2}{2} \quad (2-1)$$

Where :

- $\Delta P$  = pressure drop (Pa)
- $l$  = channel length (m)
- $d$  = channel width/depth (m)
- $v$  = fluid velocity (m/det)
- $f$  = losses factor

For roughness factor , pressure drop calculated by for laminar flow :

$$f \dots = \dots \frac{64}{Re} \quad \text{where} \quad Re \dots = \dots \rho \frac{vd}{\mu} \quad (2-2)$$

Meanwhile for the cross area change, solved by the equation form as follow :

$$\Delta P \dots = \dots \rho \frac{u_2^2}{2g} \left[ \frac{1}{C_c} - 1 \right]^2 \quad (2-3)$$

In which :

- $u_2$  = flow velocity at downstream
- $C_c$  = area rasio upstream/downstream

### 2.3.3. Reactant Consumption

Analytically the species concentration distribution from simulation would be verified by theoretical prediction of reactant consumption rate. Faraday law states current as the function of number of electron, reactant consumption rate and Faraday Constant, in the following equation :

$$i = n F J \quad (2-4)$$

$i$  = generated current (A, ampere)

$n$  = number of ionized electron (reduction=4, oxidation=2)

$F$  = Faraday constant = 96485 Coulomb/mol

$J$  = consumption rate of reactant (mol/s)

And for the output parameter of simulation, would be evaluated using ideal gas law to obtain species mol rate, as follow:

$$P V = N R_{univ} T \quad (2-5)$$

With the explanation of parameters :

- $P$  = species preesure (atm)
- $V$  = spesies mol rate (mol/s) =  $J$
- $R_{univ}$  = universal gas constant  
= 0,0821 litre.atm/mol.K
- $T$  = species temperature ( $^{\circ}$ K)

## 3. Analysis and Result

### 3.1. Computational Model

Using EFD software could be briefly explained the step of modelling consists of:

#### 3.1.1. Solid modelling

It is geometry model that contains domain area of working fluid. In this model must be defined the solid boundary of wall also inlet and outlet sides. The area of reaction surface of diffusion membrane is 50 cm<sup>2</sup>.

#### 3.1.2. Boundary Condition

Giving the boundary value at inlet and outlet sides (control surface) as the operation criteria. At inlet side defined by the mass flow condition of each hydrogen and oxygen as reactant and oxidant. Meanwhile at the outlet given by condition of pressure as written in table 1 before. For mass transport or diffusion, it has to enter the value of properties such as porosity, permeability, thickness and the pressure drop through membrane.

#### 3.1.3. Meshing

It is the method of generating control element to solve numerical calculation of mathematical differential from the governing laws. For momentum conservation, could be



solved meshing on the surface of symmetry plane of channel path. Whereas for species conservation, it is used the isometric model of domain that covers channel area and membrane material (catalyst layer).

### 3.1.4. Mesh Optimization

This is the way of analyze the exactly control element been generated to get the better accuracy numerical calculation.

### 3.1.5. Calculation Goals

It has the aim to assist observing convergence calculation by giving the equation of pressure drop between upstream and downstream (inlet and outlet).

### 3.1.6. Solver

This is a numerical calculation phase of differential equation governing momentum and mass transport phenomena. In this step the evolution of calculating parameters can be monitored in the graphical form.. As calculation goals in this simulation are static pressure and mass fraction from hydrogen gas species and oxygen.

### 3.1.7. Post Processing

Result of simulation can be observed at part of post processor through menu Cut Plot by choosing parameter static pressure and mass fraction. This thing to assist in analyzing reactant gas flow characteristic in PEM Fuel Cell channels.

## 3.2. Reactant Distribution Characteristic

In parallel channel the flow characteristics showed by the recirculation caused by the cross flow area changing and branching. Whereas in serpentine the existing bended passages in channel gives more restriction. From result of modelling revealed pressure drop is 5400 Pa and in parallel as many as 4200 Pa.

## 3.3. Drop Pressure Calculation

The pressure loss of flow happened as result of geometry form and cross area dimension difference causing the happening of energy loss. According to calculation manual by considering loss factor by surface roughness and change of cross area, there was calculation difference 600 Pa ( around 14%) compared to result of simulation. This thing could be caused by accuracy factor of calculation number applied in process of iteration by software. Despitefully also calculation approach applied is channel system analogue with plumbing system, where the different far

dimension between channel and pipe causes difference result of calculation.

## 3.4. Current Density Calculation

As approach comparison of this PEM Fuel Cell modelling system is by applying manual calculation from faraday law and ideal gas equation. Current density was determined as value benchmarking factor. From analysis calculation obtained result of difference 0,02 A to theoretical calculation. It means that deviation factor of calculation is very small.

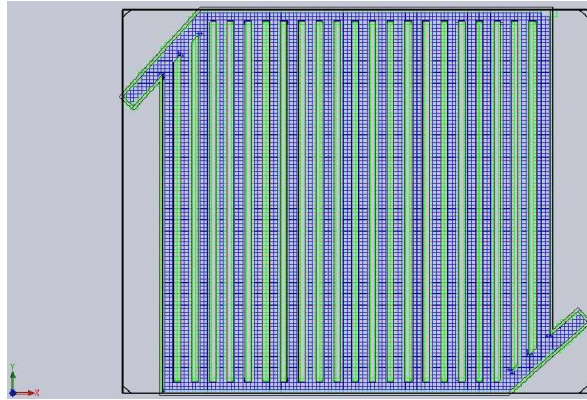
## 4. Conclusion

- a. Qualitatively flow channels hardly influences flow characteristics and also distribution of gas reactant. Flow recirculation at parallel channel resulted from by change of area and geometry flow, causing distribution of different momentum. Diffusion passes through porous media with higher level gas concentration generates non-uniformity flow.
- b. Difference result of pressure drop calculation with manual calculation caused by difference value of fluid properties and definition of computing domain less optimal as has been shown in meshing of serpentine channels. This thing is because of wide comparison between width- length is too far.
- c. Reactant gas pressure influences number of concentration of gas applied as main variable to determine level of electric current yielded.
- d. Pressure of reactant gas in reaction channel influenced by diffusion layer material , that is property level of pressure drop at diffusion material. More higher pressure drop at diffusion material hence amounts concentration of gas would increasingly rising whereas the flow velocity would decrease.
- e. Distribution serpentine channels to have pressure drop characteristic larger ones compared to parallel , this thing is as result of level of loss of flow generated by deformation of geometry channel. But loss as result of existence of opponent flow ( recirculation) very low so that accentual loss especially happened as result of bend factor.
- f. Generally modelling of PEM Fuel Cell by using tools simulation requires specific data of system material especially at diffusion material that is pressure drop influence and porosity, a real determines reactant mass diffusion rate .

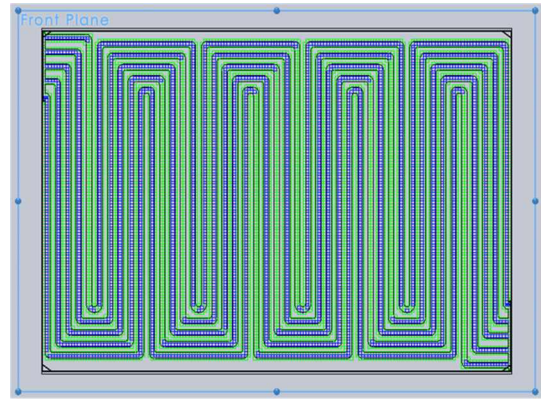
## References

1. Armstrong, K.W.(2004). *Theses : A Microscopic Continuum Model of a Proton Exchange Membrane Fuel Cell Electrode Catalyst Layer*. Virginia, Mechanical Engineering Virginia Polytechnic Institute and State University.
2. National Energy Technology Laboratory Office of Fossil Energy U.S. Department of Energy.(2004). *Fuel Cell Handbook* , seventh edition, West Virginia.
3. Guilin, H. , Jianren, F.(2006). *A Three-Dimensional, Multicomponent, Two-Phase Model for a Proton Exchange Membrane Fuel Cell with Straight Channels*, *Journal of Energy & Fuels*.
4. Hesty, N.W, Wargadalam, V.J.(2007). *Model Dua Dimensi Distribusi Fraksi Air dan Kerapatan Arus Pada Fuel Cell Berbasis Polimer (PEMFC)*, Puslitbangtek Ketenagalistrikan dan Energi Baru Terbarukan.
5. Liu, H., Zhou, T. (2005). *Transport Phenomena Analysis in Proton Exchange Membrane Fuel Cells*, *Journal of Heat Transfer*, vol. 127, No. 12, pp. 1363–1379,  
©2005 American Society of Mechanical Engineer.
6. Ma, L. et.al.(2005). *Review of the Computational Fluid Dynamics Modelling of Fuel Cells*, *Journal of Fuel Cell Science and Technology*, vol.2, No. 4, pp. 246-257.
7. Nguyen, P.T., et.al, *Computational Model of PEM Fuel Cell with Serpentine Gas Flow Channels*, *Journal of Power Sources*, Desember 2003.
8. Patankar, S. V.(1980), *Numerical Heat Transfer and Fluid Flow*, Hemisphere Publishing, USA.
9. Pillay, P. Dr., Professor, *Fuel Cells*, Concordia Power Electronics & Energy Research Group (PEER), Dept of Electrical & Computer Engineering, Concordia University.
10. Siegel , N.P. (2003). *Dissertation : Development and Validation of a Computational Model for a Proton Exchange Membrane Fuel Cell* , Mechanical Engineering Virginia Polytechnic Institute and State University, Virginia.
11. Shimpalee, S. , Greenway, S., Van Zee, J.W.(2006). *The impact of channel path length on PEMFC flow-field design* , *Journal of Power Sources*.
12. Berning, T., Djilali, N.(2003). *Three-dimensional computational analysis of transport phenomena in a PEM fuel cell—a parametric study* , *Journal of Power Sources*.
13. Versteeg, H.K, Malalasekera, W..(1995). *An Introduction to Computational Fluid Dynamics The Finite Volume, Method*, Longman Group, England.
14. Wargadalam, V. J., Rochani , S.(2006). *Evaluasi Pengaruh Kandungan Air Pada Reaktan Terhadap Kinerja Sel Tunam Membran Penukar Proton (PEMFC)*, Puslitbangtek Ketenagalistrikan dan Energi Baru Terbarukan DESDM, Puslitbangtek Teknologi Mineral dan Batubara, DESDM.

## Attachments



(a)



(b)

Figure A.1. Mesh Distribution in Parallel (a) and Parallel (b) Channels

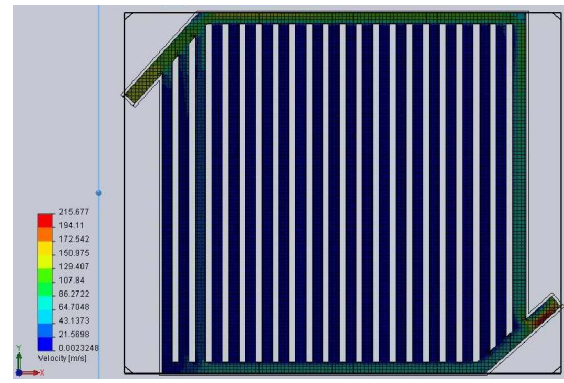
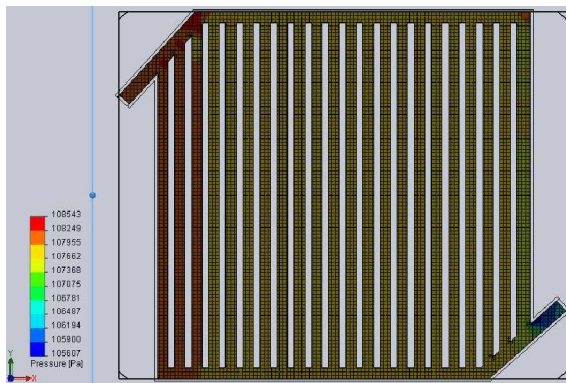


Figure A.2. Momentum Distribution in Parallel Channels

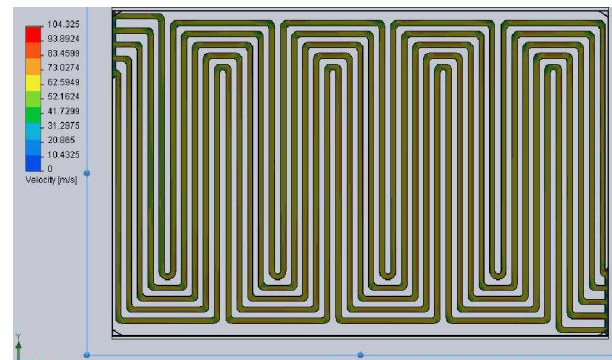
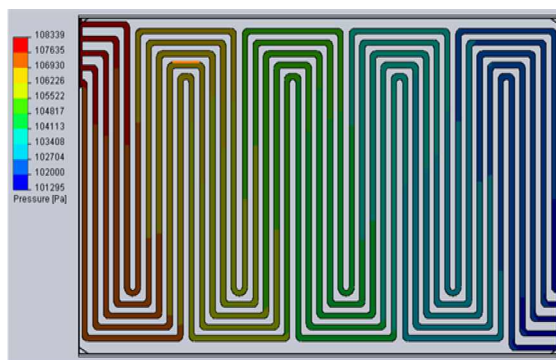
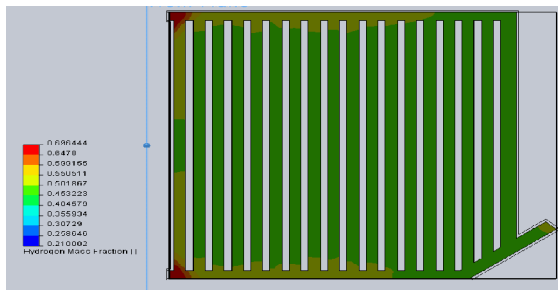
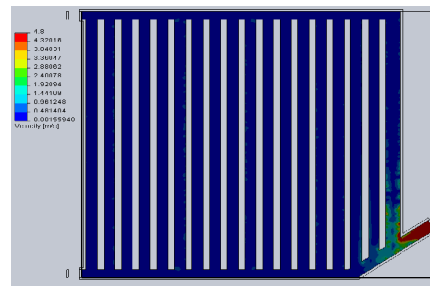


Figure A.3. Momentum Distribution in Serpentine Channels

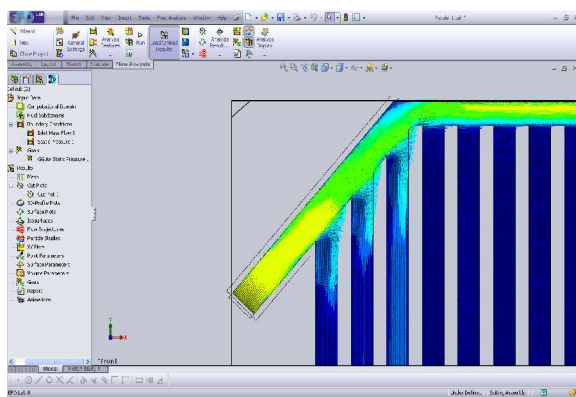


(a)

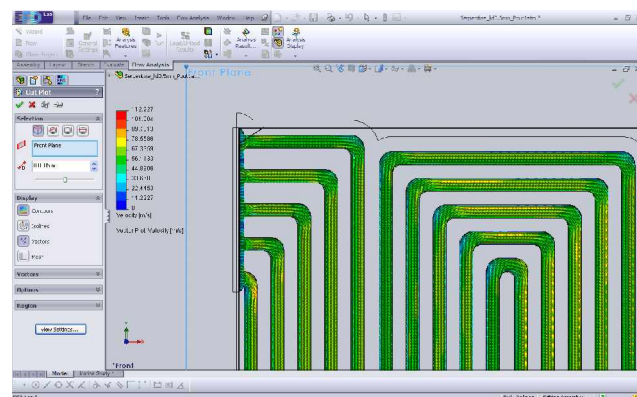


(b)

Figure A.4. Mass (a) and velocity (b) Distribution in Parallel Channel



(a)



(b)

Figure A.5. Local Velocity Distribution in Parallel (a) and Serpentine (b)

<b>Process data</b>		
Massflow total	0,04 kg/hA	
each channel	0,04 kg/hA	
	1,11111E-05 kg/sA	
velocity	75,37964961 m/s	inlet channel inclined
u	53,3014614 m/s	45 derajat
v	53,3014614 m/s	45 derajat
<b>Hidrogen Properties</b>		
rho	0,08189 kg/m3	
mhu	8,41E-06 kg/ms	
<b>Channel Dimension</b>		
width average	1,8 mm	0,0018 m
max inlet cross area	2,6 mm2	
min inlet cross area	1 mm2	0,000001 m2
Vena contracta Cc	0,384615385	
min velocity	135,6833693 m/s	
height	1 mm	0,001 m
area	1,8 mm2	0,0000018 m2
total volume	1,02E-06 m3	
header volume	13 mm3	0,000000013 m3
length	5,66E+02 mm	5,66E-01 m
each channel		5,66E-01 m
channel number	1	
Friction loss factor		
f	4,84E-02	
Reynold	1,32E+03	
<b>Pressure drop</b>		
	3,6658E+03	total
	3,5429E+03 Pa	friction loss
	1,2294E+02 Pa	narrowment loss
Simulation result	4234 Pa	
max press	107357 Pa	
min press	111591 Pa	

Table A.1. Verification of Pressure Drop on Parallel channel



<b>Process data</b>			
Massflow total	0,04 kg/hA		
each chanr	0,008 kg/hA		
	2,22222E-06 kg/sA		
<b>Hydrogen Properties</b>			
rho	0,08189 kg/m3		
mhu	8,41E-06 kg/ms		
Normal velocity	2,71E+01 m/s	inlet angle	0 deg
x dir	0,00E+00 m/s		
y dir	2,71E+01 m/s		
<b>Channel dimension</b>			
width	1 mm	1,00E-03 m	
height	1 mm	1,00E-03 m	
area	1 mm2	1,00E-06 m2	
total volume	8,21E-07 m3		
header volume	0 mm3	0,00E+00 m3	
length	8,21E+02 mm	8,21E-01 m	
per kanal		1,64E-01 m	
channel number	5		
<b>Friction loss factor</b>			
f	2,42E-01		
<b>Reynold</b>			
	2,64E+02		
<b>Pressure drop</b>			
	6,00E+03	total	
	1,20E+03	1 channel	
<b>Simulation result</b>			
max press	5483 Pa		
min press	108127 Pa		
	113610 Pa		

Table A.2. Verification of Pressure Drop on serpentine channel



**Faraday's Law : (mole and current density)**

$$i = n \cdot F \cdot N$$

**Gas Ideal's Law ( molar volume and pressure with T constant)**

$$P \cdot V = N \cdot R_{univ} \cdot T$$

$$V/N = R_{univ} \cdot T/P$$

**Data and Calculation**

Manual

	i	n	F	N	Runiv	T	P	V
	(ampere/cm <sup>2</sup> )	(elektron)	(C/mol.e)	(mol)	(L.atm/mol.K)	(°K)	(atm)	(L)
Anoda	1	2	96485	5,18215E-06	0,0821	333,15	1,068029	0,000132712

Simulation

P <sub>sim</sub>	T <sub>sim</sub>	R <sub>univ</sub>	V	N	n	F	i
(atm)	(°K)	(L.atm/mol.K)	(L)	(mol)	(elektron)	(C/mol.e)	(ampere/cm <sup>2</sup> )
1,078494942	333,15	0,0821	0,000132712	5,23294E-06	2	96485	1,009799664

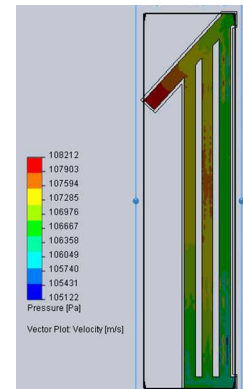
**Volume Molar**

P 1,068029 atm  
 T 333,15 K  
 Runiv 0,0821 liter.atm/mol.K  
 V/N 25,60944 L/mol

**Local Average Pressure Values (Bulk Average)**

Local parameters

Parameter	Minimum	Maximum	Average	Bulk Average	Surface area [m <sup>2</sup> ]
Pressure [Pa]	72599,8	138435	107070	106837	0,00043502
Temperature [K]	333,012	334,076	333,201	333,198	0,00043502
Density [kg/m <sup>3</sup> ]	0,0825623	0,189542	0,143575	0,144487	0,00043502
Velocity [m/s]	0,00148298	147,698	0,222424	5,23666	0,00043502
X-component of Vel	-3,74047	1,98046	0,00171822	-0,0672449	0,00043502
Y-component of Vel	-3,41653	2,74168	0,000325748	0,00399084	0,00043502
Z-component of Vel	-30,1666	147,681	-0,0977631	3,28936	0,00043502
Mach Number [ ]	1,4314E-06	0,135682	0,000218516	0,00507745	0,00043502
Fluid Temperature [ ]	333,012	334,076	333,201	333,198	0,00043502



Local parameters

Parameter	Minimum	Maximum	Average	Bulk Average	Surface area [m <sup>2</sup> ]
Pressure [Pa]	87038,7	424332	108786	111720	0,00259929
Temperature [K]	320,581	340,758	333,083	333,025	0,00259929
Density [kg/m <sup>3</sup> ]	0,0853876	0,572226	0,148359	0,152518	0,00259929
Velocity [m/s]	0,00056902	16,6885	0,0472553	0,194508	0,00259929
X-component of Vel	-7,01265	16,6884	6,38143E-05	-0,00642013	0,00259929
Y-component of Vel	-1,09981	0,257316	-0,000343652	-0,00405717	0,00259929
Z-component of Vel	-0,554637	0,538524	-0,00196644	-0,0126595	0,00259929
Mach Number [ ]	5,625E-07	0,0165715	4,66542E-05	0,000192179	0,00259929
Fluid Temperature [ ]	320,581	340,758	333,083	333,025	0,00259929

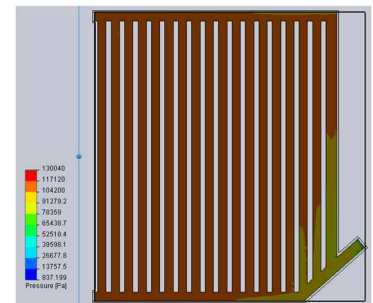


**Table A.2. Verification of Current Density**

# Experimental Study and Correlation of Two-Phase Flow Evaporation Heat Transfer Coefficient of Propane in Intermittent, Stratified Wavy and Annular Flows

Agus S. Pamitran<sup>a</sup>, Jong-Taek Oh<sup>b</sup>

<sup>a</sup>*Department of Mechanical Engineering,  
University of Indonesia, Kampus Baru UI, Depok 16424, Indonesia  
Tel : +62-21-727-0032 ext 233. Fax : +62-21-727-0033  
E-mail : pamitran@eng.ui.ac.id*

<sup>b</sup>*Department of Refrigeration and Air-Conditioning Engineering,  
Chonnam National University, San 96-1, Dunduk-Dong, Yeosu, Chonnam 550-749, Republic of Korea  
Tel : +82-61-659-6273. Fax : +82-61-659-6279  
E-mail : ohjt@chonnam.ac.kr*

## ABSTRACT

Two-phase flow heat transfer coefficients for evaporative refrigerants in intermittent, stratified wavy and annular flows were evaluated in this study. The experimental data were obtained using propane over a heat flux range of 5 to 30 kW m<sup>-2</sup>, mass flux range of 50 to 600 kg m<sup>-2</sup> s<sup>-1</sup>, saturation temperature of 0 to 10°C, and quality up to 1.0. The test section was made of stainless steel tubes with inner diameters of 1.5 mm and 3.0 mm. The flow pattern of the experimental data was evaluated with existing flow pattern maps. The experimental boiling heat transfer coefficients were compared with some existing correlations based on the flow pattern. A new correlation for flow boiling heat transfer coefficient that is based on a superposition model for refrigerants in small tubes is presented.

**Keywords:** *Propane, Flow boiling, Flow pattern, Heat transfer coefficient, Correlation, Horizontal small tubes*

## 1. INTRODUCTION

Such awareness has led to a demand for environmental friendly evaporation refrigerants in smaller evaporators, which are used in the refrigeration and air conditioning. Propane, as long term alternative refrigerants, will be important in the future for compact heat exchanger applications due to their performance and their environmental friendliness with zero Ozone Depletion Potential (ODP) and zero Global Warming Potential (GWP). Evaporation in small tubes has great advantages: high heat transfer

coefficient, significant size reduction of compact heat exchangers, and lower required fluid mass. However, heat transfer of two-phase flows in small tubes cannot be properly predicted using existing procedures and correlations because they are more suitable for large tubes and for general flow pattern condition. There are relatively few published works on two-phase flow boiling heat transfer of refrigerants in small tubes based on flow pattern. Several studies have dealt with two-phase flow boiling in small tubes, such as reported by Tran et al. (1996), Zhang et al. (2004), Pettersen (2004) and Yun et al. (2005). Wang et al. (1997) and Wojtan et al. (2005) have proposed flow pattern maps for two-phase flow boiling heat transfer. However, the existing prediction methods of heat transfer coefficient could not predict well the current experimental data for individual flow pattern.

This study was performed to obtain experimental data for propane and to evaluate the heat transfer coefficient based on flow pattern during the evaporation in small tubes. The experimental results were compared with the predictions from several existing heat transfer coefficient prediction methods. Due to the limitations of the correlation for forced convective boiling of refrigerants in small tubes, a new correlation of heat transfer coefficient based on flow pattern for evaporative refrigerant in small tubes was developed in this study.

## 2. EXPERIMENTAL FACILITY AND DATA REDUCTION

The schematic experimental facility is shown in

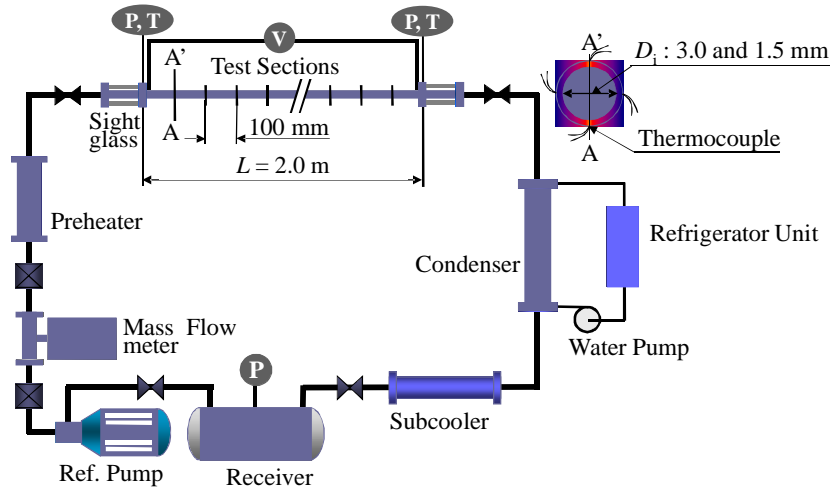


Figure 1: Experimental test facility

Test section	Horizontal circular smooth small tubes
Quality	up to 1.0
Working refrigerant	Propane
Inner diameter (mm)	3.0 and 1.5
Tube length (mm)	2000
Mass flux (kg/(m <sup>2</sup> ·s))	50 – 600
Heat flux (kW/m <sup>2</sup> )	5 – 30
Inlet $T_{in}$ (°C)	10

Figure 1. The test facility includes a subcooler, receiver, refrigerant pump, mass flow meter, preheater, and test sections. A variable A.C output motor controller was used to control the flow rate of the refrigerant. A Coriolis-type mass flow meter was installed in the horizontal layout. A preheater was installed to control the mass quality of the refrigerant before entering the test section. For evaporation at the test section, a certain heat flux was conducted from a variable A.C voltage controller. The vapor refrigerant from the test section was then condensed in the condenser and subcooler, and then the refrigerant was supplied to the receiver.

The test section was made of stainless steel circular smooth tubes with inner tube diameters of 1.5 and 3.0 mm. The test sections were uniformly and constantly heated by applying electric current directly to the tube walls, which were well insulated with foam and rubber. The outside tube wall temperatures at the top, both sides and bottom were measured at 100 mm axial intervals from where heating was started by

constant thermocouples at each site. The junctions of the copper-constantan thermocouples were attached to the lateral surface and were well electrically insulated. The local saturation pressure, which was used to determine the saturation temperature, was measured using bourdon tube type pressure gauges with 0.005 MPa scale at the inlet and the outlet of the test sections. The differential pressure was measured by a differential pressure transducer. Sight glasses with the same inner tube diameter as the test section were installed to visualize the flow. The experimental conditions used in this study were listed in Table 1. The physical properties of the refrigerants were obtained from REFPROP 8.0.

The local heat transfer coefficients at position  $z$  along the length of the test section were defined as follow.

$$h = \frac{q}{T_{wi} - T_{sat}} \quad (1)$$

The inside tube wall temperature,  $T_{wi}$  was the average temperature of the top, both right and left sides, and the bottom wall temperatures, and was determined based on the steady-state one-

dimensional radial conduction heat transfer through the wall with internal heat generation. The vapor quality,  $x$ , at the measurement locations,  $z$ , were determined based on the thermodynamic properties.

$$x = \frac{i - i_f}{i_{fg}} \quad (2)$$

The refrigerant flow at the inlet of the test section was not completely saturated. The subcooled length was calculated using Eq. (3) to determine the initial point of saturation.

$$z_{sc} = L \frac{i_f - i_{fi}}{\Delta i} = L \frac{i_f - i_{fi}}{(Q/W)} \quad (3)$$

### 3. FLOW PATTERN

The present experimental results were mapped on Wang et al. (1997) and Wojtan et al. (2005) flow pattern maps, which were developed for diabatic two-phase flows. The Wang et al. (1997) flow pattern map is a modified Baker (1954) map, developed using R-22, R-134a, and R-407C inside a 6.5 mm horizontal smooth tube. The Wojtan et al. (2005) flow pattern map is a modified Kattan et al. (1998) map, developed using R-22 and R-410A inside a 13.6 mm horizontal smooth tube. Kattan et al. (1998) used five refrigerants R-134a, R-123, R-402A, R-404A, and R-502 inside 12 mm and 10.92 mm (only for R-134a) tubes, which were heated by hot water flowing counter-currently to develop their flow pattern maps on the basis of the Steiner (1993) flow pattern map.

The predicted flow pattern for the selected current experimental data by the existing flow pattern maps of Wang et al. (1997) and Wojtan et al. (2005) can be seen in Figures 2 and 3, respectively. The Wang et al. (1997) map showed a better prediction of the flow pattern of the current experimental data for the beginning of annular flow than the Wojtan et al. (2005) map; however, the Wang et al. (1997) map could not show the prediction for dry-out condition. The flow pattern prediction of the current test results for the all test conditions with the Wang et al. (1997) flow pattern map was for the intermittent, stratified wavy, and annular flow. Figures 2 and 3 depicts that the stratified wavy flow appeared

earlier for higher mass fluxes and its regime was longer for the low mass flux condition. The annular flow appeared earlier for higher mass fluxes. The flow pattern prediction of the experimental results for all the test conditions with the Wojtan et al. (2005) flow pattern map was on intermittent, annular, dry-out, and mist flows. Because the Wojtan et al. (2005) map is developed using a conventional tube, the flow pattern transition of the present experimental data showed a delay on this map. Overall, Wang et al. (1997) flow pattern map provides a better flow pattern prediction for the current experimental results than the Wojtan et al. (2005) flow pattern map. Therefore, the heat transfer coefficient of this present study is evaluated based on the Wang et al. (1997) flow pattern map.

### 4. HEAT TRANSFER COEFFICIENTS

It is well known that the flow boiling heat transfer is mainly governed by two important mechanisms, namely nucleate boiling and forced convective heat transfer.

$$h_{tp} = h_{nb} + h_c \quad (4)$$

In two-phase flow boiling heat transfer, the nucleate boiling heat transfer contribution is suppressed by the two-phase flow, especially at high vapour quality region. At low quality region, the heat transfer coefficient is dominated by nucleate boiling heat transfer contribution, but at high quality region it is dominated by convective heat transfer contribution. This trend can be found in studies of Pamitran et al. (2007) and Choi et al. (2007). The nucleate boiling heat transfer contribution may be correlated with a nucleate boiling suppression factor,  $S$ . Another contribution of convective heat transfer may be correlated with a liquid single phase heat transfer. The  $F$  factor is introduced as a convective two-phase multiplier to account for enhanced convective due to co-current flow of liquid and vapor. A superposition model of heat transfer coefficient may be written as follow,

$$h_{tp} = Sh_{nbc} + Fh_f$$

(5) The heat transfer coefficients of the present study are compared with the results given by four

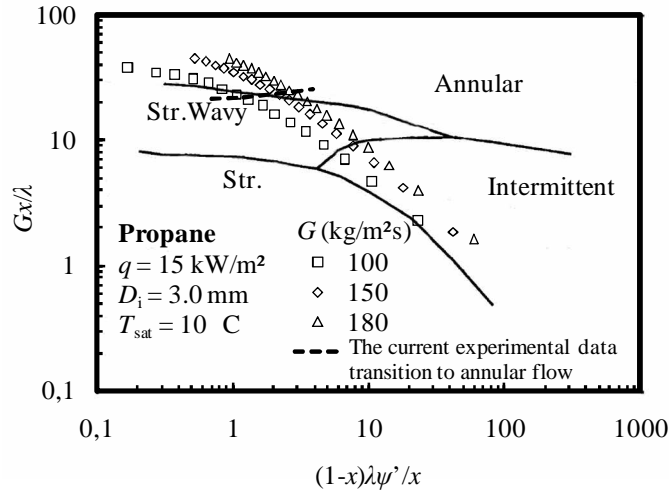


Figure 2: Present experimental results mapped on Wang et al. (1997) flow pattern map

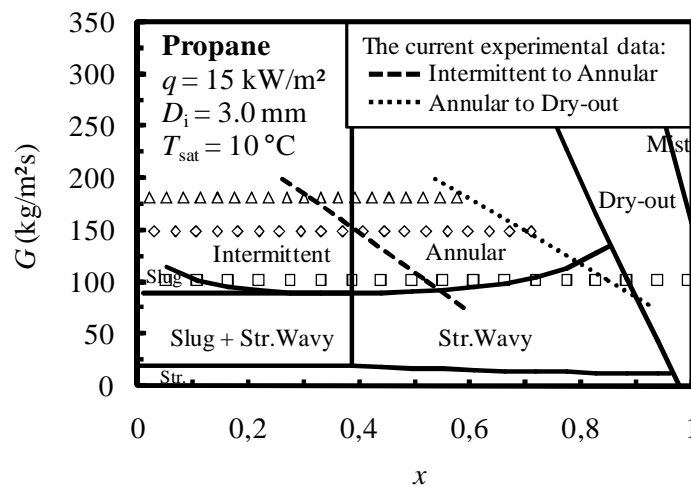


Figure 3: Present experimental results mapped on Wojtan et al. (2005) flow pattern map

Table 2: Deviation (%) of the heat transfer coefficient comparison between the present data and the prediction using existing correlations

Flow Pattern		Previous Correlations				
		Tran et al. (1996)	Shah (1988)	Jung et al. (1989)	Gungor-Winterton (1987)	Kandlikar (1990)
Intermittent	Mean Dev.	14.78	20.70	19.33	34.14	42.85
	Average Dev.	9.39	-3.63	7.86	33.66	-42.23
Stratified Wavy	Mean Dev.	14.68	23.22	24.84	29.21	63.65
	Average Dev.	-6.03	7.81	16.64	21.42	-63.65
Annular	Mean Dev.	25.01	34.59	36.01	35.42	67.70
	Average Dev.	-24.53	15.11	34.83	20.51	-67.49

correlations for boiling heat transfer coefficient as listed in Table 2. The Wang et al. (1997) flow pattern map is used to map the present experimental data. The comparison of heat transfer coefficient is based on flow pattern of intermittent flow, stratified wavy flow and annular flow. For heat transfer coefficient in intermittent flow, stratified wavy flow and annular flow, the best prediction is all given by the Tran et al. (1996). The Tran et al. (1996) correlation was developed for flow boiling heat transfer in small channels. The correlations proposed by Shah (1988) and Jung et al. (1989) also showed good prediction with the present experimental data. The Shah (1988) correlation was developed using a large data set for conventional tubes. The Jung et al. (1989) correlation was developed with pure and mixture refrigerants in conventional channels; its  $F$  factor contributed a big calculation deviation with the current experimental data.

The appearance of convective heat transfer for boiling in small tubes occurs later than it does in larger tubes because of its high boiling nucleation. Chen (1966) introduced a multiplier factor,  $F = \text{fn}(X_{tt})$ , to account for the increase in the convective turbulence that is due to the presence of the vapor phase. The function should be physically evaluated again for flow boiling heat transfer in a small tube that has a laminar flow condition, which is due to the small diameter effect. By considering the flow conditions (laminar or turbulent) in the Reynolds number factor,  $F$ , Zhang et al. (2004) introduced a relationship between the factor  $F$  and the two-phase frictional multiplier that is based on the pressure gradient for liquid alone flow,  $\phi_f^2$ . This relationship is  $F = \text{fn}(\phi_f^2)$ , where  $\phi_f^2$  is a general form for four conditions according to Chisholm (1967). For the liquid-vapor flow condition of turbulent-turbulent (tt), laminar-turbulent (vt), turbulent-laminar (tv) and laminar-laminar (vv), the values of the Chisholm parameter,  $C$ , are 20, 12, 10, and 5, respectively.

The  $F$  factor in this study is developed as a function of  $\phi_f^2$ ,  $F = \text{fn}(\phi_f^2)$ , where  $\phi_f^2$  is obtained from Eq. (6).

$$\phi_f^2 = \frac{\left(\frac{-dp}{dz} F\right)_{tp}}{\left(\frac{-dp}{dz} F\right)_f} = 1 + C \left[ \frac{\left(\frac{-dp}{dz} F\right)_g}{\left(\frac{-dp}{dz} F\right)_f} \right]^{1/2} + \frac{\left(\frac{-dp}{dz} F\right)_g}{\left(\frac{-dp}{dz} F\right)_f} \quad (6)$$

$$= 1 + \frac{C}{X} + \frac{1}{X^2}$$

The liquid heat transfer is defined by existing liquid heat transfer coefficient correlations by considering flow conditions of laminar and turbulent. For laminar flow,  $Re_f < 2300$ , the liquid heat transfer coefficient is obtained from the following correlation:

$$h_f = 4.36 \frac{k_f}{D} \quad (7)$$

For flow with  $3000 \leq Re_f \leq 10^4$ , the liquid heat transfer coefficient is obtained from Gnielinski (1976) correlation, where the friction factor is calculated from Eqs. (8) and (9).

$$f = 16Re^{-1}, \text{ for } Re < 2300 \quad (8)$$

$$f = 0.079 Re^{-0.25}, \text{ for } Re > 3000 \quad (9)$$

For flow with  $2300 \leq Re_f \leq 3000$ , the liquid heat transfer coefficient is calculated by interpolation. For turbulent flow with  $10^4 \leq Re_f \leq 5 \times 10^6$ , the liquid heat transfer coefficient is obtained from Petukhov and Popov (1963) correlation. Dittus Boelter (1930) correlation is used for turbulent flow with  $Re_f \geq 5 \times 10^6$ .

The new factor  $F$ , as illustrated in Fig. 4, is developed based on the flow pattern using a regression method. For all flow pattern, the new factor  $F$  is developed as Eq. (10).

$$F = \text{MAX} \left[ \left( 0.05 \phi_f^{2.2} + 0.76 \right), 1 \right], \text{ for } \phi_f^2 > 50$$

$$F = \text{MAX} \left[ \left( 0.64 \phi_f \right), 1 \right], \text{ for } \phi_f^2 \leq 50 \quad (10)$$

where  $\phi_f^2$  is obtained from Eq. (6).

The prediction of the nucleate boiling heat transfer for the present experimental data used Cooper (1984), which is a pool boiling correlation developed based on an extensive study.



Table 3: Coefficients for the Suppression Factor  $S$

Coefficients	Intermittent	Stratified Wavy	Annular
a	8.8083	112.2612	0.0026
b	-0.5846	2.1872	0.1786
c	0.2673	1.8048	-0.5981

Table 4: Deviation (%) of the heat transfer coefficient comparison between the present data and the prediction using the new developed heat transfer coefficient correlations

Deviation	Intermittent	Stratified Wavy	Annular	Overall
Mean	10.78	25.81	13.30	16.63
Average	-1.57	1.01	-1.36	-0.64

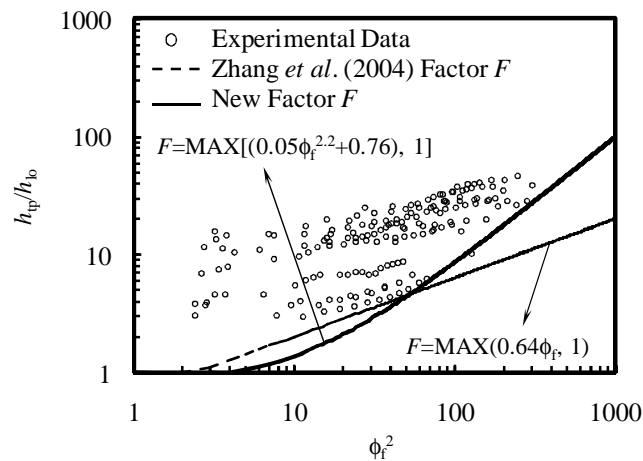


Figure 4: Two-phase heat transfer multiplier as a function of  $\phi_f^2$

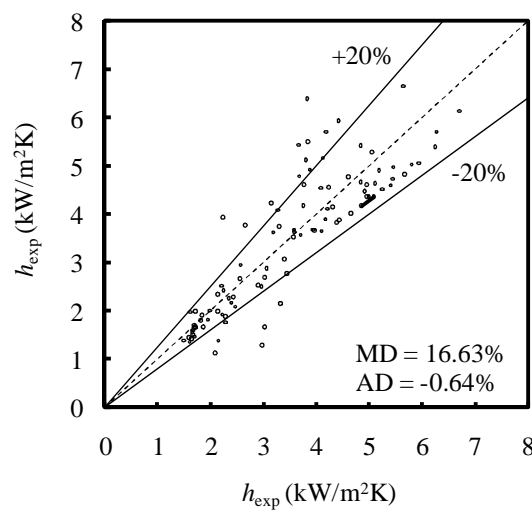


Figure 5: Diagram of the experimental heat transfer coefficient,  $h_{exp}$ , vs prediction heat transfer coefficient,  $h_{pred}$ , with the new developed heat transfer coefficient correlation

Chen (1966) defined the nucleate boiling suppression factor,  $S$ , as a ratio of the mean superheat,  $\Delta T_e$ , to the wall superheat,  $\Delta T_{sat}$ . Jung et al. (1989) proposed a convective boiling heat transfer multiplier factor,  $N$ , as a function of quality, heat flux and mass flow rate (represented by employing  $X_{tt}$  and  $Bo$ ) to represent the strong effect of nucleate boiling in flow boiling as it is compared with that in nucleate pool boiling,  $h_{nbc}/h_{nb}$ . The Martinelli parameter,  $X_{tt}$ , is replaced by a two-phase frictional multiplier,  $\phi_f^2$ , in order to consider laminar flow in small tubes. By using the experimental data of this study, the new nucleate boiling suppression factor  $S$  based on flow pattern is proposed for each flow patterns of intermittent flow, stratified wavy flow and annular flow as follow.

$$S = a (\phi_f^2)^b Bo^c \quad (11)$$

The coefficients for Eq. (11) are listed in Table 3.

The overall comparison of the experimental heat transfer coefficient,  $h_{tp, exp}$ , and the predicted heat transfer coefficient,  $h_{tp, pred}$ , is illustrated in Figure 4 and the deviation for each comparison based on

flow pattern is tabulated in Table 4. The new correlation agrees closely for the comparison with a mean deviation of 16.63% and an average deviation of -0.64%.

## 5. CONCLUSIONS

Convective boiling heat transfer experiments were performed in horizontal small tubes with propane. The current experimental data are mapped on Wang et al. (1997) and Wojtan et al. (2005) flow pattern maps. Wang et al. (1997) predicted the current experimental results flow pattern better than Wojtan et al. (2005). In comparison with the flow pattern predicted by Wang et al. (1997) and Wojtan et al. (2005) flow pattern maps, the current experimental data shows that annular flow and dry-out occur at a lower vapor quality for the evaporation with a higher heat flux, higher mass flux and a lower inner tube diameter. Stratified wavy flow appears earlier for higher mass flux condition, and the regime is longer for a lower mass flux condition. A new heat transfer coefficient correlation that is based on flow pattern for boiling refrigerants in small tubes was presented with 16.63% mean deviation and -0.64% average deviation. Further study on flow boiling heat transfer

based on flow pattern in small tubes is needed for better prediction of the heat transfer coefficients.

## 6. REFERENCES

- [1] Baker, O., 1954, "Design of pipe lines for simultaneous flow of oil and gas", *Oil and Gas J.* July, 26.
- [2] Chen, J. C., 1966, "A correlation for boiling heat transfer to saturated fluids in convective flow", *Industrial and Engineering Chemistry, Process Design and Development* 5;322-329.
- [3] Chisholm, D., 1967, "A theoretical basis for the Lockhart-Martinelli correlation for two-phase flow", *Int. J. Heat Mass Transfer* 10;1767-1778.
- [4] Choi, K. I., Pamitran, A. S., Oh, C. Y., Oh, J. T., 2007, "Boiling heat transfer of R-22, R-134a, and CO<sub>2</sub> in horizontal smooth minichannels", *Int. J. Refrigeration* 30;1336-1346.
- [5] Cooper, M. G., 1984, "Heat flow rates in saturated nucleate pool boiling—a wide-ranging examination using reduced properties", In: *Advances in Heat Transfer*. Academic Press 16;157-239.
- [6] Dittus, F. W. and Boelter, L. M. K., 1930, "Heat transfer in automobile radiators of the tubular type", *University of California Publication in Engineering* 2;443-461.
- [7] Gnielinski, V., 1976, "New equations for heat and mass transfer in turbulent pipe and channel flow", *International Chemical Engineering* 16: 359-368
- [8] Gungor, K. E., Winterton, H. S., 1987, "Simplified General Correlation for Saturated Flow Boiling and Comparisons of Correlations with Data", *Chem.Eng.Res* 65; 148-156.
- [9] Jung, D. S., McLinden, M., Radermacher, R., Didion, D., 1989, "A Study of Flow Boiling Heat Transfer with Refrigerant Mixtures", *Int J. Mass Transfer* 32(9);1751-1764.
- [10] Kandlikar, S. G., 1990, "A general correlation for saturated two-phase flow boiling heat transfer inside horizontal and vertical tubes", *Journal of Heat Transfer* 112;219-228.
- [11] Kattan N., 1996, "Contribution to the heat transfer analysis of substitute refrigerants in evaporator tubes with smooth or enhanced tube surfaces", PhD thesis No 1498, Swiss Federal Institute of Technology, Lausanne, Switzerland.
- [12] Kattan, N., Thome, J. R., Favrat, D., 1998, "Flow boiling in horizontal tubes: part 1 – development of a diabatic two-phase flow pattern map", *J. Heat Transfer* 120;140-147.

- [13] Lockhart, R. W. and Martinelli, R. C., 1949, "Proposed correlation of data for isothermal two-phase, two-component flow in pipes", *Chem. Eng. Prog.* 45;39-48.
- [14] Pamitran, A. S., Choi, K. I., Oh, J. T., Oh, H. K., 2007, "Forced convective boiling heat transfer of R0410A in horizontal minichannels", *Int. J. Refrigeration* 30;155-165.
- [15] Petukhov, B. S. and Popov, V. N., 1963, "Theoretical calculation of heat exchanger in turbulent flow in tubes of an incompressible fluid with variable physical properties", *High Temp.* 1(1);69-83.
- [16] Pettersen, J., 2004, "Flow vaporization of CO<sub>2</sub> in microchannels tubes", *Exp. Therm. Fluid Sci.* 28;111-121.
- [17] Shah, M. M., 1988, "Chart correlation for saturated boiling heat transfer: equations and further study", *ASHRAE Trans* 2673;185-196.
- [18] Steiner, D., 1993, "Heat transfer to boiling saturated liquids", *VDI-Wärmeatlas (VDI Heat Atlas)*, Verein Deutscher Ingenieure, ed., VDI-Gesellschaft Verfahrenstechnik und Chemieingenieurwesen (GCV), Düsseldorf, Germany, (J.W. Fullarton, translator).
- [19] Tran, T. N., Wambsganss, M. W., France, D. M., 1996, "Small circular- and rectangular-channel boiling with two refrigerants", *Int. J. Multiphase Flow* 22(3);485-498.
- [20] Wang, C. C., Chiang, C. S., Lu, D. C., 1997, "Visual observation of two-phase flow pattern of R-22, R-134a, and R-407C in a 6.5-mm smooth tube", *Exp. Therm. Fluid Sci.* 15;395-405.
- [21] Wojtan, L., Ursenbacher, T., Thome, J. R., 2005, "Investigation of flow boiling in horizontal tubes: part I – a new diabatic two-phase flow pattern map", *Int. J. Heat Mass Transfer* 48;2955-2969.
- [22] Yun, R., Kim, Y., Kim, M. S., 2005, "Convective boiling heat transfer characteristics of CO<sub>2</sub> in microchannels", *Int. J. Heat. Mass Transfer* 48;235-242.
- [23] Zhang, W., Hibiki, T., Mishima, K., 2004, "Correlation for flow boiling heat transfer in mini-channels", *Int. J. Heat and Mass Transfer* 47;5749-5763.

**Solar-powered Adsorption Desalination cum Cooling: experiments and simulation**

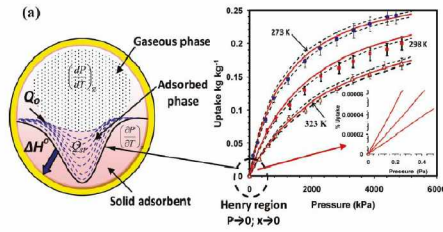
**Professor Kim Choon Ng,**  
 Mechanical Engineering Dept.,  
 National University of Singapore  
 e-mail: [mpengkc@nus.edu.sg](mailto:mpengkc@nus.edu.sg)  
 Tel: 065-65162214

Visiting Professor, WCU Programme (2009-2013)  
 Department of Nuclear & Energy Engineering  
 Jeju National University, Jeju, Korea.

**Scope of Presentation**

- Introduction to Adsorption
- Advantages of AD desalination
- Operation of AD Cycle
- Performance of the AD Process
- Life cycle cost analysis
- Conclusion

**Adsorption for other adsorbent-adsorbate pairs**  
 (Methane + AC - Maxsorb III)



**Activated carbon-hydrogen**

Chakarorty A, BB Saha, KC Ng, (Langmuir, 25(13), 7359-7367, 2009)

$$A_i = 1.091 N_A \left( \frac{m}{v_s N_A} \right)^{2/3} \exp \left\{ -\alpha \left( \frac{\Delta H^* - Q_d}{RT} \right) \right\} \quad (13) \quad x_m = \exp \left\{ -\gamma \left( \frac{\Delta H^* - Q_d}{RT} \right) \right\}$$

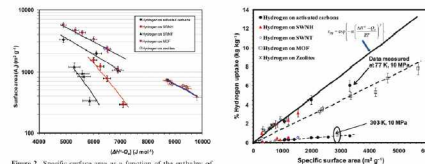


Figure 2. Specific surface area as a function of the uptake of adsorbate at zero surface coverage for the adsorption of hydrogen on (a) carbonaceous materials, (b) single wall carbon nanotubes (SWCNT), (c) single wall nanotubes (SWNTs), (d) MCFs, and (e) zeolites. Experimental data are for 77 K and 10 MPa.

Figure 3. Amount of hydrogen uptake as a function of specific surface area for (a) 77 K and 10 MPa and (b) 300 K and 10 MPa. The limiting amount of hydrogen uptake calculated by the present formulation (eq. (13)) is also shown.

$N_A$  = Avogadro constant,  $\alpha$  = surface energy distribution function,  $x_m$  = max adsorbate uptake,  $Q_d$  = least adsorption energy,  $\Delta H^*$  = isosteric heat of adsorption at zero uptake,  $\gamma$  = adsorbent surface heterogeneity factor (1 to 3).

**Adsorption phenomena**

$\Phi = \Phi(P, T, x)$

van der Waals forces

APPL PHYS LETTS 89, 171901, 2006

In an adsorbent + adsorbate system,  $Q_d$  is found to be a function of vapor uptake, and is also sensitive to temperature. Equation 19 is now written as:

$$Q_d = h_{lg} + E \left( \ln \frac{x_m}{x} \right)^{1/\alpha} + T \gamma \left( \frac{dP}{dT} \right)_x$$

$h_{lg}$  = latent heat of evaporation (kJ/kg),  
 $E$  = characteristic energy (kJ/kg),  
 $x_m$  = the max uptake,  $x$  = vapor uptake,  
 $\alpha$  = the heterogeneity constant (1.75 for silica gel+water)  
 $(dP/dT)_x = P$  versus  $T$  gradient in tables.

$$c_{ps} = c_{sa} + \left( \frac{Q_d}{T} \right) \left( 1 - \frac{1}{\alpha} \right) \left( \frac{dQ_d}{dT} \right) \quad (20)$$

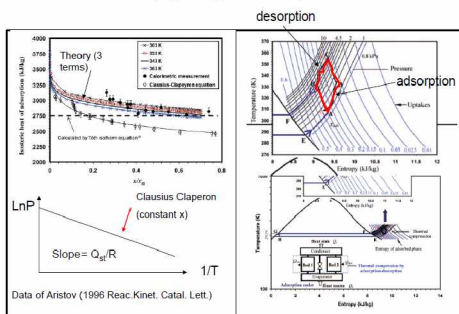
$$d\theta = c_{ps} + c_{sa} MF + \left\{ c_s - \left( \frac{\partial Q_d}{\partial T} \right) \right\} dP + \left\{ c_s - \left( \frac{\partial Q_d}{\partial T} \right) \right\} dP + (h_{lg} - Q_d) dx$$

$$\ln(P, T, x) = \ln(P, T, x) + \int_{c_s}^{c_{ps}} \frac{1}{T} dT + \int_{c_s}^{c_{ps}} \left( \frac{1}{T} - \frac{1}{T_s} \right) dT$$

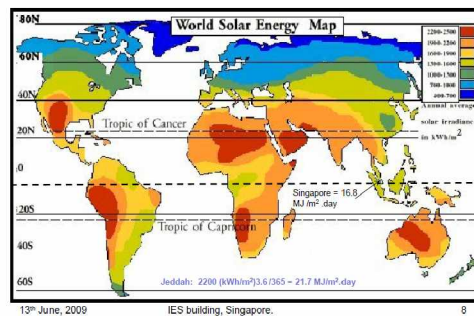
**Application ?**

- Can we design an engineering cycle to capitalize on the sorption processes so as the specific energy consumption is close to the thermodynamic limit?
- Low specific energy consumption – by how many times of the thermodynamic limit ?
- Environmental-friendly – reduced global warming,
- More than one useful effects from recovery of waste heat, We target for **Cooling and Desalination, CO<sub>2</sub> sequestration, etc.**

**Comparison of theory with experimental data**  
 (Langmuir 25(4), 2204-2211 2009)



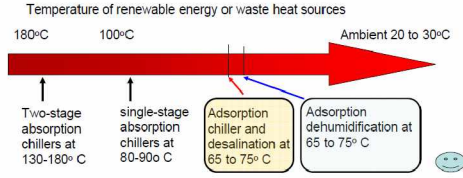
**World's Solar availability in kWh/m<sup>2</sup>.year**





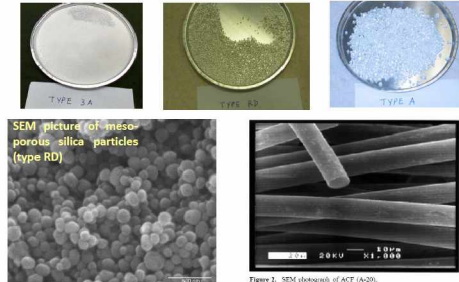
### Key to maximize solar energy utilization

1. Systems with high collection efficiency, e.g. thermal collectors (> 50%), utilize the thermal storage by water tanks – high thermal rating typically around 925 kWh/m<sup>2</sup>.year to 1100 kWh/m<sup>2</sup>.year).
2. Devise low temperature activation processes in a thermodynamic cycle.



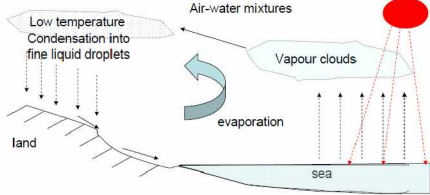
13<sup>th</sup> June, 2009 IES building, Singapore 9

### Types of silica gel



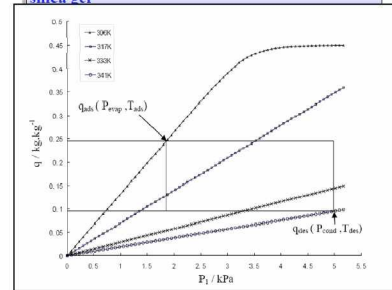
13<sup>th</sup> June, 2009 IES building, Singapore Figure 2. SEM (scanning of ACT (A20). 13

The AD cycle mimics the processes in the ambient that has a long cycle time

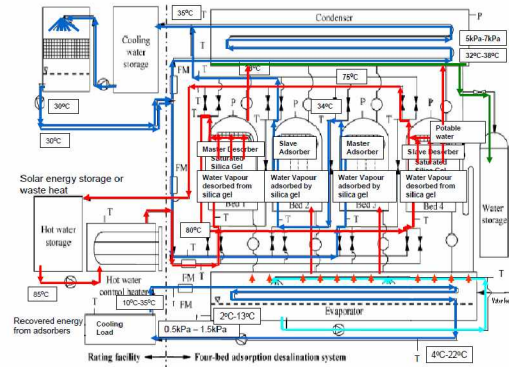
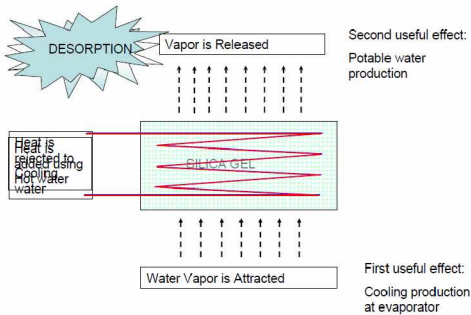


the AD cycle, it is performed in a single-component environment and cycle operates at a faster pace.  
13<sup>th</sup> June, 2009 IES building, Singapore. 10

### Isotherm data for water vapor onto the type RD silica gel



13<sup>th</sup> June, 2009 IES building, Singapore 14



### Advantages of AD Cycle

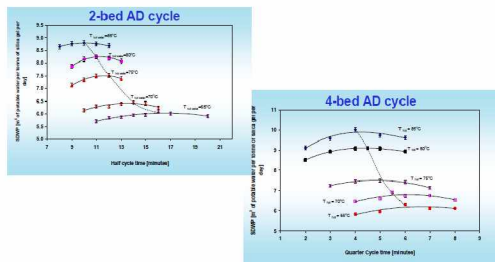
- Low-temperature waste heat from industrial processes or from solar thermal source: - deemed as "free energy"
- Low electricity usage as water pumps are used only-consumes about 1.38 kWh/m<sup>3</sup> - twice the thermodynamic limit
- Can produce two useful effects: Cooling and Potable water
- Almost no major moving parts except the valves for the vapor and coolant flows

Environmental-friendly as only silica gel and water are employed as adsorbent-adsorbate pair

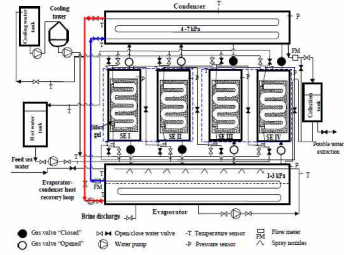


A picture of the AD prototype in NUS

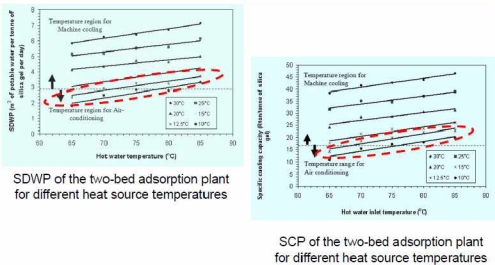
**Performance of a conventional AD cycle (Desalination)**



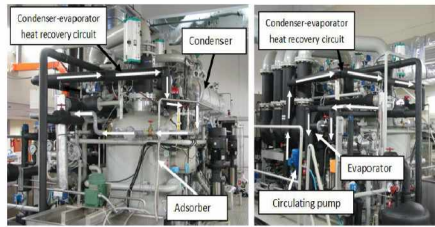
**AD cycle with heat recovery loop for evaporator-condenser (retrofitted in NUS's experiments)**



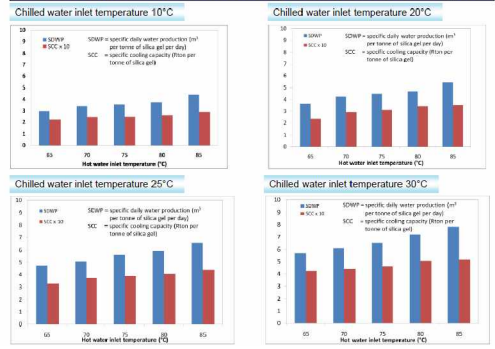
**Performance of a 2-bed cooling cum desalination cycle (conventional)**



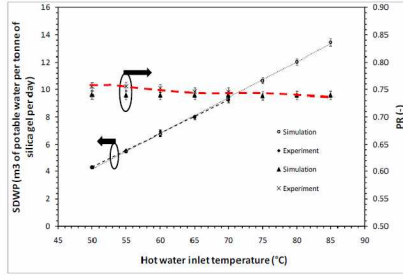
**Advanced AD cycle with evaporator-condenser loop**



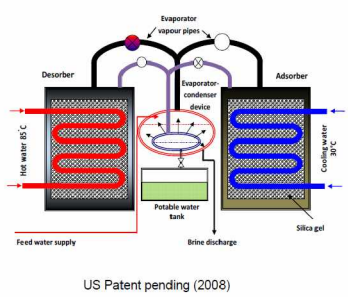
**Performance of a 4-bed cooling cum desalination cycle**



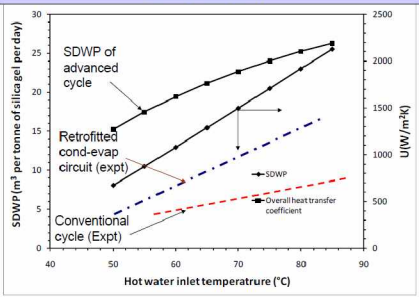
**Performance of Advanced AD cycle with the evaporator-condenser loop (Desalination)**



**Schematic diagram of an Advanced AD cycle (Patent filed in 2008, ILO, NUS)**



**SDWP & U<sub>cond/evap</sub> of an Advanced AD cycle (simulation)**





Comparison of Water production rates  
(144 kg of silical gel)

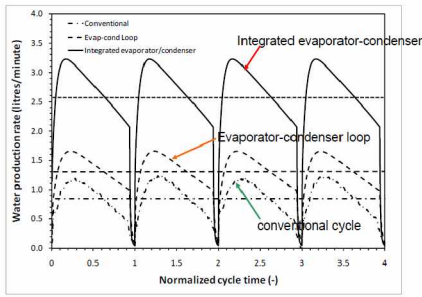


Table 7.6 Contributions to the total costs for AD and RO plants at 1000- m<sup>3</sup>/day

Unit cost factors	AD plant		RO plant_1		RO plant_2	
	(\$/m <sup>3</sup> )	(% of total)	(\$/m <sup>3</sup> )	(% of total)	(\$/m <sup>3</sup> )	(% of total)
$C_{\text{capital}}$	0.259	56.7	0.215	22.8	0.127	15.9
$C_{\text{electrical}}$	0.164	35.9	43.3	0.260	27.5	77.2
$C_{\text{membrane}}$	0.021	4.6	0.050	5.3	0.021	2.6
$C_{\text{pre-treatment}}$	0.001	0.2	0.035	3.7	0.0035	0.4
$C_{\text{chemical}}$	-	-	0.035	3.7	0.1	12.5
$C_{\text{maintenance}}$	0.012	2.6	0.061	6.5	0.039	4.9
$C_{\text{membrane}}$	-	-	0.060	6.4	0.02	2.5
$C_{\text{others}}$	-	-	0.228	24.1	0.228	28.6
Total Cost $\sum C_i$ (\$/m <sup>3</sup> )	0.457	100	0.944	100	0.799	100

(Here, the parameters  $C_{\text{pre-treatment}}$ ,  $C_{\text{chemical}}$ ,  $C_{\text{membrane}}$  and  $C_{\text{others}}$  are the pre-treatment cost, chemical cost, membrane replacement cost and cost per unit volume of the potable water, respectively.)

#1: U. Alkhei, H.S. Aybar / Desalination 184 (2005) 253-256, #2: G. Fioricca et al. / Energy Conversion and Management 44 (2003) 2217-2240

Designing for Large Commercial-scale Adsorption Desalination Plants

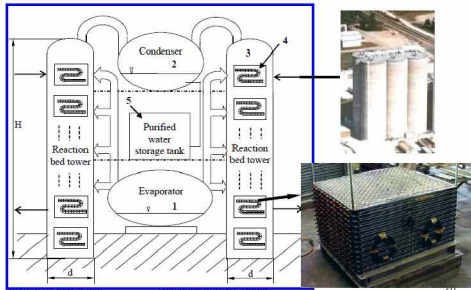


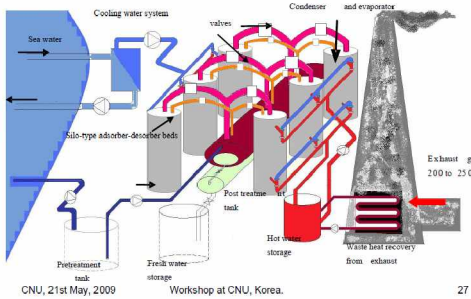
Table 7.7 CO<sub>2</sub> emissions of the conventional and AD desalination methods for a water production capacity of 1000m<sup>3</sup>/day.

Method of desalination	$TE_{\text{th}}$ (tCO <sub>2</sub> /yr) (Thermal)	$EE_{\text{elec}}$ (tCO <sub>2</sub> /yr) (Electricity)	$BE_{\text{com}}$ (tCO <sub>2</sub> /yr) (combined)	Savings if the AD cycle were used for production here $ER_{\text{AD}}$ (tCO <sub>2</sub> /yr)
MSF	1637	875	2512	= 2512-207 = 2305
MED	1383	640	2023	=2023-207 =1816
RO	0	1380	1380	=1380-207 =1173
AD	0	207	207	(reference datum)

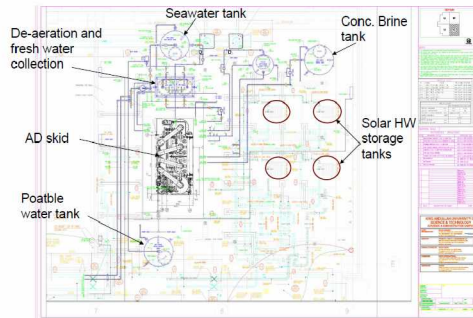
(In this table,  $TE_{\text{th}}$  is the annual CO<sub>2</sub> emission from the burning of natural gas,  $EE_{\text{elec}}$  is the emission from the generation of electricity consumed,  $BE_{\text{com}}$  is the baseline annual CO<sub>2</sub> emission and  $ER_{\text{AD}}$  is the annual CO<sub>2</sub> emission reduction by the AD plant for the same amount of desalting.)

Kyaw Thu et al., Desalination (accepted, 2009)

An Artist's impression of a large AD plant

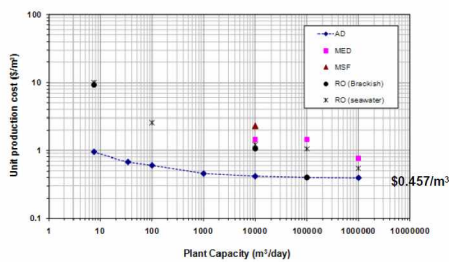


Solar-powered Adsorption Desalination plant at KAUST (Building UN3300)



Life-cycle cost comparison

(n=30 years, i=5%, Electricity rate =0.133 \$/kWh)



Recent projects of AD Cycle

Country	Function type	Plant size
Singapore	Desalination cum cooling	1. NUS (experiment prototype 5 Rtons – supported by KAUST-NUS SRP)
		2. Pizir Singapore (10 Rton – Solar powered with waste steam)
		3. Tampines Grande (2 units of 45 Rton- Solar powered plant)
		4. A co-gen plant on JTC's Jurong Island – under negotiation – 100 m <sup>3</sup> /day plant.
Saudi Arabia	Desalination cum cooling	1. KAUST (Lab prototype, advanced cycle-5 Rton and is Solar powered)
Korea	Desalination	1. Jeju National University – under the WCU programme and joint research with a Lab prototype (2 Rton)
Poland	Cooling (tapping low temperature waste heat at 65°C to 70°C)	1. Wrocław Science park building – project by NET, Poland (2 units of 25 Rton – co-generation steam powered)

### Closure

- Successfully demonstrated the AD cycle for both cooling and desalination - lowest possible specific energy consumption at 1.38 kWh/m<sup>3</sup> (twice the thermodynamic limit for desalination),
- The advanced [AD cycle](#) can operate with a heat source temperature as low as 50 to 80° C: - deemed as free source of energy,
- The life-cycle unit cost of AD cycle is US\$0.457 per m<sup>3</sup> – the lowest of all desalination methods,
- As compared to the RO plants, an emission savings of 3.2 kg of CO<sub>2</sub> per m<sup>3</sup> should the AD cycle is adopted,
- Our research was recently awarded the IES Engineering achievements awards (2009).

# Glimpses of Solar Energy Research at the Faculty of Mechanical Engineering University of Technology Malaysia Skudai, Johor Bharu, Johor

**Amer Nordin Darus<sup>a</sup>**

*<sup>a</sup>Department of Thermofluids  
Faculty of Mechanical Engineering  
Universiti Teknologi Malaysia  
81300 Skudai, Johor Bharu  
E-mail : amer@fkm.utm.my*

## ABSTRACT

This paper discusses the past and current trend of solar energy researches in the Faculty of Mechanical Engineering FKM, at The University of Technology Malaysia, UTM. Solar energy research at FKM started in the middle of 70's just after the world experiences the worst oil crisis in the world. Earlier attempts begin with modest research on low temperature applications of solar energy. Water heaters, air heaters and solar dryers were among the first series of research done. Under limited funding and low interest in research applications of solar energy only models were built. As time goes by, better equipments were purchased and more meaningful work was able to be tried. However, by then oil becomes cheaper. Oil and gas were found in the east coast of Malaysia. This again offset the interest in solar energy research. The current research in solar energy is towards power generation. Direct solar energy conversion to electrical energy is the main goal. The extensive application of solar cells is also seen to be dominating.

## 1. INTRODUCTION

Since Malaysia is situated in the equatorial region with an average radiation of 5,500 KWh per square meter, it is an ideal location for large scale solar power installations. Considering that Malaysia gets on an average 4.5 hours to 8 hours of free and bountiful sunshine everyday, the potential for solar power generation is very high. However, the real harnessing of this renewable energy source is way below its actual potential.

Malaysia has a huge reserve of natural gas and crude oil which are generally used in power generation. Moreover, these fuels are subsidized to a large extent. Besides, the price of electricity

from the national grid is also relatively cheap. Biomass based power generation is quite prominent Energy demand in Malaysia

Oil and gas have been the main energy sources in Malaysia. However, with its gas reserves estimated to last for another 33 years and oil reserves another 19 years, the Malaysian government is strengthening the role of renewable energy (RE) as the fifth cornerstone of energy generation. Many manufacturing companies in Malaysia are already trying to save energy costs. This creates opportunities to companies offering energy management services to determine ways for saving energy and costs.

Malaysia's commercial demand for energy is projected to continue its upward trend, from 1,244 Petajoule (PJ) in 2000 to an estimated 2,218 PJ in 2010. This consumption growth is mainly driven by industrialization. As it is common perception that a nation's economy and use of energy will always grow hand-in-hand, the Malaysian government, in its 8th Malaysian Plan (2001-2005) has declared RE as the country's fifth fuel in the energy supply mix to diversify its energy source. Currently, the energy supply mix in the country is made up of gas (70 percent), coal (22 percent), oil (2 percent) and hydro power (6 percent).

## 2. RENEWABLE ENERGY IN THE NINTH MALAYSIAN PLAN

The importance of RE as an enabler of strong economic growth is further reinforced in the 9th Malaysian Plan (9MP) (2006-2010), coupled with an emphasis towards Energy Efficiency (EE) both on production and utilization, while meeting environmental objectives. By 2010, RE is expected to contribute 350MW to total energy

supply in Malaysia, which is projected to reach 3,128 PJ. Biomass such as rice husks, palm oil and bio waste will be used on a wider basis mainly for power generation, followed by solar energy. In this case of solar power, the climatic conditions in Malaysia are favorable for the development of solar energy due to abundant sunshine with the average daily solar insolation is 5.5kWh/m<sup>2</sup>, equivalent to 15MJ/m<sup>2</sup>.

Under the Small Renewable Energy Power Programme (SREP), small power plants utilizing renewable energy can apply to sell electricity to the utilities companies through distribution grid systems. This project applies to all types of RE, including biomass, biogas, municipal waste, solar, mini-hydro and wind. In 2005, the 5-year Malaysian Building Integrated Photovoltaic Technology Application Project (MBIPV) was also launched to promote wider utilisation and application of photovoltaic technology in buildings, with the hope that this will eventually create a sustainable and widespread MBIPV market in Malaysia - and possibly grid-connected photovoltaic systems. Several small-scale solar projects have already been implemented to explore the viability of using solar applications for everyday business.

### 3. SOLUTION FOR ENERGY CRISIS AND ENVIRONMENTAL ISSUES

The EE strategies under the 9MP aim at energy saving features in the industrial and commercial sectors. In this regard, EE features such as efficient lighting and air-conditioning systems as well as encouraging the establishment of a comprehensive energy management system. Under the Malaysian Industrial Energy Efficiency Improvement Project (MIEIP), energy audits to identify ways for potential energy savings are undertaken in 11 energy-intensive industries, which are cement; ceramics; food; glass; iron and steel; pulp and paper; rubber and wood; oleo-chemical; plastic; and textile industries.

On the government front, new sources of energy such as solar and wind will be developed with emphasis on utilizing cost-efficient technology as well as strengthening capacity building under the 9MP. In this regard, efforts will be undertaken to co-ordinate R&D activities of the various energy-related research centers. The government has also launched several fiscal incentives to stimulate the emergence of RE and EE activities and

technologies. These incentives include pioneer status, investment tax allowance and import duty and sales tax exemption for equipment used in energy conservation. For the private sector, an increasing number of local companies are already taking advantage of RE technologies to begin reaping energy costs and revenue. It is expected that as Malaysian industry becomes increasingly aware of the bottom-line benefit of EE equipment and applications, demand for these should rise as well.

### 4. LOOKING BACK IN SOLAR ENERGY RESEARCH AT FKM

Solar energy research begins in the mid seventies at the Faculty of Mechanical Engineering, FKM at The University of Technology Malaysia, UTM.

### 5. WATER HEATERS

We begin investigating the application of solar energy in water heating. A simple thermal driven flow water heater was built.

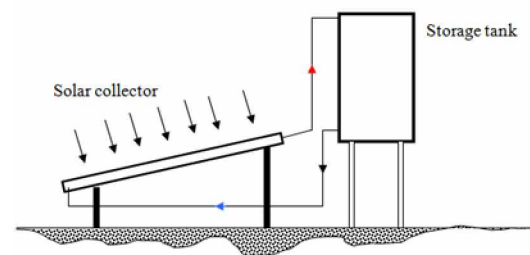


Figure 1 Solar Water Heater

In this early work on water solar heating the main objective is to obtain the highest temperature of the water as possible. Temperatures of the absorber, glass cover and water inlet and outlet temperatures were measured. Heat losses from the collector were determined. Useful energy gained by the water is also calculated. However the most challenging measurement is to measure the flow rate of water in this thermal driven solar energy water heater.

Many types of solar water heater absorber were investigated. These are shown below.

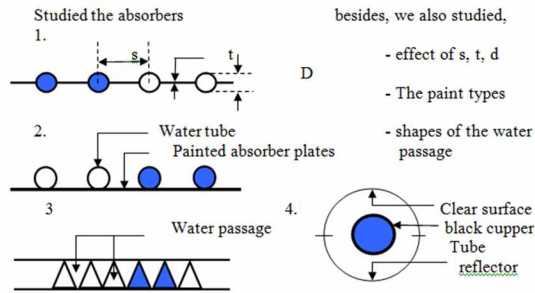


Figure 2 Flat plate water heater absorbers

In one of our early endeavors in solar energy we built a methane digester. It was found that the digester works best at certain temperature, say 35°C. We then build a water jacket for the digester and the water was heated using simple solar water heater, see figure below.

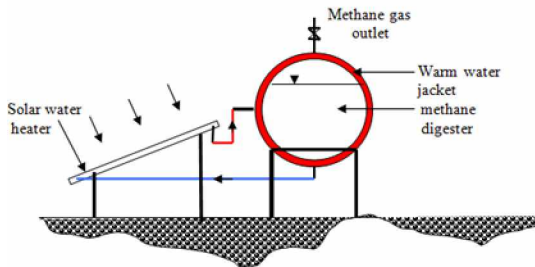


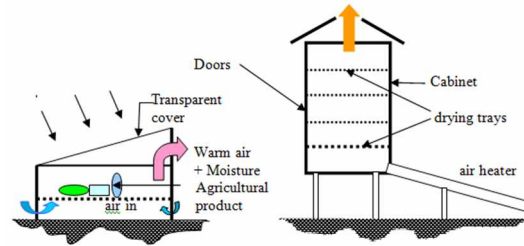
Figure 3 Methane digester heated by solar water heater

Higher production of methane gas was obtained as we kept the digester at the required temperature found earlier.

## 6. SOLAR DRYERS AND AIR HEATERS

We then move to investigate the application of solar energy in drying. It is well known that most of the agricultural products need some form of drying before they are stored. Paddy, coffee and cocoa are some common commodities that need drying.

We built and studied many kinds of dryers then. Some examples are shown below.

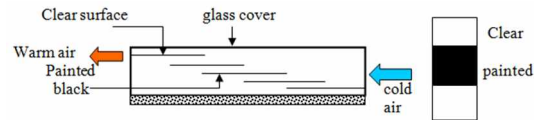


a. box type dryer

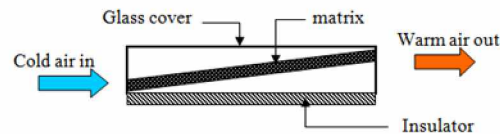
b. Cabinet dryer

Figure 4 Solar dryers

The main component of the solar dryer is the air heater. Similar to solar water heater, the air temperature needs for drying depend strongly on the design of the solar absorber. However for drying purposes usually only an increase of 10 to 15°C is needed. When the product is over dried we lost the aroma and also its taste. It is a delicate matter.



a. lapped glass type



b. matrix type air heater

Figure 5 Sample air heaters being studied

## 7. SOLAR REFRIGERATION AND SOLAR AIR CONDITIONING

Some experiments on solar cooling were also undertaken. We built a simple solar refrigeration. There are several types of refrigeration systems. But the most suitable for solar energy application is the absorption type. In this system the



compressor in the traditional vapor compression refrigerator was replaced with a generator, absorber and rectifier, refer figure below.

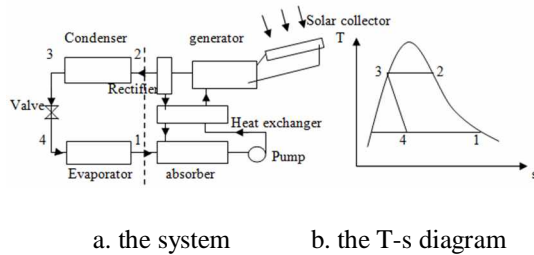


Figure 6 The vapor absorption solar energy refrigeration system

The system shown produces ice. We later built a more compact system where the refrigerant filled the whole system including the solar collector. Thus in this compact system the solar collector itself acts a generator.

In both systems the valve is actually a capillary tube. We have some problem with this capillary tube. The refrigerant used was ammonia – water. The ammonia-water mixture is very corrosive. We face a great deal of leakage problems. Black iron was used in the construction of the experimental rig. Here again we face great deal of difficulties in determining the actual refrigerant flow – rate. The cooling load is just the amount of heat needed to solidify liquid water into ice. The compact refrigeration system fails to produce ice, but some coldness was attained.

Natural extension of solar refrigeration cooling is obviously air conditioning. Thus instead of cooling water to produce ice, the cooling load now becomes the cooling of air. See, following figure.

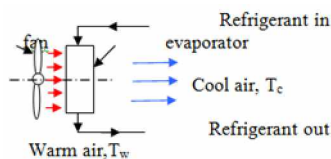


Figure 7 Cooling the air directly

Actually solar air conditioning is very attractive indeed. We are giving a chance to do some simulation studies in cooling a section of the Sultanah Zanariah Library of UTM. In fact, we were also requested to solar air – condition the walk – way from the Dewan Sultan Iskandar to the Sultan Ismail Mosque in the campus. However, analysis and simulation results show that these projects are not economically viable. The cost of solar cells to run the compressor is very expensive. Solar absorption system was not proposed as earlier study showed it is also not economical too.

## 8. SOLAR SIMULATOR

As solar energy research depends greatly at the mercy of the sun, a solar simulator was built in the late 80's. With the help of the Electricity Engineering Faculty, we build a model solar simulator.

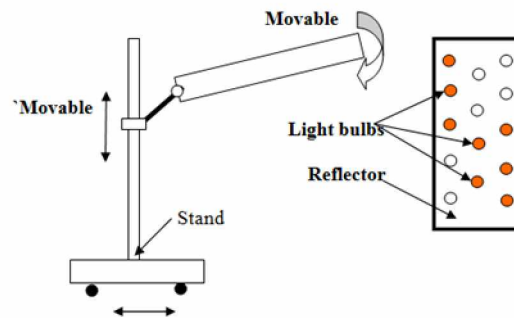


Figure 8 Solar Simulator

With this simulator, we were able to perform some work indoor. However, we fail to capture the actual solar environment outdoor. The effect of wind and dust on the solar collector cover of flat plate solar collectors was not able to be appreciated.

In those days, in the 80's and early 90's we used to hold conferences and seminars on solar energy among the local universities such as the University of Malays, UM, the National University, UKM, the University of Science, USM and the University of Agriculture. Most of our findings were shared and discussed in this annual seminar on solar energy. Many fruitful and proactive attempts are collectively undertake to foster the interest on solar energy applications in the country. However, almost at the same time, oil prices get low and lower. The interest in solar energy is ebbing.

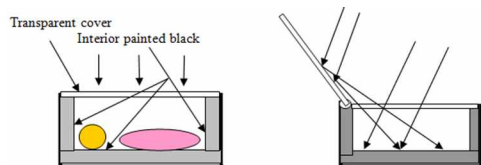


At FKM we also do some work in solar cooker. We built and tested a few. We did some experiments and well as simulation studies. Several designs are proposed and simulated.

## 9. SOLAR COOKERS

Solar Cookers are very popular in desert areas. Many studies were done in India and Middle Eastern countries especially in Turkey and Syria.

At FKM the research on solar cookers are merely to demonstrate and investigate whether the local sun rays are able to be utilized to cook some local dishes.



a. box type solar cooker    b. enhancing the solar cooker with a reflector

Figure 9 Solar Cooker

The studies show solar cooker is only able to cook some local dishes. The time taken to accomplish a dish is much longer as compared with the existing conventional wood burning stove. The only advantage of solar cooker is that it is pollution free and almost no cost incurred in operating it. The idea of cooking outside the house is not favorable for our women folks.

The studies show with proper reflectors added a higher temperature could be attained.

## 10. SOLAR STILLS

The idea of constructing and investigating the solar still is triggered when we were visiting an oil palm mill. The amount of waste water produced by the mill is tremendously large. We proposed a solution by constructing a solar still. In fact a solar dryer was also proposed to dry up the solid waste produced by the mill. The solid waste can be turned into in-house boiler fuel.

As a start we build a simple model of a solar still.

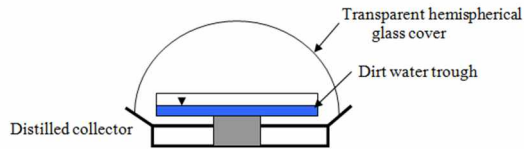


Figure 13 A typical solar still

The results show that solar still is capable of purifying the waste water. However, in the locality of the mill, it is not possible to have the area needed to construct and built the required solar still. Furthermore, during raining seasons the solar still seems fail to function effectively.

## 11. COMING OF THE SOLAR CELL TO FKM

At the beginning of the year 2000 solar cell is introduced to FKM. The Solar Car Research Group is busy designing solar powered car. The body is aerodynamically designed and constructed to reduce the drag coefficient to the very minimum. The car is then shipped to Australian desert to race in the World Solar Powered Car Racing, an annual event for solar car enthusiasts.

The annual gathering of the solar powered car designers and makers in the Northern Australian desert at Alice Springs have some effect to FKM as whole. The interest in solar energy starts to blossom.

In fact FKM organized the annual solar powered bicycle race from Johor Baru, a city in the south to Taiping, a small town in the northern part of Malaysia. The racing event is really a crowd puller. A good coverage of the race creates a lot of interest among the general public especially schools children. We receive a lot of invitation to give talk and road show of the solar energy powered car was regularly made.

Some schools request that solar energy awareness should be part of their curriculum. In fact, the writer is requested to write up a syllabus in Solar Energy and this subject should be offered as an elective subject in the Mechanical Engineering Curriculum.

Popularity of the solar powered car and bicycle runs short. It lasted for only 3 to 4 years. The main reason for its failure is lack of funding. Solar powered car and bicycle are not research oriented. No research was done in solar cell, The research part of the solar cell and battery are taken by the Department of Applied Physics, Faculty of Science, UTM. We become the user.

## 12. CONCLUSION

Solar energy research is a never ending activity in FKM. The interest in solar energy is always high. Currently we are engaging our effort in solar power generation. Organic Rankine Cycle taking solar energy as the main heat source is reviewed. With the current advancement of computer technology and efficient commercial engineering software, more meaningful computer simulation studies will be attempted.

Solar cooling of buildings is always been our main interest in studying solar energy. Better systems of solar refrigeration have to be experimented. New systems will be simulated using data taken from the experiments. Thermoelectric refrigeration system is also being studied.

Smaller models of solar energy systems will be studied. With better measuring devices and instrumentations these smaller models will cut costs but in same time save space and have a higher level of portability. Experimental can be performed anyway, indoor or outdoor.

In order to increase the efficiency or the coefficient of performance of the solar energy systems, exergy analysis will be performed.

## REFERENCES

- [1] Lunde, P.J., (1980), *Solar Thermal Engineering*, John Willy, New York
- [2] Kreith, F, and Kreider, J., (1980) *Solar Engineering*, Hemisphere, New York
- [3] Swa, H.A, (1975), *Methane Digester*, Bachelor of Engineering Thesis, Faculty of Mechanical Engineering, University of Technology, Malaysia,
- [4] Muhammad Shafie Mat Ali, (2004), *Solar Water Heater, An Experimental Study*, Bachelor of Engineering Thesis, Faculty of Mechanical Engineering, University of Technology Malaysia,
- [5] Mohamed Mahadir Mohd Shafie, (2005), *Heat Transfer Analysis of a Solar Cooker*, A Simulation Study, Bachelor of Engineering Thesis, Faculty of Mechanical Engineering, University of Technology, Malaysia
- [6] Mohd Ezani Mahzan, (2005), *Design and Construction of Solar Cloth Dryer*, Bachelor of Engineering Thesis, Faculty of Mechanical Engineering, University of Technology, Malaysia
- [7] Rita Azura Roslan, (2005), *An Experimental Study on Solar Still*, Bachelor of Engineering Thesis, Faculty of Mechanical Engineering, University of Technology, Malaysia
- [8] Reza Sharil Mohd Said, (2006), *An Experimental Study of a Solar Cooker*, Bachelor of Engineering Thesis, Faculty of Mechanical Engineering, University of Technology Malaysia
- [9] Mohd Syukri Hashim, (2006), *An Experimental Study of Solar Still with Reflector*, Bachelor of Engineering Thesis, Faculty of Mechanical Engineering, University of Technology, Malaysia
- [10] Mohd Zaki Akhtar, (2005), *Determination of Solar Radiation Distribution of Malaysia, An Empirical Method*, Bachelor of Engineering Thesis, Faculty of Mechanical Engineering, University of Technology, Malaysia
- [11] Dalbir Singh s/o Atar Singth, (2006), *Parametric Study of Solar Vapor Compression Cooling System*, Bachelor of Engineering Thesis, Faculty of Mechanical Engineering, University of Technology, Malaysia
- [12] Cheng Eng Cong, (2006), *Feasibility Study of Solar Energy Powered of An Organic Rankine Cycle*, Bachelor of Engineering Thesis, Faculty of Mechanical Engineering, University of Technology, Malaysia
- [13] Sia Toh Ching, (2007), *An Exergy Analysis of A Flat Plate Solar Collector*, Bachelor of Engineering Thesis, Faculty of Mechanical Engineering, University of R\Technology, Malaysia

# Experimental Study of Confined Biogas Pulse Detonation Combustion

Mazlan A. Wahid\*, Haffis Ujir, Khalid M. Saqr and Mohsin M. Sies

*High-Speed Reacting Flow Laboratory, Faculty of Mechanical Engineering  
Universiti Teknologi Malaysia, 81310 Skudai, Johor - MALAYSIA  
Tel: +6075534565 - Fax: +6075534565  
\* E-mail : mazlan@fkm.utm.my*

## ABSTRACT

An experimental rig consisting of a stainless steel tube with inner diameter of 100mm, a data acquisition system, ignition control unit and gas filling system was built in order to measure the characteristics of biogas detonation such as, pressure history, velocity and cell width. Two types of hydrocarbon fuels were used for comparison in this investigation; propane and natural gas with 92.7% methane. Synthetic biogas was produced by mixing 65% natural gas with 35% carbon dioxide. The oxygen concentration in the oxidizer mixture was diluted with nitrogen gas at various percentage of dilution. Results showed that natural gas and biogas are not sensitive to detonation propagation compared to propane. For biogas, methane, and propane it was found that in smooth inner-wall tube, detonation occurs if the percent of dilution gas is not more than approximately 8%, 10% and 35%, respectively. In order to decrease the tube length required for detonation transition, an array of obstacles with identical blockage ratio was placed inside the tube near to the ignition source. The effect of combustion wave-obstacle interaction was also investigated.

## Keywords

*Detonation, Deflagration to detonation transition, Pulse combustion, Biogas*

## 1. INTRODUCTION

Biogas systems can assist in the fight against global warming by burning the methane from organic waste, instead of letting it escape into the atmosphere where it adds to the greenhouse effect. The methane contained within biogas is 20 times more potent as a greenhouse gas than carbon dioxide. Years ago, before the use of biogas was discovered, gas produced by the water treatment system in a factory was burned or released to the atmosphere. When the benefit of

biogas was discovered, most of the factories start to build pipe line from the digestion plant to transport the biogas to their burner. Poor pipeline system that transporting the biogas could lead to accidentally ignited combustion. This type of incident is most likely to occur in a biogas system in non-industrial environment where safety is the last thing considered. Furthermore, biogas can contain a few percentage of reactive material such as hydrogen sulphide ( $H_2S \sim 1-5\%$ ) and hydrogen ( $H_2 \sim 0-1\%$ ). These reactive materials could increase the possibility of the biogas to be ignited and propagate as detonation wave.

Detonation wave is a shock wave coupled with a chemical reaction where the wave is considered to be self-energized [1]. It can be explained as the shock front provides auto-ignition condition to the combustible mixture within its propagation path. Consequently, the triggered chemical reaction provides energy to sustain the shock wave. It is shown in figure 1 that in detonation wave, after the shock front, there is a reaction zone that separates from the shock wave by induction zone. The induction zone exists due to ignition delay of the chemical reaction. In contrast, explosion such as blast wave is a "lifeless" decay since it obtained from a high pressure vessel [1].

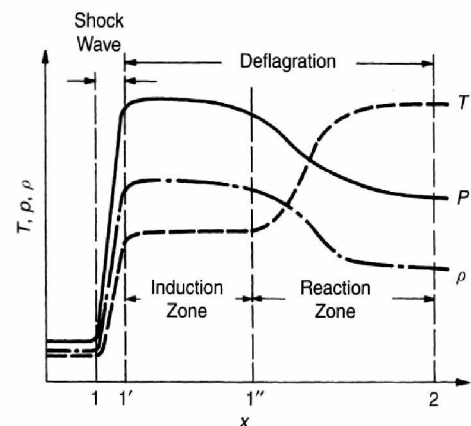


Figure 1. Variation of physical properties through a detonation wave [2]

In a fuel-oxidizer mixture where the oxidizer contains 100% oxygen, detonation propagation can be initiated with a small amount of ignition energy. Increasing dilution gas such as nitrogen in the mixture will decrease the possibility of detonation to be initiated. In a fuel-air mixture, the method of direct ignition energy that is required to initiate detonation is more than 1kJ which is not practical to be used in a transportation system [3].

Multiple point spark ignition had been proven to assist combustion wave to propagate as detonation wave [4-6]. Not only via high ignition energy; detonation can also be generated using a deflagration to detonation transition (DDT) technique. DDT occur when deflagration combustion propagation transit to detonation combustion wave propagation due to the generated turbulence that increase the intensity of the combustion process. This technique requires some set up of internal configuration within the flame propagation channel. Different types of fuel require different type of configuration. Some fuel requires a few meters of obstacle set up to create DDT. To apply this kind of pulse combustion in a propulsion system, the length of DDT should be shortened. This research is focused on the possibility of shortening the length of DDT in pulse combustion process of hydrocarbon fuel in low amount of oxygen addition via configuration of obstacle.

The present article aims to report an experimental study conducted to characterize biogas detonation. The experiments were conducted using the detonation tube facility in the High-Speed Reacting Flow Laboratory, Universiti Teknologi Malaysia. A schematic of such detonation facility is illustrated in figure 2. The results reported in the present article are of high significance for two major disciplines: power generation and process loss prevention and safety. The results reported in this article include the CJ and measured detonation velocities for propane, natural gas and biogas in air. The pressure history of DDT for the three fuels is also reported.

## 2. EXPERIMENTAL SETUP

The detonation tube is connected to a filling station through 2 ball valves. The filling station that is equipped with digital pressure gauge, gaseous filling valves, vacuum pump and circulation pump was built. Plumbing schematic diagram is shown in Figure 3. Flexible hoses that are capable to hold burst pressure of 40 bars and able to hold vacuum pressure are used in the

filling station. Gases were filled into the tube using the partial pressure method and controlled using individual gas filling valve valves. The gases are stored in high pressure tanks that are located near to the filling station. From the tanks, the flow rate was regulated using individual gas regulator and connected to the filling station through high pressure hose. Types of gases that are connected to the filling station are propane, synthetic biogas, oxygen, nitrogen and natural gas with 97.2% methane.

The gases were introduced to the plumbing line through individual ball valves and controlled based on reading from a SUNX digital pressure gauge. The resolution of the pressure measurement using this gauge is approximately 0.009 bars. After the final pressure was achieved, a magnetic drive circulation pump was switched on for about 5-10 minutes to ensure that the fuel and oxidizer were properly mixed.

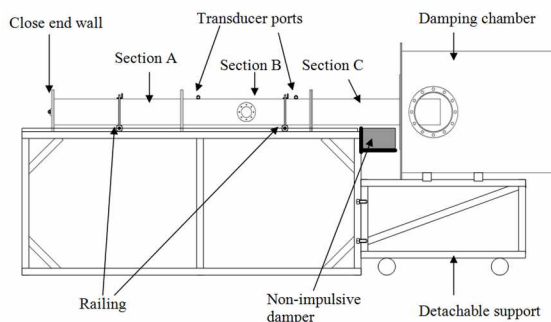


Figure 2, Single Pulse Detonation Tube

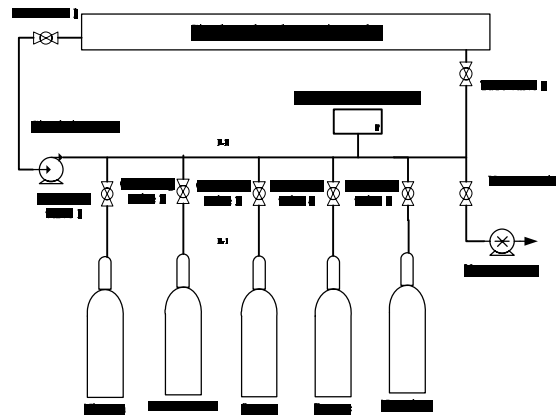


Figure 3. Gas filling system for the detonation tube

The detonation tube was attached with 3 piezoelectric pressure transducers (PT1, PT2 and PT3) shown in Figure 4. Signals from these transducers were conditioned using a signal conditioner (5135, Kistler) before feeding through a connector block (SCC68, National Instrument). An analog to digital converter card (NI-PCI 6257)

An analog to digital converter card (NI-PCI 6257) was used to capture signal from the transducers. DAQ software was designed to record, display and post-process the measurements using LabView 7.1 platform.

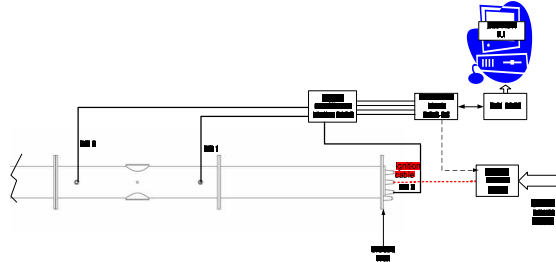


Figure 4. Pressure transducers and DAQ connection

The velocity of the combustion wave was determined by dividing the length between PT1 and PT2 with the time for the combustion wave propagate from PT1 and PT2. The arrival of the combustion wave was defined as the first arrival of peak pressure after the ignition at those pressure transducers. Deflagration characterized by gradual pressure rise with value normally around 1 to 3 bars for both PT1 and PT2. Detonation characterized by sharp pressure rise normally reaching around 35 to 50 bars for both PT1 and PT2. In this study, deflagration-to-deflagration transition (DDT) process before PT1 was not being observed. DDT was recognized by the detection of deflagration pressure rise at PT1 and detonation pressure rise at PT2.

The cell width of detonation propagation is useful data to predict the allowable space for detonation wave to propagate. In the section C of the detonation tube, a sheet of zinc covered with thin soot film on 1 side was placed flush to the inner wall. The zinc sheet was bent and fixed inside the tube by inserting it into an additional slot that attached between flanges that was connecting section B and section C. Figure 5 shows the placement of the zinc sheet in the section of the tube.

An array of obstacles was built in order to study the effect of obstacles on combustion wave acceleration and the onset of DDT. Detonation wave can be initiated from deflagration wave when the combustion wave propagates within an obstructed channel. Based on study done by Dorofeev [7], the optimum blockage ratio was about 0.44, refer to equation 1.

$$BR = 1 - \left(\frac{d}{D}\right)^2 \quad (1)$$

Figure 3.10 shows three obstacle configurations. The configuration of obstacle is set at 500mm which is equal to the required length for C<sub>3</sub>H<sub>8</sub>-air mixture to be accelerated toward detonation wave.

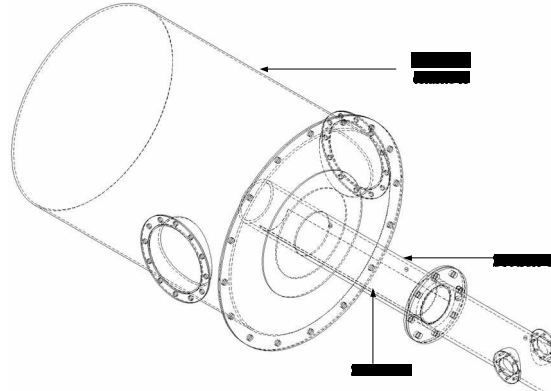


Figure 5. Soot film arrangement

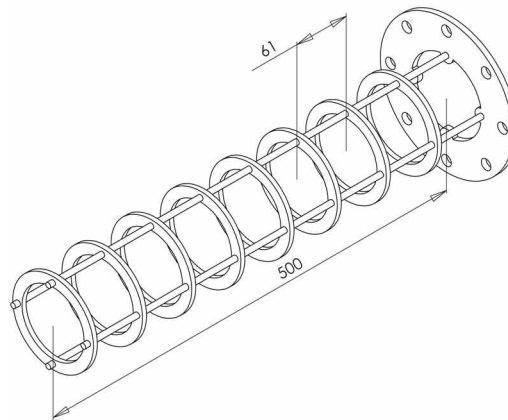


Figure 5. Dimensions of the obstacles array (mm)

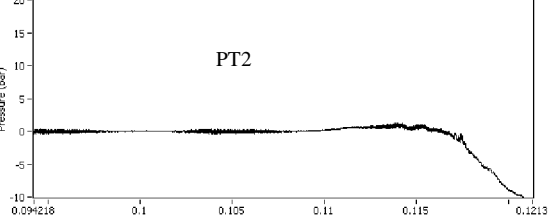
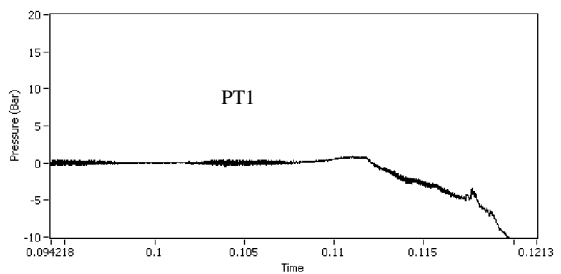
### 3. RESULTS AND DISCUSSION

Experiments were conducted at initial pressure of 1.01325 bars (1 atm) and at room temperature of 300K. The mixture of fuel-oxidizer was set at stoichiometric for the experiments with the obstacles installed. Since the tube was unable to be completely evacuated, the remaining air left after the evacuation process was taken into account in the partial pressure filling process. The calculations of the value for the Chapman-Jouguet (CJ) velocity and pressure for the mixtures were performed using NASA-CEA software.

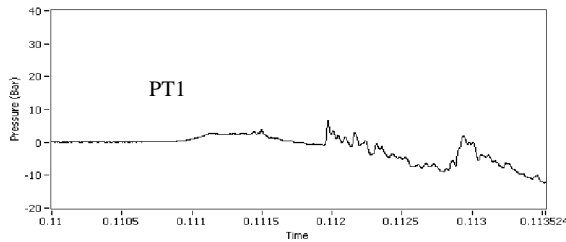


### 3.1 Pressure Signals in Deflagration and Detonation

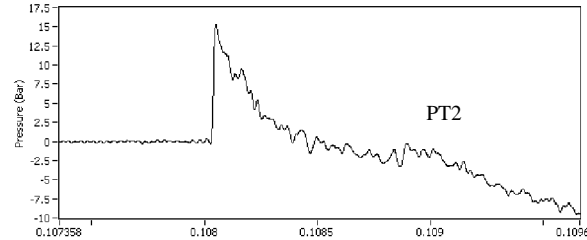
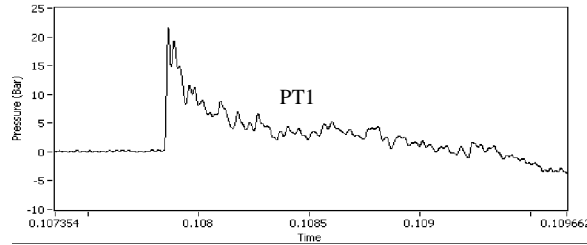
Deflagration mode of pulse combustion was identified by gradual pressure rise with value normally around only 2 to 3 bars for both PT1 and PT2. Detonation mode of pulse combustion was characterized by sharp pressure rise normally reaching around 20 to 50 bars for both pressure transducers. Deflagration to detonation transition (DDT) that occurred between PT1 and PT2 was determined by gradual pressure rise at PT1 and sharp pressure rise at PT2. Figure 6 shows the example of signal pattern for these three cases for a test fuel.



(a) Typical pressure history for deflagration at PT1 and PT2



(b) Typical pressure history for DDT between PT1 and PT2



(c) Typical pressure history for detonation between PT1 and PT2

Figure 6. Pressure signal patterns from PT1 and PT2 for the three modes of combustion

### 3.2 Unobstructed Tube Results

Figure 7 shows the single pulse combustion wave velocities for propane, natural gas and biogas in an unobstructed channel. In the experiments with no obstacle, detonation occurs in the propane mixtures which contain high percentage of oxygen which is  $\geq 75\%$ . Detonation did not occur for the natural gas and biogas mixtures for any percentage of N<sub>2</sub> addition. These indicate that combustion of propane has higher possibility to propagate as detonation wave compared to natural gas or biogas

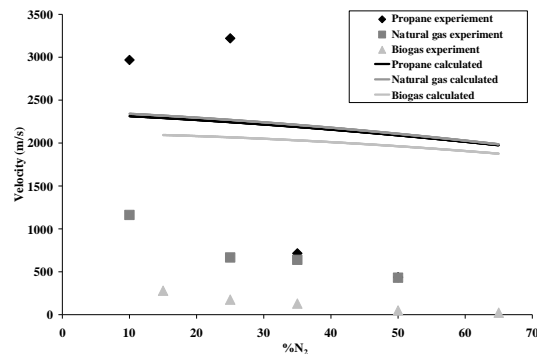


Figure 7. Pulse combustion wave velocity of propane / natural gas / biogas + oxygen at various percentage of nitrogen dilution in an unobstructed channel. The NASA-CEA calculations are shown as lines

As shown in figure 7, the detonation velocities of propane mixtures at 10% and 25% of nitrogen dilution have higher velocity compared

to the theoretical CJ velocity. This shows that the detonation wave was in an over driven condition while propagating from PT1 to PT2 and still has not reached the stable Chapman-Jouguet condition. However, it is believed that the detonation wave stabilized when it entered the third section of the tube (Section C). This was confirmed by the soot trace pattern that indicates the detonation was fully developed at the third section. Most of the natural gas mixtures propagate in high speed turbulent deflagration regime except for the lean mixture with  $\geq 35\%$  nitrogen dilution which propagates in slow turbulent deflagration regime. By using biogas, the propagation of the combustion wave for all dilution mixtures were in slow turbulent deflagration regime. This is due to dilution cause by the presence of the carbon dioxide gas in the mixture.

### 3.3 Obstructed Tube Results

As indicated in figure 8, combustion wave velocity of propane mixture with 35% nitrogen dilution was slightly below CJ velocity for experiment conducted in an obstructed tube. By using obstacles, the nitrogen dilution can be increased up to 50% for detonation to be initiated within 500mm after ignition. With further increment of nitrogen dilution in the oxidizer, the combustion wave propagates as high speed turbulent deflagration. This indicates that to initiate detonation wave propagation in high percentage of nitrogen dilution, one requires a increase the number of obstacles. It has been measured by Ciccarelli et. al [8], that using 0.43 blockage ratio orifice obstacle with 1 tube diameter for the orifice plate spacing, the combustion wave velocity of propane-air mixture reached  $\sim 600\text{m/s}$  (high speed turbulent deflagration) at a distance of 2m. Detonation propagation of natural gas mixture was observed at 50% of nitrogen in the obstacle configuration. Failure to initiate detonation wave in  $>50\%$  nitrogen in natural gas mixture is due to cell width of the detonation front which require larger tube diameter as well as the obstacle length. Combustion wave of biogas was accelerated toward detonation propagation for mixture with up to 35 % nitrogen dilution in the obstacle configuration. By increasing the nitrogen dilution, the detonation wave propagation of biogas was failed to be initiated.

As shown in figure 9, there are cases where propagation pressure for natural gas was higher

than propane, i.e; natural gas mixture with 10% nitrogen dilution in no obstacle configuration. This was due to the transition to detonation process. In the mixtures involved the transition process for propane mixture was almost complete and reaching the steady state CJ pressure. While for natural gas mixtures, the combustion wave propagation was still affected by the overdriven wave when it was passing the particular pressure transducer. As a comparison, in the case of natural gas mixture with 50% nitrogen without the use of obstacle, pressure at PT1 was lower compared to PT2 which was higher than CJ pressure, while in the same mixture composition but by using obstacle, pressure at PT1 was higher compared to PT2 which was near to CJ pressure. In the first case, the transition occurred near to PT2 while in the second case where the obstacle was longer, the transition occur before (just after leaving the obstructed zone) PT1.

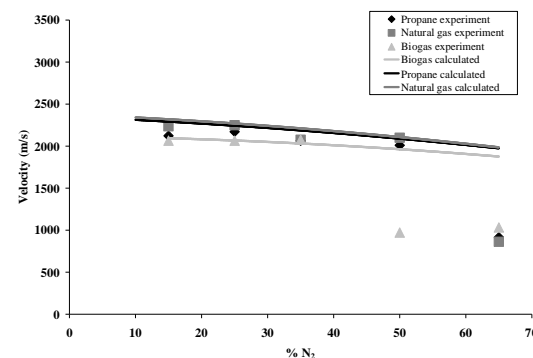


Figure 8. Propagation velocity of pulse combustion wave in obstructed channel. NASA-CEA calculations are shown as lines

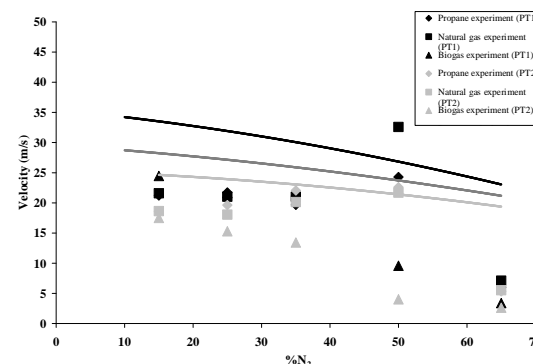
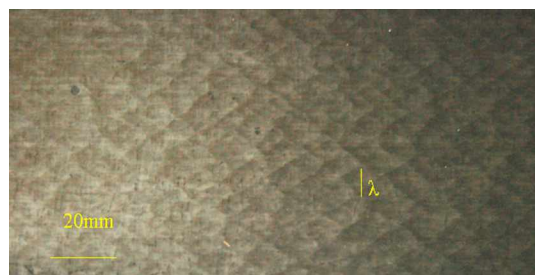


Figure 9. Combustion wave propagation pressure in an obstructed channel. NASA-CEA calculations are shown as lines

### 3.4 Cell Width ( $\lambda$ ) Criterion of Detonation

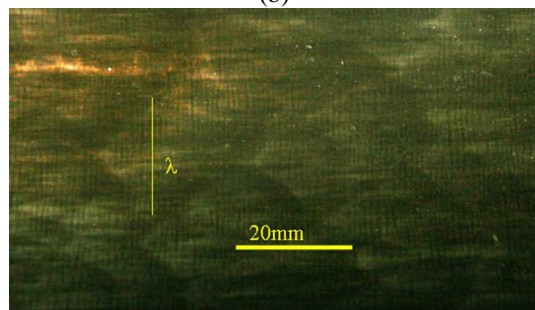
Measurement of cell width of the pulse combustion waves was made at the section C of the tube. However, for cases where neither detonation nor DDT was detected, the soot layer was just swept away by the combustion wave. This is because a deflagration combustion wave does not have unique macroscopic transverse waves that propagate within the combustion wave. An example for the captured detonation cell width is shown in figure 10.



(a)



(b)



(c)

Figure 10. (a) Propane-oxygen mixture with 35% nitrogen dilution; with the use of obstacle, ( $\lambda_{ave}=3.86\text{mm}$ ) (b) Natural gas-oxygen mixture with 35% nitrogen dilution; with the use of obstacle, ( $\lambda_{ave}=12.09\text{mm}$ ) (c) Biogas - oxygen mixture with 15% nitrogen dilution, with the use of obstacle ( $\lambda_{ave}=13.55\text{mm}$ )

It was reported by Shepherd et. al [9], for a sensitive mixture, the cell width is smaller compared to a less sensitive mixture. As shown in figure 11, propane mixtures that were successfully

propagated as detonation wave produced smaller cell width compared to natural gas mixtures and biogas mixtures with the same amount of dilution. For the same fuel, the cell width increases with the increase of dilution which reduced the sensitivity of the mixture. Even though a numerical model of detonation cell width was developed [10], the value of measured cell width in this research is compared only with experimental values gathered by other research.

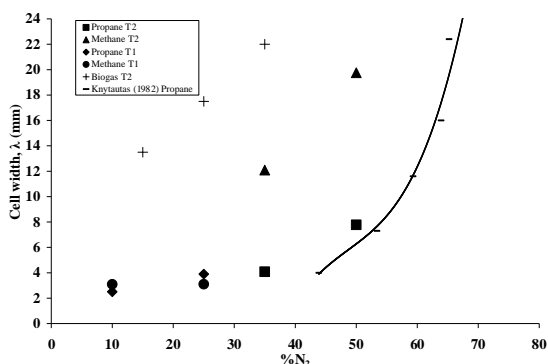


Figure 11. Cell width of successfully detonated mixtures

## 7. CONCLUSION

Pulse combustion of biogas and hydrocarbon-oxygen mixtures were investigated, experimentally using a single pulse combustion tube and through calculations based on theories of 1-D inviscid flow. Three types of hydrocarbon fuels were used in the experiments namely propane and natural gas which contain 92.7% methane and synthetic biogas which contain 65% methane and 35% carbon dioxide. Mixtures were diluted using nitrogen at various percentages of dilution. Mixture composition was determined and prepared using partial pressure technique.

Experiments were done at atmospheric condition, 1 atm and 300K. Determination of propagation velocity and pressure was done using fast response pressure transducers. Conventional soot film technique was used to determine the shock front structure. Combustion wave was accelerated by turbulence enhancement technique via arrangement of orifice obstacle. Experiments were done with and without the use of obstacle. From the discussion of measured and calculated data, the following conclusions can be drawn:

1. The velocity data from the experiments with no obstacle shows that propane is more sensitive toward detonation propagation compared to natural gas and biogas. However, for both

hydrocarbon fuels, the probability to the onset of detonation is decreased with the increase of nitrogen dilution. Thus, by preparing injector of dilution gas such nitrogen at the place where the possibility of accident is high the gas pipeline could suppress accidentally ignited combustible mixture and decrease the possibility of detonation to be initiated.

2. Combustion wave of biogas can be accelerated toward detonation propagation by using 500mm length of orifice obstacle with the percentage of nitrogen up to 35%. By increasing the length of the obstacle, the onset of detonation can occur within higher percentage of nitrogen dilution. Presence of obstacle in biogas or natural gas pipeline such as excessive gasket, valve and junction within short distance could accelerate accidentally ignited mixture toward detonation. Precaution or any mean of ventilation should be applied at where the number of obstacle is high in the gas pipeline.

3. From the cell width data, for same percentage of nitrogen dilution, propane mixture produces smaller cell width structure compared to natural gas and biogas. Based on  $dc=13\lambda$  criterion, this indicate that detonation wave of propane mixture can propagate at smaller tube diameter compared to natural gas mixture.

## ACKNOWLEDGMENT

The authors would like to acknowledge the support provided by the Malaysian Ministry of Higher Education (MOHE) under the FRGS grant number 78046.

## REFERENCES

- [1] A.K. Oppenheim, "Introduction to Gasdynamics of Explosions", International Centre For Mechanical Sciences, Udine 1970,
- [2] K.K.Kuo, Principles of Combustion, 2nd ed, John Wiley & sons, Inc. 2005
- [3] E. Schultz, E. Wintenberger and J. Shepherd., GALCIT Report: "Investigation of Deflagration-to-Detonation Transition for Application to Pulse Detonation Engine Ignition System", Pasadena
- [4] D.C. Bull, J.E. Elsworth, G. Hooper, " Initiation of Spherical Detonation in Hydrocarbon/Air Mixtures", Acta Astron, Vol.5, 11; 997-1008, 1978
- [5] V.P. Zhukov, A.E. Rakiin, A.Yu. Starikovskii, "Detonation Initiation By High-Voltage Pulsed Discharges", 45th AIAA Aerospace Sciences Meeting and Exhibit, 2007-1029.
- [6] I. B. Schild, A. J. Dean," Influence of Spark Energy, Spark number and Flow Velocity ON Detonation Initiation in a Hydrocarbon-fueled PDE", 41th AIAA Aerospace Sciences Meeting and Exhibit, 2005-4211
- [7] S. B. Dorofeev, V. P. Sidorov, M. S. Kusnetsov, I. D. Matsukov, V. I. Alekseev, "Effect of Scale on The Onset of Detonation", Shock Wave (2000) 10: 137-149
- [8] G. Ciccarelli, C.J. Fowler, M. Bardon, "Effect of Obstacle Size and Spacing on The Initial Stage of Flame Acceleration in a Rough Tube", Shock Wave (2005) 14(3): 161-166
- [9] J. E. Shapherd, I. O. Moen, S. B. Murray, P. A. Thibault, "Analysis of the cellular structure of detonation", 21 Symposium (Intl) on Combustion, 16, 149-1658, 1986
- [10] A. I. Gavrikov, A. A. Efimenko, S. B. Dorofeev, " A Model for Detonation Cell Size Prediction from Chemical Kinetics", Combustion and Flame 120:19-33 (2000)

# Transient Flow Effect due to Geometrical Characteristics of Pressure-Swirl Gasoline Direct Injection (GDI) Atomizers

Azhar Abdul Aziz<sup>a</sup>, Mas Fawzi Ali<sup>a</sup>, Zulkarnian Abdul Latiff<sup>a</sup>

<sup>a</sup>Automotive Development Centre (ADC)  
Faculty of Mechanical Engineering  
Universiti Teknologi Malaysia  
azhar@fkm.utm.my

## ABSTRACT

Transient flow due to geometrical characteristics of pressure-swirl atomizers were investigated using a commercial computational fluid dynamics code. The geometrical characteristics under study were three different shapes of needle tips as well as two different angles of tangential swirl slots. The calculations took the advantages of fast and low cost computing by applying 2D-axisymmetric swirl solver together with multiphase Eulerian volume of fluid to represent each case without sacrificing much accuracy. The result of the calculations yielded data such as mass flow rate, initial spray cone angle, and liquid sheet thickness at nozzle exit. Comparing measured static mass flow rate of an actual pressure-swirl atomizer at several fuel-air pressure differentials validated the calculated data. The calculated data showed that a point-tip needle combined with strong swirl strength has the lowest discharge coefficient, the largest initial spray cone angle, and the thinnest liquid sheet at nozzle exit.

## Keywords

*atomizer, CFD, direct-injection, Eulerian, gasoline, transient flow*

## 1. INTRODUCTION

Gasoline Direct Injection (GDI) was proven as a successful approach to reduce exhaust harmful emission and improves fuel economy [1]. With the installation of a GDI system in an engine it improves throttle response, fuel cut-off during acceleration, and rapid combustion stabilization. The heart to GDI is its mixture control [2], and pressure-swirl atomizers. These elements have been identified as the components that facilitate the necessary spray mixture for successful application of GDI technology in automotive engines. Its advantages includes a compact hollow-cone spray which produces fine droplets with increasing fuel-ambient pressure differential,

the suppression of spray penetration with the increase of ambient pressure, and a simple yet cost effective construction compared to other types of atomizers.

Lefebvre [3] described a classical theory on spray evolution that emerges from the orifice of a pressure-swirl atomizer and Cousins et al. [4] is shown in Figure 1. The evolution of the spray as the injection pressure is increased from zero, consists of several stages, i.e. i) dribble, ii) distorted pencil, iii) onion, iv) tulip, and v) atomization. The discharge coefficient and initial spray angle would differ for each stage until it reaches an asymptote value in the final stage.

The internal geometries of the pressure-swirl atomizers have great effect on the resultant spray characteristics [5, 6]. Among the types of pressure-swirl atomizers, variations of its internal geometries are pronounced. The internal geometry of pressure-swirl atomizers varies among developers in terms of final orifice lengths and diameters as well as swirl slots (helical, axial, and tangential). Nevertheless, the geometry of the needle tip remains unstudied with the exception of the work by authors [7].

The importance of pressure-swirl atomizers internal geometries becomes more pronounced when the spray has reached a steady state. Upon reaching a steady state, the discharge coefficient and the initial spray angle of a pressure-swirl atomizer largely depends on its internal geometry and the fluid properties [8, 9]. In addition, the authors [7] also found that the internal geometry affects the resultant liquid sheet thickness



downstream of the pressure-swirl atomizers. During transient state, the time for the spray to reach the steady state of atomization is critical especially in GDI application where the fuel was injected at high frequency [4]. Therefore, an injector configuration with the least time to reach the stable stage ( $v$ ) is highly desirable.

Regions of interest that depicts the most important transient flows would be a few millimeters inside and outside the final nozzle orifice. However, it is nearly impossible to perform an experiment to study the transient flow within these regions. Thus, a CFD approach to predict the probable transient flow characteristics is highly helpful in understanding the effect of altering several important internal geometries. According to Arcoumanis et al. [6], the most suitable approach to represent the actual event is by using volume of fluid multiphase model, which consists of mainly two phases: (i) liquid fuel, and (ii) air. In the work, just implemented, similar multiphase approach was used but the case studies were simplified into 2D axisymmetric swirl representations.

## 2. COMPUTATION

The internal nozzle geometry similar to the *Mitsubishi* GDI atomizer was arbitrarily selected as a base case study. The cross-section of such atomizer is shown in Figure 2(a). This study computes the transient formation of liquid fuel emerging from the geometrically similar pressure-swirl atomizer except for three variations of needle valve tips, and two different swirl intensities. The region of particular interest is shown in Figure 2(b), where the swirling motion of the liquid fuel initiated and ended with atomization just downstream the final orifice. The studied atomizer can be generally categorized as follows:

- Atomization approach: high-pressure, swirl, single fluid
- Actuating mechanism: electromagnetic (solenoid)
- Nozzle opening: inwardly
- Swirl generator: tangential slots
- No. of holes: single
- Spray pattern: hollow-cone

The flow inside the pressure-swirl atomizer and its near nozzle vicinity can be simplified into two phases: (i) liquid fuel, and (ii) air. In this study, an Eulerian multiphase model was used with n-Heptane representing the liquid fuel. The internal flow was calculated with the following assumptions:

1. the ambient air is initially quiescent
2. the transient effect of the needle lift is negligible
3. needle lift is at maximum and its distance is constant at 50 micron
4. pressure drop from high pressure fuel line to the injector tangential slot is virtually negligible
5. the flow is adiabatic and incompressible
6. the flow is fully turbulence and the effects of molecular viscosity are negligible
7. all fuel entering the needle seat passage from all the tangential slots has the same vector relative to the axis of symmetry.

The representation of assumption no. 7 is shown in Figure 3(a). A single swirl inlet angle  $\alpha$  parallel to the tangential slot was chosen to represent the each swirl intensity investigated. The directional vector components are listed as:

- Strong swirl components: axial=0, radial=-0.617, tangential=-0.787
- Weak swirl components: axial=0, radial=-0.899, tangential=-0.438

The above assumption allows the application of 2D axisymmetric swirl solver, which greatly reduces the computing cost. The calculation domain, which is represented as a 3D volume of fluid shown in Figure 2(c), is therefore simplified into a 2D region shown in Figure 3(b). It consists of only three sections: (i) valve seat passage, (ii) final orifice, and (iii) a few millimeters downstream the nozzle exit. The 2D rotating surfaces for each case were meshed using a scheme size of 0.05 mm. With this scheme size, the resulting number of cells for each case is approximately 3,000 cells. The minimum and maximum face areas were approximately 0.2e-03 mm<sup>2</sup> and 1.0e-03 mm<sup>2</sup> respectively. Then, the grid was a further refined using solution-adaptive refinement feature. After refinement, the number of cells for each case increased to 11,000 cells approximately. The final minimum and maximum area of the faces were closing to 0.2e-06 mm<sup>2</sup> and

1.0e-06 mm<sup>2</sup> respectively. The mesh density values were selected after several calculation attempts as a trade-off between accuracy and computing cost.

All six configurations are shown in Table 1. For each configuration, a computation was done for fuel-ambient pressure differential from 3.0 MPa to 10.0 MPa with a step size of 0.5 MPa. The renormalization group (RNG)  $k$ - $\epsilon$  turbulence model was chosen for this study due to several considerations [10]:

1. Extends the  $k$ - $\epsilon$  turbulence model with strong theoretical basis of determining constants without empiricism
2. Computationally more robust than standard  $k$ - $\epsilon$  model, plus its ability to replace wall function with a fine grid
3. Compared with standard  $k$ - $\epsilon$  model, the RNG model is more accurate for separated flow, stagnation point flow and swirling flow

### 3. RESULTS AND DISCUSSION

The validation of the calculation was done by measuring the static flow rate of a *Mitsubishi* GDI pressure-swirl atomizer at fuel-ambient pressure differential from 3.0 MPa to 10.0 MPa, with a step size of 1.0 MPa. The result of the measurement and the result from the calculation made under similar condition are shown on Figure 4. It can be seen that all the calculated values showed lower static flow rate compared to the actual measurement. Such difference maybe caused by the fuel flowing through the narrow gap between the needle valve and its guide that is not considered in these calculations. Although the calculated mass flow rates are about 6% to 48% lower than the measured value, the overall trend is the same and the discrepancy is consistent through the investigated pressure differential ranges.

The steady state phase contour of the CFD calculation is shown in Figure 5. It was observed from the calculation that the thin liquid sheet has fully developed and reached its steady state in less than 0.16 ms after start of injection (SOI). However, the analysis was arbitrarily done with data taken at 0.32 ms after SOI. It was found that when it reached a steady state, the resulting initial spray angle remains virtually unchanged for each case throughout the ranges of pressure

differentials applied. Such trend showed similarity with calculations and measurements made by Ren et al. [11] to study the influence of pressure differential on spray cone angle. Thus with negligible differences, the spray angle for each case is considered constant throughout the fuel-air pressure differentials from 3.0 MPa to 10.0 MPa.

The effect of each case study on the discharge coefficient is shown in Figure 6. All the trends show much similarity with the Lefebvre [3] classical theory, except between stage (iii) and (iv). For all these cases, the discharge coefficient between (iii) and (iv) shows large fluctuation. Nevertheless, the fluctuation is more pronounced with relatively stronger swirl intensity. As far as needle shape is concerned, surprisingly the extrude-tip needle showed the minimal time to reach the atomization stable stage (v), while the round-tip needle showed the largest discharge coefficient fluctuation in stage (iii) and (iv). To validate this result with actual transient measurement may not be possible because such instantaneous mass flow rate measurement would not be possible even with the latest measuring device. Although this result may not be supported by any experimental work, it still would give a good insight of such phenomena.

Figure 7 shows the liquid film thickness at nozzle exit for each case configuration. The sheet thicknesses were obtained from CFD output data of volume fraction of liquid fuel, where 50% volume fraction was taken as a borderline between the phases of liquid and gas. Also included in the Figure is a related empirical correlation found by Suyari and Lefebvre [12]. The correlation is given by

$$t_f = 2.7 \left[ \frac{d_0 \dot{m}_L \mu_L}{\Delta P \rho_L} \right]^{0.25} \quad (1)$$

The data of liquid sheet thickness from CFD calculation showed relatively good agreement with Suyari-Lefebvre correlation for a pressure-swirl injector static flow of 900 cc/min rated at 5.0 MPa. Although Suyari-Lefebvre correlation is fairly simple and failed to describe any effect of injector needle shape and swirl intensity, all the

liquid sheet thickness relation with fuel-air pressure differential show similar trend.

Next, the theoretical droplet SMDs were calculated from liquid sheet thicknesses and half spray cone angles obtained from the CFD calculations. The result for each case configuration is shown in Figure 8. The theoretical droplets SMD were calculated using Wang-Lefebvre SMD correlation [13], which is given by:

$$\text{SMD} = 4.52 \left( \frac{\sigma \mu_L^2}{\rho_A \Delta P^2} \right)^{0.25} (t_f \cos \theta)^{0.25} + 0.39 \left( \frac{\sigma \rho_L}{\rho_A \Delta P} \right)^{0.25} (t_f \cos \theta)^{0.75} \quad (2)$$

#### 4. CONCLUSIONS

This investigation was about comparing three types of needle geometry of pressure-swirl atomizers with two different swirl intensities. The study was done at fuel-air pressure differential from 3.0 to 10.0 MPa with a step size of 0.5 MPa. From the result obtained, several conclusions are derived:

1. The use of 2D axisymmetric swirl multiphase Eulerian enables rapid and adequate CFD calculation of the internal flow and near nozzle vicinity of pressure-swirl atomizers.
2. The configuration with low swirl strength showed more stable fluctuation of discharge coefficient between stages (iii) to (iv).
3. The round-tip needle combination shows the largest fluctuation of discharge coefficient. This would suggest that both point-tip and extrude-tip needle have less time needed to reach the stable zone (v). Indeed, this would be an excellent advantage in the application of short pulse width.
4. Results from the calculations suggest that relatively high fuel-air pressure differential, lower discharge coefficient, stronger swirl intensity, thinner liquid film, and larger cone angle produce better atomization.
5. Needle-tip geometry either alone or mated with swirl strength does affect atomization by means of influencing the

resulting discharge coefficient, liquid film thickness and the initial spray cone angle.

6. At fuel-air pressure differential ranging from 3.0 to 10.0 MPa, point-tip needle combined with high swirl intensity generally produce lowest discharge coefficient, thinner liquid film, larger spray cone angle. Thus, it should produce smaller droplet size than extrude-tip and round-tip needle.
7. Needle tip geometrical shape and swirl generator configuration should be a considerable factor in designing fuel injectors especially for GDI application.

#### ACKNOWLEDGEMENTS

The authors are grateful to the Malaysian Ministry of Science, Technology and Innovation (MOSTI, ref 03-02-06-0000 PR0005/03) for the generous funding given to this project. The authors are also grateful to the technicians of the Automotive Development Centre (ADC) of UTM in making the project a success.

#### REFERENCES

- [1] Zhao, F., Harrington, D. L., and Ming, C. L. "Automotive Gasoline Direct-Injection Engines". SAE International. 2002
- [2] Ohsuga, M., Shiraishi, T., Nogi, T., Nakayama, Y., and Sukegawa, Y. "Mixture Preparation for Direct-Injection SI Engine". SAE Paper. 970542
- [3] Lefebvre, A. H. "Atomization and Sprays". Hemisphere Publication. 1989
- [4] Cousins, J., Ren, W. M., and Nally, S. "Transient Flows in High Pressure Swirl Injectors". SAE Paper. 980499
- [5] Preussner, C., Doring, C., Fehler, S., and Kampmann, S. "GDI: Interaction between Mixture Preparation, Combustion System and Injector Performance". SAE Paper. 980498
- [6] Arcoumanis, C., Gavaises, M., Argueyrolles, B., and Gazlin, F. "Modeling of Pressure Swirl Atomizers for GDI Engines". SAE Paper. 1999-01-5000
- [7] Aziz, A. A., and Ali, M. F. "Numerical Investigation on the Needle-shape of Hollow-Cone Pressure-Swirl Type Gasoline Direct Injector". SAE Paper. 2006-01-1002
- [8] Dumas, M., and Laster, R. "Liquid-film Properties for Centrifugal Spray Nozzles". Chem. Eng. Prog., pp. 518-526, 1953
- [9] Dombrowski, N., and Hasson, D. "The Flow Characteristics of Swirl Centrifugal Spray Pressure Nozzles with Low Viscosity Liquids". AIChE Journal, Vol. 15, no 4, p 604. 1969.

[10] Yakhot, V., and Orszag, S. A. “Renormalization Group Analysis of Turbulence – Basic Theory”, J. Sci Computing, 1: 3-51. 1986

[11] Ren, W. M., Shen, J., and Nally Jr., J. F. “Geometrical Effects Flow Characteristics of a Gasoline High Pressure Swirl Injector”. SAE Paper. 971641

[12] Suyari, M., and Lefebvre, A. H. “Film Thickness Measurements in a Simplex Swirl Atomizer”. AIAA J. Propul. Power. 2(6):528-533. 1986

[13] Wang, X. F., and Lefebvre, A. H. “Mean Droplet Size from Pressure-Swirl Nozzles”. AIAA J. Propul. Power. 3(1):11-18. 1987

- $d_0$  final orifice diameter (mm)
- $k$  turbulence kinetic energy ( $m^2/s^2$ )
- $\dot{m}_L$  mass flow rate (g/s)
- $t_f$  thickness of liquid film at nozzle exit ( $\mu m$ )
- $t$  time (ms)

**LIST OF NOTATIONS**

**ABBREVIATIONS**

- CFD Computational Fluid Dynamics
- GDI Gasoline Direct Injection
- RNG Renormalization Group
- SOI Start of Injection
- SMD Sauter Mean Diameter
- VOF Volume of Fluid

**LATIN SYMBOL**






- A point-tip needle; strong swirl (-)
- B extrude-tip needle; strong swirl (-)
- C round-tip needle; strong swirl (-)
- D point-tip needle; weak swirl (-)
- E extrude-tip needle; weak swirl (-)
- F round-tip needle; weak swirl (-)

**GREEK SYMBOL**

- $\alpha$  swirl inlet angle ( $^\circ$ )
- $\Delta P$  pressure differential between liquid fuel and ambient (MPa)
- $\epsilon$  turbulence dissipation rate ( $m^2/s^3$ )
- $\mu_L$  liquid fuel viscosity ( $Ns/m^2$ )
- $\rho_A$  ambient air density ( $kg/m^3$ )
- $\rho_L$  liquid fuel density ( $kg/m^3$ )
- $\sigma$  surface tension ( $J/m^2$ )
- $\theta$  initial half spray cone angle ( $^\circ$ )

**TABLE**

Table 1: Case study configurations

Config.	Needle valve tip			Swirl intensity	
	Point	Extrude	Round	Strong	Weak
A					
B	•			•	
C		•		•	
D	•		•		•
E		•			•
F			•		•

Figures

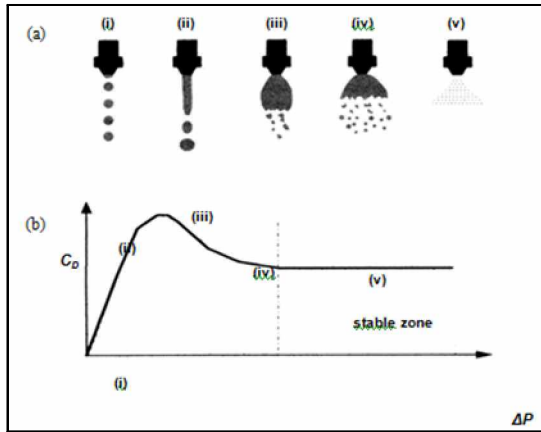


Figure 1: (a) Evolution of liquid structure with injection pressure [3], and (b) Evolution of discharge coefficient for a pressure-swirl atomizer [4].

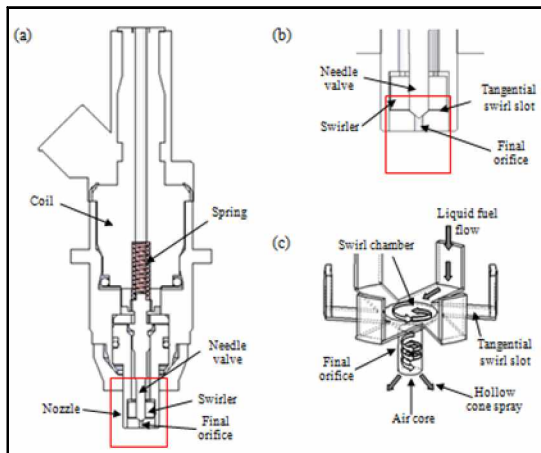


Figure 2: (a) Cross-section of a GDI injector, (b) geometrical region that has great influence on the spray characteristics, (c) volume of fluid of the tangential swirl slots, swirl chamber, and final orifice.

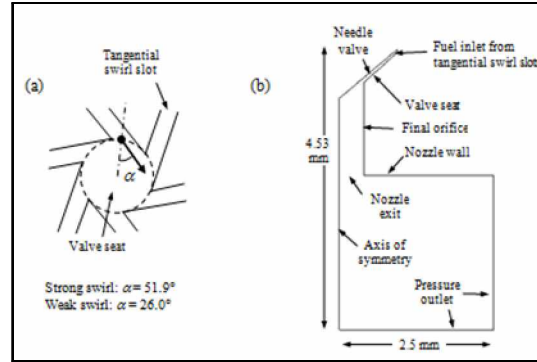


Figure 3: (a) is representation of fuel inlet vector entering needle seat passage from angled tangential slots, viewed from nozzle exit (b) boundaries of the 2D rotating region for configuration A and D (point tip needle).

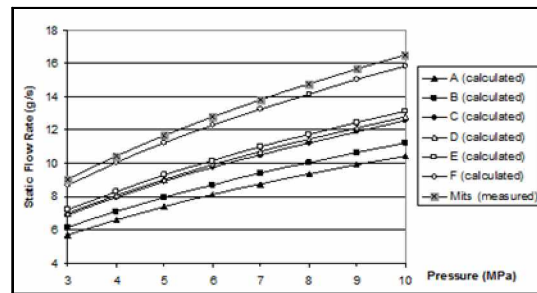


Figure 4: Calculated and measured static mass flow rate of several atomizer configurations.

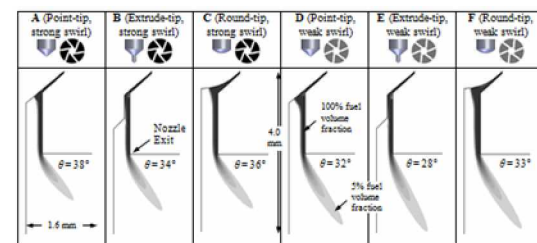


Figure 5: Volume fraction of liquid fuel at 0.32 ms after start of injection, plotted in grayscale. The color black represent liquid fuel volume fraction 100%. Half spray cone angle ( $\theta$ ) is given by the direction of densest liquid sheet exiting the nozzle.



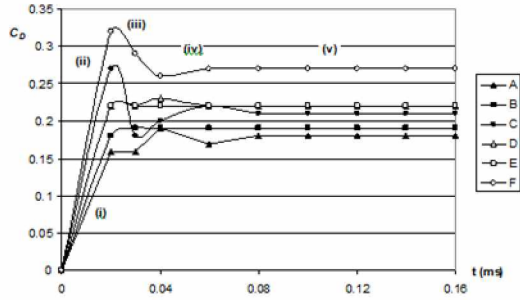


Figure 1: Effect of several combinations of needle-tip shape and swirl intensity on discharge coefficient.

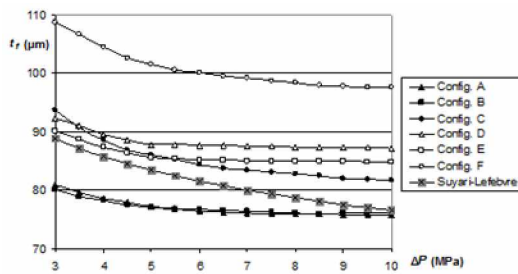


Figure 2: Liquid sheet thickness,  $t_f$  at Nozzle Exit of each case configuration with pressure differential,  $\Delta P$  ranges from 3.0 to 10.0 MPa.

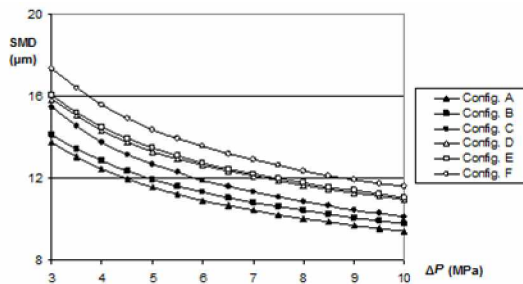


Figure 3: Theoretical droplet SMD calculated using Wang-Lefebvre correlation given by Equation (2) with liquid sheet thickness and spray cone angle obtained from CFD calculations.

# Swirl Intensity Effect on Premixed Jet Flame

Mohd Heady Jalaluddin, Mohd Ibthisham Ardani, Mazlan A. Wahid

Faculty of Mechanical Engineering,  
Department of Thermofluid  
Universiti Teknologi Malaysia  
UTM Skudai, Johor, Malaysia

## ABSTRACT

In this paper the effect of swirl intensity on premixed jet flame is investigated. Flame structure under various swirl number is studied. Flame characteristics such as height, pattern and color under swirling environment are also determined for the premixed flame. Particle Image Velocimetry is used to analyze the streamline, vorticity and velocity vector of the swirl generated from the burner. From the observation it can be said that changes of velocity, swirl number and equivalence ratio lead to changes of flame shape, appearance, height and mixture between air and fuel. In general, the higher the swirl number, the premixed flame becomes more stabilized by the formation of circulation zone near the exit port.

### Keywords

*Swirl intensity, Particle Image Velocimetry*

## 1. INTRODUCTION

### 1.1 Type of Swirl

The swirling motion can be categorized into weak and strong swirl based on its swirl intensity. Swirl categorized as a weak if the swirl number is lesser than 0.4. The low swirl creates significant lateral pressure gradients only. If the swirl number is greater than 0.6 the swirl is called high swirl. In this case, the radial and axial pressure gradients large enough to cause an axial recirculation to form of a central toroidal recirculation zone (CTRZ). [1]

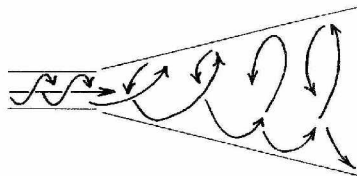


Figure 1: Lateral pressure gradient

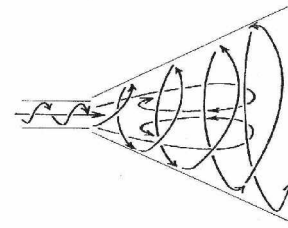


Figure 2: Radial and axial pressure gradient

In high swirl case, the flow becomes turbulent and several regions of reverse flow are created, where the fuel flow is actually circling back in a direction opposite to the original flow ("recirculation"). In most conventional burners the fuel is not mixed with air prior to entering the flame zone, but the recirculating turbulent flow around the blockage entrains air into the fuel stream. A flow of fuel and air recirculates in turbulent eddies. The pattern of recirculatory flow is relatively stable. Between a location of reverse flow and normal flow there is a continuous gradient of fuel-air mixture flow values, including many locations where the flow rate exactly matches the burn rate, or flame speed. These locations are where the flame is anchored. To either side of the location where the flame speed matches the fuel-air flow velocity, the fuel-air flow rate is too fast or too slow or the amount of entrained air results in a fuel mixture that is too rich or too lean to support continuous burn. If the flame speed is altered by outside influences such as air from outside the fuel stream or fluctuations in the fuel-air mixture stream, the burn point can move to an adjacent location where the fuel-air mixture stream velocity will be correct for the new flame speed value. Thus conventionally, recirculation has been a necessary condition to stabilize the flame in burners.

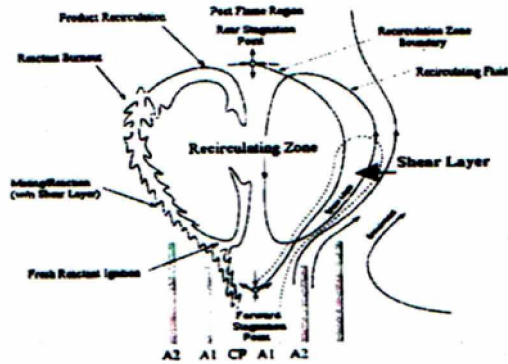


Figure 3: Sketch of swirling flow field. [2]

## 1. EXPERIMENTAL SETUP

The experimental setup diagram for Flame visualization and analysis is shown in Figure 3 and experimental setup for Particle Image Velocimetry (PIV) System and analysis is shown in Figure 5. Swirl can be generated by several methods, namely use of vanes, rotating tube and tangential or axial entry. In this experiment, swirl is generated by a burner which was designed consists of cylindrical swirler section attached to concentric nozzle and settling chamber. Weak swirl is produced by four tangential air injectors fitted to the rim of the swirler section. Typical swirl intensities needed for flame stabilization are very low [3].

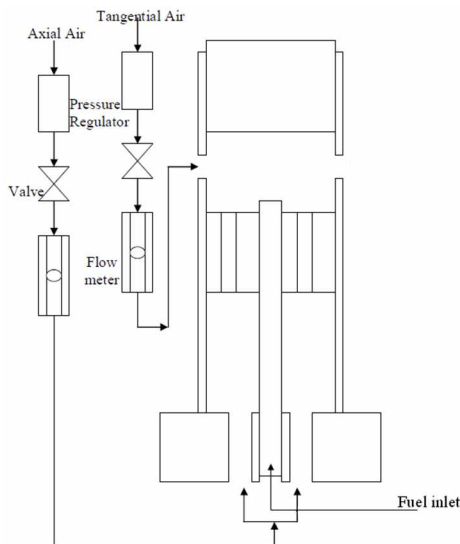


Figure 4: The diagram of the experimental setup.

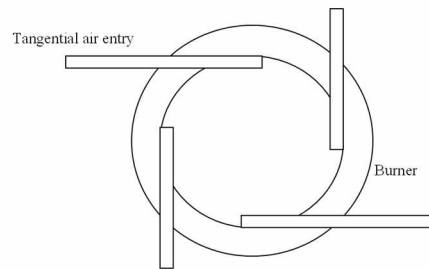


Figure 5: Top schematic view of the burner at swirl section

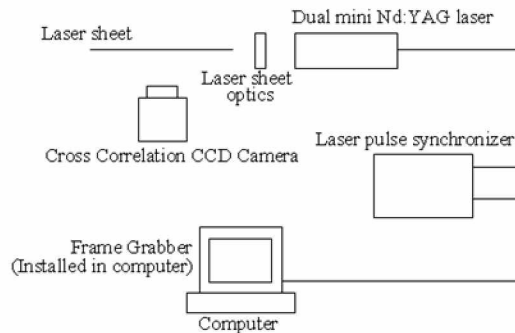


Figure 6: The example of Schematic PIV Diagram

The laser light source is double pulsed so that two images of each seeding particle are recorded by the camera. In this study, Particle Image Velocimetry (PIV) was used. Images are recorded directly with a CCD camera and frame-grabber, and can be studied without the necessary delay and overhead associated with the scanning of photograph. The application of PIV allows for a simple realization of the cross-correlation technique for pairs of two separate images. It removes the ambiguity of the sign of the displacement and improves signal dynamics. Setup for experiment PIV system consists of system control, flow imaging, image capture and image analysis and display.

In this study, the effect of several parameters on the flame shape, color, stability and height is considered. The parameters varied during experiment were swirl number ( $S$ ), Equivalence ratio ( $\phi$ ), Reynolds number ( $Re$ ), Fuel mole fraction ( $X_{fuel}$ ), tangential air flow rate, axial air flow rate, fuel flow rate and flame height.

### 2.1.1 Swirl Number

Swirl number,  $S$ , measure the degree of swirling motion of the flow. Low swirl phenomena ( $S \leq 0.4$ ) typically are for which the swirl velocity does not cause the flow structure to be drastically changed. Flames with low degree of swirl have a

limited practical interest mainly due to the instability problems. At high degree of swirl ( $S \geq 0.6$ ), radial and axial pressure gradients are large enough to cause an axial recirculation in the form of a central toroidal recirculation zone (CTRZ), which is not observed at lower degrees of swirl. Swirl is defined as follows,

$$S = \frac{G_{\theta}}{G_B R_B}$$

where ;

$G_B$  = axial flux of angular momentum

$G_{\theta}$  = axial flux of axial momentum

$R_B$  = burner radius

### 2.1.2 Equivalence Ratio ( $\phi$ )

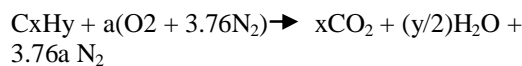
Mixture equivalence ratios represent the characteristic of the mixture. Equivalence ratio is commonly used to indicate quantitatively whether a fuel and oxidizer mixture is rich, lean, or stoichiometric. For fuel-rich mixtures,  $\phi > 1$ , for fuel-lean mixture,  $\phi < 1$ , and for a stoichiometric mixture,  $\phi$  equals unity. The equivalence ratio is defined as:

$$\phi = \frac{\left[ \frac{A}{F} \right]_{stoic}}{\left[ \frac{A}{F} \right]_{exp}}$$

where the stoichiometric air-fuel ratio is given as;

$$\left[ \frac{A}{F} \right]_{stoic} = \left( \frac{m_{air}}{m_{fuel}} \right)_{stoic} = \frac{4.76a MW_{air}}{1 MW_{fuel}}$$

The stoichiometric air-fuel ratio is determined by writing simple atom balances, by assuming that the fuel reacts to form an ideal set of products. For this study, we use a mixture of 40% propane and 60% butane fuel, is used. So, for a hydrocarbon fuel, the stoichiometric relation can be expressed as;



where ;

$$a = x + y/4$$

Stoichiometric in the above equation is a term where complete combustion occurs. For

example, the stoichiometric quantity of oxidizer is just that amount of oxidizer needed to completely burn a quantity of fuel. So, the stoichiometric air-fuel ratio is just the right ratio of air and fuel to have a complete burning process or a complete combustion process.

### 2.1.3 Fuel Mole Fraction ( $X_{fuel}$ )

Fuel mole fraction is an important and useful parameter used to characterize the composition of a mixture, apart from mass fraction. For a multi component mixture of gases composed of  $N_1$  moles of species 1,  $N_2$  moles of species 2, and so forth. The mole fraction of species  $i$ ,  $X_i$  is defined as the fraction of the total number of moles in the system that are species  $i$ . So, mole fraction can be defined as:

$$X_i = \frac{N_i}{(N_1 + N_2 + N_i + \dots)} = \frac{N_i}{N_{TOTAL}}$$

where ;

$N$  = number of mole

It is known that mole fraction is base on volume, so the fuel mole fraction in this study can be determined by dividing the fuel volume flowrate over the total volume flowrate of air and fuel. Thus, the fuel mole fraction can be determined using this equation;

$$X_{fuel} = \frac{\dot{Q}_{fuel}}{(\dot{Q}_{fuel} + \dot{Q}_{air})} = \frac{\dot{Q}_{fuel}}{\dot{Q}_{Total}}$$

where ;

$\dot{Q}$  = Volume flow rate ( $m^3/s$ )

Fuel mole fraction is a dimensionless parameter. From the definition, it is known that the sum of all the constituent mole fractions of the mixture must be unity, or;

$$\sum_i X_i = 1$$

In this study, note that the sum of fuel mole fraction,  $X_{fuel}$ , and the air mole fraction,  $X_{air}$ , must be unity, that is;

$$X_{fuel} + X_{air} = 1$$

### 3. DISCUSSION

The effects of swirl number for several equivalence ratios on the characteristics of premixed shape lead to changes in its appearance and behavior.

#### 3.1 Observation of Swirl Flame

Figure 7 and Figure 8 shows the effect of swirl number on premixed flame. Figure 7 is for the fuel with  $\varnothing=1.54$  whereas Figure 8 is for the fuel with  $\varnothing=1.98$ .

The increase of swirl number shows the radical changes on flame structure and their respective height.

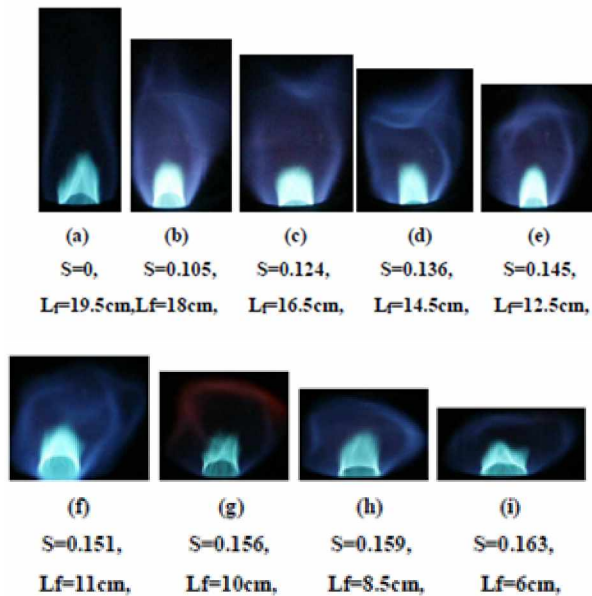


Figure 7. Effect of swirl number on premixed flames,  $\varnothing=1.54$

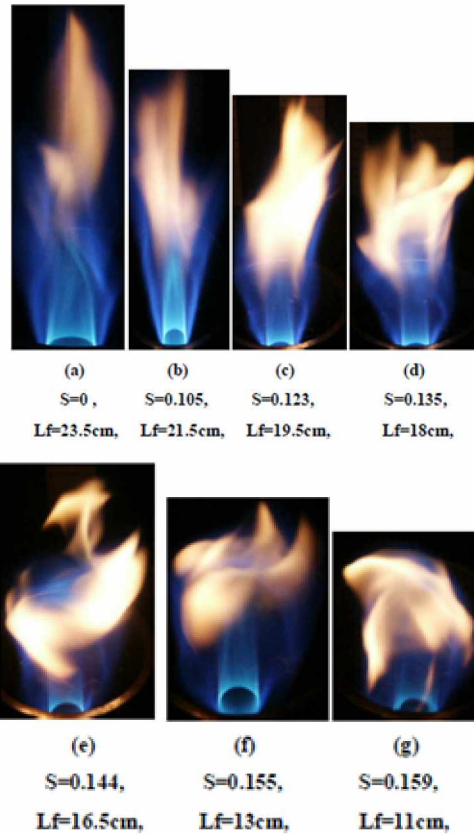


Figure 8. Effect of swirl number on premixed flames,  $\varnothing=1.98$

Figure 9 shows the effect of swirl number on flame height for various mixtures of equivalence ratios. The flame height reduction appears as curve with negative gradient when swirl number increase.

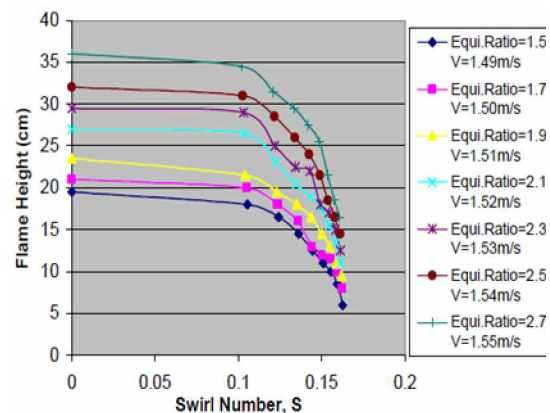


Figure 9: Flame height (cm) versus swirl number, S



### 3.2 Particle Image Velocimetry (PIV) Analysis

Figure 10 to 34 shows smoke streamline picture for various swirl number, velocity vector map (Average Filter after masking vector map), vorticity and streamline.

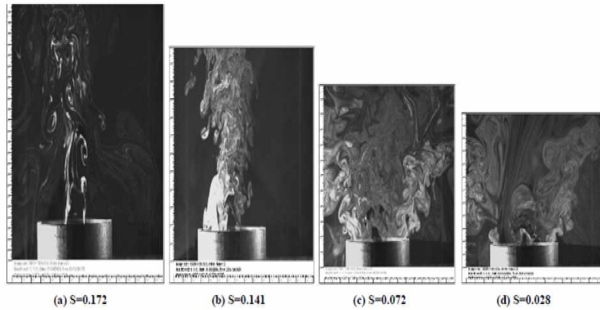


Figure 10 : Smoke streamline picture for various swirl number

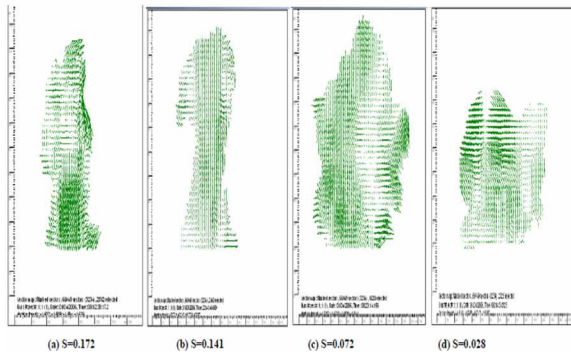


Figure 11 : Velocity Vector Map (Average Filter after Masking Vector Map)

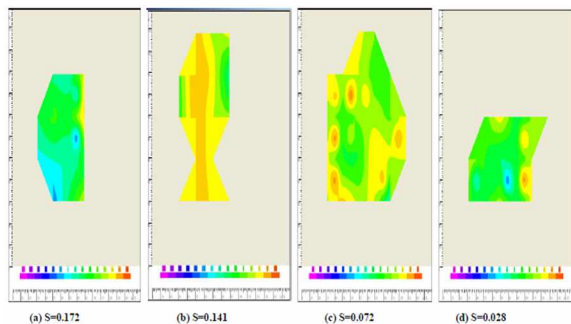


Figure 12 : Vorticity

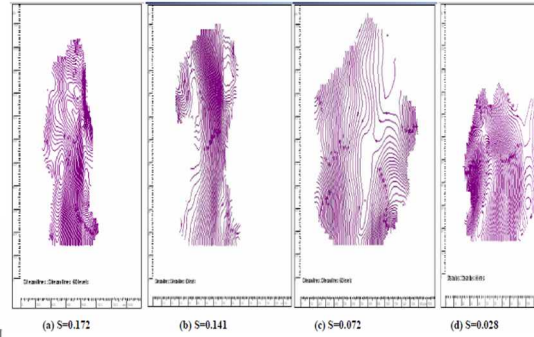


Figure 13 : Streamline

From smoke picture of Figure 10 it can be seen that when swirl number,  $S$  increases the flame becoming more chaotic, recirculation zone appear and consequently the flame height will be lower. Vorticity is one of the parameter that shows the tendency for elements of the fluid to spin. The smoke streamline image implies the flow circle's enforcement or flow swirling movement inside the circulation zone. From observation, the vorticity increases if swirl number is increases.

### 5. CONCLUSION

As the conclusion it can be said that swirl helps in mixing and thus enhances combustion, shortens the flame height and helps to stabilize the flame. From the observation it can be said that changes of velocity, swirl number and equivalence ratio lead to changes of flame shape, appearance, height and mixture between air and fuel. In general, the higher the swirl number, the premixed flame becomes more stabilized by the formation of circulation zone near the burner exit port.

### ACKNOWLEDGMENT

The authors would like to thank Universiti Teknologi Malaysia and the Malaysian government for supporting this research activity.

### REFERENCES

- [1] J. Warnatz, U. Maas, R.W. Dibble, 'Combustion', Springer-Verlag Berlin, Heidelberg, New York, 3rd Edition; 2000.
- [2] A.K. Gupta, M.J. Lewis and M.Daurer "Swirl Effects on Combustion Characteristics of Premixed Flames".
- [3] R. K Cheng, 'Velocity and Scalar Characteristics of Premixed Turbulent Flames Stabilized by Weak Swirl', Combustion and flame, 1995.

# Liquid Fuel Vaporization System

**Mazlan Abdul Wahid, Mohsin Mohd Sies,  
Mohd Khairrul Mohd Suhaimi, Mohd Ayub Sulong**

*Faculty of Mechanical Engineering, Universiti Teknologi Malaysia,  
81310 UTM Skudai, Johor, Malaysia*

## ABSTRACT

This research focused in the development of liquid fuel vaporization system. Thermodynamic parameters considered to transform the fuel from liquid to gas state, are preheat temperature, vaporization chamber temperature, spraying pressure and vaporization chamber pressure. This transformation requires two important sub processes which are preheating and atomizing of the liquid fuel. In this research, diesel fuel is preheated at 100°C, 150°C, 200°C, 250°C, 300°C, and 350°C. This temperature has been identified to be lower than the auto ignition temperature of the diesel fuel at critical pressure. The next stage, which is atomization process, is achieved through the injection of liquid fuel at various elevated pressure, namely at 60, 80 and 100 bar. Atomization process transforms the liquid fuel into a very fine liquid droplet where the surface area of the liquid fuel is significantly increased. SUPERTRAPP calculation is made for n-heptane, n-dodecane and surrogate diesel, as a quantitative baseline and guidance in developing the liquid fuel vaporization system. From the baseline calculation, at 1 bar stoichiometric fuel-air mixture is fully vaporize at 276 K, 359 K, and 389 K for n-heptane, n-dodecane and surrogate diesel respectively. Fuels at higher molecular weight will vaporized at higher preheat temperature. This has been confirmed by the shadowgraphy technique that is used to observe the vaporization process of diesel qualitatively.

## Keywords

*Fuel Vaporization, Diesel Fuel, Atomization, Shadowgraphy*

## 1. INTRODUCTION

Liquid Fuel is one of the most practical sources of energy that have been used in internal combustion

engine and propulsion system. Liquid fuel has been widely used for land vehicle, aerospace, marine and also stationary combustion equipment such as furnace and boiler. Different type of fuels namely gasoline, diesel, kerosene, JP-8 and JP-10 are from hydrocarbon base, which are usually denoted by the general formula  $C_nH_m$ . These hydrocarbon fuels exist in all phases namely solid, liquid and gas. Every type of liquid fuels gives difference chemical structure, physical and thermodynamics properties.

Tucker (2005) constructed a flash vaporization system (FVS) for detonation of hydrocarbon fuels in a pulse detonation engine (PDE). In the research four hydrocarbon base fuels which are n-heptane, isooctane, aviation gasoline, and JP-8 has been tested. A high pressure fuel flash vaporization system was designed and built to reduce and eliminate the time required to evaporate the fuel droplets. Since these fuels vary in volatility and octane number its present a clear picture on the benefits of flash vaporization. From the results, the FVS has quickly provided a detonable mixture for all tested fuels without coking or clogging the fuel lines. The most significant achievement of the research was the detonation of flash vaporized JP-8 and air. The results show that the flash vaporized JP-8 used 20 percent less fuel to ignite the fuel air mixture twice as fast (8 ms from 16 ms) when compared to the unheated JP-8 combustion data. The FVS has been validated as a reliable method to create the droplet free mixtures required for liquid hydrocarbon fueled PDEs.

The general nature of the processes involved in spray combustion in ideal case for the combustion of a dilute spray is shown in Figure 2.1. System containing droplet diffusion flames are characterized by their yellow nature. [1, 2]

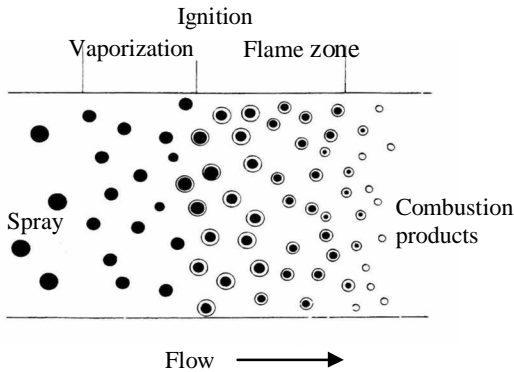


**Figure 2.1:** A diagrammatic model of idealized heterogeneous spray combustion. [1, 2]

### 3. ATOMIZATION PROCESS

In combustion it is necessary to atomize and distribute the liquid fuel in a controlled manner within the combustion chamber. The performance of the combustion unit is critically dependent upon the drop size produced by the atomizer and the manner in which the combustion air mixes with the droplets. Atomizer produce a fine spray of liquid fuel by injecting a narrow diameter jet or by increasing the surface area of a sheet of the liquid fuel until it becomes unstable and break down. [1, 2]

Within this project, the pressure jet atomizer which is diesel injector was used. This technique depends simply upon forcing the liquid fuel through an orifice under pressure to form an unstable jet of high velocity which disintegrates after leaving the orifice. In this way flat or conical spray sheets can be produced. The shape, spatial distribution and the droplet sizes produced by pressure jet atomizers are dictated by the geometry of the atomizer. An important feature of plain-orifice (non-swirling) pressure atomizers is that the flow rate is proportional to the square root of the pressure difference: [1, 2]

$$\dot{m}_L = 35.1 C_D D_o^2 (p_L \Delta P_L)^{1/2} \quad (2.9)$$

Where  $\dot{m}_L$  is the mass liquid flow rate,  $C_D$  is the discharge coefficient, which is related to the

area of the hole and its length/diameter ratio,  $D_o$  is the orifice diameter,  $p_L$  the liquid density and  $\Delta P_L$  the differential pressure of the liquid. [1, 2]

In practice, for a given nozzle the following relationship holds:

$$\frac{\text{Flow rate}}{(\text{Pressure Differential})} = \text{const. (Flow Number)} \quad (2.10)$$

The flow number (F.N) is a characteristic parameter of any plain stem pressure atomizer. A certain critical pressure must be attained before the atomization process occurs. This restricts the turn-down ratio of the atomizer which is the ratio of maximum to minimum liquid fuel flows. The upper limit is normally limited by the pressure attainable by the pump in the fuel handling system. [1, 2]

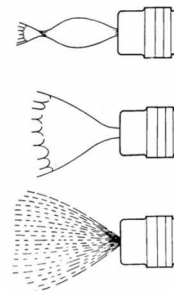


**Figure 3.1:** Stages in development of atomization by a pressure jet, (a) bubble formation at low fuel pressure, (b) partial sheet atomization at intermediate fuel pressure, and (c) finely divided spray at high fuel pressure. [1, 2]

In practice, Sauter mean droplet diameters ( $d_{32}$ ) are in range 90 to 200  $\mu\text{m}$ . [1, 2] The Sauter Mean Diameter (SMD) is used to describe a characteristic droplet with a volume to surface ratio that is equal to that of the spray as a whole. The volume mean diameter  $D_{30}$  which is defined for a discrete distribution as: [6]

$$D_{30} = \sqrt[3]{\frac{\sum N_i \delta_i^3}{\sum N_i}} \quad (2.11)$$

Where  $N_i$  is the number of droplets of diameter,  $\delta_i$ . The volume mean diameter is the average droplet volume of the spray. The surface mean diameter is the area or surface of the droplets with a surface area equal to the mean surface area and is given by: [6]

$$D_{30} = \sqrt{\frac{\sum N_i \delta_i^2}{\sum N_i}} \quad (2.12)$$

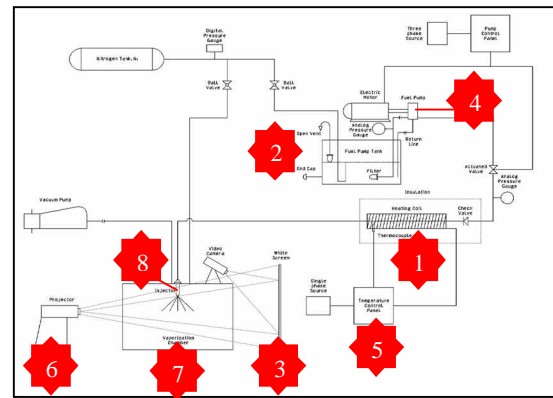
Where  $N_i$  is the number of droplets, and  $\delta_i$  is the average diameter of the size range. The SMD is defined as the volume to surface mean diameter and is given by: [6]

$$SMD = D_{32} = \frac{D_{30}^3}{D_{20}^2} \quad (2.13)$$

And is the diameter of an equivalent droplet with a ratio of volume to surface area equal to that of the entire spray. [6]

#### 4. EXPERIMENTAL SETUP

The development of the fundamental rig is very crucial to make sure the experiment can be conducted smoothly. The fundamental rig consisted of three main subsystems which are liquid fuel vaporization system, fuel handling unit and Shadowgraph setup. Each of the subsystem consists of several other components. The whole fundamental setup is presented in figure 4.1.



- |  |                    |  |                           |
|--|--------------------|--|---------------------------|
|  | Heater             |  | Temperature Control Panel |
|  | Fuel Pump          |  | Projector                 |
|  | Screen             |  | Vaporization Chamber      |
|  | Pump Control Panel |  | Injector                  |

**Figure 4.1:** The photo of LFVS setup at High speed Reacting flow Research Laboratory (HiRef)

The liquid fuel vaporization unit consists of fuel atomizer\injector, vaporization chamber, heating element, vacuum pump and nitrogen tank. The main function of this subsystem is to provide safe medium and confine space for atomizing and vaporizing process to occur. The chamber is firstly vacuumed by the vacuum pump to send out all the gases within the vaporization chamber, this is for safety precaution. Secondly, only the nitrogen gas is being charged into the vaporization chamber since nitrogen is not one of the combustion agents. Although this method are not very practical, since the chamber size is very large and it is hard to fully vacuum the chamber, but at least the air and oxygen content has been reduced to the safe point. After that, the pressurized and heated liquid fuel from the fuel handling unit system will be atomized through the diesel injector\atomizer.

Heating element is very important part for the success of the liquid fuel vaporization system. The fuel is heated just before entering the injector diesel to increase the internal energy of the fuel. the suitable range of the heater temperature for this experiment is between 27°C (ambient

temperature) to 400°C. The heater is provided with built in check valve to avoid backward flow of the heated fuel when the fuel pressure increase. The electric heating element is controlled by temperature control panel. The user needs to input the desired temperature into the controller, the thermocouple brought the output data, which is the actual fuel temperature within the pipe line, if the fuel temperature is lower than the desired temperature, the heater is switched on but when the fuel temperature is above the desired temperature, the heater is automatically switched off by the multi circuit breaker within the control panel.

The diesel injector which acts as an atomizer within this system is used to generate small droplets during the fuel injection process for preheated fuel. This single spring diesel injector is used in one of the HINO injection systems. The injector is used in spray combustion of compression ignition engine for HINO GENERATOR, EH500. This diesel injector is used within the experiment, since the injector can withstand at relatively high pressure and temperature. The nozzle type designation for this diesel injector is ND-DLLA150S31-33ND97 which is manufactured by DENSO Company.

The diesel injector mechanism is fully operated by mechanical concept. From the high pressure fuel line the liquid fuel is flowed into the injector fuel inlet. Within the diesel injector, there is small fuel line connecting the fuel inlet with the valve body (Figure 3.8). There is a finely machined needle valve which uncovers and covers the tiny nozzle orifices for the liquid fuel to flow out and avoid the low pressure atomization. The needle is only opened for the liquid fuel to flow through the nozzle holes when the liquid fuel pressure achieved at certain high pressure. This pressure can be controlled by the user with adjusting the nozzle retaining screw which change the pressure of the compression spring within the diesel injector, since the spring that pushes the pin.

This chamber is designed to provide the confine space for liquid fuel to completely atomize and vaporize. The chamber is fabricated to withstand with atmospheric pressure and high elevated temperature. Several equipments had been attached to this liquid fuel vaporization chamber, such as outlet line to the vacuum pump and inlet line from the nitrogen tank. This fully transparent glass chamber allowed the light to pass through it,

so the image of atomized and vaporized fuel can be projected on the white screen.

Another important subsystem of this experiment rig is the fuel handling unit. The fuel handling unit consists of the fuel filters, fuel pump, solenoid valves, and pump control panel. This subsystem will supply and pressurize the liquid fuel before entering the liquid fuel vaporization system.

Fuel pump is one of the components of the fuel handling unit. This component is used to pressurize the liquid fuel before the fuel injected into the vaporization chamber through diesel injector. The TECO fuel pump is generated by the 3-phase induction motor which is fabricated by Tong Yuan Elec. & Mach. Pvt. Ltd.

All these valves are controlled by the electronic control panel system (figure 3.12). This control panel will control the output pressure of the pump. This fuel pump also equipped by one analog pressure gauge. The pressure range for this pump is between 0 to 3600 psi which is about 0 to 248.211 bar.

#### 4.1 Shadowgraph Setup

A bright point light source is needed to cast a sharp shadow on the screen, in this experiment, the Canon LV-S3 projector is used to produce the white light beam. The projected image is casted on the white screen and the image produced is recorded by JVC everio G GZ-MG630 video camcorder. From the calculation (equation 2.18) the magnification of the shadowgram with respect to the schlieren object is 1.333, since the distance between the screen and point light,  $h$ , is 2 m and the distance between the screen and shlieran object, diesel injector,  $g$ , is 0.5 m. This parameters need to be taken into consideration, since its will affect the sensitivity or the contrast, geometric blur and diffraction blur of the casted image.



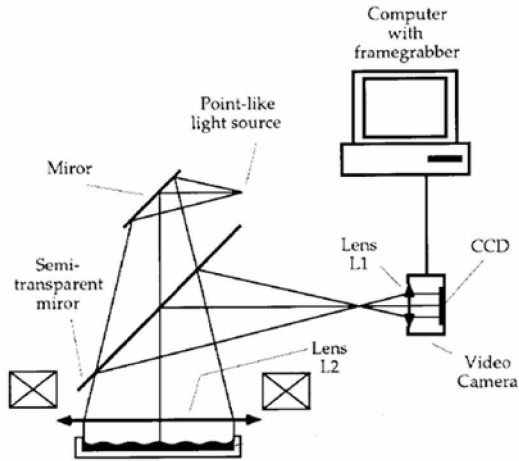


**Figure 4.2:** The schematic diagram for the shadowgraph setup.

### 5. BASELINE GENERATION

The computed baseline data is important for the development of the fundamental liquid fuel vaporization system. This chapter will cover all the procedure for data generation using this code, data calculation and plotting the graphs. Also method for entering the new component into the database and the important technique will be explained within this chapter. The fuels that will be studied using SUPERTRAPP are n-heptane, n-dodecane and the new entry data is surrogate diesel.

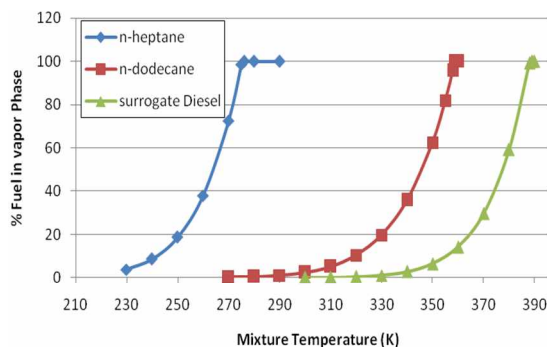


**Figure 5.1:** Percentage of fuel in vapor phase for stoichiometric mixture at 1 bar.

At the mixture temperature required to achieve 100% vapor with the n-heptane, only 0.45% vapor of n-dodecane and no vapor occur for the surrogate diesel (Figure 5.1). This shows the importance of the liquid fuel vaporization system to achieve a vaporized of the surrogate diesel and other heavy fuels.

the fuel vapor should not condense back into a liquid. If the chamber pressure is increased, the minimum mixture temperature to maintain the fuel in the vapor state would also increase. The increase in chamber pressure from 2 to 3 bar increases the minimum mixture temperature by 7°C for surrogate diesel (Figure 5.2).

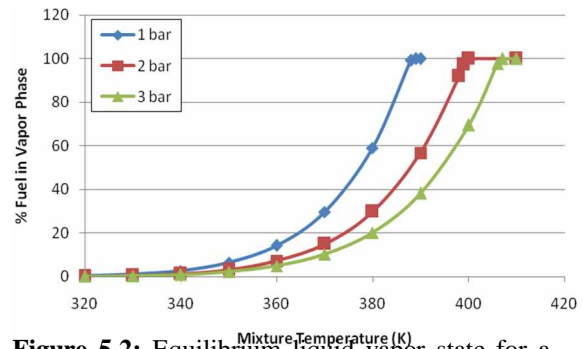


**Figure 5.2:** Equilibrium liquid vapor state for a stoichiometric surrogate diesel and air mixture at various chamber pressures.

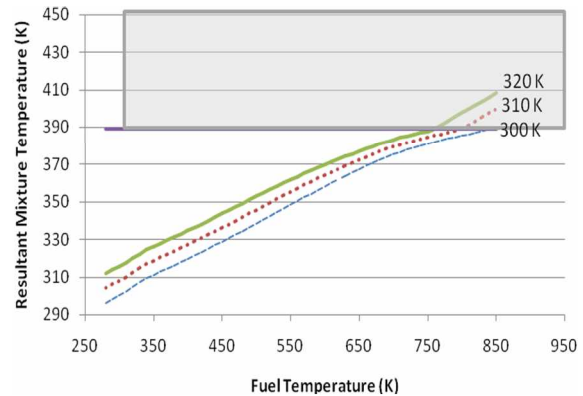


**Figure 5.3:** Stoichiometric surrogate diesel air mixture liquid vapor equilibrium in the chamber for 3 air temperatures at 1 atm. Fuel injection pressure at 60 bar.

From the generated models, there are no significant change in the flash vaporization region (hatched region) and the minimum resultant mixture temperature for the surrogate diesel to vaporize still at 389 K. The are small variances, the fuel temperature needed to vaporize is slightly increased for several Kelvin when the fuel injection pressure increase.

## 6. RESULTS AND DISCUSSION

### 6.1 Injection Pressure at 60 bar

This section illustrates the sequence of the injection process of the diesel fuel at 60 bar and heated with heating element at various different temperatures. The phase of the diesel achieved just after the injection process can be determined. The figure 6.6 shows the 60 bar injection process sequences of diesel fuel at 350°C.

#### 6.1.6 60 bar, 350°C

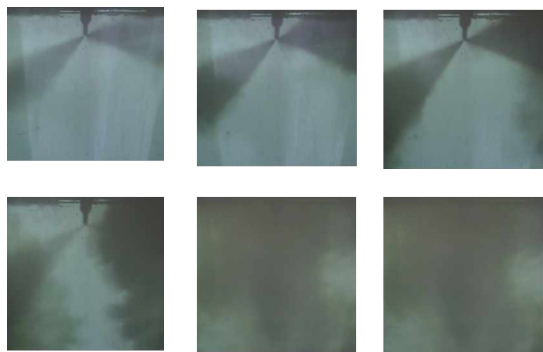


**Figure 6.6:** 60 bar injection process sequence for 350°C.

From figure 6.6, the 60 bar injected fuel is still in the liquid state. At 350°C (.15 K), the injected fuel is flash and fully vaporized.

## 7. CONCLUSIONS

It can be concluded that, this project has successfully fulfilled its objective that is to study and develop the liquid fuel vaporization system for fundamental combustion process. The understanding of the computer database, SUPERTRAPP, and model generation is successfully made within this project.

## ACKNOWLEDGMENT

Mr. Mohsin B. Mohd Sies, Researcher – Detonation Characteristics of Liquid Biofuels, Vote. 78358. Fundamental Research Grant Scheme (FRGS) funded by The Ministry of Higher Education for RM167,000. October 2008 – September 2010.

## REFERENCES

- [1] Alan Williams. Combustion of Liquid Fuel Sprays. London: Butterworths, 1990.
- [2] Alan Williams, Farid Nasir Hj. Ani. Pembakaran Semburan Bahan Api Cecair. London: Butterworths, 1990.
- [3] Yunus A. Cengel, Michael A. Boles. “Fuels and Combustion.” Thermodynamics an Engineering Approach. New York: McGraw-Hill, 2006.
- [4] Yunus A. Cengel, Michael A. Boles. “Gas-Vapor Mixtures and Air Conditioning.” Thermodynamics an Engineering Approach. New York: McGraw-Hill, 2006.
- [5] John B. Heywood. “Thermo chemistry of Fuel-Air Mixtures.” Internal Combustion Engine Fundamentals. Singapore: McGraw-Hill International Edition, 1988.
- [6] K. Colin Tucker. “A Flash Vaporization System for Detonations of Hydrocarbon Fuels in a Pulse Detonation Engine.” Ohio: Air Force Institute of Technology, 2004.
- [7] Kristin L. Panzenhagen. “Detonation Branching in A PDE with Liquid Hydrocarbon Fuel.” Ohio: Air Force Institute of Technology, 2004.

## COPYRIGHT

All papers submitted must be original, unpublished work not under consideration for publication elsewhere. Authors are responsible to obtain all necessary permission for the reproduction of tables, figures and images and must be appropriately acknowledged. The paper is not defamatory; and the paper does not infringe any other rights of any third party.

The authors agree that the Technical Committee’s decision on whether to publish the paper in the Conference’s proceedings shall be final. The authors should not treat any communication from the Technical Committee members who reviewed their work as an undertaking to publish the paper.

Prior to final acceptance of the paper, authors are required to confirm in writing that they hold all necessary copyright for their paper and to assign this copyright to the Conference Organizer.

# Characteristics of Turbulent Whirling Flow in an Asymmetric Passage

Khalid M. Saqr<sup>a</sup>, Mohsin M. Sies<sup>a</sup>, Hossam S. Aly<sup>b</sup>, Mazlan Abdul Wahid<sup>a</sup>

<sup>a</sup>*High-Speed Reacting Flow Laboratory, Faculty of Mechanical Engineering,  
Universiti Teknologi Malaysia  
81310 Skudai, Johor  
MALAYSIA  
Email : mazlan@fkm.utm.my*

<sup>b</sup>*F Department of Aeronautical Engineering, Faculty of Mechanical Engineering  
Universiti Teknologi Malaysia,  
81310 Skudai, Johor  
MALAYSIA*

## ABSTRACT

We investigate the physics of whirling flow in an asymmetric passage. A 3D RANS CFD model was built and solved to predict the steady state flow field variables in a 500 mm long asymmetric cylindrical passage. Turbulent velocity fluctuations were modeled using the Reynolds stress turbulence model. The paper presents an insight to the flow pattern, recirculation zone, velocity profiles and pressure gradients in such flow configuration. The significance of the presented qualitative results lies in the potential applications of such flow configurations in gas-phase combustors.

## 1. INTRODUCTION

When any flow has a significant tangential velocity component, and the flow terminals are not coplanar, it is impossible to reduce the problem to a two dimensional model. In this case, the flow behavior distinguishingly exhibits significantly three dimensional gradients of the flow field variables. Grasping these qualities is essential to establish a comprehensive understanding of such complex flow configuration for the vast range of applications it involves. When the cylindrical flow geometry is axially asymmetric, the whirling flow exhibits separation and reattachment regions around the asymmetry location. This adds double fold complexity to the problem in the time-independent solution, let alone transient states.

Whirling and swirling flows are fundamentally different. In the context of polar coordinates, the first expresses a flow stream with axial and tangential velocity components. While the latter expresses a flow stream with solely a tangential velocity component. Unlike swirl flows, whirl flows have attracted much less consideration from the fluid dynamics research community. Sturov has studied whirling axisymmetric turbulent flow experimentally as a case study on turbulent eddies [1]. Five years later, the same problem was studied numerically, by reducing it to a two dimensional axisymmetric model [2].

During the 1970s, there has been a growing attention to study flames created in flow fields which have significant tangential velocity components; namely swirling flames. Swirling flow fields are distinguishingly characterized by a central recirculation zone (i.e. CRZ). Swirling flow spreads as it moves downstream, and the centrifugal force creates a low pressure region in the centre of the flow. At a certain point downstream, this low pressure region causes the vortex to collapse inwards on itself in a phenomenon known as vortex breakdown [3]. This vortex breakdown phenomenon is the main characteristic of the CRZ. The CRZ provides a reversal flow field, in which two main actions take place. First is the mixing and enthalpy retrieval between combustion products and new fuel and air charges. Second is the matching between reaction times and flow times, which is the major flame stabilizing mechanism [4]. The swirling flows and their associated flames have been extensively studied during the last four decades [5-10].

Based on the previous experimental observation of Gabler et al [11], when the inlet air exhibits dominating tangential velocity components, the flame tends to gain increased stability, sometimes even out of the flammability limit of the fuel. In their experimental setup, the fuel nozzle was fixed eccentric to the centerline of the cylindrical combustor and the air was admitted in pure tangential flow. In the present work, we present a novel flow configuration for combustion applications. The cylindrical combustion chamber presented in this paper is asymmetric with respect to its axis. The air inlets are located on the sidewalls which result from such eccentricity; air flows in absolute tangential directions from such ports. Each flow stream, when passes along the eccentricity locations, it becomes similar to the backward-facing step flow. This ensures that the air remains attached to the cylinder walls. Thus, the tangential component of velocity remains dominant. The present study is concerned only about the cold air flow within such configuration; therefore, the fuel inlets are not modeled. The results are qualitative descriptions of the spatial distributions of the flow field variables, which are cornerstones to comprehend the nature of such flow.

## 2. FLOW PHYSICS

Air was allowed to flow with a constant velocity of 15 m/s inside an asymmetric cylindrical passage as shown in figure 1. The flow outlet condition was set to ambient pressure. Both wall and flow temperatures were assumed to remain constant by neglecting the heat transfer between the fluid and the passage. The asymmetry is composed by shifting the centerline of each half of the cylinder in the Y direction. This creates two backward-facing steps for the whirling flow, which is believed to enhance the flow stability.

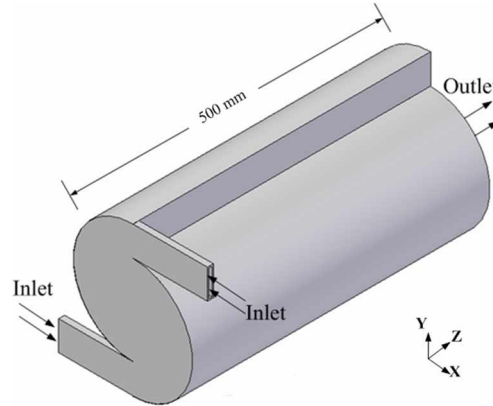


Figure 1. Schematic showing the flow passage, inlets and outlet ports in Cartesian coordinates

## 3. MATHEMATICAL AND NUMERICAL DETAILS

### 3.1 Governing Equations

The whirling flow in an asymmetric geometry was mathematically modeled using the three dimensional conservation equations of mass, momentum and energy for steady state, viscous compressible flow. In Cartesian coordinates, these equations are:

Conservation of mass:

$$\nabla \cdot (\rho V) = 0 \quad (1)$$

Conservation of momentum:

X Component

$$\nabla \cdot (\rho u V) = -\frac{\partial p}{\partial x} + \frac{\partial \tau_{xx}}{\partial x} + \frac{\partial \tau_{xy}}{\partial y} + \frac{\partial \tau_{zx}}{\partial z} + \rho f_x \quad (2)$$

Y component

$$\nabla \cdot (\rho v V) = -\frac{\partial p}{\partial y} + \frac{\partial \tau_{xy}}{\partial x} + \frac{\partial \tau_{yy}}{\partial y} + \frac{\partial \tau_{zy}}{\partial z} + \rho f_y \quad (3)$$

Z component

$$\nabla \cdot (\rho wV) = -\frac{\partial p}{\partial z} + \frac{\partial \tau_{xz}}{\partial x} + \frac{\partial \tau_{yz}}{\partial y} + \frac{\partial \tau_{zz}}{\partial z} + \rho f_z \quad (4)$$

The density was assumed to change as a function of the operating pressure while neglecting the effect of the local relative pressure field; the flow was considered to be incompressible.

### 3.2 Numerical approach

The governing equations were discretized using the finite volume method and the solver used a decoupled approach to treat the velocity and pressure terms. The SIMPLE (Semi Implicit Procedure for Pressure Linked Equations) algorithm was used to couple the velocity and pressure terms in the flow domain which was discretized using the least-squares cell based scheme. The number of cells in the computational domain was 1160113 hexahedral cells. This number was determined based on a grid independency study which showed that cell size smaller than  $7.46 \times 10^{-10} \text{ m}^3$  does not show significant accuracy increase in the solution.

The turbulent velocity fluctuations were modeled using the Reynolds Stress Model (RSM) [12]. Compared to eddy viscosity turbulence models, the RSM provides further accuracy in predicting flow configurations with high streamline curvature including swirling and rotating flows. The superiority of the RSM in modeling such types of flows comes from the added transport equations for the Reynolds stress terms and dissipation rate. The use of RSM in simulating flows with rapid strain rate changes in combustors, cyclones and other rotating flow applications has been reported successful in numerous researches [13-16]. The model equations in the 3D Cartesian space are [17]:

$$\begin{aligned} \frac{\partial}{\partial t} (\rho \overline{u'_i u'_j}) + \frac{\partial}{\partial x_k} (\rho u_k \overline{u'_i u'_j}) &= -\frac{\partial}{\partial x_k} [\rho \overline{u'_i u'_j u'_k} + p(\delta_{ij} u'_k + \delta_{ik} u'_j)] + \\ & D_{i,j} \left[ \mu \frac{\partial}{\partial x_k} \left( \frac{\overline{u'_i u'_j}}{\epsilon} \right) \right] - \rho \left( \overline{u'_i u'_k} \frac{\partial u'_j}{\partial x_k} - \overline{u'_j u'_k} \frac{\partial u'_i}{\partial x_k} \right) - \rho \overline{G_{ij}} + \rho \overline{P_{ij}} \\ \rho \left( \frac{\partial u'_i}{\partial x} + \frac{\partial u'_j}{\partial y} \right) &- 2\mu \frac{\partial u'_i}{\partial x} \frac{\partial u'_j}{\partial y} - 2\rho \Omega \left( \overline{u'_i u'_k} \epsilon_{ijk} + \overline{u'_j u'_k} \epsilon_{jik} \right) \\ & \phi_{ij} = \text{Pressure Strain} \quad \epsilon_{ij} = \text{Dissipation} \quad F_{ij} = \text{Pr production by System Rotation} \end{aligned}$$

## 4. RESULTS AND DISCUSSION

### 4.1 Flow pattern

A stream function was implemented to plot the flow streamlines in the 3D space, as in figure 2. The flow enters the passage from the tangential ports and advances in spiral motion which is dominated by the tangential velocity component. It is also observed that the flow maintains a dominant swirling velocity component along the passage, though the swirl velocity angle appears to vary. This is shown in figure 2-a. However, the spiral streamlines indicate that the flow gains axial velocity component. This is due to the friction with the passage walls. When the flow passes over the eccentricity wall, two separation zones develop, as in figure 4-b. In such zones the flow circulates in a cylindrical bubble, as in the backward-facing step flow. The separation zones cause the flow to remain attached to the walls and stimulate the dominance of the whirling motion. This is due to the loss in momentum in the separation zones.

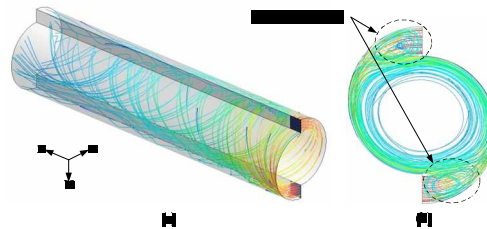


Figure 2. Flow streamlines in (a) isometric view showing the swirling curvature and (b) front view showing the separation zones

### 4.2 Recirculation zone and velocity profiles

The whirling flow was found to exhibit a large recirculation zone in the center region of the passage, as shown in figure 3. In such central recirculation zone (CRZ), the flow has a negative axial velocity. On the boundary between the CRZ and mean flow, where the axial velocity is almost zero, a high shear stress layer is formed. In swirling flows, the flow spreads as it moves downstream, and the centrifugal force creates a low pressure region in the centre of the flow. At a certain point downstream, this low pressure region causes the vortex to collapse inwards on itself in a process known as vortex breakdown [19]. This creates a recirculation zone in the



centre of the flow. In swirl stabilized flames, this becomes essential to provide sufficient time, temperature and turbulence for a complete combustion of the fuel [20, 21]. However, the role of the recirculation zone in the whirling flow in hand, when comes to flame stability, might be different. In case of premixed flame, the fresh mixture should be introduced tangentially to the whirl combustor. The products would, then, be concentrated in the central region of the combustor. The recirculation zone, in such case, would enhance the mixing between the reactant mixture and the exhaust gases, this in turn might decrease the NO<sub>x</sub> emission and provide complete burning of the mixture. However, the analysis of reacting flow in such configuration is beyond the scope of the current study.

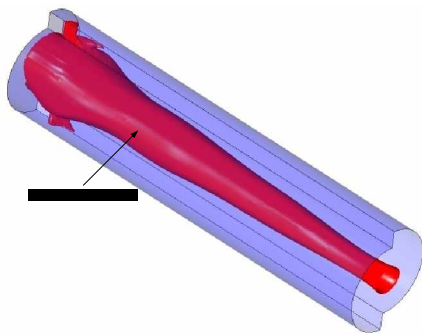


Figure 3. Central recirculation zone bounded by the zero axial velocity isosurface

The 2D axial and tangential velocity profiles are shown in figure 4. In figure 4-a, the reverse velocity in the CRZ region is found to have values ranging from 0.75 to 4.00 m/s. In figure 4-b, the regions where the tangential velocity is in its maximum value is very near to the inlet ports. While the minimum tangential velocity, approximately 0.2 m/s, is found in the CRZ region. The location and values of the velocity components sheds some light on the formation mechanism of the CRZ. Such mechanism is believed to be analogues to that of the CRZ in swirling flows. The vortex breakdown in the CRZ decelerates the flow velocity and creates volume of toroidal vortices.

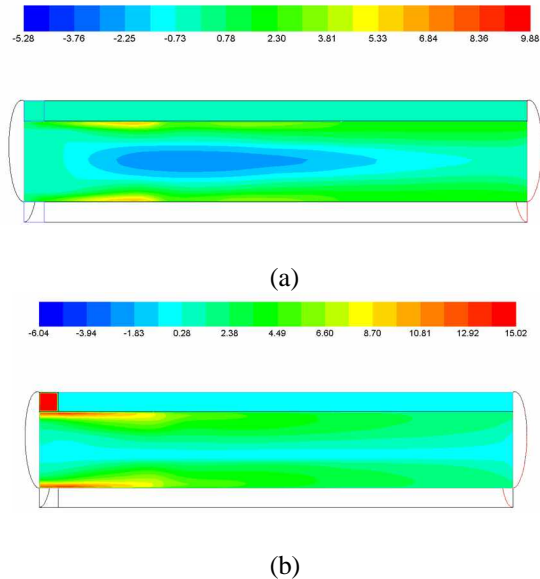


Figure 4. (a) Contours of axial velocity showing the recirculation zone (b) Contour of tangential velocity. Units in m/s

### 4.3 Pressure gradients

Pressure gradients in the whirling flow configuration are plotted in figure 5 at two locations parallel to the mean axis of the passage; one at the center and the second near to the wall. The negative pressure gradient at the central region of the flow is an indication of the vortex breakdown phenomenon, which supports the idea that the recirculation zone for the whirling flow develops in a way analogous to that of the swirling flow.

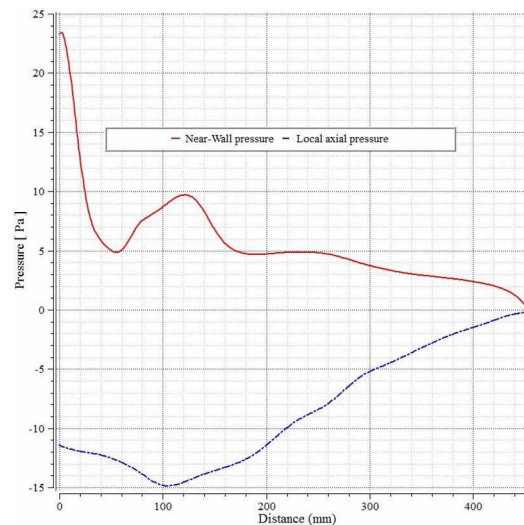


Figure 5. Pressure gradients in two locations of the passage

## 5. CONCLUSION

The whirling flow in an asymmetric passage was numerically investigated using a steady state RANS model. The flow was found to exhibit separation and reattachment downstream the eccentricity step. A recirculation zone, characterized by inverse velocity and negative pressure gradient was found to exist in the central region of the flow. The paper sheds the light on the basic characteristics of whirling flow, which is essential to comprehend for combustion applications. Further investigation on the mechanism of formation for the recirculation zone, mixing characteristics and turbulence properties of such flow configuration is necessary.

## REFERENCES

- [1] G.E. Sturov (1974) Some Problems in Study and Industrial Application of the Eddy Effect [in Russian], Kuibyshev. Aviats. Inst., Kuibyshev, p. 211.
- [2] V. V. Tret'yakov and V. I. Yagodkin (1979) Mathematical Analysis of Whirled Turbulent Flow Through a Pipe, *Inzhenerno-Fizicheskii Zhurnal*, V01. 37, No. 2, pp. 254-259
- [3] Y. Wang, V. Yang, and R.A. Yetter (2004) Numerical Study on Swirling Flow in an Cylindrical Chamber, 42nd AIAA Aerospace Sciences Meeting, Reno, Nevada.
- [4] Y.A. Eldrainy, K.M. Saqr, H.S. Aly and M.N.M Jaafar CFD Insight of the Flow Dynamics in a Novel Swirler for Gas Turbine Combustors, *International Communications on Heat and Mass Transfer* [In Press]
- [5] J.M. Beer and N.A. Chigier (1972) *Combustion Aerodynamics*, John Wiley & Sons Inc. New York
- [6] A.K. Gupta, D.G. Lilly and N. Syred (1984) *Swirl Flows*, Abacus Press.
- [7] X. X. Dang, J. X. Zhao and H. H. Ji, Experimental study of effects of geometric parameters on combustion performance of dual-stage swirler combustor, *Hangkong Dongli Xuebao/Journal of Aerospace Power* 22 (2007), no. 10, 1639-1645.
- [8] Y. Fu, J. Cai, A. M. Elkady, S. M. Jeng and H. Mongia (2005-a) Fuel and equivalence ratio effects on spray combustion of a counter-rotating swirler, 43rd AIAA Aerospace Sciences Meeting and Exhibit - Meeting Papers, pp. 6757-6770
- [9] Y. Fu, S. M. Jeng and R. Tacina (2005-b) Characteristics of the swirling flow generated by an axial swirler, *Proceedings of the ASME Turbo Expo*, pp. 517-526.
- [10] Y. Fu, J. Cai, S. M. Jeng and H. Mongia (2007) Characteristics of the swirling flow generated by a counter-rotating swirler, *Collection of Technical Papers - 43rd AIAA/ASME/SAE/ASEE Joint Propulsion Conference*, pp. 6721-6731.
- [11] Gabler, H.C., Yetter, R., and Glassman, I., Asymmetric Whirl Combustion: A New Approach for Non-Premixed Low NO<sub>x</sub> Gas Turbine Combustor Design, *Proceedings of the 34th AIAA/ASME/SAE/ASEE Joint Propulsion Conference*, AIAA Paper 98-3530, Cleveland, OH, July 1998.
- [12] M. M. Gibson and B. E. Launder. Ground Effects on Pressure Fluctuations in the Atmospheric Boundary Layer. *J. Fluid Mech.*, 86:491-511, 1978.
- [13] Artit Ridluan, Smith Eiamsa-ard, Pongjet Promvong, Numerical simulation of 3D turbulent isothermal flow in a vortex combustor, *International Communications in Heat and Mass Transfer*, Volume 34, Issue 7, August 2007, Pages 860-869
- [14] A.F. Najafi, M.H. Saidi, M.S. Sadeghipour, M. Souhar, Numerical analysis of turbulent swirling decay pipe flow, *International Communications in Heat and Mass Transfer*, Volume 32, Issue 5, April 2005, Pages 627-638
- [15] R. Palm, S. Grundmann, M. Weismuller, S. Saric, S. Jakirlic, C. Tropea, Experimental characterization and modelling of inflow conditions for a gas turbine swirl combustor, *Engineering Turbulence Modelling and Experiments* 6, Elsevier Science B.V., Amsterdam, 2005, Pages 835-844

- [16] M. R. Halder, S. K. Dash, S. K. Som, A numerical and experimental investigation on the coefficients of discharge and the spray cone angle of a solid cone swirl nozzle, *Experimental Thermal and Fluid Science*, Volume 28, Issue 4, March 2004, Pages 297-305
- [17] Launder, B. E., Reece, G. J. and Rodi, W. (1975), Progress in the Development of a Reynolds-Stress Turbulent Closure, *Journal of Fluid Mechanics*, Vol. 68(3), pp. 537-566.
- [18] Gibson, M.M., and Launder, B.E, 1978 Ground Effects on Pressure Fluctuations in the Atmospheric Boundary Layer. *Journal of Fluid Mechanics*, 86 pp:491-511
- [19] Y. Wang, V. Yang, R.A. Yetter, Numerical study on swirling flow in an cylindrical chamber, 42nd AIAA Aerospace Sciences Meeting, Reno, Nevada, 2004.
- [20] J.M. Beer, N.A. Chigier, *Combustion Aerodynamics*, Applied Science Publisher, London, 1972.
- [21] N. Syred, J.M. Beer, Combustion in swirling flows: a review, *Combustion and Flame* 23 (1974) 143–201.

# Thermal Conversion of Biomass using Microwave Irradiation

Farid Nasir Ani<sup>a</sup>, Arshad Adam Salema

<sup>a</sup>Faculty of Mechanical Engineering,  
Universiti Teknologi Malaysia,  
81310 Skudai, Johor Bahru,  
Malaysia.

## ABSTRACT

A novel microwave radiation heating technique was used to pyrolyse the oil palm biomass (fiber and shell) waste into bio-oil. Thermal treatment of whole (as received) oil palm biomass was done in a modified domestic microwave oven using fluidized bed technology. It was demonstrated that biomass are poor absorber of microwaves and cannot be pyrolysed or generate vapor on its own to form bio-oil. Therefore, appropriate microwave-absorbing material i.e. biomass carbonaceous char was used to initiate the pyrolysis process thus producing the bio-oil. Effect of this microwave absorber on the yield of the bio-oil is presented in the paper. Particular attention on the temperature profile was also illustrated during microwave heating of oil palm biomass. Preliminary physical and chemical characteristics of bio-oil were investigated to confirm the nature of bio-oil. Image analysis of char revealed the quality that can be maintained during microwave heating. As the microwave travels with speed of light, it was found that the vapors were generated as soon as microwave was ON and it stops as microwaves are OFF. This significantly reduces the time and energy for thermal conversion. Further efforts are showing encouraging results, which will demonstrate the advantage of microwave in terms of saving time and energy and the quality of products.

## Keywords

*Oil palm biomass; Microwave heating, fluidized bed, temperature profiles, bio-oil, char*

## 1. INTRODUCTION

Obtaining highly organic chemicals for various applications such as fine chemicals, fertilizers, resins and others including biofuels for automotive is the main aim of thermally treating the biomass waste. Fast pyrolysis as one of the thermochemical process converts the biomass into bio-oil (liquid), char (solid) and flue gas in the

temperature range of 400 to 600°C in absence of oxygen. Fast pyrolysis process not only reduces the volume of waste significantly, but also allows recovery of value-added products. With fast pyrolysis the yield of the liquid i.e. bio-oil or bio-fuels is maximized depending on the process conditions. In our laboratory, the fast pyrolysis system has been already developed and established to obtain bio-oil from various biomasses (Ani et al., 2008).

Heating source forms important parameters in obtaining yield and quality of the bio-oil. Traditional methods include conventional heating methods i.e. external heating by conduction, convection or radiation (Chen et al., 2008). This conventional heating method suffers from certain drawbacks including heat transfer resistance, heat losses to surrounding, utilization of portion of heat supplied to biomass materials, damage to reactor due to electric heating etc. Microwave energy has gained interest in recent decades as an alternative source of heating technique for pyrolysis of plastic (Pingale and Shukla, 2008; Ludlow-Palafox and Chase, 2001), sewage sludge (Domínguez et al., 2008, Menéndez et al., 2002), biomass (Yu et al., 2007; Huang et al., 2008; Guo et al., 2006; Wan et al., 2009), wood (Miura et al., 2004).

Microwaves are electromagnetic waves with frequency between 300 MHz to 300 GHz.

However, two most common frequencies used are 0.915 and 2.45 GHz as per the industrial, scientific and medical (ISM) commission.

Previously the microwaves dominated the area of food processing, drying, ceramic curing, and other heating applications. Now a days, microwaves are being explored in various new applications because of their inherent advantages over conventional or traditional methods. Jones et al., 2002 have stated that microwaves are extremely efficient in selective heating of materials without any loss of heat due to bulk heating nature. Others include higher heating rates, no direct contact between the heating source and materials, reduced

equipment size and space. Besides this, significant time and energy saving without any environmental damage as clean source of energy adds to its application in novel areas (Jones et al., 2002). The application of microwave in different fields of waste and environmental engineering is reported in the literature (Jones et al., 2002 and Appleton et al., 2005). The key merit of the microwave pyrolysis as stated by Miura et al., 2004 is the prevention of undesired secondary reactions that leads to formation of impurities in the product by decreasing the yield of desired compounds.

The objective of the paper is to apply the electromagnetic energy into thermal energy depending on the dielectric or electromagnetic property of the absorbent materials. Unlike the conventional thermal heating, microwaves penetrate into core of the materials whereby the molecules get vibration due to high frequency and thus create the heat (see Fig. 1). As can be seen from Fig. 1b that the temperature in case of microwave heating is higher at the centre (red colored region) compared to conventional heating whereby the heat is transferring from surface towards the colder region in the centre. Hence, volumetric heating (Fig. 1a) is observed in microwave since every molecule equally generates heat, provided the penetration depth of the microwaves into the materials is sufficient.

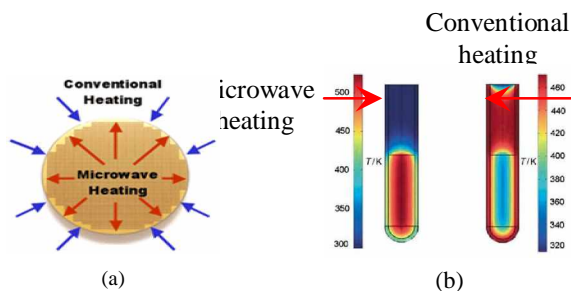


Figure 1 Difference in microwave and conventional heating a) single particle heating b) bulk heating analysis using finite element method for 1 min heating

Gradually microwave pyrolysis of biomass has achieved a pace in recent times. This includes pyrolysis of fir sawdust (Guo et al., 2006), corn stover (Yu et al., 2007), coffee hulls (Domínguez et al., 2007), rice straw (Huang et al., 2008), Pine wood sawdust (Chen et al., 2008), biomass (Wan et al., 2009). Nevertheless, none has conducted microwave pyrolysis of oil palm biomass till date. Particularly, the effect of microwave absorber on

the temperature profile and yield of bio-oil was found lacking in the literature. Therefore, it was interesting to know the performance of oil palm biomass under microwave radiations. Nevertheless, advance heating technique such as microwave might bring a revolutionary phase in the thermo-fluid research area which might open other applications fields.

The present work reveals the pyrolysis of oil palm biomass through novel microwave technique to obtain bio-oil. Moreover, the effect of biomass to microwave absorber such as carbonaceous char ratio in present study on the yield of bio-oil was the main aim of the study. Further, temperature profile of the oil palm biomass under microwave radiation and characterization of the bio-oil was given a particular attention.

## 2. EXPERIMENTAL SET-UP

Oil palm biomass waste (fibers and shells) were obtained from Kulai palm oil mill situated in the state of Johor, south of Malaysia and were used as experimental samples. The effect of varying the quantity of microwave absorber (oil palm shell carbon char) on the yield of bio-oil and its characteristics was examined. The ratio of biomass to microwave absorbing material was varied at 1:0, 1:0.25 and 1:0.5. The amount of oil palm biomass was maintained constant. For this initial research work, microwave power (450 W), time of radiation (20 min), nitrogen gas flow rate (20 liter per minute) and amount of oil palm biomass (50 gm) was kept constant. The only parameter varied was the microwave absorber.

The experiments were carried out in a modified domestic microwave oven of 2450 MHz magnetron (OM75P-31) of 1 kW. The system was equipped with a Triple Distribution System (TDS), which can evenly distribute the microwaves throughout the oven. Experimental set-up for the modified microwave system is as shown in Fig. 2. This consists of microwave cavity, fluidized bed quartz glass reactor (100 mm I.D. and 150 mm height), perforated steel distributor plate (1 mm holes), and a condensing unit. Microwave cavity was modified in order to accommodate the fluidized bed quartz reactor. Nitrogen gas was supplied before commencement of the experiment and was lowered down to set a value to about 20 LPM during run of the experiment. This was to create an inert environment as well as to sweep the vapor out of



the reactor in order to condense into bio-oil. Temperature of the process was measured using two K-type thermocouples (inside and surface of bed) connected to Pico data acquisition system, UK and further this was linked to personal computer for continuous recording of data.

Conventionally oil palm shell biomass was also pyrolysed in an electric furnace (Carbolite, UK) by supplying the nitrogen gas. Image analysis of obtained char was conducted under ZEISS microscope image analyzer (Axiotech model), Germany attached with Sony digital color video camera (SSC DC-338P model). The images of microwave pyrolysed and conventionally obtained char were compared. The oil palm shell sample size for this comparison was as received i.e. large size. The images were captured at different microscope resolution. 5X, 10X, 20X, 50X.

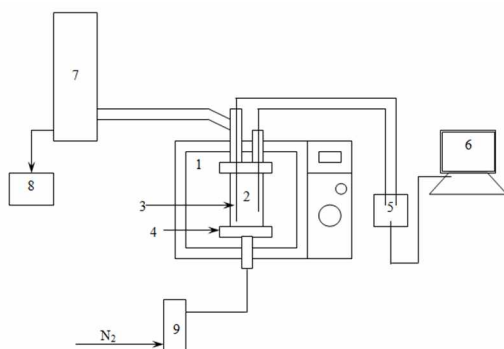


Figure 2 Schematic diagram of microwave pyrolysis process: 1. microwave cavity, 2. quartz glass fluidized bed reactor, 3. thermocouples, 4. distributor plate, 5. temperature data acquisition system, 6. personal computer, 7. condensing unit, 8. bio-oil collector, 9. rotameter

For each experiment, 50 gm of oil palm biomass and desired amount of microwave absorber were mixed well and charged into the fluidized bed quartz reactor. Microwave reactor system was purged with nitrogen gas for about 10 min to ensure inert environment during pyrolysis. Microwave was switched on to generate the radiation for the set power (450 W) and time (20 min). The vapor generated out of the reactor was condensed using continuous ice water at about 5 to 10°C. Bio-oil obtained from microwave pyrolysis of oil palm shell was collected and sealed in glass bottles to avoid any changes in its properties for further analysis. Oil remained in the

equipments was also determined via weight difference of the equipments before and after the experiments. Thus total bio-oil, and solid char residue was weighted at the end of the experiments to investigate the yield. Bio-oil was subjected to viscosity measurement using Petrotech equipment available in Petroleum Engineering Department, UTM, and pH value was determined using Eurotech pH tutor. FT-IR spectra of bio-oil were performed using Thermo Corporation FT-IR analyser manufactured in Madison, WI, U.S.A. model Nicolet Avatar 370 DTGS.

### 3. RESULTS AND DISCUSSIONS

#### 3.1 Temperature Profile

Figure 3 shows the temperature profiles during microwave pyrolysis of oil palm shell (OPS) and oil palm fiber (OPF) without any microwave absorber. It can be observed that absence of microwave absorber i.e. 0 %, results in the maximum bed temperature (T1) to about 100°C and 80°C for OPS and OPF respectively. Apparently, no pyrolysis or evolution of vapor took place at this stage, though water evaporation was noticed. This proves those biomasses are poor absorber of microwaves. The increase in temperature at this stage is due to presence of moisture or water inside the biomass. Water is good microwave absorber (Zhang and Datta, 2003) and thus can generate minimal amount of heat that can evaporate the water within the biomass. Hence, once the microwave encounters the biomass, the moisture absorbs the microwaves and creates a dielectric polarization whereby the water molecules try to align themselves according to the radiation, which finally leads to friction within the molecules generating energy in form of heat. This heat is sensed as increase in temperature. Initially the temperature raised linearly but almost came to stable value after some time. This is because the water or moisture comes to super heated point as soon it absorbs the microwaves, which cause sudden increase in temperature. However, once the water is evaporated from the biomass, there is no material, which can cause the heat since other biomass constituents do not absorb the microwaves. Therefore, the temperature comes to a stable form.

The addition of microwave absorber particularly the biomass carbonaceous char not only helped in

increase of temperature as shown in Fig. 4 but also initiated the pyrolysis process by generating the vapors. These vapors were trapped via condensing unit forming bio-oil whose yield depended on amount of microwave absorber used as discussed in later section of this paper. It was observed that it took few seconds to generate the vapors from oil palm biomass as the microwave was switched ON. Hence, microwave absorbers played a role in absorbing the microwave and transferring it to heat the biomass materials. This assisted to increase the bed temperature, T1 in the present study to about 200°C for 1:0.25, 200°C for 1:0.5 and 300°C for 1:1 ratio of oil palm shell (OPS) biomass to microwave absorber. Even though this temperature is below the reported (Islam and Ani, 2000) temperature to initiate the pyrolysis i.e. around 450 °C, the possible reason might be the measurement of temperature in microwave cavity. This is because the core or centre of the biomass particles is at higher temperature compared to surface due to penetration behavior of microwaves into the materials. Therefore, according to Guo and Lua, 2000, the sample internal temperature is ten or hundred degrees higher than that of surface. The possibility of interference of metal thermocouple with microwaves cannot be ignored. Further, the thermocouple was placed at two locations only in the reactor, measuring that particular reading. The fact that other location might have reached much higher temperature than 400°C due to hot spot as found in multi-mode domestic microwave ovens. However, in case of oil palm fiber (OPF), the temperature profile showed much higher temperature averagely 800°C compared to OPS. This could be due to types of biomass used. OPF are much lighter and thin in diameter or thickness compared to OPS. Thus, heat is transferred differently.

Domínguez et al., 2008, mixed carbon char to achieve high temperature for sewage sludge pyrolysis. They reported that the char obtained from pyrolysis of biomass are good microwave receptors. Other study (El Harfi et al., 2000) used carbon grains of about 0.5 wt % with oil shale sample to pyrolyse under microwave radiation to allow uniform temperature or heating. Menéndez et al., 2002, revealed temperature profile of microwave pyrolysis of sewage sludge with and without carbon char obtained during pyrolysis. A maximum temperature of about 900 °C was achieved in just 2 min with addition of 5 wt% carbon char with sewage sludge compared to only 200°C without any char. Higher temperature

recorded during their study might be also due to presence of high moisture in the sample.

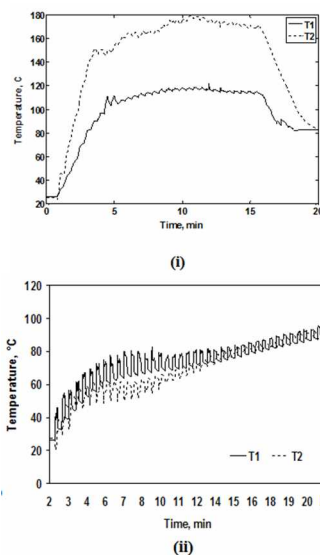
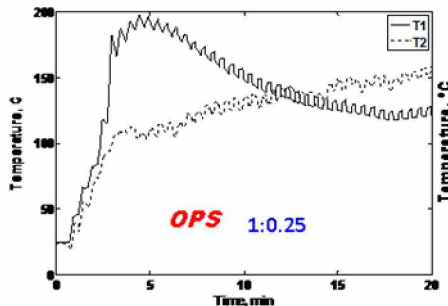


Figure 3 Real time temperature profile of oil palm i) shell, ii) fiber under microwave radiation without any microwave absorbers; Microwave power – 450 W



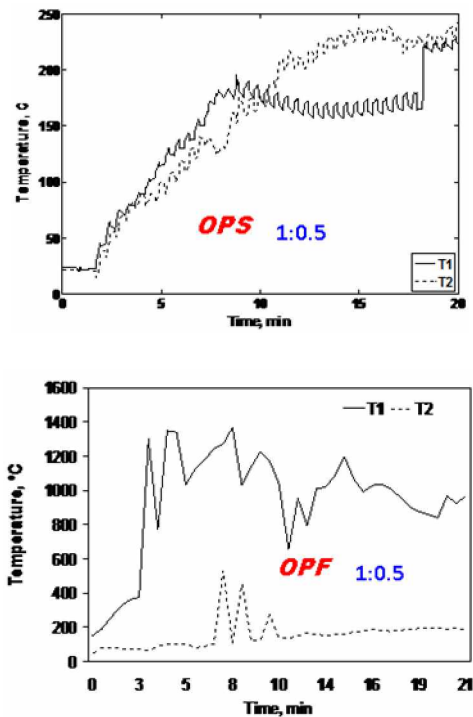


Figure 4 Effect of biomass to microwave absorber ratio on real time temperature profile of oil palm shell (OPS) and oil palm fiber (OPF); Microwave power – 450 W

The sinusoidal nature in the temperature profiles in Figs 3 and 4 shows the discrete working nature of the magnetron from where the microwaves are generated. Basically, all domestic microwave ovens works in this type of mode. This means that the temperature shoots to higher value when the magnetron is in ON mode and drops to a certain level when the magnetron is in OFF mode. The temperature profile of OPF during microwave pyrolysis was observed to be more fluctuating and inconsistency compared to OPS. This might be due to the material interaction with microwaves. Since the materials properties plays an important role in microwave treatment rather than the microwaves itself. Further, the fluidization of the materials might also contribute in an inconsistency temperature profile. In the present study, the fluidization was not achieved as desired and microwaves could not penetrate or absorbed homogenously.

Another interesting investigation as discussed before is the volumetric heating nature of the materials in which the internal section of the bed, was much hotter or at higher temperature than that of surface. Fig. 4 shows this profile where the

bed temperature T1 was almost higher than that of bed surface temperature T2. Obviously in case of OPF, it was clearer. According to our knowledge, the char formation during pyrolysis also plays an important role under microwave radiation. Thus, microwave pyrolysis of OPF produced char much faster due to its low density and size. Conversely, formation of char in OPS was slower due to large and hard particles. It is evident that quicker the formation of char from biomass will enhance more microwaves to be absorbed by newly formed char and consequently higher temperature as can be predicted for OPF. This shows that the energy conversion or absorption within the material is also dependent on the penetration depth of the microwaves. A comprehensive understanding regarding this was reported by Thostenson and Chou, 1999. However, without any microwave absorbing material the temperature profile in Fig. 3 revealed that the bed temperature T1 was lower in case of OPS or almost same in case of OPF than the surface temperature T2 measured just above the surface of the bed. The reason might be the water or moisture molecules that are vaporized immediately when being exposed to microwaves and is deposited on the surrounding walls of the reactor. This water droplets also absorbs the microwaves and increases the temperature above the bed region thus maintaining the surface temperature T2 with that of bed temperature T1.

#### 4. EFFECT OF BIOMASS TO MICROWAVE ABSORBER RATIO ON THE BIO-OIL YIELD

The yield of bio-oil increased with microwave absorber till ratio of 1:5 and thereon decreased as shown in Fig. 3. Thus, the maximum bio-oil yield was obtained at biomass to microwave absorber ratio of 1:0.5. It was assumed that as the amount of microwave absorber is small, biomass could not get enough heat to pyrolyse the material. Conversely, higher amount of microwave absorber might have lead to localized heating of char material alone. Yet the exact reason for this has to be investigated and understood since the heating characteristics of microwave is very fast.

The only concise study (Guo et al., 2006) has been performed till date to determine the influence of microwave absorption media on pyrolysis of fir sawdust. In this study ionic liquid

and glycerol was used as microwave absorber to conduct the pyrolysis in domestic microwave. The results of this study showed optimal ratio for maximum bio-oil yield at 3:1 and 2:1 for glycerol to biomass and ionic liquid to biomass respectively. This clearly shows that selection of microwave absorber also plays a role in optimal bio-oil production. Nevertheless, the authors have also failed to explain the detailed influence of biomass to microwave absorber ration on the yield of bio-oil.

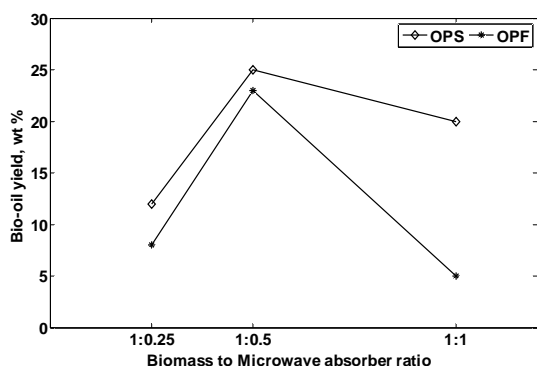


Figure 5 Effect of microwave absorber on yield of bio-oil

## 5. PYROLYSIS PRODUCT CHARACTERIZATION

### 5.1 Bio-oil

Physically the obtained bio-oil from microwave pyrolysis was golden yellowish in color for both OPS and OPF. Further, it was tested for pH and viscosity. The pH was found to be in range of 2.9 to 3.0. This indicated that bio-oil is acidic in nature because of presence of organic acids compounds. Hence, it has to be stored in a vessel with appropriate construction of material such as stainless steel or polyolefins.

The viscosity of bio-oil was found to be 0.0164 and 0.0125 cm<sup>2</sup>/s at 25 and 40 °C respectively. The viscosity of bio-oil decreases with increase in temperature much faster compared to petroleum crude oil (Bridgwater, 2004). In present, study its viscosity decreased by 25 % when temperature was increased from 25 to 40 °C. Another reason for more viscous nature is the presence of solvents in the bio-oil such as acetone or methanol. Since in the present work acetone was used to clean the bio-oil attached to the condenser

surface and other equipments, otherwise the viscosity of the bio-oil would have been higher. Presence of water in high percentage also reduces the viscosity of the bio-oil.

Fig. 6 and Fig. 7 show the FT-IR spectra for as received (large size) and small size (850 μm) OPS bio-oil produced via microwave technique. It clearly shows that their peak patterns are almost similar with some additional peaks observed in small sized OPS bio-oil. The possible functional group and its compounds are shown in Table 1.

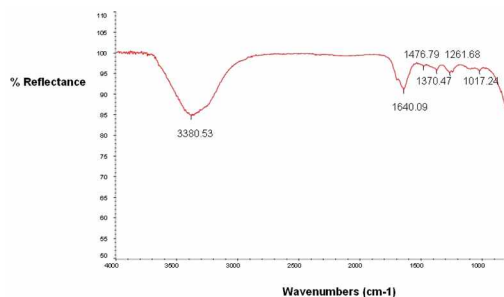


Figure 6 FTIR analysis of whole or large size OPS bio-oil obtained from microwave pyrolysis

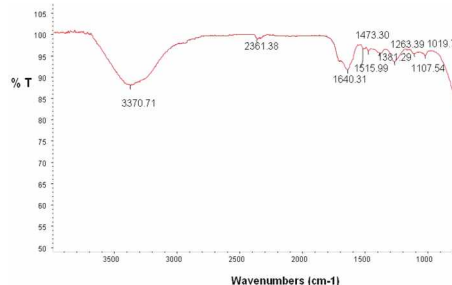


Figure 7 FTIR analysis of 850 μm OPS bio-oil obtained from microwave pyrolysis

The presence of significant peaks between 1640 and 1700 cm<sup>-1</sup> could be due to C=O stretching vibrations indicating compounds such as ketones, phenols, carboxylic acids or alcohols. Another indication of alcohols including phenols can be found in the range of 3200 and 3400 cm<sup>-1</sup> as O-H stretching. However, broad O-H stretching vibration between 3200 and 3600 cm<sup>-1</sup> may be due to water impurities also. The peaks between 1300 and 950 cm<sup>-1</sup> showing the C-O and O-H stretching vibrations may be due to the presence primary, secondary and tertiary alcohols, phenols, ethers and esters. This fast screen technique of FT-IR was used to observe the extent and

presence of hydroxyl group to confirm the phenolic compounds. However, detailed analysis through GC-MS would demonstrate the actual presence of chemical entities.

Table 1: FT-IR analysis for functional group in OPS bio-oil

Wave numbers, cm <sup>-1</sup>	Functional group	Class of compounds
3200 – 3600	O-H	Polymeric, water impurities
3000 - 2800	C-H	Alkanes
1780 – 1640	C=O	Ketones, aldehydes, carboxylic acids
1680 – 1580	C=C	Alkenes
1550 – 1490	-NO	Nitrogenous compounds
1475 – 1350	C-H	Alkanes
950 – 1300	C-O	Primary, secondary and tertiary alcohols,
	O-H	phenol, esters, ethers
900 – 650	O-H	Aromatic

## 6. CONCLUSIONS AND FUTURE WORK

Microwave pyrolysis of oil palm biomass (fiber and shell) for as received was carried out. Pyrolysis under microwave radiation took place at low temperature. The temperature profiles were observed during microwave pyrolysis of OPS and OPF. Microwave absorbers were found to increase the pyrolysis temperature largely in case of OPF and to smaller extent in case of OPS. Poor fluidization behavior might have contributed in an inconsistency temperature profiles. However, with the help of microwave heating the temperature could be raised to higher value in few seconds thus considerable saving in time and energy. Microwave absorber not only contributed in increasing the temperature or initiating the pyrolysis process but also affected the yield of bio-oil. The physical characterization showed acidic nature of bio-oil with decrease in viscosity against temperature. The FT-IR analysis revealed

probable compounds such as ketone, aldehyde, phenols and carboxylic acids with water impurities. Further confirmation about the presence of chemical compounds depends on more detailed study of microwave pyrolysis bio-oil from oil palm biomass and is currently under process which will be published in future articles. Future work is being carried out to develop and investigate other potential parameters and process conditions affecting the pyrolysis process of different biomass in novel microwave system.

## ACKNOWLEDGEMENTS

The authors are grateful for E-Science funding from Ministry of Higher Education, Malaysia for financial supports. In addition, the authors thank the staff from Faculty of Mechanical Engineering and Faculty of Science, Universiti Teknologi Malaysia for their help in obtaining the Image Analysis and FT-IR respectively.

## REFERENCES

- [1] Ani, F. N., Yi L. X., and Salema A. A. Continuous Fast Pyrolysis of Oil Palm Solid Wastes for Bio-Oil Production. In Proceeding of 5<sup>th</sup> International Conference on Combustion, Incineration, Pyrolysis and Emission Control, 16-19 December 2008, Chiang Mai, Thailand.
- [2] Appleton, T.J., Colder, R.I., Kingman, S.W., Lowndes, I.S., and Read, A.G. Microwave technology for energy-efficient processing of waste. *Applied Energy*, 81 (2005) 85-113.
- [3] Bridgwater, A.V. Biomass fast pyrolysis. *Thermal Science*, 8(2) (2004) 21 – 49.
- [4] Chen, M-Q., Wang, J., Zhang, M-X., Chen, M-G., Zhu, X-F., Min, F-F., Tan, Z-C. Catalytic effects of eight inorganics additives on pyrolysis of pine wood sawdust by microwave heating. *Journal of Analytical and Applied Pyrolysis*, 82 (2008) 145-150.
- [5] Domínguez, A., Fernández, Y., Fidalgo, B., Pis, J.J., and Menéndez, J.A. Bio-syngas production with low concentrations of CO<sub>2</sub> and CH<sub>4</sub> from microwave-induced pyrolysis of wet and dried sewage sludge. *Chemosphere*, 70 (2008) 397-403.
- [6] Domínguez, A., Menéndez, J.A., Fernández, Y., Pis, J.J., Valente Nabais, J.M., Carrott, P.J.M., Ribeiro Carrott, M.M.L. Conventional and microwave induced pyrolysis of coffee hulls for the production of a hydrogen rich fuel gas. *Journal of Analytical and Applied Pyrolysis*, 79 (2007) 128-135.
- [7] El harfi, K., Mokhlisse, A., Chanâa, M.B., and Outzourhit, A. Pyrolysis of the Moroccan oil shales under microwave radiation. *Fuel*, 79 (2000) 733-742.



- [8] Guo, J., and Lua, A.C. Preparation of activated carbons from oil-palm-stone chars by microwave induced carbon dioxide activation. *Carbon*, 38 (2000) 1985-1993.
- [9] Guo, X., Zheng, Y., and Zhou, B. Influence of absorption medium on microwave pyrolysis of fir sawdust. In *Second International Conference on Bioinformatics and Biomedical Engineering*, May 16-18, Shanghai, China.
- [10] Huang, Y.F., Kuan, W.H., Lo, S.L., and Lin, C.F. Total recovery of resources and energy from rice straw using microwave-induced pyrolysis. *Bioresource Technology*, 99 (2008) 8252-8258.
- [11] Islam, M.N., and Ani, F.N. Techno-economic of rice husk pyrolysis, conversion with catalytic treatment to produce liquid fuel. *Bioresource Technology*, 73 (2000) 67-75.
- [12] Jones, D.A., Lelyveld, T.P., Mavrofidis, S.D., Kingman, S.W., and Miles, N.J. Microwave heating applications in environmental engineering – A review. *Resources, Conversion and Recycling*, 34 (2002) 75-90.
- [13] Ludlow-Palafox, C., and Chase, H.A. Microwave-Induced pyrolysis of plastic wastes. *Industrial and Engineering Chemistry Research*, 40 (2001) 4749-4756.
- [14] Menéndez, J.A., Inguanzo, M., and Pis, J.J. Microwave-induced pyrolysis of sewage sludge. *Water Research*, 36 (2002) 3261-3264.
- [15] Miura, M., Kaga, H., Sakurai, A., Kakuchi, T., Takahashi, K. Rapid pyrolysis of wood block by microwave heating. *Journal of Analytical and Applied Pyrolysis*, 71 (2004) 187-199.
- [16] Pingale, N.D., and Shukla, S.R. Microwave assisted ecofriendly recycling of poly (ethylene terephthalate) bottle waste. *European Polymer Journal* 44 (2008) 4151-4156.
- [17] Popescu, S., Misawa, T., Ohtsu, Y., Fujita, H., Sanematsu, S. New microwave reactor for paper-based waste neutralization. *Resources, Conservation and Recycling*, 52 (2008) 671-677.
- [18] Thostenson, E.T., and Chou, T.-W. Microwave processing: fundamental and applications. *Composites: Part A Applied Science and Manufacturing*, 30 (1999) 1055-1071.
- [19] Wan, Y., Chen, P., Zhang, B., Yang, C., Liu, Y., Lin, X., and Ruan, R. Microwave-assisted pyrolysis of biomass: Catalyst to improve product selectivity. *Journal of Analytical and Applied Pyrolysis*, 86 (2009) 161-167.
- [20] Yu, F., Deng, S., Chen, P., Liu, Y., Wan, Y., Olson, A., Kittelson, D., and Ruan, R. Physical and Chemical properties of bio-oils from microwave pyrolysis of corn stover. *Applied Biochemistry and Biotechnology*, 136-140 (2007) 957-970.
- [21] Zhang, H., and Datta, A.K. Microwave power absorption in single and multiple item foods. *Transaction of Institution of Chemical Engineers*, 81 (2003) 257-265.

# A Study of Transient flow in a lid-driven square cavity

Nor Azwadi Che Sidik<sup>a</sup>, Muhammad Ammar Nik Mu'tasim<sup>b</sup>

<sup>a</sup>*Faculty of Mechanical Engineering, Universiti Teknologi Malaysia  
UTM Skudai, Johor, Malaysia,  
azwadi@fkm.utm*

<sup>b</sup>*Faculty of Mechanical Engineering, Universiti Teknologi Malaysia  
UTM Skudai, Johor, Malaysia,  
ammar@ump.edu.my*

## ABSTRACT

### Abstract

In this paper, lattice Boltzmann scheme is used to simulate steady incompressible flow inside a square cavity. Numerical simulations are carried out for Reynolds number of 100, 400, 1000, 3200 and 7500. The governing equation use is the double-population lattice Boltzmann formulation. Two-dimensional nine velocity model is used for the computation of velocity field. The results obtained are compared with the results found in the literature reviews. Present study found that lattice Boltzmann scheme is able to carry out equivalent results as conventional scheme.

### Keywords

*lid-driven square cavity, lattice Boltzmann scheme, Transient flow*

## 1. INTRODUCTION

Flow in a cavity is an interesting research problem and has always been the initial interest among researchers. Numerous studies have been done to study the phenomenon of flows inside closed geometries. The most interesting type of geometries is the square cavity. This is due to its simplicity of its geometry and its boundary conditions. Many reviews of square cavity using 2-D Navier Stokes equations can be studied from authors such as Ghia et al. [1], Erturk et al.[2] and Albensoeder and Kuhlmann [3].

The lattice Boltzmann method has been known for many years as one of the alternative tools that is as competent as Navier Stokes equations. The advantage of Lattice Boltzmann Method is that it is much more accurate and easier to apply in complicated boundary conditions.[4]

Many efforts have been done on rectangular cavity rather than square cavity. Cheng and Hung [5] apply lattice Boltzmann methods to analyze the 2D vortex structure in a rectangular lid-driven cavity for various Reynolds numbers. According to Shankar and Deshpande [6], there are three advantages of studying lid driven cavity flows. The first method is that results are easy to compare from theory, numerical simulations and experiments. The second method is that the flow domain is unaffected by varies Reynolds numbers. The third is that the flow reveals the results that may occur in incompressible flows, complex flows and transition to turbulence.

In this study, we will look at the main objective which is to understand the transient flow in a lid-driven cavity under varies Reynolds numbers using lattice Boltzmann scheme.

## 2. LATTICE BOLTZMANN SCHEME

The Lattice Boltzmann Scheme is originally developed from the Lattice Gas Automata. The Lattice Boltzmann Scheme can be derived from the continuum Boltzmann Equation [7]. A Boltzmann scheme consists of two steps, a streaming step and a collision step. The statistical treatment of a system can be represented in terms of distribution function. Nor Azwadi [8] affirmed that this distribution function  $f(\mathbf{x}, \mathbf{c}, t) d\mathbf{x} d\mathbf{c}$  is the number of particles which positions and velocities are such that  $d\mathbf{x}$  and  $d\mathbf{c}$  at time  $t$ . Every particle would move from  $\mathbf{x}$  to  $\mathbf{x} + \mathbf{c}\Delta t$  if there is no collision occurs. Moreover, each particle velocity would change from  $\mathbf{c}$  to  $\mathbf{c} + a\Delta t$  in which  $a$  is the acceleration due to external forces on a particle at  $\mathbf{x}$  with a velocity of  $\mathbf{c}$ .

If no collision happens, means that there is conservation of molecules. In other words, the number of molecules  $f(\mathbf{x}, \mathbf{c}, t)d\mathbf{x}d\mathbf{c}$  is equal to the number of molecules  $f(\mathbf{x} + \mathbf{c}\Delta t, \mathbf{c} + a\Delta t, t + \Delta t)d\mathbf{x}d\mathbf{c}$ .

Therefore,

$$f(\mathbf{x} + \mathbf{c}\Delta t, \mathbf{c} + a\Delta t, t + \Delta t)d\mathbf{x}d\mathbf{c} - f(\mathbf{x}, \mathbf{c}, t)d\mathbf{x}d\mathbf{c} = 0 \quad (1)$$

However, when collision occurs, the arriving particles at the points interact with one and another and by changing the velocity direction that can be expressed as

$$f(\mathbf{x} + \mathbf{c}\Delta t, \mathbf{c} + a\Delta t, t + \Delta t)d\mathbf{x}d\mathbf{c} - f(\mathbf{x}, \mathbf{c}, t)d\mathbf{x}d\mathbf{c} = \Omega(f)d\mathbf{x}d\mathbf{c}dt \quad (2)$$

In which  $\Omega(f)d\mathbf{x}d\mathbf{c}dt$  is the lattice Boltzmann collision operator. The Eq. (2) is divided by  $d\mathbf{x}d\mathbf{c}dt$ . Next, let  $dt$  tends to zero. This would yield the Boltzmann equation for  $f$  as follows;

$$\frac{\partial f}{\partial t} + c_\alpha \frac{\partial f}{\partial x_\alpha} + a \frac{\partial f}{\partial c_\alpha} = \Omega(f) \quad (3)$$

Where as the  $\Omega(f)$  is the expression for collision operators which controls the speed of change in  $f$  during collision. If the collision is to conserve mass, momentum and energy, it is required that;

$$\int \begin{bmatrix} 1 \\ \mathbf{c} \\ c^2 \end{bmatrix} \Omega(f)d\mathbf{c} = 0 \quad (4)$$

There are two ways that the distribution function  $f(\mathbf{x}, \mathbf{c}, t)$  can be changed by this collision. The ways are as follow;

1. When collision takes place, some particles with initial velocities of  $\mathbf{c}$  would have their velocities changed due to decrease in  $f(\mathbf{x}, \mathbf{c}, t)$ .

2. On the other hand, particles that have different velocity at initial will tend to have velocity of  $\mathbf{c}$  after the collision due to the increase in  $f(\mathbf{x}, \mathbf{c}, t)$ .

The macroscopic quantities such as fluid density, momentum and energy can be found from the distribution function by considering the appropriate integral. However, due to the complicated nature of the collision integral where any replacement of collision must satisfy the conservation of mass, momentum and energy expressed in Eq. (4) is a problem when dealing with Boltzmann equation. Nor Azwadi [8] stated that:

$$\frac{\partial f}{\partial t} + c_\alpha \frac{\partial f}{\partial x_\alpha} = \frac{\partial f}{\partial t} \Big|_{collision}$$

Where ;

$$\frac{\partial f}{\partial t} \Big|_{collision} = \Omega(f)$$

Equation (6) represents the change in distribution function per unit time due to collision. Succi [9] had shown that the particular interest is in the change in distribution function  $f$  in time of order  $\tau_f$ , the average time between excessive collisions. The distribution function  $f$  can be related to the equilibrium distribution function  $f^{eq}$  via second order Taylor's series expansion, that is:

$$f^{eq}(\mathbf{x}, \mathbf{c}, t) \approx f(\mathbf{x}, \mathbf{c}, t) + \frac{\partial f}{\partial t} \Big|_{collision} (\delta t) + O(\delta t)^2$$

$$\frac{\partial f}{\partial t} \Big|_{collision} = \frac{f^{eq}(\mathbf{x}, \mathbf{c}, t) - f(\mathbf{x}, \mathbf{c}, t)}{\delta t} = \frac{f^{eq}(\mathbf{x}, \mathbf{c}, t) - f(\mathbf{x}, \mathbf{c}, t)}{\tau_f}$$

Therefore, the discretized version of the BGK Lattice Boltzmann equation can be written as follow

$$f_i(\mathbf{x} + \mathbf{c}_i \Delta t, t + \Delta t) - f_i(\mathbf{x}, t) = -\Delta t \left( \frac{f_i - f_i^{eq}}{\tau_f} \right) \quad (9)$$

The other important issues in lattice Boltzmann equations of flow is the Boundary condition. Boundary conditions used is known as the Bounce Back scheme [8]. This Boundary condition was used to obtain the no-slip velocity condition. Meaning when a particle moves to the wall node, the particle distribution scatters back to the node it has come from.

### 1. SPECIFICATION OF THE PROBLEM

For this problem, flow inside a driven square cavity was investigated numerically. The top boundary moves from left to right with a constant velocity  $U$ . Figure 1 shows the geometry of the driven square cavity. The other three boundaries which is the left, right and the bottom side (wall) are made fixed. The initial assigned value of density,  $\rho=1.0$  is applied to whole field. Next, the velocities in the interior of the cavities are set to zero. Velocity of  $U$  in  $x$  direction is applied on top of the boundary while velocity in  $y$  direction is set to zero. The bounce back boundary condition is applied on the three stationary walls. Reynolds number is defined as  $Re = UL/\nu$  where  $L$  is grid length and  $\nu$  is the kinematic viscosity.

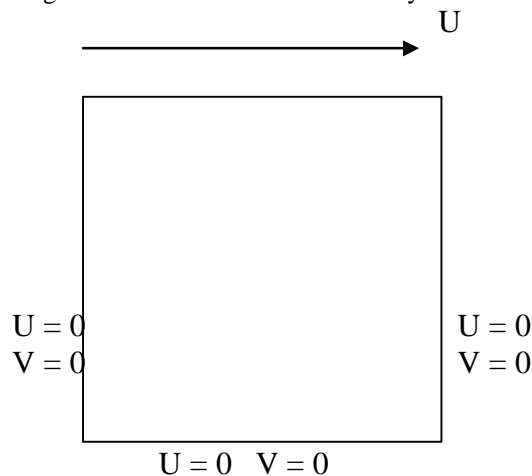


Figure 2 Geometry of square driven cavity

The grid length is set to be 300 times 300. Size of the grid was used to acquire the steady solution for the given Reynolds numbers (we need to keep a sufficiently large  $\tau$  within the stability range). The value of the Reynolds number used for this problem are  $Re=100, 400, 1000, 3200$  and  $7500$ .

### 2. RESULTS AND DISCUSSION

In this section, the numerical results for the problem obtained from the transient flow for center location from driven cavity flow using lattice Boltzmann equation are discussed.

#### 4.1 Code Validation

In order to study the center location transient flow, it was first applied for driven square cavity flow. Driven cavity flow is a standard benchmark case which has been studied by many researchers. For this problem, the velocity,  $U$  at the top wall was maintained at  $0.1$  lu/s while the velocity at the other three walls was set to  $0$  lu/s. On the other hand, the Reynolds numbers were varied from  $100$  to  $10000$ . We now compare the performance of our code for Stream functions of  $Re 400$  with the simulations applied by T.H Ji et al [10] at  $Re 400$  in Fig. 3. The fluid motion is governed by the well know Navier Stokes with the fluid properties set as constant. The vertical sidewalls and the bottom wall are made rigid. The stream flow evolves slowly to the steady state.[11]The data corresponded was nearly equal to the transient movement trajectory of the center location for the Reynolds Number  $400$  using Lattice Boltzmann Scheme.

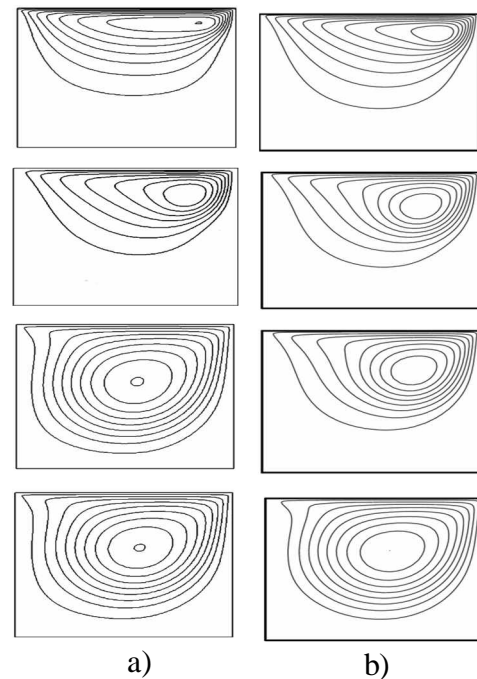


Figure 3 Stream functions in cavity flow at  $Re 400$  a) Lattice Boltzmann Scheme b) Navier Stokes Equation T.H Ji et al [11]

#### 4.2 Transient flow of Center location

Fig. 4 shows the comparison of different Reynolds number for the trajectory of the center location movement in the lid driven square cavity. The trajectory of the center location touches the lid and its initial location was roughly at the middle of the lid. The trajectory plunges straight at the right side of the lid as it drifted toward the center. It can be clearly seen that the time taken by lower Reynolds number to drift to the center are shorter comparing with the higher Reynolds number which produces a longer range of time to move to the center of the square cavity. It can be observed that the transient structure of the flow in Fig. 5 can clearly sees the vortex shape. This explains the shape trajectory when a particle is applied into the driven square cavity. P. Kosinski et al [10] acknowledge that the inertial formation of the flow at the beginning of the simulation is important since it is able to produce vortex clearly and can explain the shape of the particle trajectory.

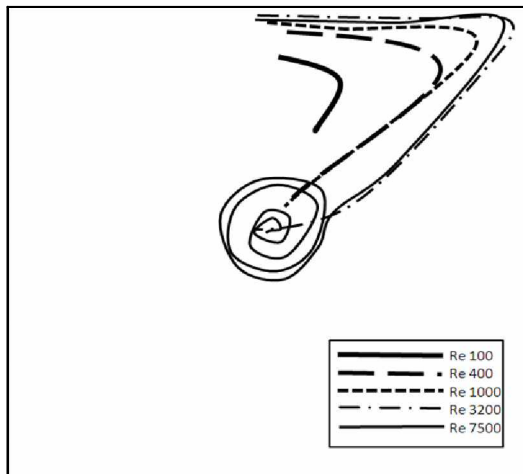


Figure 4 Center location transient movement comparison for Re 100, Re 400, Re 1000, Re 3200 and Re 7500

#### 5. CONCLUSION

A lattice Boltzmann scheme code was developed in this work to show the center location of the vortex in a lid-driven square cavity. It was carried out successfully to simulate 2-D square lid-driven cavity flow. The results obtained can be accepted and in good agreements with those of the Navier Stokes scheme and available data in the literature. The simulations show that the trajectory tends to

migrate towards the walls and the higher Reynolds number the more intense it moves to the wall. It shows here that Lattice Boltzmann Scheme carried out well as with the using the Navier Stokes Equation.

#### ACKNOWLEDGMENTS

The authors would like to thank Universiti Teknologi Malaysia and the Malaysian government for supporting this research activity.

#### NOMENCLATURE

$a$	Acceleration	$U_i$	Mean velocity components ( $i=1, 2, 3$ )
$\mathbf{c}$	Micro velocity vector	$\nu$	kinematic viscosity
$f(\mathbf{x}, \mathbf{c}, t)$	Density distribution function	$\rho$	Fluid Density
$f_i$	Discretized density distribution function	$\tau$	Time relaxation
$f_i^{eq}$	Discretized equilibrium density distribution function	$\Omega$	Collision operator
$Re$	Reynolds number ( $=U_b D_h / \nu$ )		
$T$	Local mean temperature [K]		
$t$	time		
$U$	Horizontal velocity of top plate		

#### REFERENCES

- [1] Ghia, U., Ghia, K.N. and C.Y., Shin, 1982, "High Re Solutions for incompressible Flow using the Navier-Stokes Equations and a Multigrid Method", Journal of Computational Physics, Vol 48, pp. 387-411.
- [2] Erturk, E., Corke, T.C. and Gokcol, O., 2005, "Numerical Solutions of 2-D Steady Incompressible Driven Cavity Flow at High Reynolds Numbers", International Journal for Numerical Methods in Fluids, Vol. 48, pp. 747-774.
- [3] Albensoeder, S. and Kuhlmann, H.C., 2005, "Accurate three-dimensional lid-driven cavity flow", Journal of Computational Physics, Vol. 206, pp. 536-558. Filippova, O. and Hanel, D., 1998, "Grid Refinement for Lattice-BGK Models",



- [1] Journal of Computational Physics, Vol. 147, pp. 219-228.
- [2] M.cheng, K.C hung, Vortex Structure of Steady flow in a Rectangular cavity, Computers & Fluids 35 (2006) 1046-1062
- [3] P.Shankar, M.Deshpande, Fluid mechanics in the driven cavity, Annual Review of Fluid Mechanics 32 (2000) 93-136
- [4] S Chen and G.D Doolen, Lattice Boltzmann Method for fluid flows Annual Review of Fluid Mechanics, 30:229-264, 1998
- [5] Nor Azwadi, C.S. and Tanahashi, T., 2006, "Simplified Thermal Lattice Boltzmann in Incompressible Limit", International Journal of Modern Physics, B 20, pp. 2437-2449.
- [6] Succi, S., 2001, The Lattice Boltzmann Equation for fluid dynamics and beyond, Oxford Science Publications, New York.
- [7] P.Kosinski, A.kosinska, A.C. Hoffmann, 2009 "simulation of solid particles behavior in a driven cavity flow" An International Journal on the Science and Technology of Wet and Dry Particulate Systems, Vol. 191 327-339
- [8] Tae Ho Ji, Seo Young Kim, Jae Min Hyun, 2007, "Transient mixed convection in an enclosure driven by a sliding lid", Heat Mass Transfer, 43: 629-638
- [9] Nor Azwadi, C.S and Tanahashi, T., 2007, "Three-Dimensional Thermal Lattice Boltzmanns Simulation of Natural Convection in a Cubic Cavity", International Journal of Modern Physics, B 21, pp.87-96.
- [10] Bhatnagar, P. L., Gross, E. P. and Krook, M., 1954, "A Model for Collision Processes in Gasses. 1. Small Amplitude Processes in Charged and Neutral One-Component System", Physics Review, Vol. 94, pp. 511-525.
- [11] Nor Azwadi C.S and T, Tanahashi, 2008, "Simplified Finite Difference Thermal Lattice Boltzmann Method", International Journal of Modern Physics, B 22, pp. 3865-3876.
- [12] Krafczyk, M., Tolke, J., 2009, "Second order interpolation of the flow field in the lattice Boltzmann method", Computers and Mathematics with Applications, Vol. 58, pp. 898-902.
- [13] C.Crowe, M.Sommerfeld, Y.Tsuji, Multiphase Flows with Droplets and Particles, CRC Press LLC, 1998

# Efficient Mesh for Driven Square Cavity

Nor Azwadi Che Sidik\* and Fudhail Abdul Munir\*\*

*Faculty of Mechanical Engineering, Universiti Teknologi Malaysia  
UTM Skudai, Johor, Malaysia*

*\*azwadi@fkm.utm, \*\*fudhail45@gmail.com*

## ABSTRACT

In this paper, an improved lattice Boltzmann scheme is used to simulate steady incompressible flow inside a square cavity. The newly improved scheme is applied for driven square cavity. Numerical simulations are carried out for Reynolds number equal to 5000. The governing equation used is the double-population lattice Boltzmann formulation. On the other hand, two-dimensional nine velocity model is used for the computation of velocity field. The results obtained are compared with the results found in the literature reviews. Moreover, the time needed for the solution to converge is recorded. The time obtained is compared with the time required for the conventional lattice Boltzmann scheme to converge. Present study found that the computation time can be reduced without sacrificing the accuracy of the results.

**Keywords:** driven square cavity, lattice Boltzmann scheme

## 1. INTRODUCTION

Being a part of Computational Fluid Dynamics (CFD) study, flows inside closed geometries have always been of focal attention. There have been numerous studies being carried out on flow behaviour inside a cavity. The most popular type of cavity that is studied by vast researchers is flow inside square cavity. This is probably due to its simplicity of the geometry and application of the boundary conditions. Excellent reviews on driven square cavity were written by Ghia et al. [1], Erturk et al. [2] and Albensoeder and Kuhlmann [3]. However, these researchers used the conventional CFD which is by solving 2-D Navier Stokes equations.

Over the years, there has been a rapid progress in developing the lattice Boltzmann method as an efficient alternative to conventional CFD. An essential advantage of the lattice Boltzmann method is its ease and accuracy in dealing with complicated boundary geometries. Apart from that, Filippova and

Hanel [4] stated that in the range of small to moderate Reynolds numbers, where the flow solution is not too anisotropic, the lattice-BGK method is better compared to the conventional computational fluid dynamics if dealing with flows in complex geometries as in filters or through granular materials.

According to Chew et al. [5], there are three methods to improve the standard lattice Boltzmann equation (LBE) before it can be applied to complex problems. The first method is interpolation-supplemented lattice Boltzmann equation (ISLBE) which first proposed by He and Doolen [6]. ISLBE was first used to simulate flow around a circular cylinder. He and Doolen [6] also mentioned that, there are two obvious advantages of irregular lattice grids over regular grids used in the conventional lattice Boltzmann models. The first advantage is the boundary of the cylinder is described much more accurately. The second merit of ISLBE is the mesh can be placed more densely around the cylinder. This will lead to the improvement in term of numerical efficiency.

The second method is called the differential LBE. Differential LBE is based on the solution of a partial differentiation equation. The third method is called grid refinement method which was introduced by Filippova and Hanel [4]. In this work, we will present an improved lattice Boltzmann scheme to simulate flow inside a driven square cavity. It was found that when our model is applied to simulate the driven cavity flow, a good accuracy of results could be obtained.

## 2. LATTICE BOLTZMANN METHOD

The fundamental idea of Boltzmann work is that a gas is composed of interacting particles that can be explained by classical mechanics. Since there are many particles involved, a statistical treatment is needed and is more suitable. According to Sukop and Thorne [7], the mechanics can be very simple and it contains streaming in space and billiard-like collision interactions.

The statistical treatment of a system can be represented in terms of distribution function. It was stated by Nor Azwadi [8] that this distribution function  $f(\mathbf{x}, \mathbf{c}, t) d\mathbf{x} d\mathbf{c}$  is the number of particles which positions and velocities are such that  $d\mathbf{x}$  and  $d\mathbf{c}$  at time  $t$ . Each particle would move from  $\mathbf{x}$  to  $\mathbf{x} + \mathbf{c}\Delta t$  if there is no collision occurs. Moreover, each particle velocity would change from  $\mathbf{c}$  to  $\mathbf{c} + a\Delta t$  in which  $a$  is the acceleration due to external forces on a particle at  $\mathbf{x}$  with a velocity of  $\mathbf{c}$ .

Furthermore, no collision means that there is conservation of molecules. In other words, the number of molecules  $f(\mathbf{x}, \mathbf{c}, t) d\mathbf{x} d\mathbf{c}$  is equal to the number of molecules  $f(\mathbf{x} + \mathbf{c}\Delta t, \mathbf{c} + a\Delta t, t + \Delta t) d\mathbf{x} d\mathbf{c}$ . Therefore,

$$f(\mathbf{x} + \mathbf{c}\Delta t, \mathbf{c} + a\Delta t, t + \Delta t) d\mathbf{x} d\mathbf{c} - f(\mathbf{x}, \mathbf{c}, t) d\mathbf{x} d\mathbf{c} = 0 \quad (1)$$

However, when collision occurs between the molecules the equation that can be represented for this particular case is that

$$f(\mathbf{x} + \mathbf{c}\Delta t, \mathbf{c} + a\Delta t, t + \Delta t) d\mathbf{x} d\mathbf{c} - f(\mathbf{x}, \mathbf{c}, t) d\mathbf{x} d\mathbf{c} = \Omega(f) d\mathbf{x} d\mathbf{c} dt \quad (2)$$

where  $\Omega(f) d\mathbf{x} d\mathbf{c} dt$  is the lattice Boltzmann collision operator. The equation (2) is divided by  $d\mathbf{x} d\mathbf{c} dt$ . Next, let  $dt$  tends to zero. This would yield the Boltzmann equation for  $f$  as follows;

$$\frac{\partial f}{\partial t} + c_\alpha \frac{\partial f}{\partial x_\alpha} + a \frac{\partial f}{\partial c_\alpha} = \Omega(f) \quad (3)$$

Solving Boltzmann equation would require an expression for the collision operator  $\Omega(f)$ . If the collision is to conserve mass, momentum and energy, it is required that;

$$\int \begin{bmatrix} 1 \\ \mathbf{c} \\ c^2 \end{bmatrix} \Omega(f) d\mathbf{c} = 0 \quad (4)$$

There are two ways that the distribution function  $f(\mathbf{x}, \mathbf{c}, t)$  can be changed by this collision. The ways are as follow;

1. When collision takes place, some particles with initial velocities of  $\mathbf{c}$  would have their velocities changed due to decrease in  $f(\mathbf{x}, \mathbf{c}, t)$ .
2. On the other hand, particles that have different velocity at initial will tend to have velocity of  $\mathbf{c}$  after the collision due to the increase in  $f(\mathbf{x}, \mathbf{c}, t)$ .

The macroscopic quantities such as fluid density, momentum and energy can be found from the distribution function by considering the appropriate integral. However, due to the complicated nature of the collision integral where any replacement of collision must satisfy the conservation of mass, momentum and energy expressed in Eq. (4) is a problem when dealing with Boltzmann equation. Nor Azwadi [8]

$$\frac{\partial f}{\partial t} + c_\alpha \frac{\partial f}{\partial x_\alpha} = \frac{\partial f}{\partial t} \Big|_{collision} \quad (5)$$

Where ;

$$\frac{\partial f}{\partial t} \Big|_{collision} = \Omega(f) \quad (6)$$

Equation (6) represents the change in distribution function per unit time due to collision. Succi [9] had shown that the particular interest is in the change in distribution function  $f$  in time of order  $\tau_f$ , the average time between excessive collisions. The distribution function  $f$  can be related to the equilibrium distribution function  $f^{eq}$  via second order Taylor's series expansion, that is:

$$f^{eq}(\mathbf{x}, \mathbf{c}, t) \approx f(\mathbf{x}, \mathbf{c}, t) + \frac{\partial f}{\partial t} \Big|_{collision} (\delta t) + O(\delta t)^2 \quad (7)$$

$$\frac{\partial f}{\partial t} \Big|_{collision} = \frac{f^{eq}(\mathbf{x}, \mathbf{c}, t) - f(\mathbf{x}, \mathbf{c}, t)}{\delta t} = \frac{f^{eq}(\mathbf{x}, \mathbf{c}, t) - f(\mathbf{x}, \mathbf{c}, t)}{\tau_f} \quad (8)$$

Therefore, the discretised version of the BGK Lattice Boltzmann equation can be written as follow

$$f_i(\mathbf{x} + \mathbf{c}_i \Delta t, t + \Delta t) - f_i(\mathbf{x}, t) = -\Delta t \left( \frac{f_i - f_i^{eq}}{\tau_f} \right) \quad (9)$$

## 2.1 Improved lattice Boltzmann scheme

The disadvantage of Lattice Boltzmann Method is that its poor stability condition when dealing with fluid flow with high Reynolds number. Previous work of stability analysis showed that the relaxation parameter  $\tau=0.5$  is the margin of instability. If the value of  $\tau$  is less than 0.5, instability will happens. The equation linking between relaxation parameter  $\tau$  and fluid viscosity is shown below:

$$\tau = 3\nu + 0.5 \quad (10)$$

For viscous fluid,  $\nu > 0$ . Hence,  $\tau > 0.5$ . On the other hand, the equation for Reynolds number is given as:

$$Re = UL/\nu \quad (11)$$

where  $U$  is the fluid velocity,  $L$  is length of the domain and  $\nu$  is the kinematic viscosity. From eq. (10) and eq. (11) above, there is inverse relationship between Reynolds number and the viscosity that is when Reynolds number is larger, the viscosity is smaller. When viscosity is small, the relaxation parameter will approach to the margin of instability value that is 0.5. Therefore, to maintain the stability condition at high Reynolds number, the domain length,  $L$  needs to be increased. However, when  $L$  is increased, the mesh size will be increased if uniform mesh is used. This will lead to more time is needed to perform the computation analysis. Hence, for high Reynolds numbers, the computational efficiency will be reduced as more memory is needed in LBM to store the density distributions.

Therefore, to overcome this problem, in this project, the mesh size will not be increased even though the length is increased for higher Reynolds number. For this purpose, interpolation method will be used. On a regular grid in used in conventional lattice Boltzmann model, starting from one grid site  $\mathbf{x}$ , the distribution function is advected to a neighbouring grid site during each time step. This ensure that the distribution function is known at the next time step. However, for our case, the end point of the streaming process is no longer a grid node. This means that the distribution function at grid nodes is not known at the next time step. Hence, to determine the post streaming distribution function at grid nodes, an interpolation method is used. According to He and Doolen[6], the unknown post streaming distribution function at the original grid nodes can always be approximately by interpolation using their neighbouring shifted grid nodes. In this problem, the mesh used is shown in Fig. 1. As shown in the figure, interpolation is required in the

middle of the cavity in x direction.

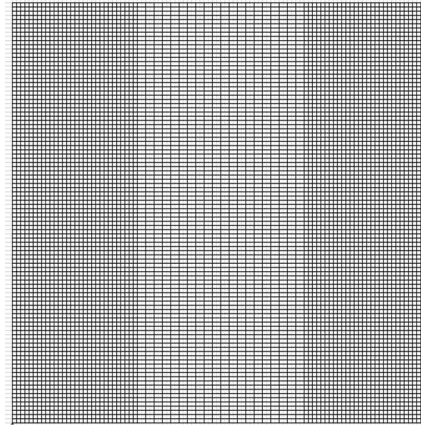


Fig. 1 Mesh for driven square cavity

## 1. SPECIFICATION OF THE PROBLEM

For this problem, flow inside a driven square cavity was investigated numerically. The top boundary moves from left to right with a constant velocity  $U$ . Figure 1 shows the geometry of the driven square cavity. On the other hand, the other three boundaries (wall) are made stationary. The initial assigned value of density,  $\rho=1.0$  is applied to whole field. Next, the velocities in the interior of the cavities are set to zero. Velocity of  $U$  in x direction is applied on top of the boundary while velocity in y direction is set to zero. The bounceback boundary condition is applied on the three stationary walls. Reynolds number is defined as  $Re = UL/\nu$  where  $L$  is grid length and  $\nu$  is the kinematic viscosity.

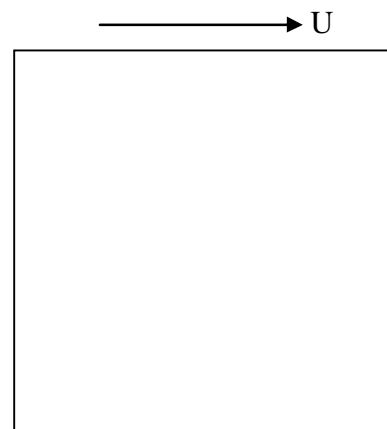


Fig. 2 Geometry of square driven cavity

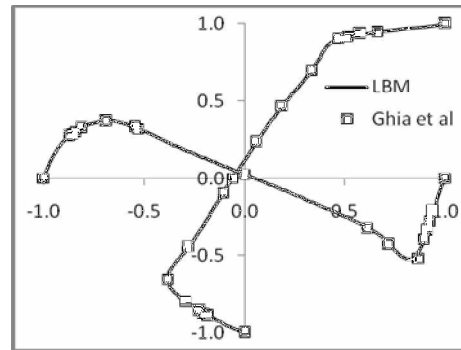
The grid length is set to be 400 times 400. Using this grid size enables us to obtain steady solution for the given Reynolds numbers (we need to keep a sufficiently large  $\tau$  within the stability range). The value of the Reynolds number used for this problem is  $Re=5000$ .

## 1. RESULTS AND DISCUSSION

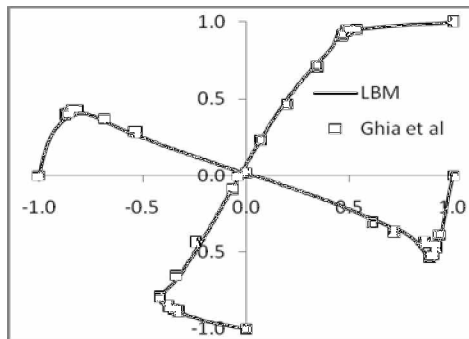
In this section, the numerical results for the problem obtained from the improved lattice Boltzmann scheme are discussed.

### 4.1 Code Validation

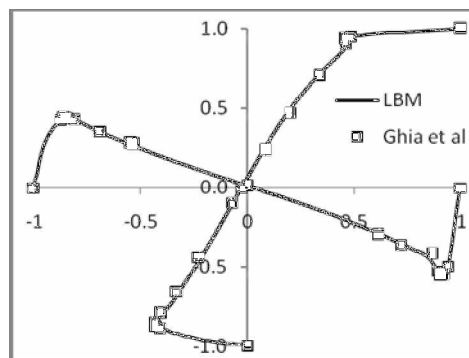
In order to validate the developed code, it was first applied for driven square cavity flow. For this type of flow, the velocity,  $U$  at the top wall was maintained at 0.1 lu/s while the velocity at the other three walls was set to 0 lu/s. On the other hand, the Reynolds numbers were varied from 100 to 10000. The graph of velocity profile at mid height was plotted. The results obtained from Ghia et al. [1] were plotted on the same graph for comparison. Figure 3 (a) to (g) shows the plotted graphs. Good agreement between lattice Boltzmann method (LBM) and the benchmark solutions has been found for every tested case.



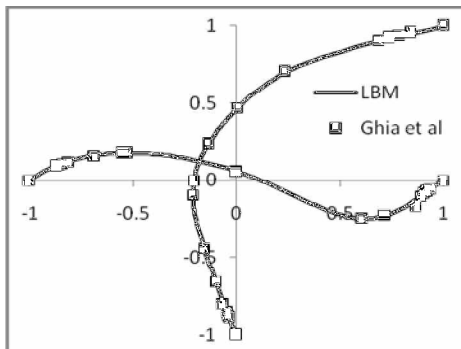
(c)  $Re=1000$



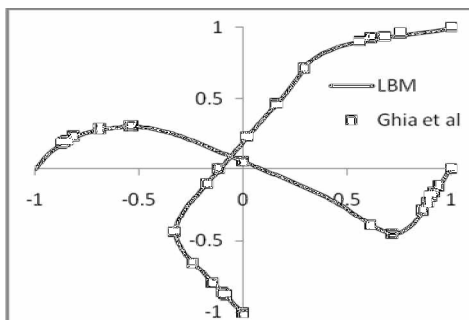
(d)  $Re=3200$



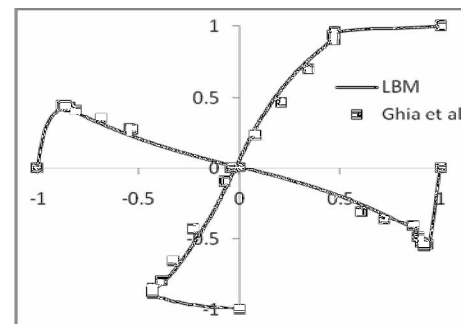
(e)  $Re=5000$



(a)  $Re=100$



(b)  $Re=400$



(f)  $Re=7500$



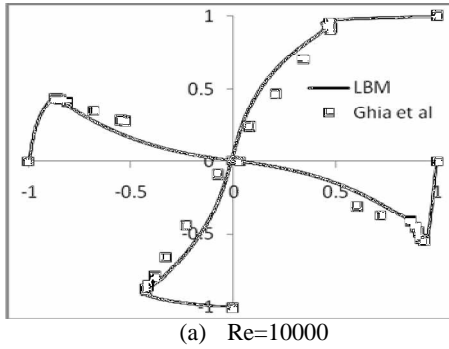


Fig. 3 Velocity profile at mid-height (x-velocity & y-velocity) of cavity for different Re number

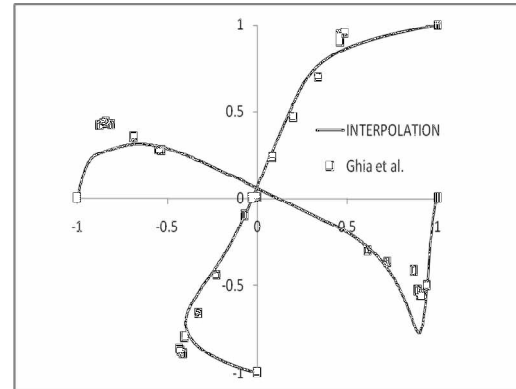


Fig. 4 Velocity profile at mid-height (x-velocity & y-velocity) of cavity for interpolation

On the other hand, Table 1 tabulates the centre of the primary vortex together with the results from Ghia et al. [1] and Hou et al.[10].

Table 1 Location of the primary vortex for square cavity

Re	100	400	1000	3200
Ref. Ghia et al. [1]	(0.6172, 0.7344)	(0.5547, 0.6055)	(0.5313, 0.5625)	(0.5165, 0.5469)
Ref Hou et al. [10]	(0.6196, 0.7373)	(0.5608, 0.6078)	(0.5333, 0.5647)	-
LBM	(0.6200, 0.7400)	(0.5600, 0.6000)	(0.5300, 0.5650)	(0.5200, 0.5400)

Re	5000	7500	10000
Ref. Ghia et al. [1]	(0.5117,0.5352)	(0.5117,0.5322)	(0.5117,0.5333)
Ref Hou et al. [10]	(0.5176,0.5373)	(0.5176,0.5333)	-
LBM	(0.5150,0.5350)	(0.5150,0.5325)	(0.5133,0.5283)

From the results presented in Table 1, we can see that the LBM is able to produce an excellent agreement with the results predicted by conventional macroscale numerical methods.

#### 4.2 Results of the improved scheme

In this section, the results obtained by using the improved scheme are shown. The graph of velocity profile at mid-height (x-velocity & y-velocity) of cavity for the tested Reynolds number is plotted. The results are compared with the results obtained by Ghia et al.[1]. The Fig. 4 shows the plotted graphs.

On the other hand, the improved lattice Boltzmann scheme is 8% faster than the conventional lattice Boltzmann scheme.

### 5. CONCLUSION

An improved lattice Boltzmann scheme code was developed in this work. It was used successfully to simulate 2-D driven cavity flow. The results obtained can be accepted and in good agreements with those of the standard lattice Boltzmann scheme and available data in the literature. Apart from reducing the computation time, the improved mesh system can be used for higher Reynolds number without causing instability as mentioned in section 2.1.

### ACKNOWLEDGMENTS

The authors would like to thank Universiti Teknologi Malaysia and the Malaysian government for supporting this research activity.

### Nomenclature

- a Acceleration
- c Micro velocity vector
- $f(x,c,t)$  Density distribution function
- $f_i$  Discretized density distribution function
- $f_i^{eq}$  Discretized equilibrium density distribution function
- Re Reynolds number ( $=U_b D_h/\nu$ )
- T Local mean temperature [K]
- t time
- U Horizontal velocity of top plate
- $U_i$  Mean velocity components ( $i=1, 2, 3$ )
- $\nu$  kinematic viscosity
- $\rho$  Fluid Density
- $\tau$  Time relaxation
- $\Omega$  Collision operator

## REFERENCES

- [1] Ghia, U., Ghia, K.N. and C.Y., Shin, 1982, "High Re Solutions for incompressible Flow using the Navier-Stokes Equations and a Multigrid Method", *Journal of Computational Physics*, Vol 48, pp. 387-411.
- [2] Erturk, E., Corke, T.C. and Gokcol, O., 2005, "Numerical Solutions of 2-D Steady Incompressible Driven Cavity Flow at High Reynolds Numbers", *International Journal for Numerical Methods in Fluids*, Vol. 48, pp. 747-774.
- [3] Albensoeder, S. and Kuhlmann, H.C., 2005, "Accurate three-dimensional lid-driven cavity flow", *Journal of Computational Physics*, Vol. 206, pp. 536-558.
- [4] Filippova, O. and Hanel, D., 1998, "Grid Refinement for Lattice-BGK Models", *Journal of Computational Physics*, Vol. 147, pp. 219-228.
- [5] Chew, Y.T., Shu, C. and Niu, X.D., 2002, "A New Differential Lattice Boltzmann Equation and Its Application to Simulate Incompressible Flows on Non-Uniform Grids", *Journal of Statistical Physics*, Vol. 107, No ½.
- [6] He, H. and Doolen, G., 1997, "Lattice Boltzmann Method on Curvilinear Coordinates System: Flow around a circular cylinder", *Journal of Computational Physics*, Vol. 134, pp. 306-315.
- [7] Sukop, M.C and Thorne, D.T., 2006, *Lattice Boltzmann Modeling : An introduction for geoscientists and engineers*, Springer, New York.
- [8] Nor Azwadi, C.S. and Tanahashi, T., 2006, "Simplified Thermal Lattice Boltzmann in Incompressible Limit", *International Journal of Modern Physics*, B 20, pp. 2437-2449.
- [9] Succi, S., 2001, *The Lattice Boltzmann Equation for fluid dynamics and beyond*, Oxford Science Publications, New York.
- [10] Hou, S.Q., Zou, Chen, S. and Doolen, G., 1995, "Simulation of Cavity Flow by the lattice Boltzmann Method", *Journal of Computational Physics*, Vol. 118, pp. 329-347.
- [11] Nor Azwadi, C.S and Tanahashi, T., 2007, "Three-Dimensional Thermal Lattice Boltzmann Simulation of Natural Convection in a Cubic Cavity", *International Journal of Modern Physics*, B 21, pp.87-96.
- [12] Bhatnagar, P. L., Gross, E. P. and Krook, M., 1954, "A Model for Collision Processes in Gasses. 1. Small Amplitude Processes in Charged and Neutral One-Component System", *Physics Review*, Vol. 94, pp. 511-525.
- [13] Nor Azwadi C.S and T, Tanahashi, 2008, "Simplified Finite Difference Thermal Lattice Boltzmann Method", *International Journal of Modern Physics*, B 22, pp. 3865-3876.
- [14] Krafczyk, M., Tolke, J., 2009, "Second order interpolation of the flow field in the lattice Boltzmann method", *Computers and Mathematics with Applications*, Vol. 58, pp. 898-902.
- [15] Frish, U., B., Hasslacher and Pomeau, Y., 1986, "Lattice Gas Automata for the Navier-Stokes Equation", *Physics Review Letter*, Vol. 56, pp. 1505-1508.
- [16] Jin, C. and Xu, K., 2006, "An adaptive grid method for two dimensional viscous flow", *Journal of Computational Physics*, Vol. 218, pp. 68-81.
- [17] Gladrow, D.W. 2000, *Lattice Gas Cellular Automata and Lattice Boltzmann Models*, Springer Verlag, New York.
- [18] He, X. and L.S., Luo, 1997, "Lattice Boltzmann Model for the Incompressible Navier-Stokes Equation", *Journal of Statistical Physics*, Vol. 88, pp.927-944.
- [19] Luo, L.S. and X., He, 1997, "A Priori Derivation of the Lattice Boltzmann Equation", *Physics Review*, E 56, pp. 6811-6817.
- [20] Shu, C., Chew, Y.T., Niu, X.D., Peng, Y., Zheng, H.W., and Liu, N.Y., 2008, "Progress in the development and application of lattice Boltzmann method", *Asian Congress of Fluid Mechanics*, Daejeon, Korea.

# Study of Flow Behaviour in Triangular Cavity

Nor Azwadi Che Sidik\* and Fudhail Abdul Munir\*\*

*Faculty of Mechanical Engineering, Universiti Teknologi Malaysia  
UTM Skudai, Johor, Malaysia*

\*azwadi@fkm.utm, \*\*fudhail45@gmail.com

## ABSTRACT

In this paper, fluid flow behaviour of steady incompressible flow inside a triangular cavity was studied. Numerical calculations were done for three types of triangular cavity. The numerical investigations were conducted for different Reynolds numbers by using lattice Boltzmann scheme. The governing equation used is the double-population lattice Boltzmann formulation. On the other hand, two-dimensional nine velocity model was used for the computation of velocity field. The results obtained were compared with the results found in the literature reviews. Present study found that the flow patterns are significantly affected by the triangle geometry.

## Keywords

Triangular cavity, lattice Boltzmann scheme

## 1. INTRODUCTION

Being a part of Computational Fluid Dynamics (CFD) study, flows inside closed geometries have always been of focal attention. There have been numerous studies being carried out on flow behaviour inside a cavity. The most popular type of cavity that is studied by vast researchers is flow inside square cavity. This is probably due to its simplicity of the geometry and application of the boundary conditions. Excellent reviews on driven square cavity were written by Ghia et al. [1], Erturk et al. [2] and Albensoeder and Kuhlmann [3]. However, the results for the square cavity cannot be applied to other important geometries such as a triangular cavity.

In this paper, the problem under consideration is the steady motion of an incompressible viscous flow in a triangular cavity of arbitrary geometry. The incompressible flow inside a triangular driven cavity is also an interesting subject like the driven square cavity flow. This type of flow was investigated numerically by Erturk and Gokcol [4], Li and Tang [5] and Ribbens et al. [6]. According to Erturk and Gokcol [4], there have been very limited numerical

studies found in the literature on the steady incompressible flow inside a triangular driven cavity. In addition to that, all of those mentioned researches were done by solving 2-D Navier Stokes equations.

In present study, an alternative method to conventional CFD which is lattice Boltzmann scheme will be used to solve the 2-D steady incompressible triangular cavity flow. We will compare our results with the numerical studies found in literature. Apart from that, we will also compare the streamline pattern of the triangular flow with results from previous researches. The main objective of this study is to understand the fluid behaviour in triangular cavity by using lattice Boltzmann scheme.

## 2. LATTICE BOLTZMANN METHOD

The fundamental idea of Boltzmann work is that a gas is composed of interacting particles that can be explained by classical mechanics. Since there are many particles involved, a statistical treatment is needed and is more suitable. According to Sukop and Thorne [7], the mechanics can be very simple and it contains streaming in space and billiard-like collision interactions.

The statistical treatment of a system can be represented in terms of distribution function. It was stated by Nor Azwadi [8] that this distribution function  $f(\mathbf{x}, \mathbf{c}, t) d\mathbf{x} d\mathbf{c}$  is the number of particles which positions and velocities are such that  $d\mathbf{x}$  and  $d\mathbf{c}$  at time  $t$ . Each particle would move from  $\mathbf{x}$  to  $\mathbf{x} + \mathbf{c}\Delta t$  if there is no collision occurs. Moreover, each particle velocity would change from  $\mathbf{c}$  to  $\mathbf{c} + a\Delta t$  in which  $a$  is the acceleration due to external forces on a particle at  $\mathbf{x}$  with a velocity of  $\mathbf{c}$ .

Furthermore, no collision means that there is conservation of molecules. In other words, the number of molecules  $f(\mathbf{x}, \mathbf{c}, t) d\mathbf{x} d\mathbf{c}$  is equal to the number of molecules  $f(\mathbf{x} + \mathbf{c}\Delta t, \mathbf{c} + a\Delta t, t + \Delta t) d\mathbf{x} d\mathbf{c}$ . Therefore,

$$f(\mathbf{x}+\mathbf{c}\Delta t, \mathbf{c}+a\Delta t, t+\Delta t) d\mathbf{x}d\mathbf{c} - f(\mathbf{x}, \mathbf{c}, t) d\mathbf{x}d\mathbf{c} = 0 \quad (1)$$

However, when collision occurs between the molecules the equation that can be represented for this particular case is that

$$f(\mathbf{x}+\mathbf{c}\Delta t, \mathbf{c}+a\Delta t, t+\Delta t) d\mathbf{x}d\mathbf{c} - f(\mathbf{x}, \mathbf{c}, t) d\mathbf{x}d\mathbf{c} = \Omega(f) d\mathbf{x}d\mathbf{c} dt \quad (2)$$

where  $\Omega(f) d\mathbf{x}d\mathbf{c} dt$  is the lattice Boltzmann collision operator. The equation (2) is divided by  $d\mathbf{x}d\mathbf{c} dt$ . Next, let  $dt$  tends to zero. This would yield the Boltzmann equation for  $f$  as follows;

$$\frac{\partial f}{\partial t} + c_\alpha \frac{\partial f}{\partial x_\alpha} + a \frac{\partial f}{\partial c_\alpha} = \Omega(f) \quad (3)$$

Solving Boltzmann equation would require an expression for the collision operator  $\Omega(f)$ . If the collision is to conserve mass, momentum and energy, it is required that;

$$\int \begin{bmatrix} 1 \\ \mathbf{c} \\ c^2 \end{bmatrix} \Omega(f) d\mathbf{c} = 0 \quad (4)$$

There are two ways that the distribution function  $f(\mathbf{x}, \mathbf{c}, t)$  can be changed by this collision. The ways are as follow;

1. When collision takes place, some particles with initial velocities of  $\mathbf{c}$  would have their velocities changed due to decrease in  $f(\mathbf{x}, \mathbf{c}, t)$ .
2. On the other hand, particles that have different velocity at initial will tend to have velocity of  $\mathbf{c}$  after the collision due to the increase in  $f(\mathbf{x}, \mathbf{c}, t)$ .

The macroscopic quantities such as fluid density, momentum and energy can be found from the distribution function by considering the appropriate integral. However, due to the complicated nature of the collision integral where any replacement of collision must satisfy the conservation of mass, momentum and energy expressed in Eq. (4) is a problem when dealing with Boltzmann equation. Nor Azwadi [8]

$$\frac{\partial f}{\partial t} + c_\alpha \frac{\partial f}{\partial x_\alpha} = \left. \frac{\partial f}{\partial t} \right|_{\text{collision}} \quad (5)$$

Where ;

$$\left. \frac{\partial f}{\partial t} \right|_{\text{collision}} = \Omega(f) \quad (6)$$

Equation (6) represents the change in distribution function per unit time due to collision. Succi [9] had shown that the particular interest is in the change in distribution function  $f$  in time of order  $\tau_f$ , the average time between excessive collisions. The distribution function  $f$  can be related to the equilibrium distribution function  $f^{eq}$  via second order Taylor's series expansion, that is:

$$f^{eq}(\mathbf{x}, \mathbf{c}, t) \approx f(\mathbf{x}, \mathbf{c}, t) + \left. \frac{\partial f}{\partial t} \right|_{\text{collision}} (\delta t) + \mathcal{O}(\delta t)^2 \quad (7)$$

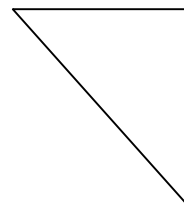
$$\left. \frac{\partial f}{\partial t} \right|_{\text{collision}} = \frac{f^{eq}(\mathbf{x}, \mathbf{c}, t) - f(\mathbf{x}, \mathbf{c}, t)}{\delta t} = \frac{f^{eq}(\mathbf{x}, \mathbf{c}, t) - f(\mathbf{x}, \mathbf{c}, t)}{\tau_f} \quad (8)$$

Therefore, the discretised version of the BGK Lattice Boltzmann equation can be written as follow

$$f_i(\mathbf{x}+\mathbf{c}_i\Delta t, t+\Delta t) - f_i(\mathbf{x}, t) = -\Delta t \left( \frac{f_i - f_i^{eq}}{\tau_f} \right) \quad (9)$$

### 3. SPECIFICATION OF THE PROBLEM

In this study, three different types of triangle geometries were considered. The first type is an isosceles triangle with the 90° being at the top right corner. On the other hand, the second type is an isosceles triangle with 90° being at the top left corner. The third type is isosceles triangle with 90° at the corner angle. Figure 1 depicts the geometry of the three triangles.



(a) 90° at top right corner

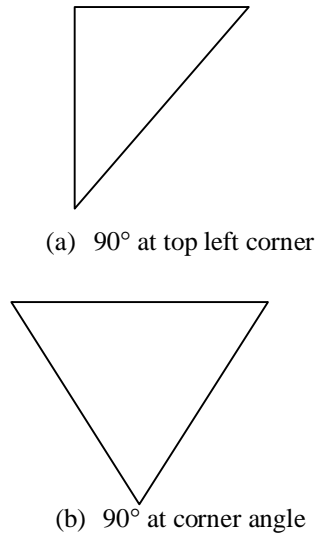


Fig. 1 Geometry of different triangular cavity

For each case, velocity,  $U$  of 0.1 lu/s is applied on top side of the triangle. Reynolds number is defined as  $Re = UL/\nu$  where

$$U = \text{top wall velocity}$$

$$L = \text{grid length}$$

$$\nu = \text{dynamic viscosity}$$

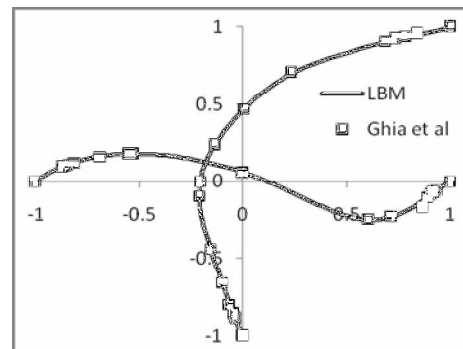
Meanwhile, for the boundary conditions, the velocity of the other two sides of the triangle is set at 0 lu/s. For isosceles triangle with 90° at top right corner and 90° at top left corner, the grid size used for each triangle is 201 x 201 at the beginning of calculation. This grid size was then increased to 301 x 301 for higher Reynolds number. For the case of isosceles triangle with 90° at corner angle, the initial grid size used was 301 x 201. This size was further increased up until 601 x 301 for higher Reynolds number. Using this grid size enables us to obtain steady solution for these various Reynolds numbers (we need to keep a sufficiently large  $\tau$  within the stability range). Then, the Reynolds numbers were varied from 100 to 10000

## 1. RESULTS AND DISCUSSION

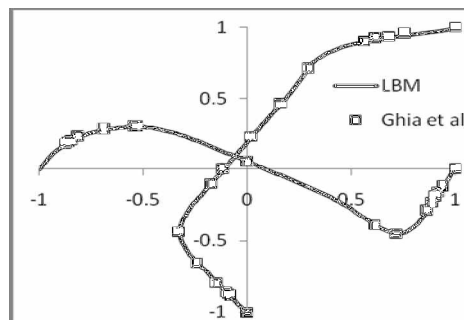
In this section, the numerical results for the problem obtained from lattice Boltzmann scheme are discussed. Reynolds numbers within the range of  $100 \leq Re \leq 10000$  were investigated numerically.

### 4.1 Code Validation

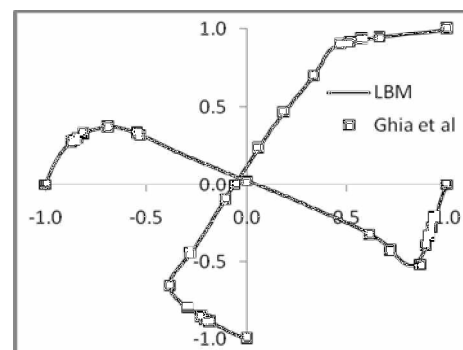
In order to validate the developed code, it was first applied for driven square cavity flow. For this type of flow, the velocity,  $U$  at the top wall was maintained at 0.1 lu/s while the velocity at the other three walls was set to 0 lu/s. On the other hand, the Reynolds numbers were varied from 100 to 10000. The graph of velocity profile at mid height was plotted. The results obtained from Ghia et al. [1] were plotted on the same graph for comparison. Figure 2 (a) to (g) shows the plotted graphs. Good agreement between lattice Boltzmann method (LBM) and the benchmark solutions has been found for every tested case.



(a) Re=100

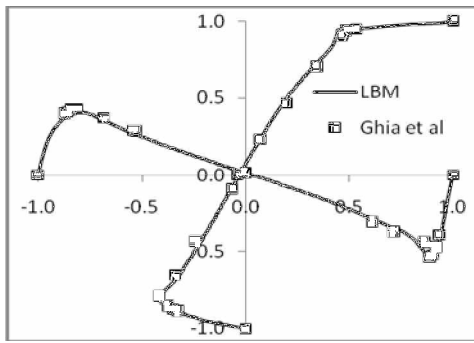


(b) Re=400

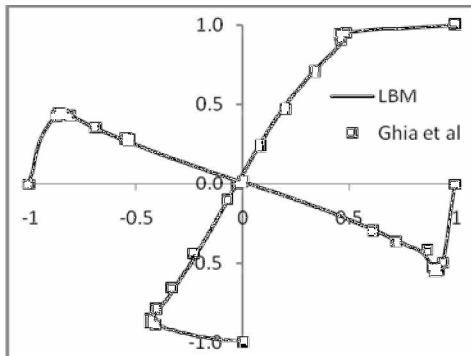


(c) Re=1000

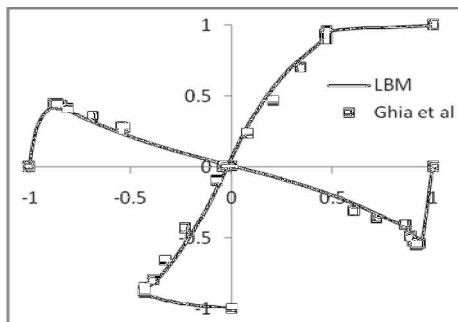




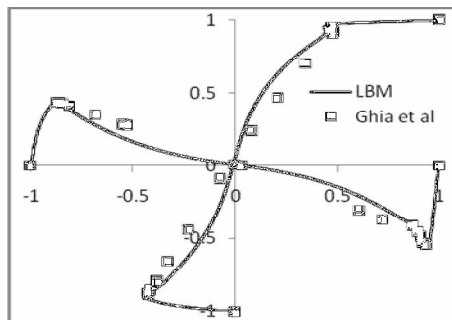
(a) Re=3200



(b) Re=5000



(c) Re=7500



(d) Re=10000

Fig. 2 Velocity profile at mid-height (x-velocity & y-velocity) of cavity for different Re number

#### 4.2 Isosceles triangle with 90° at the top right corner

Figure 3 (a) to (f) shows the streamline patterns for isosceles triangle with 90° at the top right corner. From the figures shown, there are two significant features revealed by the streamline contours. The first feature is that the number of vortices is increased when the Reynolds (Re) numbers are increased. As we can see in Fig. 3 (d), the number of vortex is increased from previous which are two to three when the Re number is 1500. On the other hand, the second significant feature is that the centre of the primary vortex moves downstream to the right as Reynolds number is increased. For instance, Fig. 3 (a) depicts the centre of the primary vortex being located at 4/5 of the bottom vertex. However, this centre moves downward to 3/5 of the bottom vertex as the Reynolds number increases.

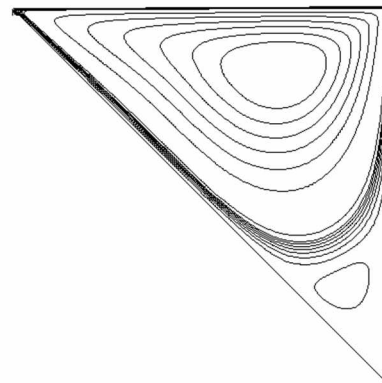
Apart from the streamline patterns, the location of the primary vortex was also compared with the results found in the literature. Table 1 tabulates the centre of the primary vortex together with the results from Hou et al. [10].

Table 1 Location of the primary vortex for isosceles triangle with 90° at the top right corner

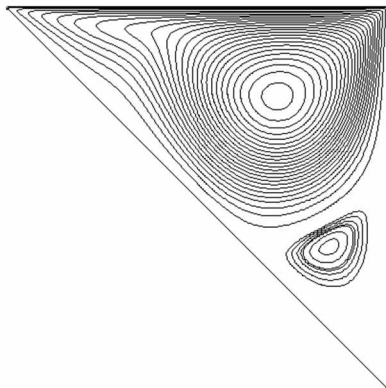
Re	100	500	1000
LBM	(0.7100,0.8300)	(0.7100,0.7650)	(0.7000,0.7550)
Ref[ 10 ]	(0.7090,0.8320)	(0.7070,0.7676)	(0.6992,0.7559)

Re	1500	2000	2500
LBM	(0.7000,0.7467)	(0.7000,0.7467)	(0.7000,0.7433)
Ref[ 10 ]	-	-	(0.6973,0.7441)

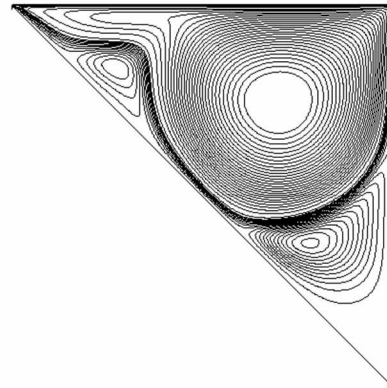
In general, the results in present study are in good agreement with the results from Hou et al[10].



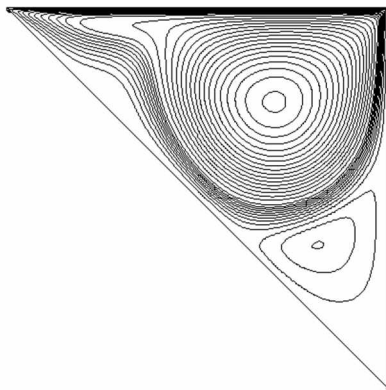
(a) Re=100



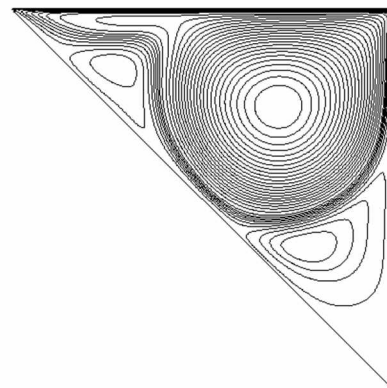
(a) Re=500



(d) Re=2000



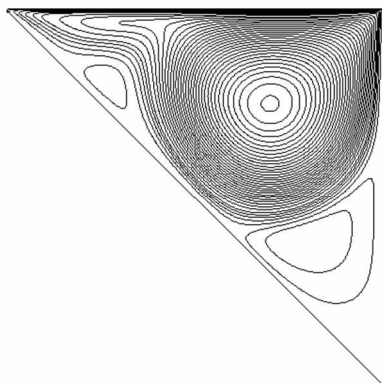
(b) Re=1000



(e) Re = 2500

Fig 3 Streamline pattern for isosceles triangle with 90° at the top right corner

#### 4.3 Isosceles triangle with 90° at the top left corner



(c) Re= 1500

Figure 4 (a) to (f) shows the streamline contours for the isosceles triangle with 90° at the top left corner. From the figures, it is noticed that the primary vortex moves upstream to the right as Reynolds (Re) number is increased. This is contrary to the results obtained in previous section. On the other hand, the number of vortex also increases when the Re number is higher which is similar to results in section 4.2. For example, for Re numbers from 100 to 1000, the total number of vortex is two. However, when the Re number is increased to 1500 the third vortex appears in the streamline pattern. Hence, the

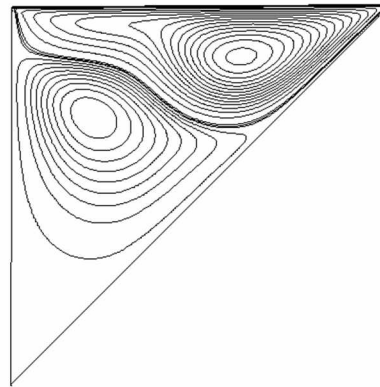
new total number of vortex is three for  $1500 \leq Re \leq 2500$ . It is also noticed that the streamline contour is significantly different from the results in section 4.2 even though Re number is maintained. One of the obvious differences is the size of the primary vortex which is smaller as compared to the previous case in section 4.2 even though the same Re number is used.

Table 2 Location of the primary vortex for isosceles triangle with  $90^\circ$  at the top right corner

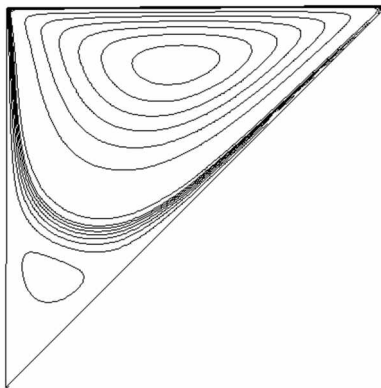
Re	100	500	1000
LBM	(0.4450,0.8500)	(0.5550,0.8500)	(0.6050,0.8650)
Ref[4]	(0.4473,0.8516)	(0.5469,0.8496)	(0.6094,0.8691)

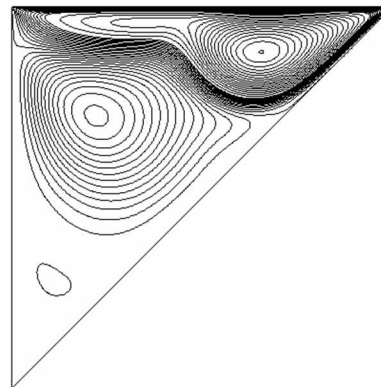
Re	1500	2000	2500
LBM	(0.6567,0.8833)	(0.6900,0.8933)	(0.7167,0.9033)
Ref[4]	(0.6582,0.8848)	(0.6953,0.8965)	(0.7227,0.9043)



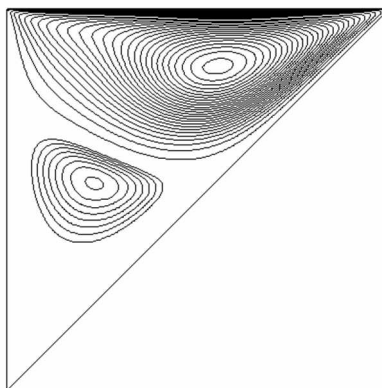
(c) Re=1000



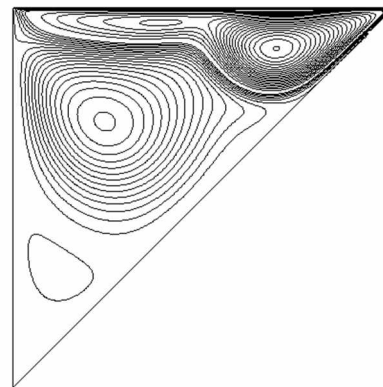
(a) Re=100



(d) Re=1500



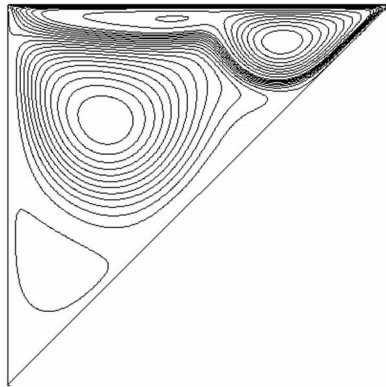
(b) Re=500



(e) Re=2000

Table 3 Location of primary vortex for isosceles triangle with 90° at the corner angle

Re	Location of primary vortex	
	x	y
100	0.5450	0.7600
400	0.6100	0.7500
700	0.5950	0.7150
1000	0.5875	0.7150
3000	0.7400	0.8200
5000	0.7350	0.8100
7000	0.7583	0.6200
10000	0.4117	0.5375



(a) Re=2500

Fig. 4 Streamline patterns for isosceles triangle with 90° at the top left corner

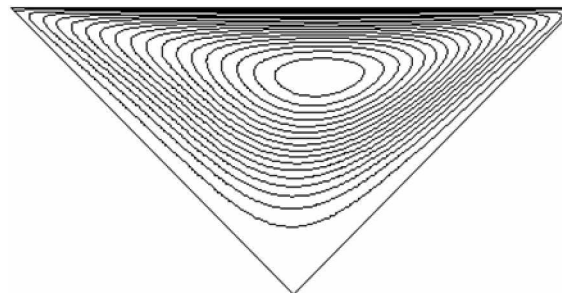
### 4.3 Isosceles triangle with 90° at the corner angle

In this section, flow contours with different Reynolds (Re) numbers are presented. The results of this computation are the streamline patterns plotted for different Re number as shown in Fig. 5. The flow patterns reveal two significant features.

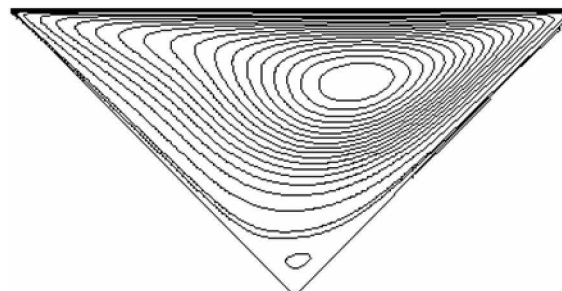
Firstly, as Re numbers are increased, the primary vortex (eddy) moves downstream to the right. For an instance, at Re=100, the location of primary vortex is roughly at 4/5 from the bottom vertex as shown in Fig. 5 (a). Apart from the secondary vortex, no other vortex is visible for Re=100. However, for Re=400, there is secondary vortex located near the stagnant corner of the triangle as shown in Fig. 5 (b). The shape of this secondary vortex becomes larger as Reynolds numbers is further increased as shown in Fig. 5(d) to Fig. 5 (h).

The second significant feature is the number of vortices in the cavity which is increased as the Re number is increased. Fig.5 (e) shows that the third secondary vortex appears for Re=3000, located about 3/5 from the bottom corner of the cavity. The primary vortex moves further upstream to the left before splitting into another secondary vortex when Re=5000, as shown in Figure 5(f). For Re=7000 and Re=10000, the numbers of vortex in the cavity are five and six respectively.

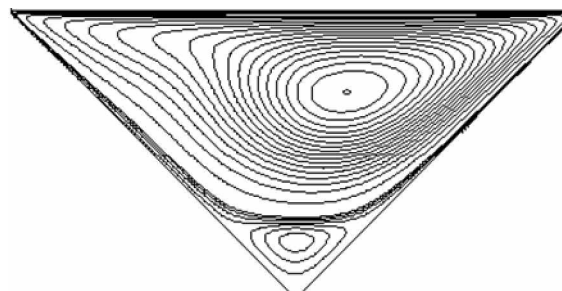
Table 3 shows the location of the centre of the primary vortex. There is no comparison between the results obtained with results found in literature as the specifications of the problem in present study are different.



(a) Re=100

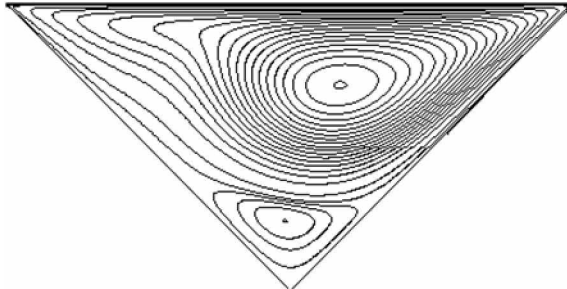


(b) Re=400

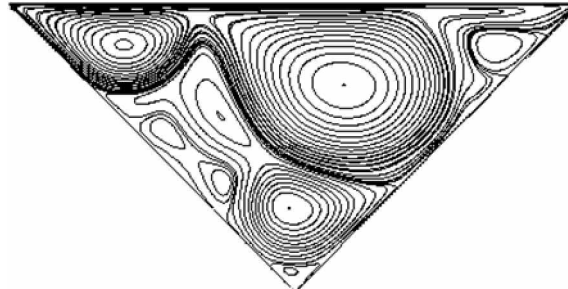


(c) Re=700

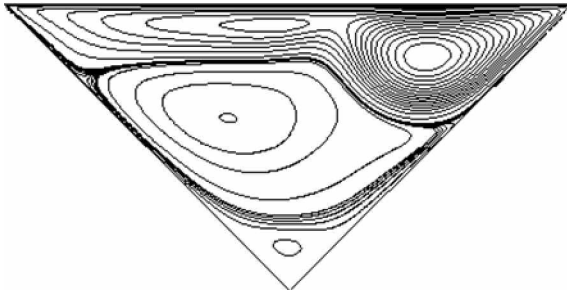




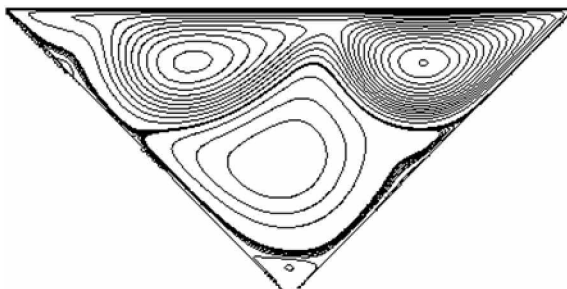
(a) Re=1000



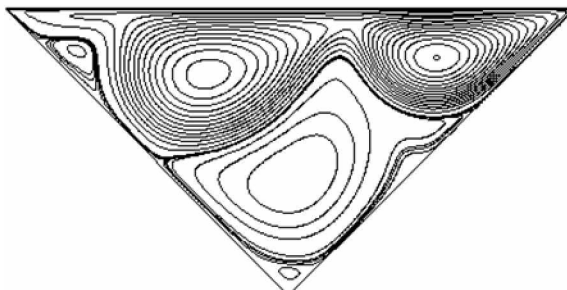
(e) Re=10000



(b) Re=3000



(c) Re=5000



(d) Re=7000

## 5. CONCLUSION

In general, the flow in a triangular cavity is similar to the flow in a square cavity in terms of its physical flows Ribben et al [6]. In this paper, Lattice Boltzmann method (LBM) was used to investigate the steady fluid in a triangular driven cavity. The numerical scheme used proved to be reliable and able to provide steady solution for various Reynolds numbers. In addition to that, the scheme is also more efficient in terms of time consumption. Although our calculation stopped at Re=10000, the numerical solution could be carried out for higher Re without any problem.

Apart from that, it is obvious from the results obtained that the fluid flow behaved significantly different as the Reynolds number increased. In addition to that, the streamline patterns show that the flow structures in a triangular cavity are significantly affected by the geometry of the triangle.

## ACKNOWLEDGMENTS

The authors would like to thank Universiti Teknologi Malaysia and the Malaysian government for supporting this research activity.

## Nomenclature

$a$	Acceleration
$c$	Micro velocity vector
$f(x, c, t)$	Density distribution function
$f_i$	Discretized density distribution function
$f_i^{eq}$	Discretized equilibrium density distribution function
$Re$	Reynolds number ( $=U_b D_b / \nu$ )
$T$	Local mean temperature [K]
$t$	time
$U$	Horizontal velocity of top plate



$U_i$	Mean velocity components (i=1, 2, 3)	[13]
$\nu$	kinematic viscosity	
$\rho$	Fluid Density	
$\tau$	Time relaxation	[14]
$\Omega$	Collision operator	

## REFERENCES

- [1] Ghia, U., K.N., Ghia and C.Y., Shin, 1982, "High Re Solutions for incompressible Flow using the Navier-Stokes Equations and a Multigrid Method", *Journal of Computational Physics*, Vol 48, pp. 387-411.
- [2] Erturk, E., Corke, and Gokcol, O., 2005, "Numerical Solutions of 2-D Steady Incompressible Driven Cavity Flow at High Reynolds Numbers", *International Journal for Numerical Methods in Fluids*, Vol. 48, pp. 747-774.
- [3] Albensoeder, S., and Kuhlmann, H.C., 2005, "Accurate three-dimensional lid-driven cavity flow", *Journal of Computational Physics*, Vol. 206, pp. 536-558.
- [4] Erturk, E., and Gokcol, O., 2007, "Fine grid numerical solutions of triangular cavity flow", *The European Physical Journal Applied Physics*, Vol. 38, pp. 97-105.
- [5] Li, M., and Tang, T., 1996, "Steady Viscous Flow in a Triangular Cavity by Efficient Numerical Techniques". *Computers Mathematics Application*, Vol. 31, No 10, pp. 55-65.
- [6] Ribbens, C.J., Watson, L.T., Wang, C.Y., 1992, "Steady Viscous Flow in a Triangular Cavity", *Journal of Computational Physics*, Vol. 112.
- [7] Sukop, M.C and Thorne, D.T., 2006, *Lattice Boltzmann Modeling : An introduction for geoscientists and engineers*, Springer, New York.
- [8] Nor Azwadi C.S and T, Tanahashi, 2006, "Simplified Thermal Lattice Boltzmann in Incompressible Limit", *International Journal of Modern Physics*, B 20, pp.2437-2449.
- [9] Succi, S., 2001, *The Lattice Boltzmann Equation for fluid dynamics and beyond*, Oxford Science Publications, New York.
- [10] Hou, S., Q., Zou, S., Chen and G., Doolen, 1995, "Simulation of Cavity Flow by the lattice Boltzmann Method", *Journal of Computational Physics*, Vol. 118, pp. 329-347.
- [11] Nor Azwadi C.S and T, Tanahashi, 2007, "Three-Dimensional Thermal Lattice Boltzmann Simulation of Natural Convection in a Cubic Cavity", *International Journal of Modern Physics*, B 21, pp.87-96.
- [12] Bhatnagar, P. L., E. P., Gross, and M., Krook, 1954, "A Model for Collision Processes in Gases. 1. Small Amplitude Processes in Charged and Neutral One-Component System", *Physics Review* 94, pp. 511-525.
- [13] Nor Azwadi C.S and T, Tanahashi, 2008, "Simplified Finite Difference Thermal Lattice Boltzmann Method", *International Journal of Modern Physics*, B 22, pp. 3865-3876.
- [14] Dawson, S.P., S., Chen and G., Doolen, 1993, "Lattice Boltzmann Computations for Reaction-Diffusion Equations", *Journal of Chemical Physics*, Vol. 98, pp. 1514-1523.
- [15] Frish, U., B., Hasslacher, and Y., Pomeau, 1986, "Lattice Gas Automata for the Navier-Stokes Equation", *Physics Review Letter*, Vol. 56, pp. 1505-1508.
- [16] Gladrow, D.W, 2000, "Lattice Gas Cellular Automata and Lattice Boltzmann Models", Springer Verlag, New York.
- [17] He, X. and L.S., Luo, 1997, "Lattice Boltzmann Model for the Incompressible Navier-Stokes Equation", *Journal of Statistical Physics*, Vol. 88, pp.927-944.
- [18] Luo, L.S. and X., He, 1997, "A Priori Derivation of the Lattice Boltzmann Equation", *Physics Review*, E 56, pp. 6811-6817.

# Design and Fabrication of a 200N Thrust Rocket Motor Based on $\text{NH}_4\text{ClO}_4 + \text{Al} + \text{HTPB}$ as Solid Propellant

Mastura Ab Wahid\*, Wan Khairuddin Wan Ali

*Department of Aeronautics, Faculty of Mechanical Engineering,  
Universiti Teknologi Malaysia, 81310 UTM Skudai, Johor, Malaysia.*

*\*mastura@fkm.utm.my*

## ABSTRACT

The development of rocket motor using potassium nitrate, carbon and sulphur mixture has successfully been developed by researchers and students from UTM and recently a new combination for solid propellant is being created. The new solid propellant will combine a composition of Ammonium perchlorate,  $\text{NH}_4\text{ClO}_4$  with aluminium, Al and Hydroxyl Terminated Polybutadiene, HTPB as the binder. It is the aim of this research to design and fabricate a new rocket motor that will produce a thrust of 200N by using this new solid propellant. A static test is done to obtain the thrust produced by the rocket motor and analyses by observation and also calculation will be done. The experiment for the rocket motor is successful but the thrust did not achieve its required thrust.

## 1. INTRODUCTION

There are many rockets that have been manufactured by advanced countries and some of them are, the famous Apollo 13, Discovery, Atlas Centaur and many more. All these rockets use different energy source such as chemical, nuclear and solar. As a developing country, Malaysia also is learning to develop its own technology. Universiti Teknologi Malaysia, UTM, is one of the institutions that is trying to develop rockets using solid propellant. For each composition of propellant there is an optimum configuration for the design of its rocket motor. UTM before this had successfully developed rocket motor using potassium nitrate and sucrose (KS) and now a new composition of solid propellant using Ammonium Perchlorate, ( $\text{NH}_4\text{ClO}_4$ ), Aluminum and HTPB as the binder is being developed. It is only natural that a new rocket motor should be designed and fabricated in order to test this new propellant.

## 2. METHODOLOGY

In order to calculate the design of a rocket motor using ammonium perchlorate (AP) + aluminum (AL) + HTPB, few parameters have to be obtained first. They are the specific impulse, the burning rate which is found from the strand burner test, the composition of the chemicals, the chamber temperature which the burning temperature of the propellant, the molar mass which is obtained from the chemical composition calculation, the total density of the propellant, the molecular mass, the characteristic exhaust velocity and also the exhaust coefficient.

To get this value, software called CHEM is used. This software uses a few basic assumptions to calculate the parameters stated above. One of its assumptions is that the vehicle or rocket exit pressure is equal to the ambient pressure to get the optimum expansion ratio. The chamber pressure is set to be 500psi and the burning time is 3 seconds. The composition of the solid propellant which will be inputted in CHEM is as shown in table 2.1 and the result obtained from CHEM is shown in table 2.2. By using the value in table 2.2, the design dimension can be calculated by applying the rocket motor theory. Table 2.3 shows the final configuration of the rocket motor. Table 2.4 shows the total stress and safety factor for the casing of the rocket motor.

Table 2.1: Composition of the propellant

Chemical	Composition (%)
Ammonium Perchlorate	66
Aluminum (Al)	21
HTPB	13

Table 2.2: Data for rocket motor design

Parameter	Value
Density	1792.55 kg/m <sup>3</sup>
Temperature	3477K
gamma, $\gamma$	1.1887
Molecular weight	13.023 kg/kmol
Specific impulse (Frozen equilibrium)	239.3s
C-star burning rate, $r$	1.016 cm/s

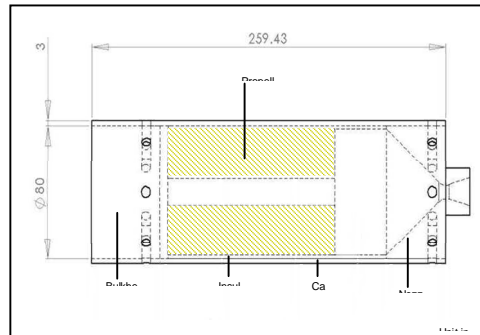


Figure 2.1: Dimension of the rocket motor

Table 2.3: Rocket motor design calculations

Parameters	Value
Coefficient of exhaust, $C_F$	1.478
Exhaust velocity, $c$	2347.66 m/s
Mass flow rate,	0.085 kg/s
Throat area, $A_t$	0.39cm <sup>2</sup>
Exit area, $A_2$	2.13cm <sup>2</sup>
Nozzle area ratio, $\epsilon$	5.46
Throat velocity, $v_t$	1552.8 m/s
Exit velocity, $v_2$	3462.2 m/s
Exit temperature, $T_2$	1969.24 K
Throat mach no	0.956
Exit mach no	2.83

### 3. FABRICATION

In order to fabricate a rocket motor, there are two (2) parts which are the propellant mould and the rocket motor. In the propellant mould, three components will be the machine; they are the propellant mould compressor, base and also core. As for the rocket motor, three components will be machined which are the casing or body, the bulkhead and the nozzle. During machining a tolerance of  $\pm 0.2\text{mm}$  is set as to give tolerance for component matching. Table 3.1 shows the material used for each part.

Table 2.4: Loadings and safety factor

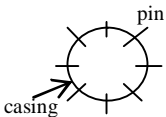
Category	Loading	Safety factor
Casing Material: Mild steel 1018 $\sigma_y = 220\text{MPa}$ $\sigma_u = 400\text{MPa}$	$\sigma_1 = 26.43\text{MPa}$ $\sigma_\theta = 52.86\text{MPa}$ $\sigma_R = 59.10\text{MPa}$	6.77
Pin Material: Stainless steel $\tau_y = 250\text{MPa}$ $\sigma_u = 724\text{MPa}$ $\sigma_y = 276\text{MPa}$	$\tau_{\text{pin}} = 88.34\text{MPa}$	8.2
Continuous joint 8 pins 	$F_{\text{tensile}} = 2.379\text{ kN}$	10.44
	$F_{\text{shear}} = 1.5\text{ kN}$	4.7

Table 3.1: Parts and their material

Category	Material
Rocket motor	
• Nozzle	Mild steel
• Bulkhead	Mild steel
• Insulator	Paper and cardboard
• Casing	Mild steel
Propellant mould	
• Propellant mould compressor	Aluminium
• Base	Aluminium
• Core	Aluminium

The main machining for the rocket motor and also propellant mould compressor is lathing. To create a convergent and divergent section on the nozzle, we used boring method. Figure 3.1 shows machining for the nozzle.



Figure 3.1: Nozzle machining

### 3. EXPERIMENT SETUP

The surface of the rocket motor casing, bulkhead and the nozzle is sanded first before attaching them together so that a smooth flow of air can be achieved. The bulkhead and nozzle is then wrapped with pipe tape to avoid air leakage. A steel tube is then placed inside the insulator with the compressed propellant so that the free surfaces inside the insulator will not burnt out and choke the throat.

After assembling all the components, it is placed on the table for static test. The rocket motor is clamped on the table by using a u-bolt as shown in figure 4.1. The igniter is then placed inside the rocket motor and the connecting wires are connected to the power supply. Then a cage is placed on top of the table to avoid the rocket motor from flying away as in figure 4.2. After checking all parts are engaged and camera has been setup, the vault door is closed and all observers in the lab must be equipped with headphones. Then the igniter is fired up.



Figure 4.1: Rocket motor testing setup



Figure 4.2: Caging of the rocket motor

## 4. RESULT AND DISCUSSION

### 5.1 First test

First test fail. Figure 5.1 shows the result of the first test. When the igniter lit up, the rocket exploded and the casing was detached from the bulkhead and move away. After checking the aftermath of the experiment, there are few reasons why the rocket motor failed. Below are the analyses of failure:



(a)



(b)

Figure 5.1: The outcome from first testing: (a) sheared bolt (b) Remaining insulator

#### a. Structure fault

The bolt of the rocket motor cannot withstand the pressure exerted by the combustion of the propellant. That is why from figure 5.1(a), we can see that the

- i. bolt is sheared due to high pressure.
  - ii. There are air leakages. The casing of the rocket motor is not totally a circular tube therefore there are areas which are air-tight and some are air-leak areas.
- b. Choking
- i. The insulator is made of paper and when it is burnt it traps the flow of the air at the throat. This causes choking and as a result the air inside pushed the bulkhead forward but the escaped air pushed the whole casing backward. Therefore, the high pressure causes the bolt to shear.
  - ii. Figure 5.1(b) shows the final condition of the insulator of burning complete. The crumbs of the paper follow the flame flow and choked the throat.
- c. Propellant temperature
- i. Before testing, the propellant must be cured in an oven. For the first test the propellant is used directly from the oven and inserted inside the rocket motor casing. This causes the initial temperature of the propellant to be high and causes the chamber pressure to increase too.

throat is 16mm and after the crust had envelope the nozzle throat, the throat diameter is reduced to 11mm. This crust was formed due to excess used of aluminium. This may result in choking if the nozzle throat diameter is meant for Mach number 1. In order to avoid the blockage, the throat should be enlarged to about 20 – 30 % from the calculated diameter.

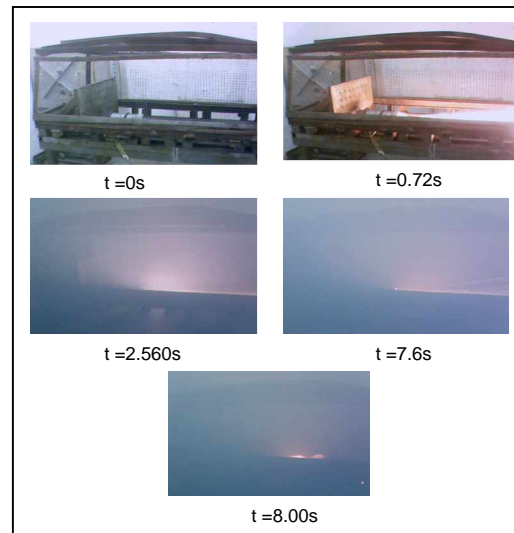


Figure 5.3: Timeline of propellant burning

For the second test, some changes are made to the rocket motor and they are:

- a. The throat diameter is enlarged to 16mm to avoid choking.
- b. The bolt is changed from steel bolt to stainless steel bolt and the diameter from 5mm to 8mm.
- c. Type of bolt is change from normal to countersunk bolt.

### 3.2 Second Test

#### 5.2.1 Observation analysis for the second test

The static test was successful. Figure 5.3 below shows the rocket motor ignition. As shown from figure 5.3, the burning rate obtained from the observation is 7.6s. As can be seen at time,  $t=8.00$  s the flames produced are due to the burning of insulator paper and not the propellant.

Nozzle condition:

As shown in figure 5.4, there is a crust formed on the throat area. This may be also the reason of choking for the first test. The initial diameter of

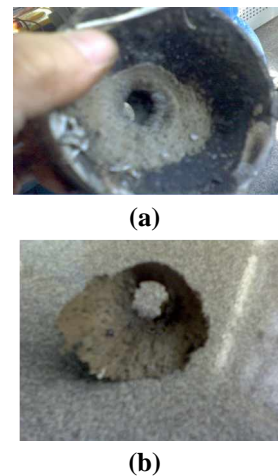


Figure 5.4: Condition inside the nozzle

#### 5.2.2 Numerical Analysis

As mention before the propellant used is less than it supposed to, therefore the performance for the rocket motor can be estimated by back calculations. From the experiment, the value of density of the propellant and the mass flow rate can be obtained. After obtaining these values, the



chamber pressure of the rocket motor is estimated by using CHEM software and an iteration method. The converged value of chamber pressure is taken and the performance of the rocket is recalculated. Table 5.2 shows the calculated estimated performance of the rocket motor.

Table 5.1: CHEM output

Parameter	Value
Density	1434.23 kg/m <sup>3</sup>
Chamber Temperature	3290K
Chamber Pressure (converged value)	194.24 kPa
gamma, $\gamma$	1.1911
Molecular weight	14.93 kg/k-mol
Specific impulse (Frozen equilibrium)	104.1s
C-star	1423.01m/s

Table 5.2: Estimated performance of rocket motor

Parameters	Value
Coefficient of exhaust, CF	0.163
Exhaust velocity, c	231.95 m/s
Mass flow rate,	0.02745 kg/s
Throat area, At	2.011x10 <sup>-4</sup> m <sup>2</sup>
Specific impulse	23.644s
Throat velocity, vt	1411.32 m/s
Throat pressure, Pt	109.981kPa
Throat temperature, Tt	3033.05 K
Throat mach no	0.955
Force	6.37N

From this approximation, it can be seen that the flow at the throat is near to the sonic flow. Since the exit pressure is more than the ambient pressure, the flow is an under-expanding nozzle. This can also be seen from figure 5.3 at time = 0.72 seconds where the flow still expands outside the nozzle. The specific impulse also is less than the value computed by CHEM. This is due to the exit pressure is not equal to the ambient pressure, thus exit velocity is not equal to exhaust velocity.

### 3. CONCLUSION

The objective of the project in terms of fabrication of the rocket motor is achieved even though the thrust required was not met, this is because during testing the rocket motor did not fail. As estimated from the analysis calculation, it is found that the force is much lesser than the 200N therefore the main objective is not met. The time of burning for the rocket motor is about 7.6 s. Thus from this it can be seen that, the solid propellant of ammonium perchlorate and aluminium and HTPB has high

combustion energy even though only 200g of propellant is used instead of 600g.

### ACKNOWLEDGMENTS

I would like to acknowledge my supervisor, Prof. Ir. Dr. Wan Khairuddin b Wan Ali for his patience and guidance. En Mohd Rozi b Perang and En Amir b Aziz for giving me a lot of help in terms of machining and also ideas. I would also like to acknowledge other lecturers in the department for interesting ideas and comments. To technicians of Aero Lab which had spared me some of their time to teach me methods of fabrications and also ideas, I thank you. Finally, to UTM library, thank you for the many books, reports, papers, air-cond etc. that they have provided in giving me the environment to get ideas and knowledge.

### Nomenclature

$\tau_y$	= Yield shear stress
$\sigma_u$	= Ultimate tensile strength
$\sigma_y$	= Yield strength
$F_{tensile}$	= Tensile force
$F_{shear}$	= Shear force
$\gamma$	= Specific Heat Ratio

### REFERENCES

- [1] George P.S, Rocket Propulsion Element: An Introduction To Engineering Rockets, 6<sup>th</sup> Ed, John Wiley & Sons. Inc. (1992)
- [2] Jack D.M, Elements Of Propulsion, AIAA Education Series. (2006)
- [3] Alain D, Solid Rocket Propulsion Technology, Pergamon Press. (1993)
- [4] National Aeronautics and space administration (1970), 'Solid Rocket Motor Cases' journal.

# Development of Ammonium Perchlorate + Aluminium Base Solid Propellant

Norazila Othman<sup>a</sup>, Wan Khairuddin Wan Ali<sup>b</sup>

Department of Aeronautics, Faculty of Mechanical Engineering, Universiti Teknologi Malaysia,  
81310 UTM Skudai, Johor, Malaysia

<sup>a</sup>norazila@fkm.utm.my

<sup>b</sup>wankhai@fkm.utm.my

## ABSTRACT

Rocket propellant has been identified as a component that played an important role in the development of rockets. The ejected material in rocket propulsion is due to material called propellant. Without propellant, a rocket cannot be launched. Due to this reason, many have started to conduct research on new chemical compound of propellant with new technique if needed. The objectives of this study are to study the thermo-chemistry aspect of the composition and to determine the burning characteristics parameters. For this reason, this dissertation presented a detail preparation of developing a solid propellant using Ammonium Perchlorate (AP) as an oxidizer, Aluminum (Al) as fuel and Hydroxyl Terminated Polybutadiene (HTPB) as the binder. To determine the propellant performance such as burning rate, testing was conducted. From testing result the propellant composition oxidizer-fuel (76/11) at pressure 110 Psi gave the maximum burning rate. From test results the empirical constant, 'a' and pressure exponent 'n' were calculated for each different propellant compositions.

### Keywords

*Rockets, solid propellants, AP, Al, HTPB, burning rate, thermo-chemistry, empirical constant, pressure exponent.*

## 1. INTRODUCTION

The design of solid propellant needs to take into account on the composition of the mixture before and after the combustion. This is usually dictated by the total impulse needed. Equation equilibrium is

very important during calculating the heat produced from the reaction, temperature in combustion chamber and determining other characteristics of the propellant, especially when testing the various composition of the compound.

The result from this study will be used to determine the suitability of the propellant compound and the method of processing the compound. From the experimental results, the best propellant performance for any application can be selected which will in turn increase the overall performance of the rocket. These projects also hope to explore the various theories involved in rocketry and to discover the technique and method for preparation and testing of the solid propellant. The difficulty of finding enough information and lacking of a database will hopefully be addressed from this study.

## 2. METHODOLOGY

Theoretical analyses have been conducted on the AP + Al mixture to obtain the chemical formula, characteristic formula, molecular weight, stoichiometric ratio, specific heat gas ratio, reaction equation, characteristic velocity, effective exhaust velocity, and thrust force coefficient. Analyses were done using theoretical calculations and the computer program CHEM.

*Propellants were prepared using the compression method, which was found to be the most suitable method to obtain a more compact propellant. This method enables the removal of almost all of the trapped air inside the propellant grains, leaving only less than five percent behind. The absence of air bubbles would produce a low burning-rate and high mass propellant as desired [3]. An in-house designed and constructed propellant test rig was used for burning-rate tests at atmospheric pressure. The test rig consists of propellant stand, igniter, and automatic timer. From the burning-rate tests at atmospheric pressure, burning-rate data were obtained. In general, propellant performance can be*

approximated from burning-rate data at different pressures.

### 3. THEORITICAL

The products of AP, Al and HTPB reaction was assumed to consist of ten products. During the reaction the assumptions taken were [1]:

- The reaction was only between AP, Al and HTPB.
- CO, H<sub>2</sub>, Al<sub>2</sub>O<sub>3</sub>, N<sub>2</sub>, HCl, H, H<sub>2</sub>O, AlCl, Cl, and CO<sub>2</sub> were assumed the only product of the reaction process. Other components were ignored to simplify the calculation analysis.

The law of conservation of energy states that the enthalpy of the reactants is equal to the enthalpy of the products.

$$\sum_{\text{Reactants}} n_i [h_f + \Delta h]_i = \sum_{\text{Products}} n_e [h_f + \Delta h]_e$$

Burning rate test was conducted to determine the performance of the propellant where it is usually expressed in cm/sec, mm/sec and known as burning rate,  $r$ . The commonly accepted formula to calculate the burning rate is given by [2]:

$$r = ap^n$$

### 4. PROPELLANT FABRICATION

Procedure for the preparation of Ammonium Perchlorate composite propellant (APCP) compound includes the properties and thermo-chemistry characteristic of each ingredient which are AP, Al and HTPB.

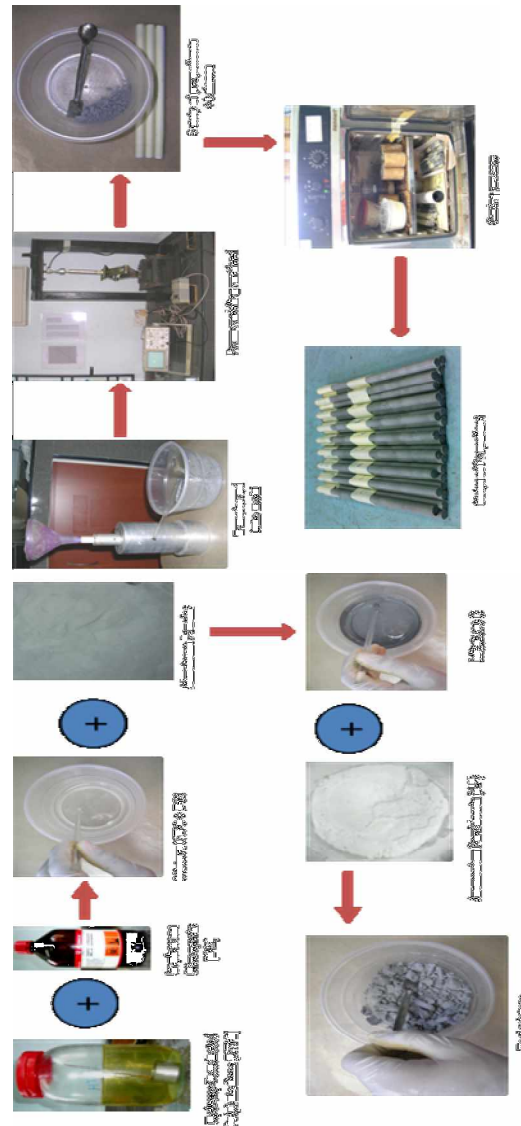


Figure 1: Propellant fabrication

The propellant was pour into the propellant grain mold and compressed. After a uniform propellant compound has been produced, it can then be inserted to the propellant casing. The empty casing which is the mold for the grain is inserted into a cylinder retainer to support the mold when it is subjected to compression forces.

The prepared compound was poured into the casing in a small amount at an each time and was compressed between each pouring using a cylinder rod. When the casing is nearly full, care must be taken to prevent any spillage of the dangerous material. The compression during this stage must be done slowly and carefully. The compression mould method is chosen to produce the propellant variants

since this method produces propellants with a higher density compared to other methods.

### 5. BURNING RATE TESTING

This is a very simple technique and known as Wire Cutting Technique. A small sample of the propellant is burned in a closed firing vessel at a certain constant pressure. Each propellant sample called strand, is in the form of a thin stick. The strand is electrically ignited at one end and the time duration for the strand to burn along its length is measured [2].

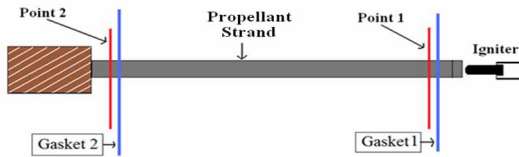


Figure 2: Wire Cutting Technique

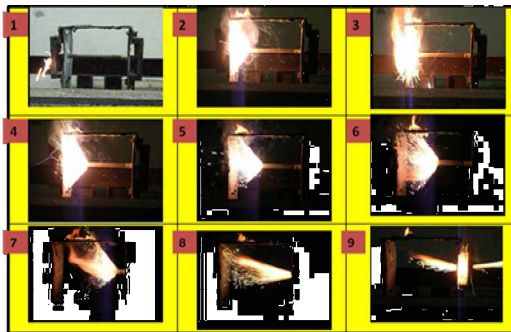


Figure 3: Combustion flame

The strands are usually inhibited along their whole length to ensure that burning only occur perpendicular to the surface. The combustion flame from the solid propellant is brightness due to the fuel that used which is Al and this combustion flame is cigarette type.

### 6. RESULTS AND DISCUSSIONS

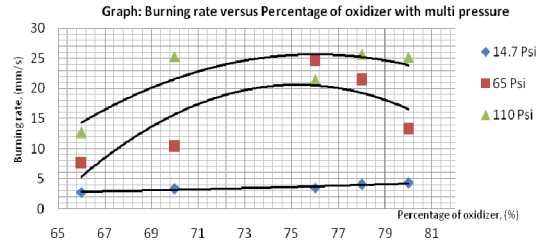


Figure 4: Graph burning rate versus percentage of oxidizer with multi pressure

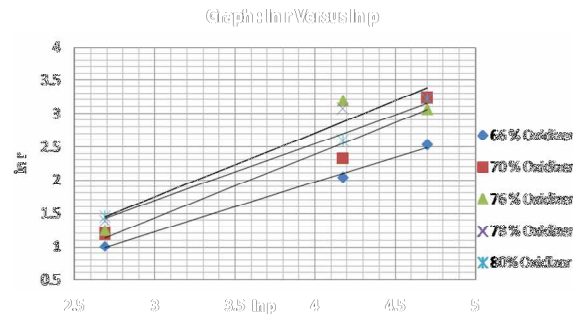


Figure 5: Graph ln r versus ln P

Table 1: Result for 'a' and 'n'

% of Oxidizer	Empirical constant, 'a'	Pressure exponent, 'n'
66	0.9	1.318
70	0.95	0.987
76	1.21	1.112
80	1.2	1.088
78	1.3	1.132

From graph, the propellant composition oxidizer-fuel (76/11) at pressure 110 Psi gave the maximum burning rate. From the theories, the value of 'n' mostly within the range 0.2 - 0.8. Any 'n' values that greater than one shows that the burning rate is highly sensitive to the chamber pressure. For 'n' less than 0.2 or approaching zero, the burning rate test is unstable and if 'n' is less than zero, i.e. negative it shows that the propellant is restartable [1]. Based on the result obtained from this project, the values for n's were greater than one and this shows that the burning rate of these propellants were highly sensitive or influenced by the chamber pressure. Based on the result of 'a' which indicate higher value greater than 1, it is suspected that the initial grain temperature was higher than the room

temperature. It was suggested that in between testing the Crawford bomb should be allowed to cool down to room temperature and less than one lower than room temperature.

The burning rate for each propellant composition was depended on the pressure applied during compression method. Since the pressure applied could vary during compression method, it was advisable to produce three set of samples for each propellant compositions. This will allow three burning rate testing to be carried out for each propellant composition. Averaging can be done on the basis of three samples which will reduce any error [3].

## 7. CONCLUSIONS

The following conclusions can be drawn based on the findings of the study:

1. The thermochemistry study can be determined by using the thermochemical data from JANAF Thermochemical Table.
2. The parameters that influence the burning rate are chamber pressure, particle size of oxidizer, initial temperature of the propellant, and O/F ratio.

## ACKNOWLEDGMENT

Firstly, I would like to express my heartiest appreciation to Prof. Dr. Ir. Wan Khairuddin B. Wan Ali for providing the guidelines before completing this thesis. He is so dedicated for giving me a lot of advices and taught me the methodology for the development of solid propellant.

Lastly, thank you to my college under same supervisor who incessantly shared their information and perception, especially my closed friend Rosmaliza Mat Yaacob and others, such as Mastura, Alif Hafifi, Khairul, Shahrul Ikhwan, Mr. Amir Aziz, a master student and Mr. Mohd Rozi Perang, a Research Officer for sharing their ideas and suggestions that helped me so much to complete this thesis.

## REFERENCES

- [1] Naminosuke Kubota, (2007), *Propellants and Explosives*, 2<sup>nd</sup> Edition, Wiley-VCH
- [2] Sutton, G.P and Oscar Biblarz, 7<sup>th</sup> Ed. (2001), *Rocket Propulsion Element*, John Wiley & Sons, MIT.
- [3] Rizalman Mamat (2002), *Ciri-ciri Propelan Roket Pepejal Berasaskan Kalium*, Universiti Teknologi Malaysia, Tesis sarjana.



# Reduction of Time Consumption For Simulating Lid-Driven Cavity Flow Using Lattice Boltzmann Method (LBM)

H. M. Faizal<sup>a</sup>, C. S. Nor Azwadi<sup>b</sup>

<sup>a</sup>Faculty of Mechanical Engineering,  
Universiti Teknologi Malaysia,  
81310 UTM Skudai, Johor, Malaysia  
mfaizalhasan@gmail.com

<sup>b</sup>Faculty of Mechanical Engineering,  
Universiti Teknologi Malaysia,  
81310 UTM Skudai, Johor, Malaysia  
azwadi@gmail.com

## ABSTRACT

2-D driven cavity flow is the widely studied benchmark problem by many researchers of computational fluid dynamics field in terms of accuracy, numerical efficiency and others. Lattice Boltzmann Method (LBM) is one of the numerical methods for simulating this type of flow. For solving cavity flow with high Reynolds Number, the saving in time consumption is really appreciated. Therefore, as the initial study, averaging method for reducing CPU time has been proposed for solving lid driven cavity flow with low Reynolds Number. The results show that the averaging method can save time consumed for simulation. For instance, in the case of Reynolds Number 80, the proposed averaging method can save about 12% of the original CPU time (without averaging method).

## Keywords

*lid driven cavity, Lattice Boltzmann Method, averaging method*

## 1. INTRODUCTION

The simplicity of the geometry makes the lid driven cavity flow problem is one of the most studied fluid problems by researchers. In addition, it is easy to code and easy to apply boundary conditions. Even though the problem looks simple in many ways, the flow in a cavity retains all the flow physics with counter rotating vortices appear at the corners of the cavity.

There are many researchers already made their researches on the lid-driven cavity flow with high Reynolds Number. For instance, Erturk et. al., Erturk & Gokcol, Barragy & Carey, Schreiber &

Keller, Benjamin & Denny, Liao & Zhu, Ghia et. al. have presented solutions of steady 2-D incompressible flow in a driven cavity for Re 10,000. Among these researchers, Barragy & Carey have also presented solutions for Re=12,500. Moreover, Erturk et. al. and also Erturk & Gokcol have presented steady solutions up to Re=20,000 [2].

The above studies are all numerical studies. There are very few experimental studies in the literature on the driven cavity flow. Koseff & Street, Prasad & Koseff have done several experiments on three dimensional driven cavity with various spanwise aspect ratios (SAR). These experimental studies present valuable information about the physics of the flow in a driven cavity.

A simulation of incompressible viscous flow within a two-dimensional (2D) square cavity by using Lattice Boltzmann method (LBM) had been done by Arumuga D. P. et. al with variety of Reynolds numbers [1]. The samples of result from their simulation are shown as below.

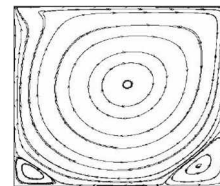


Figure 1. Re 1000

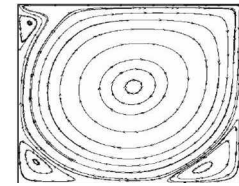


Figure 2. Re 3200

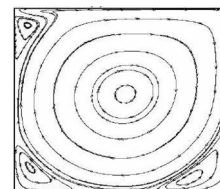


Figure 3. Re 5000

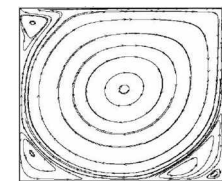


Figure 4. Re 7500

Based on previous explanation, we know that the study on the flow of lid-driven is very important. However, time consumption need to be reduced especially when solving the flow with high Reynolds number. Because of that, in this project, the method to reduce CPU time is introduced and the test had been done on the flow with low Reynolds Number.

## 2. GOVERNING EQUATIONS FOR INCOMPRESSIBLE LATTICE BOLTZMANN MODEL

Incompressible Lattice Boltzmann model was derived by discretizing the continuous Boltzmann transport equation

$$\frac{\partial f}{\partial t} + c \frac{\partial f}{\partial x} = \Omega(f) \tag{1}$$

Where the density distribution function  $f = f(x_i)$  used to simulate the density and velocity fields, is the microscopic velocity, and  $\Omega$  is Bhatnagar-Gross-Crook collision model.

In this case, collision term is very complicated and needs to be simplified in practical calculations. One of the simplification methods is by replacing the collision term with single relaxation time BGK model.

$$\frac{\partial f}{\partial t} + c \frac{\partial f}{\partial x} = \frac{1}{\tau} (f^{eq} - f) \tag{2}$$

Here

$$\Omega(f) = \frac{1}{\tau} (f^{eq} - f)$$

Equation (2) is known as the evolution equation of the density distribution function. Then, the equilibrium distribution function is discretised and is defined as;

$$f_i^{eq} = \rho w_i \left[ 1 + 3(c_i \cdot u) + \frac{9}{2}(c_i \cdot u)^2 - \frac{3}{2}u^2 \right] \tag{4}$$

The value of  $w_i$  which exists in the above equations depends on the direction of the microscopic velocity of the particle distribution function. In this study, nine velocity model is used. Therefore, the value of  $w_i$  are

$$w_1 = 4/9, w_{2,4,6,8} = 1/9, w_{3,5,7,9} = 1/9$$

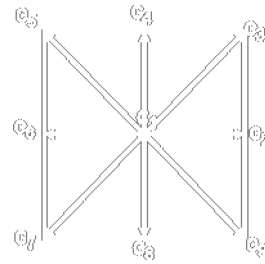


Figure 5.9 velocity model

Then, the macroscopic variables can be evaluated as the moment to the distribution function as follow;

$$\rho = \int f dc \tag{5}$$

$$\rho u = \int c f dc \tag{6}$$

Then, when the Chapman-Enskog expansion is applied, the above equations can lead to the macroscopic continuity and momentum.

$$\nabla \cdot \bar{u} = 0 \tag{7}$$

$$\partial_t \bar{u} + (\bar{u} \cdot \nabla) \bar{u} = -\frac{1}{\rho_0} \nabla p + \nu \nabla^2 \bar{u} \tag{8}$$

The viscosity  $\nu$ , for D1Q9 is related to the time relaxation as follow

$$\nu = \frac{2\tau - 1}{6} \tag{9}$$

or

$$\tau = 3\nu + 0.5 \tag{10}$$

“Averaging” method can be applied at certain area in lid driven cavity. Based on the literature (refer to Figure 1 to Figure 4), the center area of lid driven cavity is considered not critical in term of vortex formation. It is found that counter rotating vortices appear at the corners of the cavity at various Reynolds Number, Re. Therefore, in this project, center area is focused to apply the averaging method. We assume that the velocity changes, either x or y-direction are very small when the particle move to the next node in this center area.

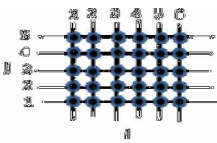
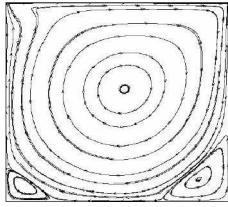


Figure 6. Before modification

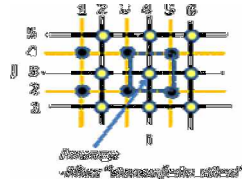


Figure 7. After modification

For averaging method, the formula is given as below.

$$f(k,i,j) = (f(k,i-1,j-1) + f(k,i+1,j+1) + f(k,i-1,j+1) + f(k,i+1,j-1)) / 4$$

where  $k$  is direction,  $i$  is coordinate at x-direction and  $j$  is coordinate at y-direction.

## 2. ALGROTIHMS

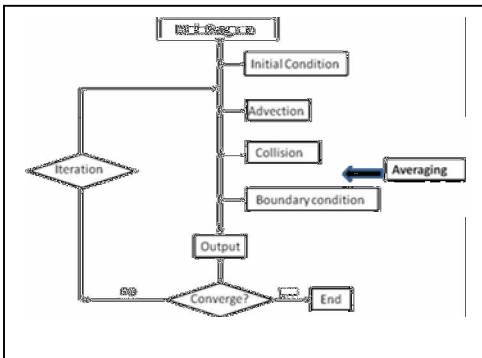


Figure 8. Simulation Algorithm When “Averaging” Method Included

“Averaging” method is utilized between “collision” and “boundary condition”. The nodes with the average value of density distribution function will be used to the next procedure until convergence consideration. If converge, the data of these nodes are used as simulation results. If the simulation does not converge yet, the data of these nodes will be used for the next iterations.

## 3. SIMULATION PARAMETER

The configuration of the cavity flow consists of a 2-D square cavity which top plate moves from left to right direction with a uniform velocity. Meanwhile, the other walls are fixed. The velocity components  $u_x$  and  $u_y$  are in x and y-direction respectively. In

this study, the simulation is done on 32 x 32 lattice units. Initially, the velocity at all nodes, except the top plate, is set to zero. The x-velocity of the top plate is  $U=0.1$  and the y-velocity is zero. Uniform fluid density is used, which 1.0 and is imposed initially. The equilibrium distribution is calculated using Equation (4) and  $f_i$  is set equal to  $f_i^{(0)}$  for all

node at  $t=0$ . The distribution function can be found by a succession of propagation and collision processes. Then, “averaging” method is applied to the center area (bounded with four edges point: (9,11), (9,25), (25,11) and (25,25)). By utilizing this method, the CPU time until equilibrium is achieved can be reduced slightly. At the end of each process, the distribution function is set to equilibrium state. In this simulation, no slip velocity condition is implemented and bounce-back boundary condition is used on all the walls. When a fluid particle encounters an object such as wall or other particles, the collision occurs and the fluid particle is simple rebounded off the object in the direction it originated. This phenomenon is called bounce-back boundary condition. The velocity components are obtained through the calculation of particle distribution function. This simulation is validated with previous study which has been done by Ghia for Reynolds Number 100. Meanwhile, the reduction of time consumption is calculated for the case of Reynolds Number 100 and 80 by comparing it with the results obtained from algorithm without “averaging” method.

## 4. RESULTS AND DISCUSSION

### 5.1 Validation of Results

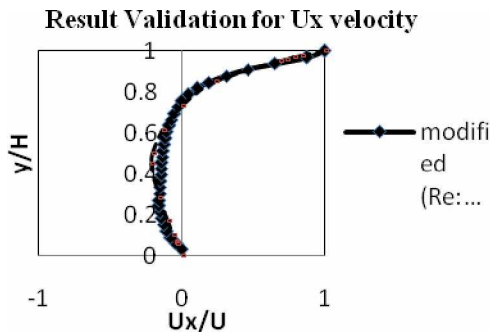


Figure 9. Result Validation for Ux velocity

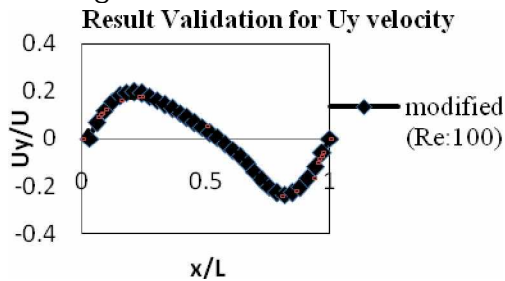


Figure 10. Result Validation for Uy velocity

From the Figure 9 above, the x-velocity obtained from the modified case (using “Averaging” method) shows much agreement with the result by Ghia (1982) except for certain locations (from  $y/H:0.3$  to  $y/H:0.7$ ) which show slightly different.

Based on Figure 10, the y-velocity obtained from modified case shows much agreement with the result from Ghia (1982). All the points seems overlap to each other except at about  $x/L : 0.2$  to  $x/L : 0.3$ . This shows that “averaging” method is suitable for simulation especially for low Reynolds Number, Re. However, for simulating the high Re, further study is necessary in order to ensure that this “averaging” method able to produce accurate result even though at disorganized or chaotic flow.

### 5.2 Reduction of Time Consumption

Figure 11 and Figure 12 show patterns of plot which are almost same for both cases (original case and modified case). In addition, the CPU time can be saved until almost 21%.

Based on Figure 14, the plot pattern for both cases (before and after modification) show the similar

shape. Besides that, based on Figure 15, the value of x-velocity for modified case is also slightly different if compared with the value for original case. When Reynolds Number increased becomes higher, the difference between plots for both cases clearly can be observed especially for x-velocity. Due to the matters, it is expected the increase in mesh number may give more accurate result. As information, the reduction of time consumption for Reynolds Number 80 is about 12%.

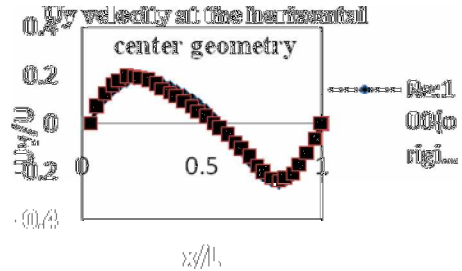


Figure 11. Result for Ux velocity

Table 13. CPU time for Before and After For Re 100

Before [CPU time]	After [CPU time]	Improvement[%]
168.1379	133.2841	20.72930018

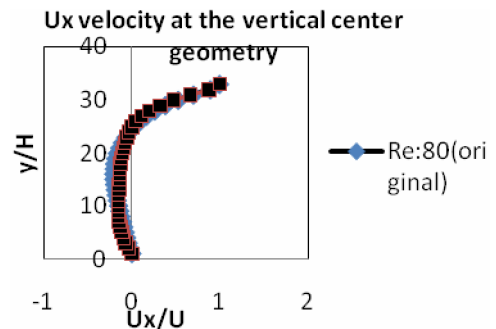


Figure 14. Result for Ux velocity

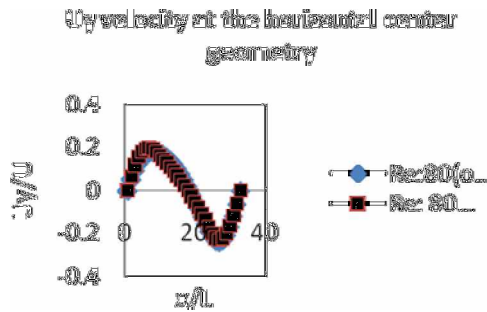


Figure 15. Result for  $U_y$  velocity

Table 16. CPU time for Before and After Modification

For Re 80

Before [CPU time]	After [CPU time]	Improvement [%]
119.4188	105.2695	11.84846942

## 5. CONCLUSION

“Averaging” method has been used to simulate the lid-driven cavity with low Reynolds Number,  $Re$ . It seems very effective in reducing the time consumption especially for low  $Re$ . When  $Re$  becomes higher, the difference of result appears if compared between the modified case and original case. It is expected that these differences can be reduced by increasing the mesh used in simulation.

Finally, future works are still needed to ensure that Lattice Boltzmann Method (LBM) can simulate the lid-driven cavity flow with high Reynolds Number accurately.

## ACKNOWLEDGMENTS

The authors acknowledge the Universiti Teknologi Malaysia for giving cooperation and full of support in this research activity.

## NOMENCLATURE

$y$	Location in y-axis	$Re$	Reynolds Number
$x$	Location in x-axis	$U_x$	Velocity in x-direction
$L$	Total length in x-direction	$U_y$	Velocity in y-direction
$H$	Total height in y-direction	$\rho$	Fluid Density
$U$	x-velocity of top plate		

## References

- [1] Arumuga, D. P., Anoop K. D.. “Incompressible Viscous Flow Simulation in the Lid-Driven Cavity by Lattice Boltzmann Method”, Indian Institute of Technology Guwahati.
- [2] Ercan Erturk [2008]. “Discussion on Driven Cavity Flow”, Int. Journal for Numerical Methods in Fluids (2008)
- [3] Albensoeder, S., Kuhlmann, H.C.[2005]. “Accurate three-dimensional lid-driven cavity flow”, *Journal of Computational Physics* 206, 536–558.
- [4] Abouhamza, A., Pierre, R. [2003]. “A Neutral Stability Curve for Incompressible Flows in a Rectangular Driven Cavity”, *Mathematical and Computer Modelling* 38, 141-157.
- [5] Nor Azwadi Bin Che Sidik [2007]. “The Development of Simplified Thermal Lattice Boltzmann Models for the Simulation of Thermal Fluid Flow Problems”, PhD Thesis 2007.
- [6] H.M. Faizal, C.S.N. Azwadi [2008]. “Initial Study on Flow Behaviour Around Four Circular Cylinders with Different Reynolds Number by Using Lattice Boltzmann Scheme”, International Graduate Conference on Engineering and Science 2008.



# Preliminary Numerical Analysis on Helicopter Main-Rotor-Hub Assembly Wake

Iskandar Shah Ishak<sup>a</sup>, Shuhaimi Mansor<sup>a</sup>,  
Tholudin Mat Lazim<sup>a</sup> and Muhammad Riza Abd Rahman<sup>a</sup>

<sup>a</sup>Department of Aeronautical Engineering  
Faculty of Mechanical Engineering  
Universiti Teknologi Malaysia  
81300 Skudai, Johor, Malaysia  
\*shah@mail.fkm.utm.my

## ABSTRACT

This research aims to improve basic understanding of the viscous unsteady flow observed behind the helicopter main-rotor-hub-assembly which may lead to helicopter tail shake phenomenon. The numerical study was done at a grace of a commercial Computational Fluid Dynamics (CFD) code, FLUENT on a simplified main-rotor-hub assembly using stub blades. In this study, the aerodynamic flow field was computed using the Reynolds-Averaged Navier-Stokes (RANS) equations. The Multiple Reference Frames (MRF) method was applied to simulate the main-rotor-hub-assembly rotation at 1400 rpm with free stream velocity, or forward flight speed of 5, 20 and 30 m/s at zero angle of attack, respectively. Results depict at higher free stream velocity more pressure fluctuations, which could translate to bigger aerodynamic forces excitation, occurred at the vicinity of helicopter tail plane.

### Keywords

*Unsteady flow, helicopter tail shake phenomenon, Computational Fluid Dynamic*

## 1. INTRODUCTION

Helicopter tail shake phenomenon is a long dragged issue that adversely affected the overall performance, occupants' comfort and handling qualities of helicopter. It is an interaction of a turbulent wake with the structure part of tail [1]. The contributors of the wake, not the least, are main-rotor-hub assembly, pylon, engine intakes and exhausts. In this research, focus will be on main-rotor-hub assembly's wake as it is believed to be the major contributor of the problem [2]. This allows the simulation to be conducted using blade-stubs configuration [3,4,5]. Blade-stubs configuration is a combination of main-rotor-hub assembly with shorter rotor blades.

## 2. CFD MODELLING DESCRIPTIONS

Reynolds-Averaged Navier-Stokes (RANS) equation models which solve ensemble-averaged Navier-Stokes equations [6] were used for this computational fluid dynamic study. The simulations were run at a grace of a 64-bit Core 2 Quad computer with Multiple Reference Frames (MRF) approach was applied to simulate the main-rotor-hub-assembly rotation at 1400 rpm.

This numerical investigation used an ellipsoidal fuselage based on NASA standard model [7] with the axes ratio of longitudinal to lateral axes is 4.485. For this research work, the longitudinal axes were taken as 1120 mm. A simplified main-rotor-hub assembly with short rotor blades were designed and is shown by Fig. 1.



Fig. 1 Model for CFD analysis

## 3. RESULTS ANALYSIS

All simulation results presented throughout this paper were run at main-rotor-hub assembly rotation of 1400 rpm with zero angle of attack. Figures 2 and 3 show the path lines of turbulent intensity for 20 and 30 m/s of free stream velocity, respectively. They depict the maximum value of turbulent intensity (%) becomes higher with the increment of free stream velocity, or forward flight speed. This is reasonable as higher free stream velocity should

cause more flow unsteadiness for the same main rotor rpm.

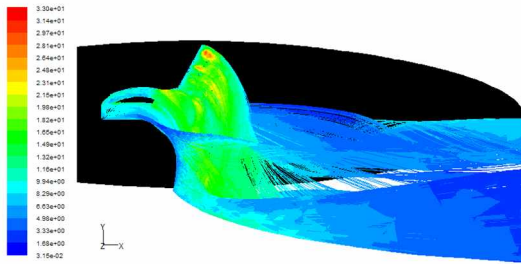


Fig.2(a) Path lines from 'main-rotor-hub assembly' (top view)

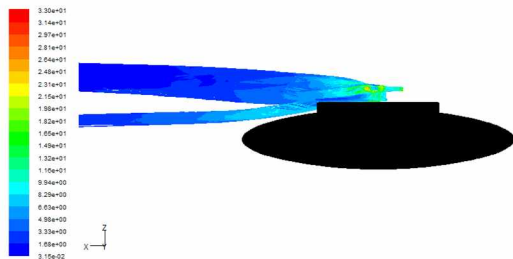


Fig.2(b) Path lines from 'main-rotor-hub assembly' (side view)

Fig. 2 Path lines coloured by turbulent intensity (%) at 20 m/s

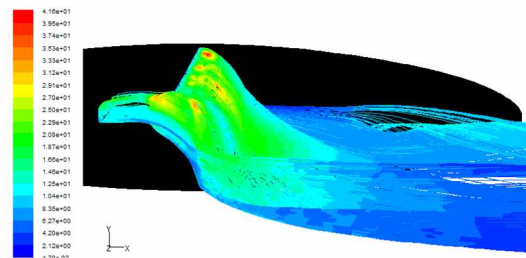


Fig.3(a) Path lines from 'main-rotor-hub assembly' (top view)

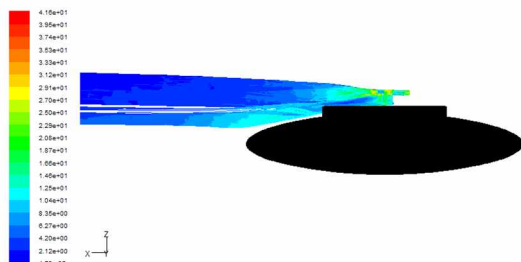


Fig.3(b) Path lines from 'main-rotor-hub assembly' (side view)

Fig. 3 Path lines coloured by turbulent intensity (%) at 30 m/s

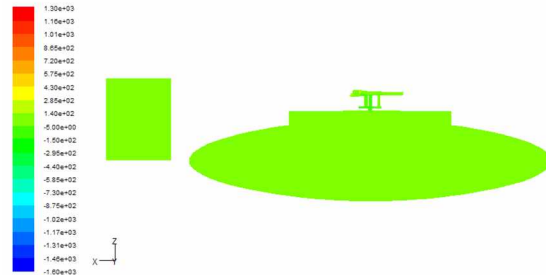


Fig. 4(a) Free stream velocity at 5 m/s

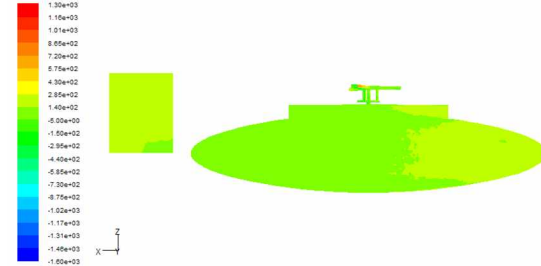


Fig. 4(b) Free stream velocity at 20 m/s

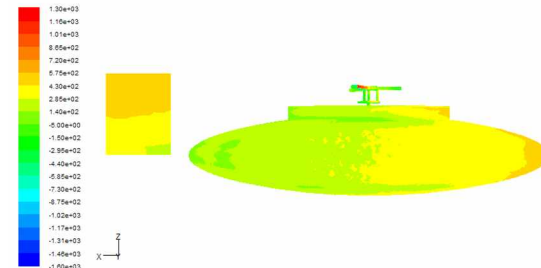


Fig. 4(c) Free stream velocity at 30 m/s

Fig. 4 Contours of total pressure (Pa)

Figure 4 translates the fluctuation of total pressure at the vicinity of vertical tail i.e. 'vertical-tail-plane', is becoming more with the increment of free stream velocity. Table 1 summarizes the maximum and minimum values of total pressure inside this 'vertical-tail-plane'.

Table 1 Total pressure (Pa) in 'vertical-tail-plane'

V (m/s)	Total Pressure (Pa)		$\Delta$ Facet (Pa)
	Facet Max.	Facet Min.	
5	13.82	1.36	12.46
20	226.76	64.79	161.97
30	508.73	158.99	349.74

Table 1 indicates the range from minimum to maximum value of total pressure i.e.  $\Delta$  Facet, is linearly related with free stream velocity. This result translates more aerodynamic forces excitation occurred with higher forward flight, signalling could mean more tail shake problem.

### 3. CONCLUSIONS

This preliminary numerical study has shown some interesting wake characteristics on helicopter tail shake phenomenon. At a very low free stream velocity or forward flight speed, the total pressure fluctuation inside the vicinity of tail plane is found to be significantly small. This could be the low energy of free stream is not adequate enough to 'blow' the highly unsteady wake of main-rotor-hub assembly towards the tail plane. Nevertheless, it does not necessarily mean higher forward flight velocity will always trigger higher pressure fluctuation as the very high energy free stream might somehow 'soother' the wake in the vicinity of tail plane. Hence, further investigation is much required to be done to have a more comprehensive understanding of this helicopter tail shake phenomenon.

### ACKNOWLEDGMENTS

Authors like to thank Muhammad Khaidhir Bin Jamil from Universiti Teknologi Malaysia for his initial help of this project.

### REFERENCES

- [1] P.G. de Waad and M. Trouvé, May 1999, "Tail shake vibration, National Aerospace Laboratory (NLR)", American Helicopter Society Annual Forum.
- [2] C. Castellin, 2007, *Email Conversation*, Eurocopter ETAGA Aerodynamic Team.
- [3] A. Cassier, R. Weneckers and J-M Pouradier, May 1994, "Aerodynamic development of the tiger helicopter", 50th American Helicopter Society Forum.
- [4] C. Hermans et al., 1997, "The NH90 helicopter development wind tunnel programme", European Aerospace Societies Conference, Cambridge UK.
- [5] Eurocopter, 2006, "Eurocopter Slide Presentation", France.
- [6] March 2005, "Introductory FLUENT Notes" , FLUENT V6.2.
- [7] P.F. Lorber, T.A. Egolf, 1988, "An Unsteady Helicopter Rotor-Fuselage Interaction Analysis", NASA Contractor Report 4178.

# Virtual Investigation of Free Convection from Concentric Annulus Cylinder by the Finite Difference Lattice Boltzmann Method

O.Shahrul Azmir<sup>a</sup>, C. S. Nor Azwadi<sup>b</sup>

<sup>a</sup>*Faculty of Mechanical & Manufacturing Engineering,  
Department of Plant and Automotive,  
Universiti Tun Hussien Onn Malaysia (UTHM),  
86400 Parit Raja, Batu Pahat Johor,  
shahrula@uthm.edu.my*

<sup>b</sup>*Faculty of Mechanical & Manufacturing Engineering,  
Department of Thermo-Fluid,  
Universiti Teknologi Malaysia (UTM),  
81310 Skudai, Johor,  
azwadi@fkm.utm.my*

## ABSTRACT

This paper presents numerical study of flow behavior from a heated concentric annulus cylinder at various Rayleigh number  $Ra$ , Prandtl number  $Pr$  while the aspect ratio is fixed to 5.0 of the outer and inner cylinders. The Finite Different Lattice Boltzmann Method (FDLBM) numerical scheme is proposed to improve the computational efficiency and numerical stability of the conventional method. The proposed FELBM applied UTOPIA approach (third order accuracy in space) to study the temperature distribution and the vortex formation in the annulus cylinder. The comparison of the flow pattern and temperature distribution for every case via streamline, vortices and temperature distribution contour with published paper in literature were carried out for the validation purposes. Current investigation concluded that the UTOPIA FDLBM is an efficient approach for the current problem in hand and good agreement with the benchmark solution.

## Keywords

*UTOPIA, Free convection, finite difference, lattice Boltzmann, concentric cylinder*

## 1. INTRODUCTION

Free convection or known as “natural convection” in an annulus concentric cylinder has been extensively investigated due to the variety of technical applications and practicality such as heat transfer in thermal storage system, electrical transmission cables (Nor Azwadi and Tanahashi, 2007), heat exchanger (Inamuro, Yoshino and

Ogino, 1995), etc. Among the problems related to free convection, many researchers focused their investigation on the heat transfer and fluid flow behavior from differentially heated walls in a square or cubic cavity (Rohde, Kandhai, Derksen and Akker, 2003)(Jami, Mezrhab, Bouzidi and Lallemand, 2006). However, the heat transfer mechanism and fluid flow behavior in a concentric annulus cylinder are strongly depended on the aspect ratio which is defined as a ratio of the diameter of the outer to the inner cylinder. The temperature different between the heated inner cylinder and cold outer cylinder contributes the density gradient and circulate the fluid in the annulus (Nor Azwadi and Tanahashi, 2007). The next important dimensionless parameters are the Rayleigh and Prandtl numbers, which affect the heat transfer mechanism, the flow pattern and the stability of the transitions of flow in the system.

The lattice Boltzmann method (LBM), a mesoscale numerical method that will be used in present study, is an alternative computational approach to predict wide range of macroscale heat transfer and fluid flow behaviour (Shan, 1997). Moreover, LBM is considerably as a well-known approach for the finite difference, finite element and finite volume techniques for solving the Navier-Stoke equations. LBM has been used for nearly a decade due to its simplicity and easy implementation. Due to its ability to incorporate particles interactions at the microscopic level, LBM fits for simulation the behavior of complex flow system (He, Zou, Lou and Dembo 1997), turbulent (Jonas, Chopard, Succi and Toschi, 2000), multiphase (McNamara and Alder, 1993),

and others (Mezrhab, Jami, Abid, Bouzidi and Lallemand, 2006) (Azwadi and Tanahashi, 2006).

In the finite different formulation of LBM, the governing equations are discretized in the space and time and solved using third order accuracy scheme (UTOPIA). There are many other discretization methods proposed earlier in the literature. However, due to the hyperbolic nature of the Boltzmann equation, the UTOPIA scheme is the best choice due to its high accuracy and flexible boundary treatment (Nor Azwadi, 2009).

This paper is organized as follows. Section two briefly describes the formulation of lattice Boltzmann method and the combination of UTOPIA finite difference lattice Boltzmann (FDLBM) simulation. The specification of the problem will be discussed in section three while the section four are discussed the computational results will be discussed by comparing with the available results in the literature. The final section concludes current study.

## 2. NUMERICAL METHOD

### 2.1 Lattice Boltzmann method

The governing equation of two dimensions lattice Boltzmann scheme, discretized in space and time, can be represented as follows

$$\frac{\partial f_i}{\partial t} + c_i \cdot \nabla f_i = \Omega(f_i) + F \quad (1)$$

$$\frac{\partial g_i}{\partial t} + c_i \cdot \nabla g_i = \Omega(g_i) \quad (2)$$

where  $f$  is the particle distribution function with constant velocity  $c$  at position  $x$  and  $\Omega$  is the collision integral. Distribution function  $f$  and  $g$  are used to calculate the velocity and temperature fields and  $F$  is the external force. However, we can replace the collision integral in Eqs. (1) and (2) with the most well accepted BGK collision model version due to its simplicity and efficiency of the model (Nor Azwadi and Tanahashi, 2006). The equations that represent this model can be written as

$$\Omega(f) = -\frac{1}{\tau_f} [f_i - f_i^{eq}] \quad (3)$$

$$\Omega(g) = -\frac{1}{\tau_g} [g_i - g_i^{eq}] \quad (4)$$

where  $f^{eq}$  and  $g^{eq}$  are the equilibrium distribution functions.  $\tau_f$  and  $\tau_g$  are the time to achieve the equilibrium condition during the collision process and often called as the time relaxation for momentum and energy respectively. The BGK collision model describes that  $1/\tau$  of the non-equilibrium distribution function relaxes to the equilibrium state within time  $\tau$  during every collision process. By substituting Eqs. (3) and (4) into Eqs. (1) and (2), the so-called lattice Boltzmann BGK equation is obtained and can be written as follows

$$\frac{\partial f_i}{\partial t} + c_i \cdot \nabla f_i = -\frac{1}{\tau_f} [f_i - f_i^{eq}] + F \quad (5)$$

$$\frac{\partial g_i}{\partial t} + c_i \cdot \nabla g_i = -\frac{1}{\tau_g} [g_i - g_i^{eq}] \quad (6)$$

Eqs. (5) and (6) describe two main processes in the LBM formulation. The left hand side is the propagation process refers to the propagation of the distribution function to the neighbor nodes in the direction of its velocity and the right hand side describes the collision process of the particles distribution function. The general form of the lattice velocity model is expressed as DnQm where D represents the spatial dimension and Q is the number of connection (lattice velocity) at each node (Jonas, Chopard, Succi and Toschi, 2006).

In present study, the D2Q9 and D2Q4 are chosen due to its efficiency and flexibility for boundary treatment. The microscopic velocity components for this model can be simplified as

$$c_i = \begin{bmatrix} 0 & 1 & 0 & -1 & 0 & 1 & -1 & -1 & 1 \\ 0 & 0 & 1 & 0 & -1 & 1 & 1 & -1 & -1 \end{bmatrix} \quad (7)$$

for D2Q9

$$c_i = \begin{bmatrix} 1 & -1 & -1 & 1 \\ 1 & 1 & -1 & -1 \end{bmatrix} \text{ for D2Q4} \quad (8)$$

$c_i$  in LBM is set up so that in each time step  $\Delta t$ , every distribution function propagates in a distance of lattice node spacing  $\Delta x$ . This will ensure that the distribution function arrives exactly at the lattice node after  $\Delta t$  and collide simultaneously.



The equilibrium distribution function of the D2Q9 and D2Q4 models are expressed as follow (Nor Azwadi and Tanahashi, 2006)

$$f_i^{eq} = \rho \omega_i \left[ 1 + 3(c_i \cdot u) + \frac{3}{2}(c_i \cdot u)^2 - \frac{3}{2}u^2 \right] \quad (9)$$

$$g_i^{eq} = \frac{1}{2} \rho T [1 + 3(c_i \cdot u)] \quad (10)$$

respectively and the value of weights are depend on the microscopic velocity direction

The macroscopic density  $\rho$ , velocity  $u$  and temperature  $T$  are defined from the velocity moments of distribution function and can be calculated as follow

$$\rho = \sum_{i=0}^8 f_i \quad (10)$$

$$\rho u = \sum_{i=0}^8 c_i f_i \quad (11)$$

$$\rho T = \sum_{i=0}^8 c_i g_i \quad (12)$$

and the pressure is related to density via  $p = \frac{1}{c_s^2}$  where in lattice Boltzmann formulation,  $c_s$  is taken as  $\frac{1}{\sqrt{3}}$

The macroscopic equation can be obtained via the Chapman-Enskog expansion. The details of the derivation can be seen in (Azwadi and Tanahashi, 2006) and will not be shown here. By comparing the obtained macroscopic equations with the Navier-Stoke equation derived from Newton's law, the time relaxations  $\tau$  can be related to fluid viscosity  $\nu$  and thermal diffusivity  $\chi$  as follow

$$\tau_f = 3\nu \quad (13)$$

$$\tau_g = \chi \quad (14)$$

respectively.

### 2.2 Finite Difference Lattice Boltzmann Method

In the finite difference formulation of LBM, the governing equations are further discretize in phase space and time and solve using one of the several available methods in finite difference numerical

scheme. In present study, we choose explicit discretisation in time as follow

$$f_i^{n+1} - f_i^n + \Delta t(c_i \cdot \nabla f) = \frac{\Delta t}{\tau_f} [(f_i - f_i^{eq})] + \Delta t F \quad (15)$$

The most common finite difference discretisation scheme that normally used by the researchers is the second order accuracy of upwind scheme. However, in this paper, we applied the third order accuracy of upwind scheme (UTOPIA) for spatial discretisation in order to generate more accurate results. The UTOPIA scheme in  $x$ - and  $y$ -directions are expressed as follow

$$\left( c_x \frac{\partial f}{\partial x} \right)_i = \begin{cases} c_x \frac{f_{i-2} - 2f_{i-1} + 9f_i - 10f_{i+1} + 2f_{i+2}}{6\Delta x} & c_x \geq 0 \\ c_x \frac{-f_{i-2} + 2f_{i-1} - 9f_i + 10f_{i+1} - 2f_{i+2}}{6\Delta x} & c_x \leq 0 \end{cases} \quad (16)$$

$$\left( c_y \frac{\partial f}{\partial y} \right)_i = \begin{cases} c_y \frac{f_{j+2} - 2f_{j+1} + 9f_j - 10f_{j-1} + 2f_{j-2}}{6\Delta y} & c_y \geq 0 \\ c_y \frac{-f_{j+2} + 2f_{j+1} - 9f_j + 10f_{j-1} - 2f_{j-2}}{6\Delta y} & c_y \leq 0 \end{cases} \quad (17)$$

### 3. SPECIFICATION OF THE PROBLEM

For this problem, flow inside an annulus cylinder was investigated numerically. Figure 1 shows the geometry of the heated annulus cylinder enclosure. The boundaries are made stationary for outer cylinder and inner cylinder and no velocity are applied and are set to zero.

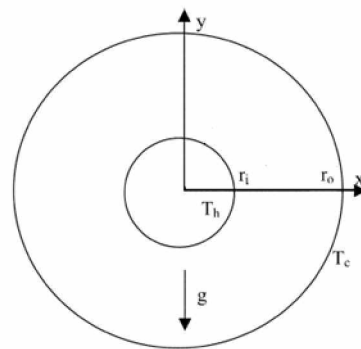


Figure 1: Free convection heat transfer in concentric annulus cylinder

where  $g$  is the gravitational acceleration and  $T_c$  and  $T_h$  are the constant temperatures of the outer and inner cylinder respectively. Two non-dimensional parameters; the Prandtl number  $Pr$ , and the Rayleigh number  $Ra$ , for heat transfer

behaviour of this problem are characterized and defined as

$$Pr = \frac{\nu}{\chi} \quad (18)$$

$$Ra = \frac{\rho\beta(T_h - T_c)L^3}{\nu\chi} \quad (19)$$

where  $\nu$  is the fluid kinematic viscosity,  $\chi$  is the thermal diffusivity and  $L = r_o - r_i$  is the characteristic length. The values of the Rayleigh number used for this study are  $10^3$ ,  $10^4$  and  $10^5$  while the grid length is set to be  $101 \times 101$ ,  $151 \times 151$  and  $201 \times 201$  respectively.

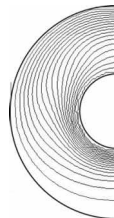
#### 4. RESULTS AND DISCUSSION

In this section, the numerical results for the problem obtained from the finite different lattice Boltzmann method in predicting the fluid flow and heat transfer problem.

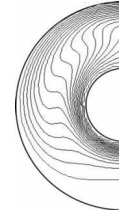
##### 4.1 Validation of Codes

In order to validate the developed codes, we will demonstrate the capability of finite different lattice Boltzmann method by consider the problem of heat transfer from a heated concentric annulus cylinder and the comparison of the results will be carried out with the benchmark solution provided by Shi, 2006.

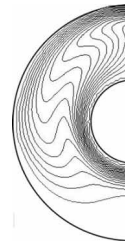
In our numerical simulation, the Prandtl numbers are set at 0.716, 0.717, 0.717, 0.718 and 0.718 for Rayleigh numbers  $2.38 \times 10^3$ ,  $9.50 \times 10^3$ ,  $3.20 \times 10^4$ ,  $6.19 \times 10^4$  and  $1.02 \times 10^5$  respectively.



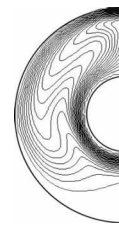
(a)  $Ra = 2.38 \times 10^3, Pr = 0.716$



(b)  $Ra = 9.5 \times 10^3, Pr = 0.717$



(c)  $Ra = 3.20 \times 10^4, Pr = 0.717$

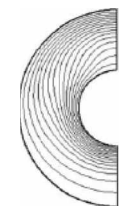


(d)  $Ra = 6.19 \times 10^4, Pr = 0.718$



(e)  $Ra = 1.02 \times 10^5, Pr = 0.718$

Figure 2: Plots of isotherms for different Rayleigh and Prandtl numbers obtained from the LBM



(a)  $Ra = 2.38 \times 10^3, Pr = 0.716$

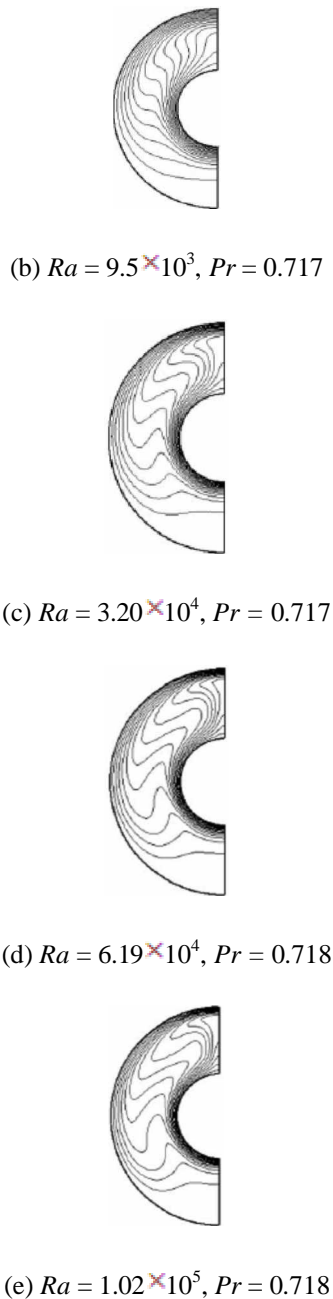


Figure 3: Plots of isotherms for different Rayleigh and Prandtl numbers obtained by Shi, 2006.

Figure 2 shows the plots of isotherms for different Rayleigh gathered from the LBM simulation while in figure 3 represent the same numerical simulation for validation purposes from established results by Shi, 2006. As it can be seen

from the figure 2 and 3, the results are almost identical and qualitatively good agreement with the benchmark solution provided by Shi, 2006.

#### 4.2 Flow and Temperature Fields at Various Rayleigh Number

In this section, we will demonstrate the computational results to discuss the effects of the Raleigh number on the heat transfer mechanism and the fluid flow behaviour in the annulus cylinder. Figure 4 shows the plots of isotherms (right) and streamline (left) for various value of Rayleigh number. In present study, we vary the values of Rayleigh number at  $10^3, 10^4, 10^5$  for aspect ratio 5.0 respectively and Prandtl numbers at 0.717.

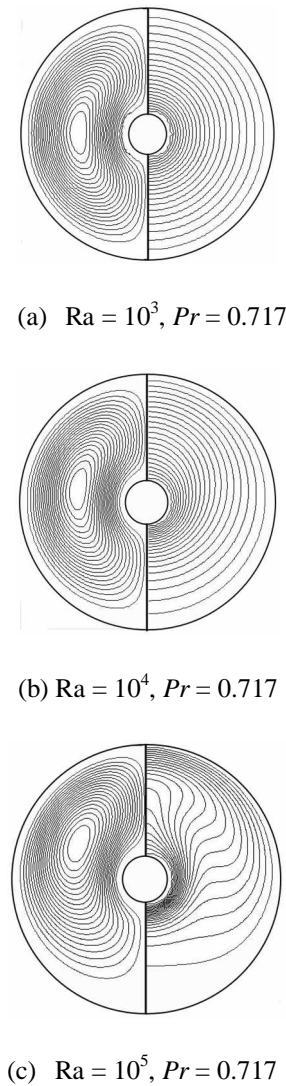
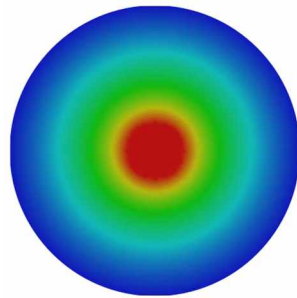


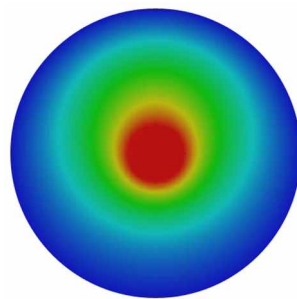
Figure 4: Plots of streamlines and isotherms at various Raleigh number.

As can be seen from Figure 4, the simulated results at all values of Raleigh showing the distorted line above the heated inner cylinder due to the buoyancy effect. This indicates that the convection is the dominant mode heat transfer mechanism at this condition. Due to the convection process, the isotherms move upward and larger plumes exits around the top of the outer cylinder indicating the present of strong thermal gradient at this region.

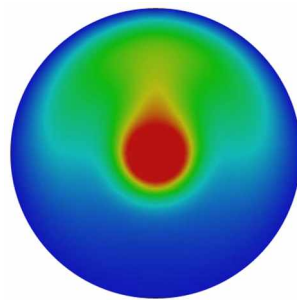
The plots of streamlines shows the main flow is formed at the upper half of the annulus. This can be seen where the center of the main vortex is located at this region. By increasing the Raleigh number, the size of vortex also increases and the isotherms are distorted more due to the stronger convection effect, leading to stable stratification of the isotherms. The vortex slightly move upward due to higher rotational flow resulted from more spacing between the two cylinders. The plots of temperature contour for every simulated aspect ratio are shown in figure 5.



(a)  $Ra = 10^3, Pr = 0.717$



(b)  $Ra = 10^4, Pr = 0.717$



(c)  $Ra = 10^5, Pr = 0.717$

Figure 5: Plots of temperature contours at various Raleigh number.

## 5. CONCLUSION

In this paper, the natural convection is annulus cylinder enclosure with localized heating from inner diameter and symmetrical cooling from outer diameter has been studies using finite difference lattice Boltzmann method. The evolution of lattice Boltzmann equation has been discretised using third order accuracy finite difference upwind scheme. The flow pattern including vortices, isothermal and streamlines can be clearly seen. All the simulated results agree well with the benchmark solution reported in the previous studies. This shows that our model has the capability to solve the thermal flow problem.

## ACKNOWLEDGMENTS

The authors would like to thank Universiti Teknologi Malaysia and the Malaysian government for supporting this research activity.

## NOMENCLATURE

$a$	Acceleration	$U_i$	Mean velocity components ( $i=1, 2, 3$ )
$c$	Micro velocity vector	$v$	<a href="#">kinematic viscosity</a>
$f(x, c, t)$	Density distribution function	$\rho$	Fluid Density
$f_i$	Discretized density distribution function	$\tau$	Time relaxation
		$\Omega$	Collision operator
$f_i^{eq}$	Discretized Equilibrium density distribution function		

a	Acceleration	$U_i$	Mean velocity components (i=1, 2, 3)
c	Micro velocity vector		
$f(\mathbf{x}, \mathbf{c}, t)$	Density distribution function	v	<a href="#">kinematic viscosity</a>
$f_i$	Discretized density distribution function	$\rho$	Fluid Density
		$\tau$	Time relaxation
		$\Omega$	Collision operator
$f_i^{eq}$	Discretized Equilibrium density distribution function		
Re	Reynolds number (= $U_b D_i / \nu$ )		
T	Local mean temperature [K]		
t	time		
U	Horizontal velocity of top plate		

## REFERENCES

- [1] Abe, T., 1997. "Derivation of the Lattice Boltzmann Method by Means of the Discrete Ordinate Method for the Boltzmann Equation", *Journal of Computational Physics* 131, pp. 241–246.
- [2] Donald, P., Ziegler (1993). Boundary Conditions for Lattice Boltzmann Simulations. *Journal of Statistical Physics*, Vol. 71, Nos. 5/6
- [3] He, X., Q., Zou, L.S., Luo, and M., Dembo 1997. "Analytic Solutions of Simple Flows and Analysis of Nonslip Boundary Conditions for the Lattice Boltzmann BGK Model", *Journal of Statistical Physics* 87, pp.
- [4] Inamuro, T., M., Yoshino, and F., Ogino 1995. "A Non-Slip Boundary Condition for Lattice Boltzmann Simulations", *Journal of Physics of Fluids* 8, pp. 1124
- [5] Jami, M., A., Mezrhab, M., Bouzidi, P., Lallemand, 2006. "Lattice-Boltzmann Computation of Natural Convection in a Partitioned Enclosure with Inclined Partitions Attached to its Hot Wall", *Journal of Physic A* 368, pp. 481-494.
- [6] Jami, M., A., Mezrhab, M., Bouzidi, P., Lallemand, 2007. "Lattice Boltzmann Method Applied to the Laminar Natural Convection in an Enclosure with a Heat Generating Cylinder Conducting Body", *International Journal of Thermal Sciences* 46, pp. 38–47.
- [7] Jonas, L., B. Chopard, S. Succi and F. Toschi, 2006. "Numerical Analysis of the Averaged Flow Field in a Turbulent Lattice Boltzmann Simulation", *Journal of Physics A* 362, pp. 6-10
- [8] Kuehn, T.H, R.J, Goldstein, 1978. "An Experimental Study of Natural Convection Heat Transfer in Concentric and Eccentric Horizontal Cylindrical Annulus", *Journal of Heat Transfer* 100, pp. 635-640
- [9] McNamara, G. and B. Alder, 1993, "Analysis of the Lattice Boltzmann Treatment of Hydrodynamics", *Journal of Physics A* 194, pp. 218-228.
- [10] Mezrhab, A., M., Jami, C., Abid, M., Bouzidi, P., Lallemand, 2006. "Lattice-Boltzmann Modeling of Natural Convection in an Inclined Square Enclosure with Partitions Attached to its Cold Wall", *International Journal of Heat and Fluid Flow* 27, pp. 456-465.
- [11] Nor Azwadi, C.S, and T., Tanahashi, 2006. "Simplified Thermal Lattice Boltzmann in Incompressible Limit", *International Journal of Modern Physics B* 20, pp. 2437-2449.
- [12] Nor Azwadi, C.S, and T., Tanahashi, 2007. "Three-Dimensional Thermal Lattice Boltzmann Simulation of Natural Convection in a Cubic Cavity", *International Journal of Modern Physics B* 21, pp. 87-96.
- [13] Nor Azwadi, C.S, and T., Tanahashi, 2008. "Simplified Finite Difference Thermal Lattice Boltzmann Method", *International Journal of Modern Physics B* 22, pp. 3865-3876.
- [14] Nor Azwadi, C.S., 2008. "Finite Difference Double Population Thermal Lattice Boltzmann Scheme for the Simulation of Natural Convection Heat Transfer", *Journal of fundamental science*, Universiti Teknologi Malaysia
- [15] Nor Azwadi, C.S., 2007. "The Development of Simplified Thermal Lattice Boltzmann Models for the Simulation of Thermal Fluid Flow Problems", Ph.D Thesis. Keio University, Japan.



- 16 Peng, Y., Y.T, Chew, C., Shu, 2003. "Numerical Simulation of Natural Convection in a Concentric Annulus between a Square Outer Cylinder and a Circular Inner Cylinder using the Taylor Series Expansion and Least Square Based Lattice Boltzmann Method", *Journal of physics* 67, pp. 026701.1-026701.6
- 17 Rohde, M., D., Kandhai, J. J., Derksen, and H.E.A., Van Den Akker, 2003. "Improved Bounce-Back Methods for No-Slip Walls in Lattice-Boltzmann Schemes: Theory and Simulations", *Journal of statistical of physics* 67, pp.066703.1-066703.10
- 18 Shi, Y., T.S., Zhao, Z.L., Gou 2006. "Finite Difference Based Lattice Boltzmann Simulation of Natural Convection Heat Transfer in a Horizontal Concentric Annulus", *Journal of Computer & Fluids A*, pp 1-15
- 19 Sridar, D., N., Balakrishnan, 2003. "An Upwind Finite Difference Scheme for Mesh Less solvers", *Journal of Computational Physics* 189, PP. 1-29.
- 20 Succi, S., 2006. "The lattice Boltzmann Equation for Fluid Dynamics and Beyond", *Oxford university press*, pp 83.

# Engineering Analysis on the Conceptual Design of Portable Hand Truck for Staircase

Muhamad Hasbullah Padzillah<sup>a</sup>, Idris Ishak<sup>b</sup>, Abdul Rahman Musa<sup>c</sup>

<sup>a</sup>*Department of Thermo-Fluids, Faculty of Mechanical Engineering,  
Universiti Teknologi Malaysia,  
81310 Skudai, Johor, Malaysia,  
hasbullah@fkm.utm.my*

<sup>b</sup>*Department of Design, Faculty of Mechanical Engineering,  
Universiti Teknologi Malaysia,  
81310 Skudai, Johor, Malaysia,  
idris@fkm.utm.my*

<sup>c</sup>*Department of Applied-Mechanics, Faculty of Mechanical Engineering,  
Universiti Teknologi Malaysia,  
81310 Skudai, Johor, Malaysia,  
arahman@fkm.utm.my*

## ABSTRACT

The main purpose of this paper is to perform engineering analysis for the designed stair climbing hand truck. Engineering analysis includes finding critical stress inside every components of the hand truck so that the materials and dimensions which are pre-assigned can be changed if necessary. Maximum deflection for each component is also investigated. Minimum torque required, as well as motor speed and power is also determined. Furthermore, analyses on the critical assembly are also performed to investigate whether the mounting techniques are reliable or not.

### Keywords

*Conceptual Design, Hand Truck, Engineering Analysis, Critical Stress, Maximum Deflection*

## 1. INTRODUCTION

As the manufacturing world advances, more and more consumer products, specifically household products were invented in order to make our life easier. Some of these products such as washing machine and refrigerator are very important but they are very heavy and cannot be transported efficiently without appropriate material handling equipment. To encounter this kind of problem, a very common material handling equipment which is a hand truck is used. Due to its ability to transport goods, hand truck is widely used in the whole world and can be considered as a one of the very important material handling device. This

research is focusing on designing hand truck that can be used for transporting goods on a staircase as well as on the flat surface. This hand truck will also have special features such as lightweight and portable. Besides that, a motorized system will be utilized so that during the climbing process, neither pulling nor pushing forces are needed from the user in order to move the hand truck upstairs. Handling capability and maximum loads that can be carried both on the flat surface and on the stairs will be the very important additional value for this hand truck.

## 2. OBJECTIVE

To develop a design of a portable hand truck which is versatile, durable and lightweight for transporting goods on a staircase as well as can operate efficiently on the flat surface as well as to develop a hand truck that can climb staircase with the very minimum effort from the user which means that a user only need to balance the loads while all the lifting process is done by the motor.

## 3. ANALYSIS ON HAND TRUCK COMPONENTS

### 3.1 Maximum Loading Conditions

The size of the loadings as well as the maximum weight is pre-determined before an analysis begins. Size and weight of the loadings shall be as large as it can, assuming the worst operating condition of the hand truck. Details of the

specifications for the loadings are provided below:

a) Dimension: 1200mm(H)x500mm(W)x400mm(D)

b) Weight :120 kg

Relative size of the loadings that will be analyzed compared to the hand truck is simulated as in Fig. 1

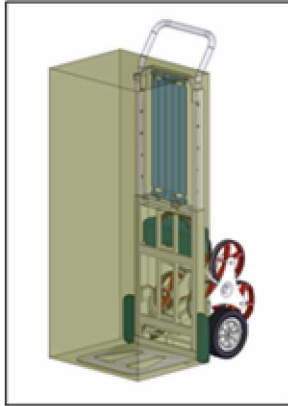


Figure 1 Relative size of loadings

### 3.2 Static Analysis

There are several reasons for performing static analysis on the structure. First and foremost, static analysis is used to obtain pulling force that is required by the user in order to operate the handtruck from its rest position.

### 3.3 Structural Analysis

Structural Analysis is slightly complicated than static analysis. It sometimes involves too much calculation if it is done manually. So, in order to aid the analysis as well as to get clearer results of the structural analysis, NASTRAN for Windows software is used. It is an engineering software that uses finite element analysis as the basic of its mathematical operations. Another software used is STRAN. Therefore some simple calculation is done manually whereas the complicated solution is obtained by NASTRAN as well as STRAN.

The purpose of performing structural analysis on this design is to:

1. Determine the critical point in each part.

2. Obtain the maximum stress exerted in each component when handtruck is carrying full loads. The maximum value acquired later on will be compared to the material's yield stress to ensure that none of the stress obtained exceed it. If there are cases like that happen, than it is confirmed that there are something wrong with the design either for materials selection or the dimensions. Those parts involved with such cases most probably will be redesigned or modified.

3. Acquire deflections occurred in the handtruck. If there are so much deflection occurs in the handtruck, it will create discomfort to user while operating the handtruck while too much deflection also indicates that errors may occur during the material selection process as well as dimensioning.

### 3.4 Graphical Result of Analysis

#### 3.4.1 Deflection of Critical Components

To obtain the exact stress distribution as well as deformation of the front nose after loading is applied, NASTRAN for Windows software is used.

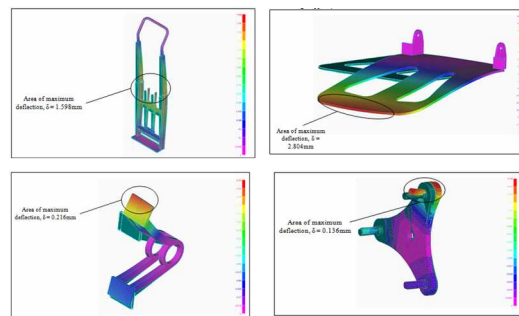


Figure 2 Graphical representation of several components' deflection

#### 3.4.1 Stress in Critical Components

To obtain the exact stress distribution as well as deformation of the front nose after loading is applied, NASTRAN for Windows software is used.

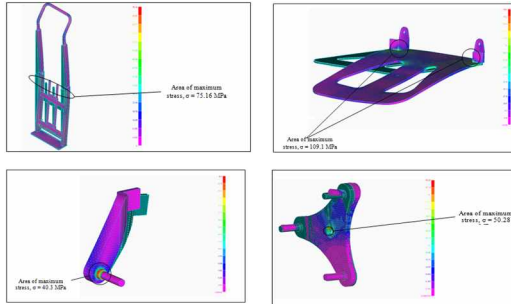


Figure 3 Graphical representation of several components' stress

## 2. CALCULATION OF MINIMUM TORQUE REQUIRED

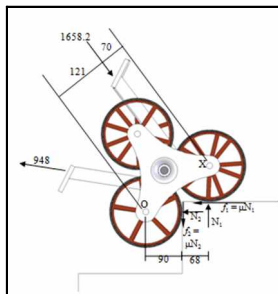


Figure 4 Free Body Diagram for finding minimum Torque required

During operation, the only contact between wheel and floor occur at wheel X. Hence, apply moment equilibrium equation at point X to obtain value of M to balance the equation and that is the minimum value of motor torque required.

$$\sum M_x = 0$$

$$948(0.055) - 1658.2(0.07) + M + \left(\frac{862}{2}\right)(0.09) = 0$$

$$\therefore M = 25.144 \text{ N}$$

Thus, minimum value of motor torque is 25.144  $\approx$  **30 Nm**

## 3. ANALYSIS ON CRITICAL ASSEMBLY

It is very important to perform additional analysis on the critical assembly especially for the part that is using bolts as the medium of assembly. This is

to ensure that the number of bolts used is enough to sustain shear force as well as axial force during the operation of handtruck. All the forces obtained from previous analysis are than applied to the bolts.

### 5.1 Assembly between main frame and motor holder

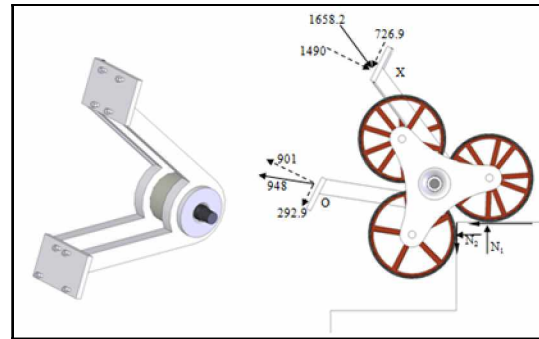


Figure 5 Free Body Diagram for analyzing critical assembly

Analysis at point X

Number of bolts, n : 4

Bolt's Diameter, d : 6 mm

Shear force exerted by bolts, V: 726.9 N

Axial force exerted by bolts, F: 1490 N

Calculating Shear stress exerted by each bolt,

$$\tau = \frac{V}{nA} = \frac{726.9}{\pi(4)(0.006)^2 / 4} = 6.43 \text{ MPa}$$

Calculating Axial stress exerted by each bolt,

$$\sigma = \frac{F}{nA} = \frac{1490}{\pi(4)(0.006)^2 / 4} = 13.17 \text{ MPa}$$

Analysis at point O

Number of bolts, n	:	4
Bolt's Diameter, d	:	6 mm
Shear force exerted by bolts, V:		292.9 N
Axial force exerted by bolts, F:		901 N

Calculating Shear stress exerted by each bolt,

$$\tau = \frac{V}{nA} = \frac{292.9}{\pi(4)(0.006)^2/4}$$

$$= 2.59 \text{ MPa}$$

Calculating Axial stress exerted by each bolt,

$$\sigma = \frac{F}{nA} = \frac{901}{\pi(4)(0.006)^2/4}$$

$$= 7.97 \text{ MPa}$$

### 5.2 Assembly between main frame and wheel holder

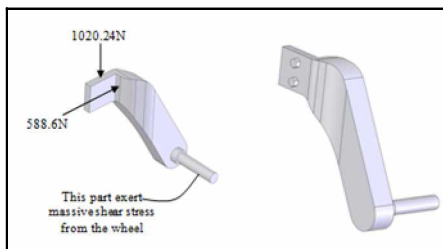


Figure 5 Free Body Diagram for analyzing critical assembly

No axial force will be exerted by bolts

Total shear force,

$$V_{total} = \sqrt{1024.24^2 + 588.6^2}$$

$$\therefore V_{total} = 1181N$$

However, since loading is shared between two wheel holder, shear force for each wheel holder,

$$V = 1181/2 = 590.5N$$

Calculating Shear stress exerted by each bolt,

$$\tau = \frac{V}{nA} = \frac{590.5}{\pi(2)(0.006)^2/4}$$

$$= 10.44 \text{ MPa}$$

### 5.3 Calculating motor speed and power requirement

Estimated Climbing Speed = 48 steps/min

$\therefore$  1 revolution of motor = 3 steps

$$\text{Motor RPM} = 48/3 = 16 \text{ RPM}$$

To calculate power requirement of the motor:

$$\text{Power} = \omega T$$

$$P = \omega T$$

$$\omega = \frac{2\pi N}{60} = \frac{2\pi(16)}{60}$$

$$\omega = 1.68 \text{ rad/s}$$

$$\therefore P = 1.68 \times 30$$

$$P = 50.3W$$

## 2. Discussion

In order to obtain the safety factor for the hand truck during maximum loadings of 120kg, a table that concludes all the design analysis is constructed. In the table 1 below, only stresses that influence the most or the one that having highest value are listed in the table.



Table 1 Summary of Design

From the table, it can be seen that some of the boxes under safety factor is written 'too large'. It indicates that value of safety factor is higher than 60 and that particular structure is definitely safe for any hand truck loadings up to 120 kg. From the table also, it can be seen that value of applicable safety factor for overall hand truck is 4.31. Allowing 20% of calculation tolerance gives safety factor of 3.4.

Components/ Parts	Materials	Maximum Bending Stress (MPa)	Maximum Axial Stress (MPa)	Maximum Shear Stress (MPa)	Maximum Deflection (mm)	Safety Factor
Front Nose (Plate)	Alloy Steel	173	-	-	2.804	4.31
Lower Frame (Rod)	Aluminum Alloy 7075-T6	-	-	12.12	-	42
Wheel Holder (Rod)	Alloy Steel	-	-	1.655	-	Too Large
Wheel Holder	Alloy Steel	62.17	-	-	0.0966	11.98
Vertical Frame	Aluminum Alloy 7075-T6	36	-	-	1.598	15.83
Motor Holder (A)	Alloy Steel	-	-2.76	-	0.216	Too Large
Motor Holder (B)	Alloy Steel	-	1.58	-	-	Too Large
Main Frame - Motor Holder	Steel Grade 8	-	13.17	6.43	-	Too Large
Main Frame - Wheel Holder	Steel Grade 8	-	7.97	2.59	-	Too Large

## 7. CONCLUSION

Engineering analysis shows that designed hand truck is able to withstand maximum load of 120 kg with a reasonable safety factor. The minimum torque calculated also shown that 30Nm torque is enough to ensure stable movement of hand truck during climbing.

## REFERENCES

- [1] Idris Ishak and Richard Lim Boon Keat, Skudai, 2007, Introduction to Basic Sketching and Rendering Techniques, Penerbit UTM.
- [2] Khairuddin Hj. Jaffar, Skudai, 1996, Protective Shield for Lorry drivers Cabin, Universiti Teknologi Malaysia.
- [3] Mohd Hafidz Mohamed Rodzi, Skudai 2004, Drop – on Traffic Bollards (Ikon Trafik Mudah Alih), Universiti Teknologi Malaysia.
- [4] Hamdan Ismail, Skudai, 1990, Rekabentuk Troli Pengangkut Barang Untuk Kegunaan di Tangga dan Pelbagai Guna, Universiti Teknologi Malaysia
- [5] Azrul Hazimin Mohamad, Skudai, 1996, Designing a Stairs Handtruck, Universiti Teknologi Malaysia
- [6] Callister, W.D, New York, 2007, Materials Science and Engineering : An Introduction, John Wiley & Sons Inc.
- [7] Boresi, A.P. and Schimidt, R.D, New York, 2002, Advanced Machanics of Materials, John Wiley & Sons Inc.
- [8] Planchard, D.C. and Planchard, M.P., 2005, SolidWorks 2005 Tutorial, Schroff Development Corporation SDC Publications.
- [9] Mohamad Kasim Abdul Jalil, Skudai, 2000, Proses dan Kaedah Rekabentuk, Penerbit UTM



# Numerical Analysis of Helicopter Tail Shake Phenomenon: A Preliminary Investigation

Iskandar Shah Ishak\*, Shuhaimi Mansor, Tholudin Mat Lazim,

Muhammad Riza Abd Rahman

Department of Aeronautical Engineering  
Faculty of Mechanical Engineering  
Universiti Teknologi Malaysia  
81310 UTM Skudai, Johor, Malaysia  
Tel: +607-5534664, Fax: +607-5566159  
\*E-mail: shah@mail.fkm.utm.my

## ABSTRACT

The flow field that governs helicopter tail shake phenomenon has often baffled the aerodynamicists and it remains as a long dragged issue that adversely affected the overall performance, occupants' comfort and handling qualities of helicopter. The objective of this research is to improve basic understanding of the viscous unsteady flow phenomenon observed behind the main-rotor-hub assembly, as the part is believed to be the major contributor of tail shake phenomenon. Using Computational Fluid Dynamic (CFD) approach, the FLUENT software was employed and the Multiple Reference Frames (MRF) method was applied to simulate the helicopter's main-rotor-hub assembly rotation. In this study, the aerodynamic flow field was computed using the Reynolds-Averaged Navier-Stokes (RANS) equations. As the induced wake, which consequently causing tail to shake differs with the rpm of main-rotor-hub assembly, this preliminary numerical investigation was performed ranging from rpm of 0 to 900, with intervals of 300 rpm. A rotor-hub-fairing was also being installed to examine its effect on wake unsteadiness of this tail shake phenomenon.

## Keywords

Flow field, helicopter tail shake, unsteady flow, computational fluid dynamic

## 1. INTRODUCTION

Tail shake is an issue of major concern for rotorcraft [1] as it is adversely affected the overall performance and handling qualities of helicopter. Vibrations transmitted from vertical tail to cockpit have also caused discomfort to the occupants [2]. It had being reported on the AH-64D Longbow

Apache helicopter, the vibration resulted in increased cockpit lateral vibration levels, which increased crew workload and reduced their ability to perform precision tasks [3].

This phenomenon is a challenging issue to understand with as it involves an interaction between aerodynamic flow excitation, which related to flight parameters & structural response, which related to structure characteristics [2]. A good understanding of this matter is necessary as a typical aspect of tail shake that it has unsteady random character, indicating that the wake induced excitation is in also unsteady of nature [2].

Tail shake phenomenon happens partly due to the unsteady flow contributed from the main-rotor-hub assembly that hit the tail part, as shown in Figure 1. Hence, it likely only to happen when there is a forward velocity i.e. during hovering or vertical climb/descent, helicopter will not encounter this tail shake problem.

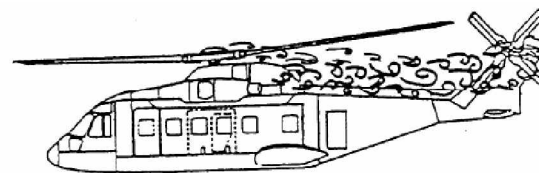


Figure 1: Schematic diagram of tail shake [2]

In this research, focus will be on main-rotor-hub assembly's wake as it is believed to be the major contributor of the problem. This allows the tail shake investigation to be conducted using blade-stubs configuration [4,5,6]. Blade-stubs configuration is a combination of main-rotor-hub assembly with short blades.

## 2. CFD MODELLING DESCRIPTION

This numerical study used **Reynolds-Averaged Navier-Stokes (RANS)** equation models which solve ensemble-averaged Navier-Stokes equations [7]. There are several types of RANS-based model and for this simulation, the two-equation models of Realizable k- $\epsilon$  model was employed.

The k- $\epsilon$  model selected is not an issue here as the research is keen on the result's trends, not the result's absolute values. The **Multiple Reference Frames (MRF)** approach was applied to simulate the main-rotor-hub-assembly rotation at various rpm.

This numerical investigation used an ellipsoidal fuselage based on NASA standard model [8] with the axes ratio of longitudinal to lateral axes is 4.485. This kind of model is selected as it avoids geometric complexity and simplifies the interactions with the wake [8]. For this research work, the longitudinal axes were taken as 1120 mm. The model is shown in Figure 2.

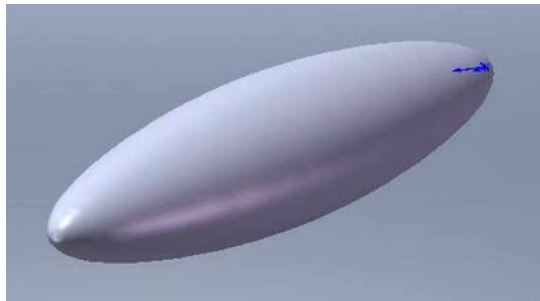


Figure 2: An ellipsoidal fuselage based on NASA model [8]

The model was simulated with a simplified main-rotor-hub assembly attached with short blades i.e. blade-stubs configuration, as shown in Figure 3. This simplified main rotor hub assembly is only meant to trigger the unsteady wake due to rotation of main- rotor-hub assembly.

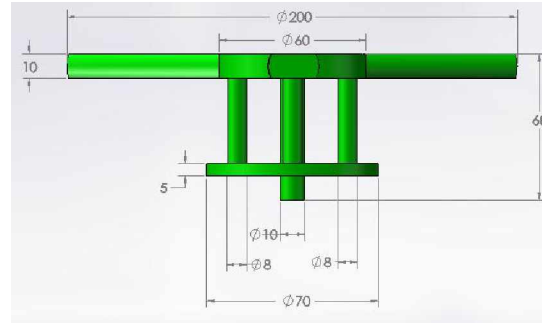


Figure 3: A simplified blade-stubs configuration

Figure 4 depicts the complete model with blade-stubs configuration and an ellipsoidal pylon.

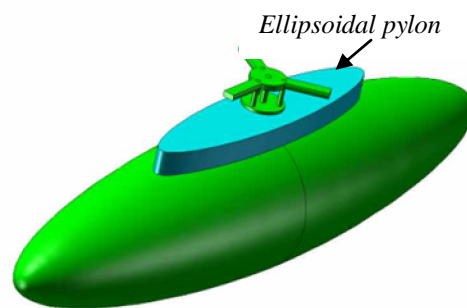


Figure 4: Model for CFD simulation

In **Geometry And Mesh Building Intelligent Toolkit (GAMBIT)**, which acts as a pre-processor for CFD analysis, a test section with a size of 2m (width) x 1.5m (height) x 5.8m (length) was virtually created for placing the model. The size of this test section is similar as the test section size of Universiti Teknologi Malaysia – Low Speed Tunnel (UTM-LST), as experimental works also be planned to compare with this CFD analysis.

In MRF method, two reference frames must be created with one at the vicinity of the rotating parts i.e. main-rotor-hub assembly. As there is no specific rule regarding the size of the frame for rotating parts, this research decided to take the distance of the frame's boundary to surface of the rotating parts to be 1 aerofoil thickness. The aerofoil thickness of the main rotor, as depicted in Figure 3, is 10 mm and hence the frame was created in such manner as shown in Figure 5.

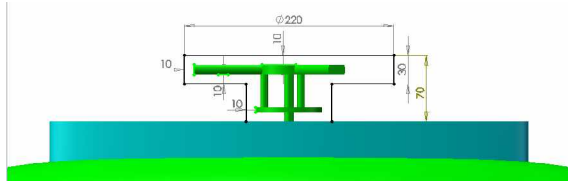


Figure 5 (a): Frame dimensions (side view)

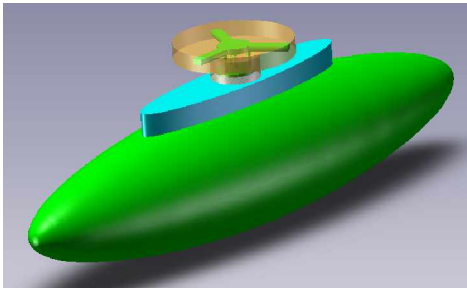


Figure 5(b): Frame for rotating parts (iso view)

Figure 5: Frame for rotating parts

### 3. RESULTS ANALYSIS

Before running the final simulation, independence grid analysis had been carried out to verify the results obtained are free from grid influence. This is important to confirm the differences of results are due to test configurations, not due to number of the grid.

All simulation results presented throughout this paper were run at wind speed, or forward flight velocity, of 40 m/s.

Figures 6 and 7 show the path lines of turbulent intensity for 0 and 900 rpm of main-rotor-hub assembly, respectively. Viewed from top as shown by Figures 6(a) and 7(a), the path lines are about symmetrical on both left and right sides for 0 rpm, contrary for 900 rpm, the path lines are unsymmetrical indicating there is strong flow interaction with the rotating main-rotor-hub assembly.

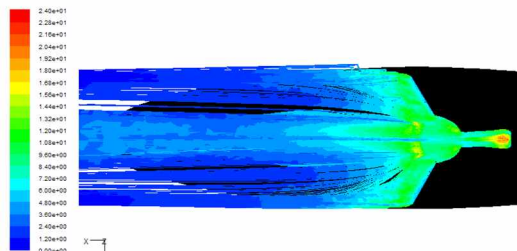


Figure 6(a): Path lines from 'main-rotor-hub assembly' (top view)

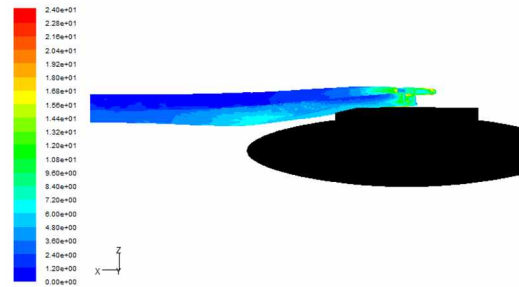


Figure 6(b): Path lines from 'main-rotor-hub assembly' (side view)

Figure 6: Path lines coloured by turbulent intensity (%) at 0 rpm

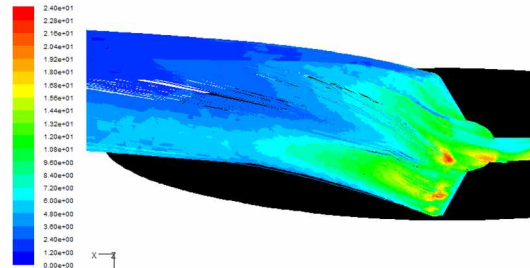


Figure 7(a): Path lines from 'main-rotor-hub assembly' (top view)

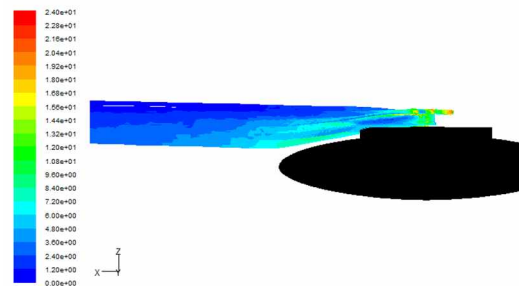


Figure 7(b): Path lines from 'main-rotor-hub assembly' (side view)

Figure 7: Path lines coloured by turbulent intensity (%) at 900 rpm

Compared to Figure 6(b), turbulent intensity is higher and wake volume is thicker in Figure 7(b). This shows rotation on main-rotor-hub assembly triggers a significant unsteady wake which could contribute to tail shake problem.



respectively. Obviously it can be noticed at 900 rpm, there is more flow unsteadiness compared to at 0 rpm.

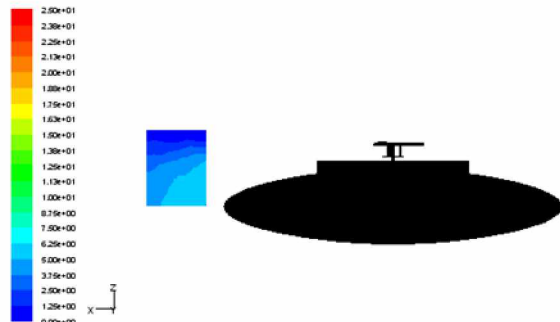


Figure 8: Contours of turbulent intensity (%) at 0 rpm (side view)

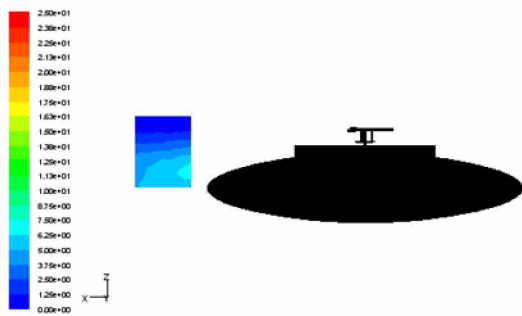


Figure 9: Contours of turbulent intensity (%) at 900 rpm (side view)

Table 1 depicts the values of turbulent intensity in this ‘vertical-tail-plane’, ranging from 0 to 900 rpm with intervals of 300 rpm. It indicates main-rotor-hub assembly rpm increases the turbulent intensity in which is tally with the experimental work done by Ishak et al. [9].

Table 1: Turbulent intensity (%) in ‘vertical-tail-plane’

Main Rotor Rpm	Turbulent Intensity (%) Facet max.
0	6.54
300	6.69
600	6.90
900	7.15

Figure 10 shows total pressure contours for different main-rotor-hub assembly rpm as pressure fluctuations could be translated into aerodynamic forces excitation which may lead to tail vibration.

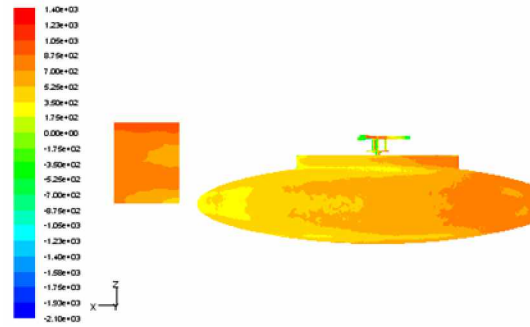


Figure 10(a): 0 rpm

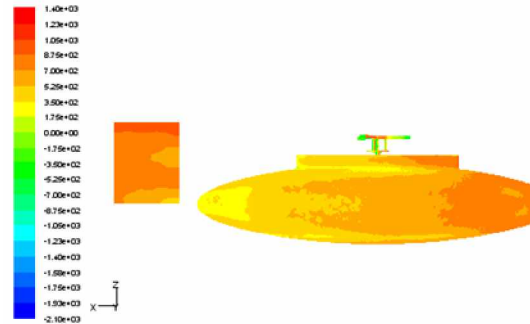


Figure 10(b): 300 rpm

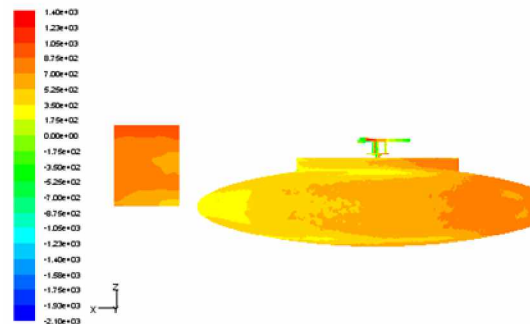


Figure 10 (c): 600 rpm

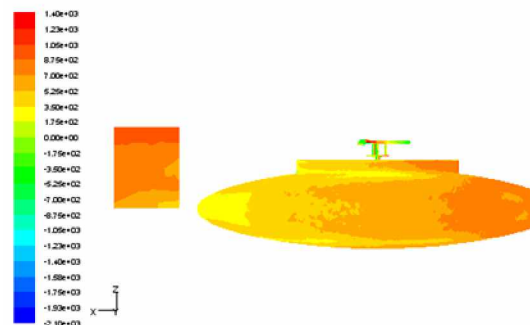


Figure 10 (d): 900 rpm

Figure 10: Contours of total pressure (Pa)

Figure 10 depicts the fluctuation of total pressure inside the ‘vertical-tail-plane’ is becoming more with the increment of main-rotor-hub assembly rpm. Table 2 summarizes the maximum and

minimum values of total pressure inside this 'vertical-tail-plane'.

Table 2: Total pressure (Pa) in 'vertical-tail-plane'

Main Rotor Rpm	Total Pressure (Pa)		$\Delta$ Facet (Pa)
	Facet max.	Facet min.	
0	940.24	349.16	591.08
300	940.67	337.17	603.50
600	941.11	324.48	616.63
900	943.08	318.36	624.72

Table 2 indicates the range from minimum to maximum value of total pressure i.e.  $\Delta$  Facet, is getting larger with the increment of main-rotor-hub assembly rpm. This result translates more aerodynamic forces excitation occurred with higher rotation of main-rotor-hub assembly, signalling could mean more tail shake problem.

To investigate the effects of covering some parts of main-rotor-hub assembly, pylon height is increased i.e. acting as a fairing, as shown in Figure 11.

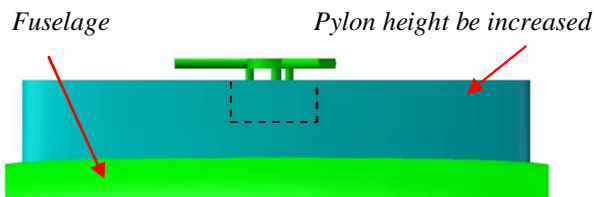


Figure 11: Model configuration with fairing

Figures 12 and 13 show path lines with fairing configuration.

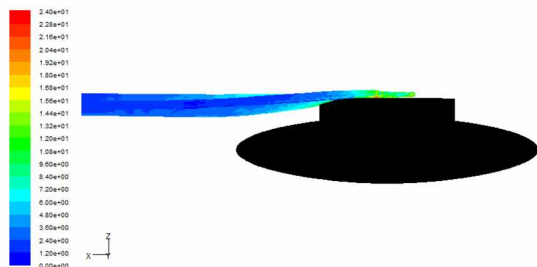


Figure 12: Path lines coloured by turbulent intensity (%) from 'main-rotor-hub assembly' at 0 rpm

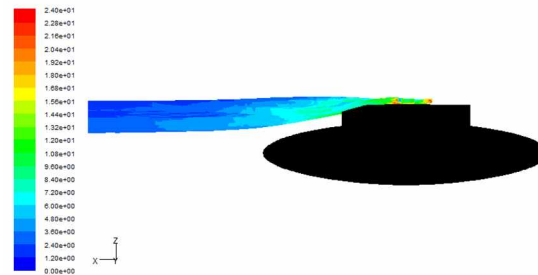


Figure 13: Path lines coloured by turbulent intensity (%) from 'main-rotor-hub assembly' at 900 rpm

The path lines demonstrated by Figures 12 and 13 behave the same trend as with configuration without fairing i.e. more turbulent intensity and wake volume at 900 rpm compares to at 0 rpm configuration.

Compares to Figure 7, Figure 13 translates with fairing configuration, the unsteady wake is reduced both in term of the wake's unsteadiness and volume.

Figure 14 shows total pressure contours for different rpm of main-rotor-hub assembly with fairing configuration. Same as depicted by Figure 10 for configuration without fairing, it narrates higher pressure fluctuation occurred at higher rotation of main-rotor-hub assembly.

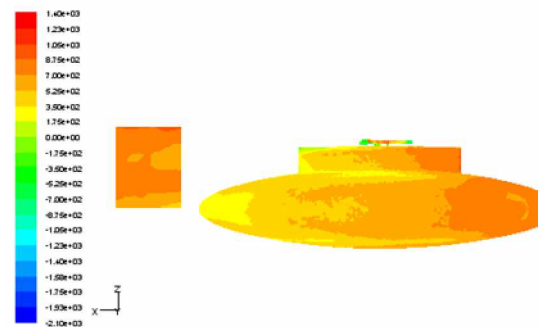


Figure 14(a): 0 rpm

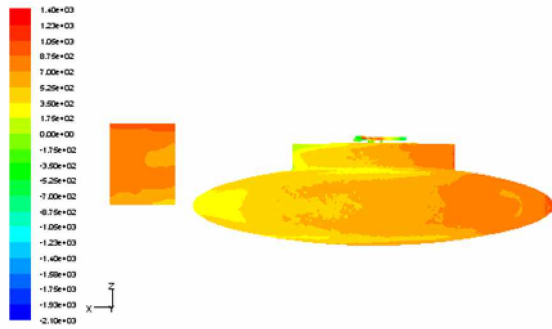


Figure 14(b): 300 rpm

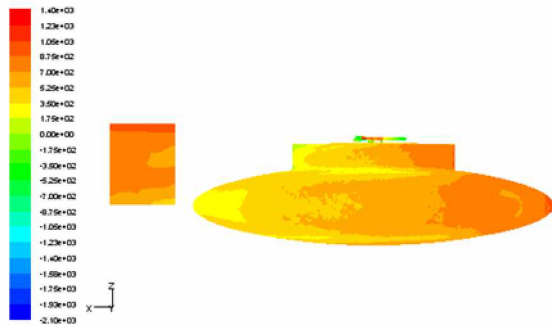


Figure 14(c): 600 rpm

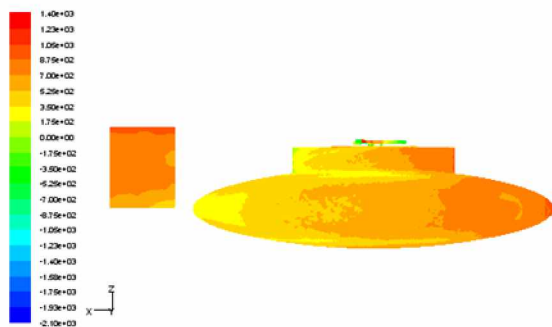


Figure 14(d): 900 rpm

Figure 14: Contours of total pressure (Pa)

Table 3 shows the maximum and minimum values of total pressure inside the vicinity of vertical plane with fairing configuration..

Table 3: Total pressure (Pa) in 'vertical-tail-plane' with fairing configuration

Main rotor rpm	Total Pressure (Pa)		$\Delta$ Facet (Pa)
	Facet max.	Facet min.	
0	936.37	356.93	579.44
300	938.12	351.54	586.58
600	937.99	348.02	589.97
900	937.41	338.21	599.20

Table 3 shows the same trend as in Table 2 i.e.

$\Delta$ Facet increases with the rpm of main-rotor-hub assembly. However its value is smaller compared to Table 2, which is good as it indicates lesser aerodynamic excitation happens which might be translated to a lesser tail shake problem.

An investigation was also being carried out trying to correlate the flow unsteadiness with aerodynamic drag, as shown by Figure 15.

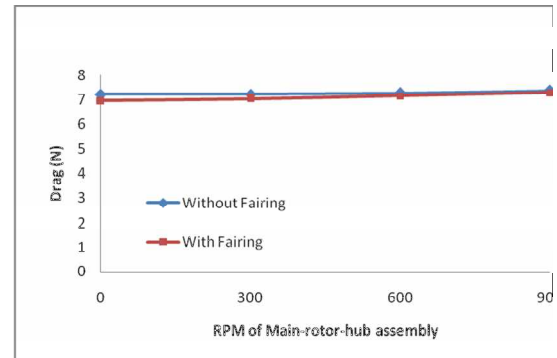


Figure 15: Drag on rpm sweep

Figure 15 reveals there is correlation between aerodynamic drag with main-rotor-hub assembly rotation i.e. the aerodynamic drag is increased with the incremental of main-rotor-hub assembly rpm. Referred back to Tables 1 and 2 which show main-rotor-hub assembly rpm increases flow unsteadiness, it seems correlation could be made between flow unsteadiness with aerodynamic drag in which higher flow unsteadiness seems generating more aerodynamic drag.

Figure 15 also depicts configuration with fairing successfully reducing drag. As depicted previously by Figure 14 and Table 3 that fairing leads to lesser flow unsteadiness, this result seems agreeable with the correlation made that flow unsteadiness could influence aerodynamic drag.

#### 4. CONCLUSION

This research works serve as a preliminary numerical study on helicopter tail shake phenomenon. Throughout the paper, some wake characteristics on an ellipsoidal helicopter fuselage model with simplified blade-stubs configuration have been presented.

Results tell main-rotor-hub assembly's rpm influences the flow unsteadiness i.e. at higher rotation, higher turbulent intensity and bigger

pressure fluctuations be triggered. This higher aerodynamic excitation likely will contribute to higher helicopter's tail vibration.

Results also reveal correlation between aerodynamic drag and flow unsteadiness where higher flow unsteadiness may contribute to higher aerodynamic drag.

Adding fairing seems will reduce aerodynamic drag, as well the wake's unsteadiness and volume. This finding could mean a lesser tail shake problem if the rotating parts of main-rotor-hub assembly being covered.

Nevertheless, conclusions drawn here are only based on simulations ran at winds speed of 40 m/s with zero angle of attack. At different range of wind speed and angle of attack, the outcomes might be dissimilar. Hence simulation works should be done at more various configurations for better comprehensive conclusions. On top of that, **Large Eddy Simulation (LES)** coupled with experimental works, are much required for a better understanding of this helicopter tail shake phenomenon.

## ACKNOWLEDGMENT

Authors like to thank Muhammad Khaidhir Bin Jamil from Universiti Teknologi Malaysia for his initial help of this project.

## REFERENCES

- [1] F.N. Coton, "Evaluation Report of UTM Research Project", University of Glasgow, July 2009.
- [2] P.G. de Waad and M. Trouvé, "Tail shake vibration", National Aerospace Laboratory (NLR), American Helicopter Society Annual Forum, May 1999.
- [3] A. Hassan, T. Thompson, E.P.N. Duque, and J. Melton, "Resolution of tail buffet phenomena for AH-64D<sup>TM</sup> Longbow Apache<sup>TM</sup>", Journal American Helicopter Society, Volume 44, 1999.
- [4] A. Cassier, R. Weneckers and J-M Pouradier, "Aerodynamic development of the tiger helicopter", 50th American Helicopter Society Forum, May 1994.

- [5] C. Hermans et al., "The NH90 helicopter development wind tunnel programme", European Aerospace Societies Conference, Cambridge UK, 1997.
  - [6] "Eurocopter Slide Presentation", France, 2006.
  - [7] "Introductory FLUENT Notes", FLUENT V6.2, March 2005.
  - [8] P.F. Lorber, T.A. Egolf, "An Unsteady Helicopter Rotor-Fuselage Interaction Analysis", NASA Contractor Report 4178, 1988.
- I.S. Ishak, S. Mansor, T. Mat Lazim.,  
 "Experimental Research On Helicopter Tail Shake Phenomenon", Issue 26, Jurnal Mekanikal, Universiti Teknologi Malaysia, December 2008

# Study on Characteristics of Briquettes Contain Different Mixing Ratio of EFB Fibre and Mesocarp Fibre

H. M. Faizal, Z. A. Latiff, Mazlan A. Wahid, Darus A. N.

Faculty of Mechanical Engineering  
Universiti Teknologi Malaysia, 81310 UTM Skudai  
Tel: (+60)7-5534657  
E-mail: mfaizal@fkm.utm.my

## ABSTRACT

Based on Malaysia Palm Oil Statistics, the production of palm biomass residues such as shell, mesocarp fibre and empty fruit bunch (EFB) increased significantly from year to year. These residues especially mesocarp fibre and EFB were dumped in areas adjacent to the palm oil mills. Therefore, briquetting technology is expected can improve this waste disposal by converting these residues into solid fuels with higher energy content per unit volume. In this paper, the physical characteristics and combustion properties of briquettes contain new proposed mixture has been investigated. This mixture composed of mesocarp fibre and EFB fibre in different weight ratios. EFB fibre is obtained after drying process by superheated steam with the pressure ranges from 1.0 to 1.5 bar and temperature ranges from 100 to 120°C. Based on several tests done for investigating the capability of new mixture of palm biomass briquettes, it was found that the briquette with weight ratio of 60:40 (EFB fibre: mesocarp fibre) satisfies the minimum requirement for commercial briquette DIN 51731. Besides, this ratio is selected due to the emphasis on the use of large portion of EFB.

## Keywords

Briquetting, briquette, palm biomass, combustion rate, shell, mesocarp fibre, EFB fibre, DIN 51731

## 1. INTRODUCTION

As reported by Malaysia Palm Oil Board (MPOB, 2006), the production of shell, mesocarp fibre and EFB in Malaysia for year 2006 are  $5.20 \times 10^6$  tonne/year,  $9.66 \times 10^6$  tonne/year, and  $17.08 \times 10^6$  tonne/year respectively. Therefore, the utilization of these residues is very important in order to

prevent waste and dumping areas adjacent to the mills.

Conversion of these residues into briquette is one of the methods to improve the properties especially in term of energy content per unit volume. As explained by Bhattacharya et al. (1996), densification (briquetting, pelletizing and baling) is a process that can improve the storage and transportation of biomass fuel.

Chin and Siddiqui (2000) have conducted an experiment to study the combustion rate on various biomass briquettes such as raw husks, sawdust and several others. The compaction pressure was within the range of 1 to 7 MPa. It was found that the burning rate increased as the binder content increased. The binding agents used in their experiment were molasses and starch.

In year 2002, an experiment that was carried out by Husain et al. (2002) explain the physical and combustion characteristics of current local briquettes contain mesocarp fibre and shell in the ratio of 60:40. They used starch as binding agent (10% of the weight of residues) with addition of water (50% of the weight of residues). They found that the combustion of heap of briquettes in the stove releases about 0.5kW, air-fuel ratio was about 10.2 and ash content was 5.8%. Besides, the average compressive strength of about 2.56 MPa is considered as a value for good resistance for disintegration.

Meanwhile, in year 2008, Nasrin et al. (2008) studied the physical and combustion characteristics of palm biomass briquettes containing EFB fibre and palm kernel cake (PKC). The weight ratio for PKC + EFB fibre + sawdust was 30:5:65. In this case, sawdust plays a role as binder. In their study, they found that the strength of briquettes increased when the sawdust was added.



Thus, in this paper, the physical and combustion properties of briquettes contain EFB fibre and mesocarp fibre with different mixing ratios were studied. One ratio then will be selected for further study in the future to investigate the effect of compaction pressure on the combustion characteristics of these briquettes such as combustion rate. The selection of ratio was based on two aspects. The first aspect is minimum requirement of commercial briquette DIN 51731 in term of gross calorific value and moisture content. Meanwhile, the second aspect is the emphasis on the use of EFB.

## 2. METHOD AND PREPARATION

The palm biomass residues (EFB fibre and mesocarp fibre) have been collected and grinded into powder.

For making briquette, EFB fibre powder and mesocarp fibre powder are mixed in weight ratio of 20:80, 40:60, 60:40 and 80:20. As binding agent, starch (20% of weight of residues) and water (80% of weight of residues). After these materials have been mixed homogeneously by using mixer, it is dried under ambient temperature for about 6 hours before pressing process.

For briquetting, constant compaction pressure is used, which was 7 MPa. Figure below shows the experimental setup for briquetting. The setup consists of YASUI hydraulic hand press, die set, load cell and data logger.



Figure 1: Experimental Setup for Briquetting

After briquetting, the briquette produced is removed from the die set and it is dried at room temperature for about 1 week to obtain stability and rigidity.

The relaxed density of briquettes is obtained by determining the volume first using stereometric method. This method has been described by Rabier et al (2006). Stereometric method is based on the measurement of the dimensions such as diameter, length, width and height. The measurement is done by using caliper gauge. By knowing the volume and mass of briquette, the relaxed density is determined by using geometric formulae.

The compressive strength of briquette is investigated by using INSTRON machine. Figure below shows the sample of briquette undergoes the compression test.



Figure 2. Briquette Undergoes Compression Test

Meanwhile, the proximate analysis has been done for raw materials and briquettes produced to investigate the moisture content, volatile matter, fixed carbon and ash content. Table 1 below shows the standard used for this proximate analysis.

Table 1: Standard Used for Proximate Analysis

Properties	Standard Used
Moisture Content	ASTM D3173
Volatile Matter	ASTM D3175
Ash Content	ASTM D3174

Then, the gross calorific value of raw materials and briquettes is investigated by using bomb calorimeter. This value is very important in order to compare with minimum requirement for commercial briquettes stated by DIN 51731.

### 3. RESULTS AND DISCUSSION

#### 3.1 For Raw Materials

The result of proximate analysis for raw materials is shown in Table 2 below. It is found that the moisture content for all raw materials are still under the average of current local practiced briquette (12.5%) and also satisfies the minimum requirement of DIN 51731 (<10%).

Table 2. Proximate Analysis for Raw Materials

ITEM	EFB	shell	mesocarp fibre
Fixed Carbon (%)	15.083	15.685	14.889
Moisture Content (%)	7.331	8.528	5.200
Volatile Matter (%)	72.962	73.208	75.111
Ash Content (%)	4.624	2.579	4.800

Meanwhile, the gross calorific value for raw materials is shown in Table 3 below. It is expected that the combination of mesocarp fibre and EFB fibre able to produce the briquette which satisfy the minimum requirement of DIN 51731 (17500 J/g). Therefore, in the following sub section, the result of different mixing ratio of EFB fibre and mesocarp fibre will be discussed.

Table 3. Gross Calorific Value for Raw Materials

Materials	Average Calorific Value (kJ/kg)
Shell	19584
Fibre from mesocarp	18098
EFB fibre	17465

#### 3.2 For Briquettes with Different Mixing Ratio

In this section, the physical characteristics and combustion properties of briquettes with different mixing ratio are discussed. The results from the tests are very useful in order to know the effect of different mixing ratio on durability and potential of briquette to be commercial briquette.

##### 3.2.1 Physical Characteristics

Figure 3 below shows the sample for briquette with mixing ratio 80:20 (EFB fibre: mesocarp fibre)



Figure 3. Image of Briquette with Mixing Ratio 80:20

The density of briquette is very important in showing the energy content per unit volume. Thus, high density is necessary in order to reduce the process of uploading the briquette to boilers.

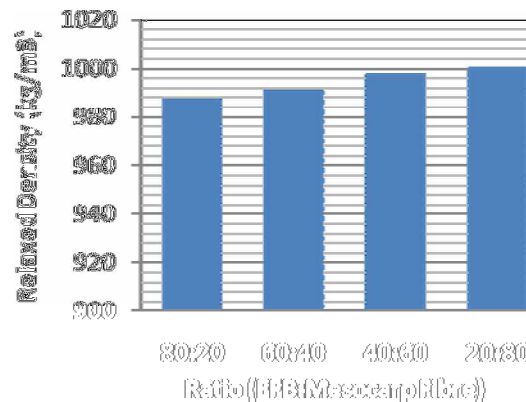


Figure 4. The Relaxed Density of Briquettes Contains Different Mixing Ratio.

As shown in Figure 4 above, there is no significant difference when mixing ratio is changed. The range of density is about 988 kg/m<sup>3</sup> to 1000 kg/m<sup>3</sup>. However, when percentage of mesocarp fibre increased, the relaxed density of briquettes also tends to increase. This is mainly due to the density of mesocarp fibre which slightly higher than the density of EFB fibre.

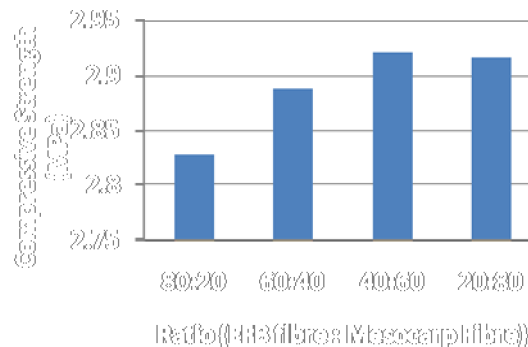


Figure 5. Compressive Strength versus Ratio

During the compression test, the briquettes were pressed until the crack can be observed. Based on Figure 5, it is found that the values of compressive strength are within the range of about 2.83 MPa to 2.92 MPa. There is no significant difference on the values of compressive strength when the weight percentage of EFB fibre increased. All the values obtained already exceeded the minimum value for good resistance to mechanical disintegration of briquette, which is about 2.56 MPa. This limit has been stated by Nor Azmmi, M. et al (2006). Besides, Husain, Z. et al (2002) obtained this value through their compression test on briquette containing mesocarp fibre and shell in the weight ratio of 60:40.

### 3.2.2 Combustion Properties

The tests for determining gross calorific value and proximate analysis have been done on briquettes contain different mixing ratio of EFB fibre and mesocarp fibre. The weight ratios involved are 20:80, 40:60, 60:40 and 80:20.

Gross calorific value for each briquette was obtained by using Bomb Calorimeter. Figure 6 below shows the result of gross calorific value for different weight percentage of EFB fibre in briquette. As shown in Figure 6 below,

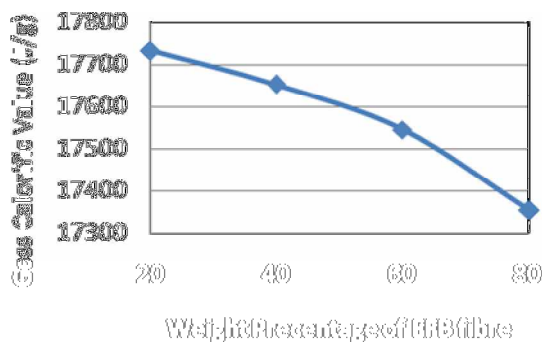


Figure 6. Gross Calorific Value versus Weight Percentage of Fibre

Based on the graph above and the gross calorific value of each raw material, it is found that the existence of mesocarp fibre causes an increase of gross calorific value for briquettes. However, the addition of starch with water has degraded slightly the gross calorific value of briquettes. As reported by Nasrin, A.B. et al (2008), the

minimum gross calorific value for commercial briquette is 17500 kJ/kg or 17500 J/g. This value is a minimum requirement stated by DIN 51731. Based on Figure 6 above, it is found that the briquettes with mixing ratio 60:40, 40:60 and 20:80 satisfy this minimum requirement.

Proximate analysis has been done on the briquettes to investigate the moisture content, volatile matter, fixed carbon and ash content for different mixing ratio of EFB fibre and mesocarp fibre.

Table 4. Proximate Analysis for Briquette with Different Mixing Ratio (EFB fibre: Mesocarp fibre)

	20:80	40:60	60:40	80:20
Ash Content	3.742	3.841	3.777	3.401
Fixed Carbon	13.354	13.502	13.963	15.478
Volatile Matter	72.175	71.935	71.523	71.000
Moisture Content	10.729	10.723	10.737	10.122

The result of proximate analysis as shown in table above shows there is no significant difference between each briquette with different mixing ratio. All the briquettes contain about 10.1 to 10.7% of moisture, 71 to 72% of volatile matter, 13.5 to 15% of fixed carbon and 3.4 to 3.8% of ash. Moisture content is one of important aspects that must be considered to show the quality of briquettes produced. Even though the moisture content of briquettes are slightly higher than DIN 51731's minimum requirement (<10.0%), it is considered still low if compared with moisture content of local practiced palm biomass briquettes (12.5%). This value has been stated by Husain, Z. et al (2002).

## 4. CONCLUSION

Due to the highest production per year of empty fruit bunch (EFB) compared to the production of mesocarp fibre and shell, briquette which contains large portion of EFB fibre is emphasized in this paper. The briquette with ratio 60:40 (EFB fibre: mesocarp fibre) is chosen as this type satisfies the minimum requirement of DIN 51731 and competitive with local practiced briquette. Due to its fibrous structure, this type of briquette will be used for future study. Due to its fibrous structure,

this type of briquette is expected will show good performance of combustion characteristics especially combustion rate and heat release.

## ACKNOWLEDGEMENT

The authors acknowledge the Universiti Teknologi Malaysia for giving cooperation and full of support in this research activity.

## REFERENCES

- [1] Bhattacharya S.C., Augustus Leon M. and Mizanur Rahman M. (1996). A Study on Improved Biomass Briquetting. *Renewable Energy Technologies in Asia*.
- [2] Cattaneo, D. (2003). Briquetting-A Forgotten Opportunity. *Wood Energy*. University of Brescia.
- [3] Chin, O.C., Siddiqui, K. M. (2000). Characteristics of Some Biomass Briquettes Prepared Under Modest Die Pressures. *Biomass and Bioenergy*. 18, 223-228.
- [4] Husain, Z., Zainac, Z., Abdullah, Z. (2002). Briquetting of Palm Fibre and Shell from the Processing of Palm Nuts to Palm Oil. *Biomass and Bioenergy*. 22, 505-509. Pergamon.
- [5] Nasrin, A.B., Ma, A.N., Choo, Y.M., Mohamad, S., Rohaya, M.H., Azali, A. and Zainal, Z. (2008). Oil Palm Biomass as Potential Substitution Raw Materials for Commercial Biomass Briquettes Production. *American Journal of Applied Sciences*. 5 (3), 179-183.
- [6] Nor Azmmi, M., Farid Nasir, A. (2006). *Pressurised Pyrolysis of Rice Husk*. Master Thesis. UTM Skudai.
- [7] Rabier, F., Temmerman, M., Bohm, T., Hartmann, H., Jensen, P. D., Rathbauer, J., Carrasco, J., Fernandez, M. (2006). Particle Density Determination of Pellets and Briquettes. *Biomass and Bioenergy*. 30, 954-963.

# The Effect of Underneath Wavy Surface to the Flow Structure Downstream of a Bluff Body

Jamaluddin Md Sheriff<sup>a</sup>, Asral<sup>b</sup>, Kahar Osman<sup>a</sup>, Muhamad Hasbullah Padzillah<sup>a</sup>

<sup>a</sup>Faculty of Mechanical Engineering,  
Universiti Teknologi Malaysia  
81310 UTM Skudai Malaysia  
E-mail: jamal@fkm.utm.my

<sup>b</sup>Faculty of Mechanical Engineering,  
Universiti Teknologi Malaysia  
81310 UTM Skudai Malaysia  
E-mail: asralst@yahoo.com

## ABSTRACT

The effect of wind forces on structures such as buildings and bridges, especially in normal direction, nearby coastal region is considered significant. The present study investigates the effect wind passing wave-like structure at the upstream to the flow downstream a bluff body. Particle Image Velocimetry (PIV) technique has been used to measure the vector of the velocity of the flow field and to capture the flow pattern in various wavy floor surfaces conditions with various vertical positions of the bluff body. The effect of four different Reynolds Numbers ( $Re$ ) was also investigated. Two dimensional numerical solutions for the same test conditions have been performed by employing  $k-\epsilon$  turbulent model. Sinusoidal surfaces were chosen to simulate the wave conditions for the wavy boundary conditions. The range of  $Re$  was between 1480 and 3300 and the wave amplitudes was in the range of 0.13 to 0.67 of the bluff body height. Comparisons were made against flow over the flat surface for the same flow conditions. For most cases studied, both numerical and experimental results, two vortices were observed to be present in the region in the vicinity close to the bluff body. Larger size of vortices appears in the upper area than those in the lower area. For low amplitude wave, the flow tends to follow the wave and resulted in large negative axial velocity components zone behind the bluff body. As the wave amplitude increases, the size of this negative axial velocity region reduces. For low amplitude wave, the band-width (range of maximum and minimum velocities) of the flow behind the bluff body, increases as  $Re$  increases. However, higher wave amplitude suppresses the flow to the same order of fluctuations. Finally, the

results also show that as the bluff body moves away from the wavy surface, its effect on the flow downstream is minimized.

## Keywords

PIV, LIF, Wavy Surfaces, Vortex, Bluff Body

## 1. INTRODUCTION

Wind driving forces are considered to be an important parameter in the design of infrastructures such as bridges and buildings located nearby coastal region. The direction of the wind loading can possibly come from the land and the sea. The energy of wind exerting on the structures depend on the flow direction to the cross- area, different direction will give different effect to them [9]. The increase of the wind speed could cause high amplitude of water wave. Consequently, the presence of this water wave will affect the flow patterns around the structures. Vortices behind the structures are affected by the geometry of the structures and the presence of water wave. These vortices can create high energy and cause vibration that could jeopardize the structures. Therefore, knowledge of the relationship between water wave and flow behaviour is important. The study of the effect three parameters, elevation, aspect ratio, and side ratio, on bluff body and thereby on the local wind forces were conducted by Lin *et al.* [5]. These parameters influence the bluff-body flow and the wind loads. Lakehal reported that only the base pressure distribution have seriously affected by turbulence intensity and surface roughness [6]. Furthermore, the study in phenomena of wind flow on the bridges were also conducted by Schewe and Larsen [12]. The Reynolds number effects have been caused by changes of the



topological structure of the wake flow. There are limited resources available on the investigation of structures of flow at the coastal or the off-shore areas which the water wave can influence the profile of flow.

The objective of this current study is to investigate the effect of wavy boundaries upon profile of flow after a bluff body. Flow behaviours the downstream region the bluff body were studied by measuring the velocity of perpendicular to the bluff body with the effect of underneath of sinusoidal wavy surfaces were measured and computed. The experiment was carried out in a wind tunnel using Particle Image Velocimetry (PIV) system. Both the magnitude and direction of the velocity vector at each particle location can be inferred, assuming here that the tracer particles are small enough that they move with the wind. The numerical study presented here were conducted with the commercial Computational Fluid Dynamics (CFD) code FLUENT.

## 2. EXPERIMENTAL SETUP

Schematic diagram of the experimental arrangement for this study is shown in Figure 1, showing the location of a bluff body in wind tunnel, a camera, and measurement plane. The bluff body was located at various positions relative to wavy surface. Detailed of bluff body arrangements are shown in Figure 2. The vertical laser sheet was aligned with the flow direction and was illuminated by the laser beam mounted on top of test section. The CCD camera was positioned in front of the tunnel and perpendicular to the light sheet. The inlet airflow was seeded with smoke of vaporizing fog oil droplets. This produced seeding particles in the order of 1  $\mu\text{m}$  in diameter. PIV driver was used to synchronize the laser and the CCD operation and data recorded were saved in the computer.

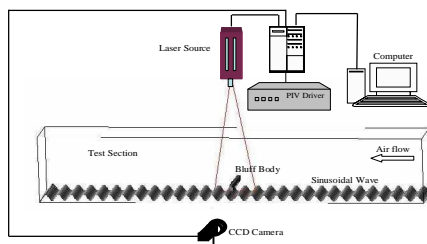


Figure 1 Schematic diagram of experimental setup and PIV system.

The total length of wind tunnel is 683 cm, and the test section dimension is 189 x 29 x 45. The front wall and top wall of the test section were fabricated with 5 mm thick transparent plexiglas. Rear wall was painted black and unmoved sinusoidal wavy surface was placed at the bottom wall. Two blowers of 0.37 HP each were installed to produce the main flow in the tunnel. The blowers are placed in the lower part of the wind tunnel in series. The flow re-circulates in the system. Gate valve was attached after the blower to control the flow rate of the air. The free stream velocity at inlet were  $U_{\infty} = 0.8$  m/s, 1 m/s, 1.5 m/s, and 1.8 m/s were assumed to have a uniform velocity distribution. The smoke generator was placed before the flow into the flow conditioner.

Bluff body with 29 x 1.5 x 3 cm in dimensions is held between walls of test section. The bluff body was always ensured to be parallel with to the wavy surface and perpendicular to the flow direction. The positions of the bluff body were varied in sixteen positions. Each set of position was tested for three different sinusoidal wavy surfaces of different amplitude. Flat surface was also included in the test. To illustrate the movement of wave, positions to the bluff body were varied horizontally along a wavy surface. The sketch of the sixteen bluff body positions can be seen in Figure 2. The position of bluff body was also varied vertically aimed to observe the effect of distance between the bluff body and the wavy surface including the flat surface.

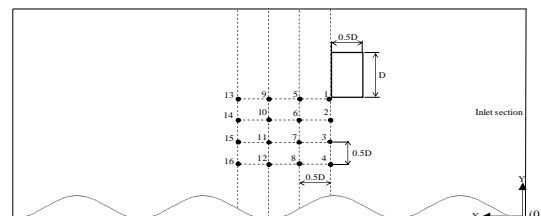


Figure 2 Sketch of the bluff body position (not to scale)

## 3. NUMERICAL APPROACH

Fluent was used as the numerical tool for the numerical calculation to simulate the flow. The first step in the simulation was preprocessing, which involved building the bluff body model in Gambit. Then finite-volume-based mesh was applied and all the required boundary conditions and flow parameters were imposed. The numerical model was then ready to be calculated and produced the desired results. The final step in

analysis was post-processing, which involves organization and interpretation of the data and images.

In this study the simulations were carried out for two-dimensional flow and the Reynolds Average Navier- Stokes Equation (rans) model was used. This choice was made due to the symmetrical behaviour of the bluff body.

The equation for conservation of mass, or continuity equation, can be written as follows:

$$\frac{\partial \rho}{\partial t} + \frac{\partial \rho}{\partial x_i} (\rho u_i) = S_m \quad (1)$$

Equation 1 is the general form of the mass conservation equation and is valid for incompressible as well as compressible flows. The source  $S_m$  is the mass added to the continuous phase from the dispersed second phase (e.g., due to vaporization of liquid droplets) and any user-defined sources.

The momentum equation has described by

$$\frac{\partial}{\partial t} (\rho u_i) + \frac{\partial}{\partial x_j} (\rho u_i u_j) = -\frac{\partial p}{\partial x_i} + \frac{\partial \tau_{ij}}{\partial x_j} + \rho g_i + F_i \quad (2)$$

where  $p$  is the static pressure and  $\rho g_i$  and  $F_i$  are gravitational and external body forces (e.g., forces that arise from interaction with the dispersed phase), respectively.

The momentum equation for Reynolds Average Naviers-Stokes has been written as:

$$\frac{\partial \rho}{\partial t} + \frac{\partial}{\partial x_i} (\rho u_i) = 0 \quad (3)$$

$$\frac{\partial}{\partial t} (\rho u_i) + \frac{\partial}{\partial x_j} (\rho u_i u_j) = -\frac{\partial p}{\partial x_i} + \frac{\partial}{\partial x_j} \left[ \mu \left( \frac{\partial u_i}{\partial x_j} + \frac{\partial u_j}{\partial x_i} - \frac{2}{3} \delta_{ij} \frac{\partial u_l}{\partial x_l} \right) \right] + \frac{\partial}{\partial x_j} (-\overline{\rho u_i u_j}) \quad (4)$$

The turbulent kinetic energy,  $k$  transport equation for The RNG  $k - \epsilon$  model, given by:

$$\frac{\partial}{\partial t} (\rho k) + \frac{\partial}{\partial x_i} (\rho k u_i) = \frac{\partial}{\partial x_j} \left( \alpha_k \mu_{eff} \frac{\partial k}{\partial x_j} \right) + G_k + G_b - \rho \epsilon - Y_M + S_k \quad (5)$$

and for dissipation rate,  $\epsilon$  written by:

$$\frac{\partial}{\partial t} (\rho \epsilon) + \frac{\partial}{\partial x_i} (\rho \epsilon u_i) = \frac{\partial}{\partial x_j} \left( \alpha_\epsilon \mu_{eff} \frac{\partial \epsilon}{\partial x_j} \right) + C_{1\epsilon} \frac{\epsilon}{k} (G_k + C_{3\epsilon} G_b) - C_{2\epsilon} \rho \frac{\epsilon^2}{k} - R_\epsilon + S_\epsilon \quad (6)$$

In these equations,  $G_k$  represents the generation of turbulence kinetic energy due to the mean velocity gradients.  $G_b$  is the generation of turbulence kinetic energy due to buoyancy.  $Y_M$  represents the contribution of the fluctuating dilatation in compressible turbulence to the overall dissipation rate. The quantities  $\alpha_k$  and  $\alpha_\epsilon$  are the inverse effective Prandtl numbers for  $k$  and  $\epsilon$ , respectively.  $S_k$  and  $S_\epsilon$  are user-defined source terms. The model constants  $C_{1\epsilon}$  and  $C_{2\epsilon}$  have values derived analytically by the RNG theory. These values, used by default in FLUENT, are  $C_{1\epsilon} = 1.42$ ,  $C_{2\epsilon} = 1.68$   $C_\mu = 0.0845$ .

#### 4. BOUNDARY CONDITIONS

The boundary conditions applied on this simulation are common to an incompressible flow. Velocity inlet boundary conditions were used to define the flow velocity, along with all relevant scalar properties of the flow, at flow inlets. Present simulation inlet assigned at the right side. Inlet was specified as velocity inlet. Pressure outlet boundary conditions assigned at domain outlet. Bluff body and wavy surface were treated as walled, stationary walled and no-slip boundary condition were applied.

#### 5. RESULT AND DISCUSSION

The following section presents the results and discussions of flow profile after bluff body resulted from the wind flow over wavy surfaces. The experiments were carried out on sixteen positions, four different Reynolds number, and four wavy boundary surfaces variations. For both experimental and numerical methods, the total running data were 416. The raw velocity vector fields were recorded for every running (the sample results are shown in Figures 5, 6, and 7). Eight selected positions are analyzed and exhibited in this paper. The data is analyzed based upon the position and quantity of the vortex or vortices. Analysis is also made for reattachment length of the flow. Other parameters are discussed depending on the nature of the flow. In order to

illustrate the expected changes in the structure of flow, the results were presented in horizontal, vertical, and Reynolds number variations. Similar discussions have also been made by Ahmed and Sharma [1], Barlow *et. Al* [2], and Sohankar [11]. The discussions are focused on the flows of behind the bluff body.

### 5.1 Horizontal Variation

Data for horizontal variations are presented for four various positions. These positions represent the minimum distance between the bluff body and the wavy surfaces. They were position 4, 8, 12, and 16 as shown in Figure 3

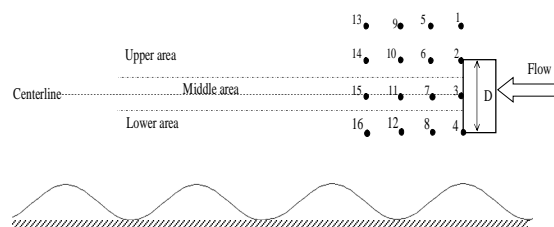


Figure 3 Definition of area of flow behind the bluff body for horizontal variation.

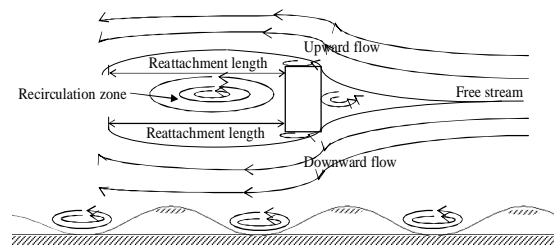


Figure 4 Schematic diagram of flow around the bluff body

The fluid flow passing the bluff body is divided into upward and downward flows at upwind face of the bluff body. This division was also has been used by Kim *et.al* [4]. To characterize the flow behaviour reattachment length will be define as the distance from the downwind face of the bluff body to the point where the separated flow returned to its original datum. In this discussion, the datum is chosen to be at the bottom face or the top face of the bluff body. This definition will be used throughout in this discussion, as seen in Figure 4. Similar approach was also has been used by Johansen *et.al* [3].

Table 1 quantifies the results showing the reattachment length and recirculation zone for experimental and numerical. The number of recirculation zone in the upper area is generally more than those present in the middle and the lower area.

### 5.2 Reynolds Number Variation

To simplify the discussion of the data, extreme positions for vertical variations are presented for location above the crest of wave and above the trough, i.e position 1, 4, 9, and 12 as shown in Figure 3. Sample velocity vectors were discussed in detail for a position of bluff body further from the wave. The qualitative and quantitative data are summarized in tabulated form, will be discussed in summary of discussion section. Flow characteristics based upon typical observation were chosen as the basis of discussion.

In this section, four cases with Reynolds number varying for the highest position the bluff body were analyzed to investigate the influence of wavy surface on flow behaviour behind the bluff body. The locations of recirculation zone and reattachment length as function of Reynolds number are obtained by investigating velocity distribution after the bluff body for experimental and numerical, as presented in Table 2. The definition of recirculation zone and reattachment length will be used throughout in this discussion, as seen in Figure 4.

Comparisons between four ground surfaces data show that the wavy surfaces with various amplitudes have significant effect on flow structure. From this current study can be investigated how the size of the recirculation zone is strongly dependent on the Reynolds number, with a quite evident growth of the recirculation zone size from Reynolds number 1480 to 3300.

Table 2 quantifies velocity vector fields displaying the reattachment length and recirculation zone for experimental and numerical results. The number of recirculation zone in the upper area is more than those present in the lower area. In the middle area less number of recirculation zone are displayed.

### 5.3 Summary of Discussion

In this section, tabulated data of characteristics of the flow for various Reynolds numbers will be discussed. The characterizations are based on the following definition:

- i) Region of negative U-velocities components behind the bluff body- this region is defined as the major activity that occurred behind the bluff body. Volatile flow in this region can affect the variation of drag coefficient for the bluff body. Vortex could be present in this region. Similar characterization has been used by Johansen *et.al* [3]
- ii) Overall bandwidth measured with referenced to crest positive and negative velocities-this bandwidth is defined as measurement of average fluctuations for U-velocities and V- velocities components for all flow Reynolds numbers for the same wave. Bigger bandwidth shows rigorous change in direction of flow.
- iii) Fluctuation of velocities with respect to variations of each Reynolds number-this fluctuation is defined as the effect of Reynolds number to the flow.
- iv) Overall downstream velocities approaching main velocity-this characteristic defines the behaviour of the flow at further downstream as it merges into the main stream flow. High gradient means the flow is approaching the main stream at a faster rate and low gradient means otherwise.

### 5.4 Flat Surface

Moving the bluff body vertically closer to the flat surface showed region of backflow is in the same order of magnitude. High Reynolds number seemed to produce the smallest region. On the other hand, Johansen *et.al* [3] showed backflow region was reduced in size. Also, the overall flow seemed to be reduced in bandwidth. As the bluff body approached the ground, the flow took longer time to merge with the main flow. Larger fluctuation was observed for low Reynolds number when the body was further away, but reversed phenomena were seen at higher Reynolds number.

### 5.5 Wave-1

These case studies were intended to study the effect of wavy surface on the flow behaviour. Wave-1 which was a small amplitude wave with slightly sloped surface was observed to change the flow behaviour. In comparison for four positions where the bluff body located above the crest and the trough of the wave, the size of the region of negative backward flow increased fifty percents as compared to that of flat surface. Again, the size of the region of backward flow was inversely related to Reynolds number, above the crest of wave increased Reynolds number the region becomes smaller for position furthest the wave and larger for position closer to the wave, however for position above the trough is in the contrary. The bandwidth remained to be in the same order. High Reynolds number produced high fluctuation for body close and further away from the wave as compared to that of low Reynolds number.

### 5.6 Wave-2

Wave-2, which had amplitude larger than that of wave-1, was imposed to observe the change of flow behaviour. In comparison of four positions where the bluff body was located above the crest and the trough of the wave, the size of the region of negative backward flow showed decreased half in size as compared to that of wave-1, even though the amplitude of wave-2 was double of wave-1. When the bluff body was located closest to the wave (position 4 and position 12) the region of negative velocity showed greater region for position 12. This is due to the fact that the flow after the bluff body was affected by the crest of the wave that it encountered right after the bluff body. As the bluff body moved further vertically upward (position 1 and position 9), the negative region of the flow was seemed to be in the same order of magnitude but both were lower than that of position 12 and higher than that of position 4. These results show that the effect of wave is diminishing but still present and will eventually reach size of 1D. For this case, the bandwidth increased in both locations as it moved further upward (position 4 to position 1 and position 12 to position 9). Comparing the results of wave-2 with that of wave-1, the latter wave showed smaller bandwidth. This shows that the increase in wave amplitude suppresses the fluctuations of flow for all Reynolds number studied. For location further upward from the wave (position 1

and position 9), the amplitude of the waves showed no significant effect to the fluctuation of the flow.

At position 1, the fluctuation of the flow decreased as the Reynolds number increased. However, as the bluff body moved closer the wave (position 4), the relationship was otherwise. For position 9, the flow again showed decreased in fluctuations as the Reynolds numbers increased but no significant changes in fluctuation for position 12 as the Reynolds numbers were varied.

### 5.7 Wave-3

Further increasing the amplitude of the wave showed further changes to the flow behaviour. Firstly, the region of negative velocity reduced drastically to approximately 20 percent of its size when moving from position 1 (highest) to position 4 (lowest) when the bluff body is above the crest of the wave. Less drastic reduction was observed when bluff body moved from position 9 (highest) to position 12 (lowest) when the bluff body was placed above the trough. For the locations of bluff body above the crest and the trough of the wave, the region of negative velocity seemed to increase. This shows that, the amplitude of the wave has significant effect on the behaviour of the flow right after the bluff body. All results are valid for all Reynolds numbers studied. Secondly, comparing the bandwidths of all flow conditions showed that for the same horizontal position of the bluff body, the bandwidth maintained its magnitude but the magnitude reduced as the bluff body moved vertically closer to the wave, i.e. approximately 70 percent. Larger fluctuation was observed for flow with low Reynolds number when the body was further away, but reversed phenomena were seen at flow with higher Reynolds number. However, no significant effect by Reynolds number to the flow fluctuation as the bluff body moved vertically closer to the wave. Finally, this case study shows no particular trend is observed with respect to the flow approaching main stream velocity. The summary of the quantitative criteria are tabulated in Table 3 and Table 4.

### CONCLUSIONS

The results of this study allow the following conclusions to be drawn:

1. For all cases studied, two vortices appeared in the region in the vicinity close to the bluff body. In some cases only one vortex appeared in this region.
2. Size of vortex in the lower area was found to be smaller than that on the upper area.
3. As the bluff body moves horizontally towards the downhill of the wave, the reattachment length also decreased and vice versa.
4. Non-symmetrical vertical profiles of the velocities were obtained for flow around bluff body with ground effect as oppose to symmetrical flow for flow around bluff body without ground effect.
5. Flow with tend to follow wave with low amplitude and this results wider size of negative region. As the amplitude increases, the size will reduce.
6. Flow bandwidth was investigated to be suppressed as the amplitude of the wave increases. The vertical distance of the bluff body only affect the magnitude of bandwidth.
7. Low amplitude wave was investigated to increase the fluctuation of the flow as the Reynolds number increase. However, for higher wave amplitude, variation in Reynolds number yields the same order of fluctuation.

### REFERENCES

- [1] Ahmed, M.R., and Sharma, S.D: An Investigation On the Aerodynamics of a Symmetrical Airfoil In Ground Effect, *Experimental Thermal and Fluid Science*, (2005). 29:633–647.
- [2] Barlow, Jewel B., Guterres, Rui, and Ranzenbach, Robert: Experimental Parametric Study of Rectangular Bodies With Radiused Edges in Ground Effect. *Journal of Wind Engineering and Industrial Aerodynamics*,(2001). 89:1291–1309.
- [3] Johansen, Stein T., Wu, Jiongyang, and Shyy, Wei: Filter Based Unsteady RANS Computation, *International Journal of Heat and Fluid Flow*, (2004), 25:10-21.
- [4] Kim, M.S., Geropp, D.: Experimental Investigation of the Ground Effect on the Flow Around Some Two-Dimensional Bluff Bodies



with Moving-Belt Technique, *Journal of Wind Engineering and Industrial Aerodynamics*, (1998), 74-76: 511-519.

[5] Lin, Ning, Letchford, Chris, Tamura, Yukio, Liang, Bo, and Nakamura, Osamu: Characteristics of Wind Forces Acting on Tall Buildings, *Journal of Wind Engineering and Industrial Aerodynamics*, (2005), 93:217–242.

[6] Lakehal, D.: Application of the  $k - \epsilon$  Model to Flow Over a Building Placed in Different Roughness Sublayers, *Journal of Wind Engineering and Industrial Aerodynamics*, (1998),73: 59-77.

[7] Matsumoto, Jun, and Kawamura, Hiroshi: DNS of Turbulent Ekman Boundary Layer Over Periodically Wavy Terrain. *Department of mechanical engineering, Science University of Tokyo, Japan*, (2001)

[8] Nakayama, A., and Sakio, K.: Simulation of Flows Over Wavy Rough Boundaries, *Center for Turbulence Research Annual Research Briefs, Kobe University*, (2002).

[9] Richards, P.J., and Hoxey, R.P.: Unsteady Flow On the Sides of a 6 m Cube. *Journal of Wind Engineering and Industrial Aerodynamics*, (2002), 90: 1855–1866.

[10] Rodi, W: Comparison of LES and RANS Calculations of the Flow Around Bluff Bodies. *Journal of Wind Engineering and Industrial Aerodynamics*, (1997), 69-71: 55-75.

[11] Sohankar, A.: Flow Over a Bluff Body From Moderate to High Reynolds Numbers Using Large Eddy Simulation, *Computers & Fluids*, (2006), 35:1154–1168.

[12] Schewe, Gunter, and Larsen, Allan: Reynolds Number Effects in the Flow Around a Bluff bridge Deck Cross Section, *Journal of Wind Engineering and Industrial Aerodynamics*, (1998), 74-76: 829-838.

**Table 1** Location of recirculation zone and reattachment length for horizontal variation.

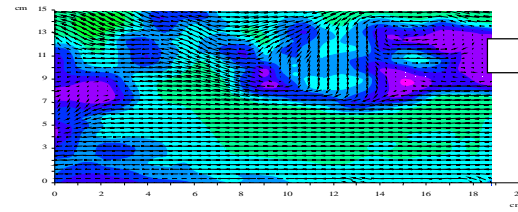
Positions	Surfaces	Experimental					Numerical				
		Location of Recirc. Zone, X/D			Reattach. Length, X/D		Location of Recirc. Zone, X/D			Reattach. Length, X/D	
		Upper Area	Middle Area	Lower Area	Upward Flow	Downward Flow	Upper Area	Middle Area	Lower Area	Upward Flow	Downward Flow
4	Flat	-	-	0.6-1.3	-	1.3	-	0.2-1.1	-	0.3	1
	Wave-1	-	0.3-1.3	0-0.3	1.2	0.3	0-0.4	5.7-6.3	-	0.9	2.3
				2.2-2.6			0.6-0.9				
	Wave-2	0-0.6	0.6-1	-	0.6	1.1	-	-	0.5-3	5.2	3.7
	Wave-3	-	0.2-0.8	-	0.6	1.1	-	0.5-2	-	2	
8	Wave-1	1.1-2	-	0-0.7	-	0.7	1-1.6	-	0-0.4	-	0.4
	Wave-2	0-0.8	-	-	-	1	-	0.7-1.3	-	0.3	-
		1.2-1.9	-	-	-	-	3.6-4.2	-	-	-	-
	Wave-3	0-0.5	0.6-1.2	-	0.5	1.3	1.5-2.4	-	0.5-1.3	2.5	1.3
								2.3-3.2			
12	Wave-1	0-0.4	1.2-1.6	-	0.4	-	1.6-2.2	-	0-0.5	-	0.5
	Wave-2	1-1.5	-	0-0.3	-	0.3	0-0.3	4-4.9	-	0.3	-
			0-0.7	-	-	0.7	0-1.3	0.4-0.8	-	1.3	0.8
	Wave-3	-	-	-	-	-	4.2-5.2	-	-	-	-
16	Wave-1	0.7-1.4	-	-	1.4	-	2.2-2.7	0.1-1	-	-	0.5
	Wave-2	2-2.3	-	0-0.7	-	0.7	2.1-3	-	0.1-0.7	-	0.5
			0-0.5	1.6-2	-	0.2	0-0.8	0.2-1	-	0.8	0.1
	Wave-3	-	-	-	-	-	-	-	-	-	-

**Table 2** Location of recirculation zone and reattachment length at position 1 for various Reynolds numbers

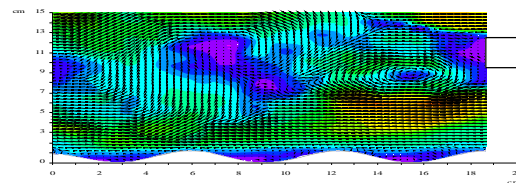
Positions	Surfaces	Experimental					Numerical				
		Location of Recirc. Zone, X/D			Reattach. Length, X/D		Location of Recirc. Zone, X/D			Reattach. Length, X/D	
		Upper Area	Middle Area	Lower Area	Upward Flow	Downward Flow	Upper Area	Middle Area	Lower Area	Upward Flow	Downward Flow
Re = 1400	Flat	-	-	0-0.8	-	0.8	-	0-1	-	2.5	0.5
	Wave-1	0.5-2.4	-	2.6-3	2.5	-	1.4-1.8	-	0-0.7	-	0.5
				0.1-0.6							
	Wave-2	2.8-3.4	-	1.3-2	-	2	0.9-1.5	-	0-0.4	1.4	0.5
	Wave-3	1.2-2	-	0.4-1.2	2	1.2	-	0-1.5	-	1	
Re = 1820	Flat	0.3-1.6	-	1.3-2	1.6	-	2-2.3	0-0.7	-	-	0.5
	Wave-1	0.4-0.8	-	-	-	-	1.5-1.9	-	0-0.4	-	0.5
	Wave-2	0.3-1	-	-	1	-	0-0.5	1.3-1.7	-	0.4	-
	Wave-3	-	-	0.7-1.2	2.2	1.6	-	0.7-1.5	-	-	1
Re = 2775	Flat	0.8-1.4	-	-	1.6	-	0-0.3	0.9-1.3	0-0.5	0.3	-
	Wave-1	3.5-3.9	-	0-2.2	-	-	0.5-1.1	-	0.2	-	
	Wave-2	1.9-2.4	-	0-0.7	-	0.7	0-0.7	1.9-2.2	-	0.7	-
	Wave-3	0-0.9	1.3-2	-	0.9	2	-	0-1.3	-	-	0.6
Re = 3300	Flat	1.1-2	-	3-3.6	-	-	-	0-1.2	-	0.4	1
	Wave-1	0-2	-	1.5-2	0.4	-	1.2-2.4	0-0.8	-	2.5	0.5
	Wave-2	0.6-1.6	-	0.6-1	1.6	1	-	0-1.2	1.3-2.3	0.7	2.2
	Wave-3	0-0.6	-	0-0.9	1.6	0.9	-	0.8-1.5	-	-	1
		0.6-1.9									

Table 3 Characteristics of flow for position 1 and position 4 (above the crest of the wave)

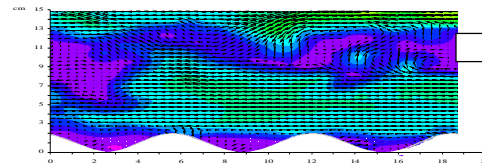
Surfaces	Characteristics of flow	Finding		
		Position 1	Position 4	
Flat	Region negative velocities behind the bluff body	2.6D	2.4D	
	Overall bandwidth measured with reference to peak positive and negative velocity	1.54U <sub>in</sub>	1.4U <sub>in</sub>	
	Overall downstream velocities approaching main velocity	Early	Late	
	Fluctuation of velocities with respect to variation of each Reynolds number	Low Reynolds number	Large	Small
		High Reynolds number	Small	Large
Wave-1	Region negative velocities behind the bluff body	3.7D	2.6D	
	Overall bandwidth measured with reference to peak positive and negative velocity	1.71U <sub>in</sub>	1.46U <sub>in</sub>	
	Overall downstream velocities approaching main velocity	Early	Early	
	Fluctuation of velocities with respect to variation of each Reynolds number	Low Reynolds number	Large	Large
		High Reynolds number	Small	Small
Wave-2	Region negative velocities behind the bluff body	1.86D	1.53D	
	Overall bandwidth measured with reference to peak positive and negative velocity	1.5U <sub>in</sub>	0.72U <sub>in</sub>	
	Overall downstream velocities approaching main velocity	Early	Late	
	Fluctuation of velocities with respect to variation of each Reynolds number	Low Reynolds number	Large	Small
		High Reynolds number	Small	Large
Wave-3	Region negative velocities behind the bluff body	2.6D	0.53D	
	Overall bandwidth measured with reference to peak positive and negative velocity	1.5U <sub>in</sub>	0.48U <sub>in</sub>	
	Overall downstream velocities approaching main velocity	Early	Late	
	Fluctuation of velocities with respect to variation of each Reynolds number	Low Reynolds number	Large	Small
		High Reynolds number	Small	Small



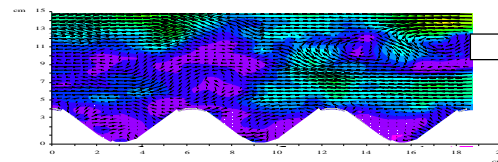
(a) Flat surface



(b) Wave-1



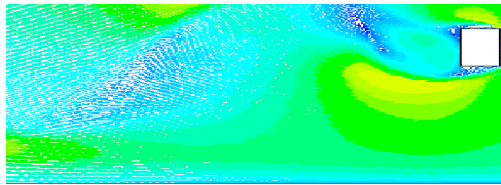
(c) Wave-2



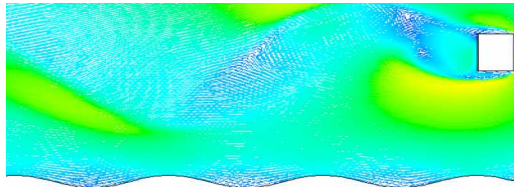
(d) Wave-3

Table 4 Characteristics of flow for position 9 and position 12 (above the trough of the wave)

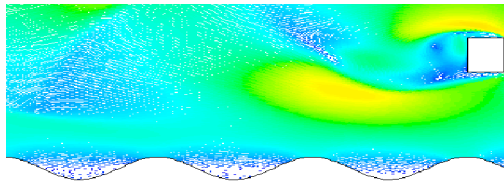
Surfaces	Characteristics of flow	Finding		
		Position 9	Position 12	
Wave-1	Region negative velocities behind the bluff body	3.7D	2.5D	
	Overall bandwidth measured with reference to peak positive and negative velocity	1.7U <sub>in</sub>	1.58U <sub>in</sub>	
	Overall downstream velocities approaching main velocity	Early	Late	
	Fluctuation of velocities with respect to variation of each Reynolds number	Low Reynolds number	Small	Small
		High Reynolds number	Small	Small
Wave-2	Region negative velocities behind the bluff body	1.8D	2.2D	
	Overall bandwidth measured with reference to peak positive and negative velocity	1.91U <sub>in</sub>	1.05U <sub>in</sub>	
	Overall downstream velocities approaching main velocity	Early	Late	
	Fluctuation of velocities with respect to variation of each Reynolds number	Low Reynolds number	Large	Small
		High Reynolds number	Small	Small
Wave-3	Region negative velocities behind the bluff body	2.5D	1D	
	Overall bandwidth measured with reference to peak positive and negative velocity	1.46U <sub>in</sub>	0.5U <sub>in</sub>	
	Overall downstream velocities approaching main velocity	Early	Late	
	Fluctuation of velocities with respect to variation of each Reynolds number	Low Reynolds number	Small	Small
		High Reynolds number	Large	Small



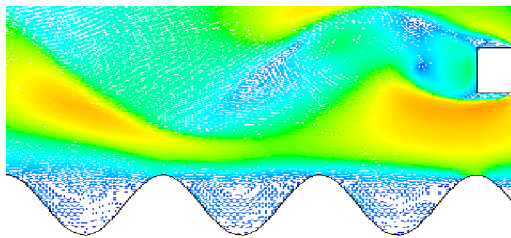
(e) Flat surface



(f) Wave-1



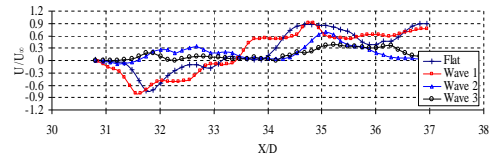
(g) Wave-2



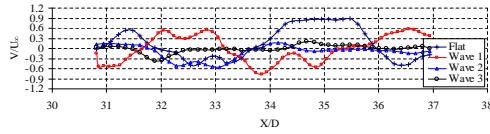
(h) Wave-3



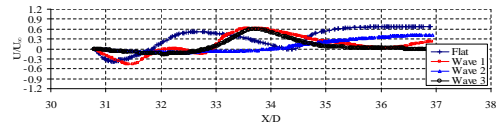
Figure 5 Velocity vector fields for position 1 in various amplitudes of wavy surface for Reynolds Number,  $Re = 2775$ , (a) to (d), experimental, (e) to (h), numerical.



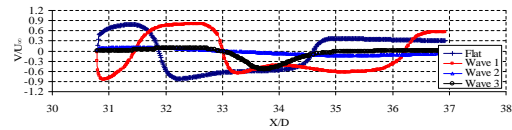
(a)



(b)

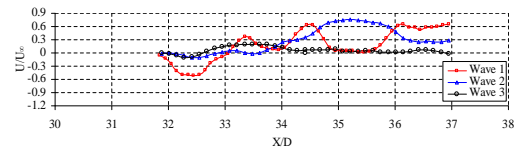


(c)

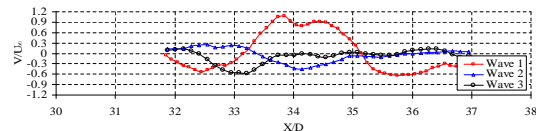


(d)

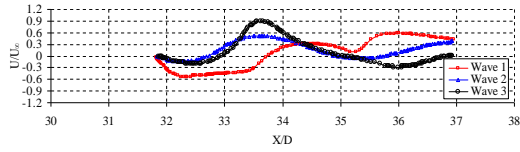
Figure 6 U-velocity and V-velocity components at centerline for position 4 (above the crest of the wave) in various amplitudes of wavy surface, (a), (b) experimental and (c), (d) numerical.



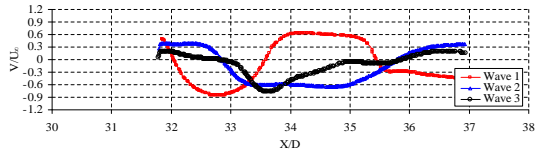
(a)



(b)



(c)



(d)

Figure 7 U-velocity and V-velocity components at centerline for position 12 (above the trough of the wave) in various amplitudes of wavy surface, (a), (b) experimental and (c), (d) numerical.

# Computational Fluid Dynamics Simulation of Stenosis Effect in Upper Human Airways

Zuhairi Sulaiman ,Nasrul Hadi Johari, Kahar Osman

<sup>a</sup>Faculty of Mechanical Engineering  
University of Technology Malaysia,  
81310 Skudai, Johor, Malaysia  
Tel : (6019) 911178  
E-mail : nhadi@ump.edu.my

## ABSTRACT

*Trachea stenosis; one of chronic obstruction pulmonary disease (COPD), inside the human lung was studied in this project as it related to flow behavior. First and second generation of normal and diseased human airways has been constructed and simulated by using numerical modeling. Stenosis, located at mid section of trachea has been varied for four sizes of airways diameters; 20, 40, 60 and 80 percent. Laminar flow with  $Re=1710$  with a boundary condition were used to visualize a normal human breathing (light exercise). Pressure gradient and air flow velocity correlations from top of trachea to the bronchi have been studied. The results showed that stenosis with more than 60 percent diameter, produced significant pressure drop downstream compared to smaller diameter at location T2. The results also showed drastic increased in flow velocity along the centerline. In general, intensive treatment is suggested for stenosis with greater than 60 percent diameter.*

## Keywords

Example:  
*Computational fluid dynamics (CFD), tracheal stenosis, airflow*

## 1. INTRODUCTION

Upper human airways geometry is a small dimension and smaller airways deep down into the lungs which are inaccessible [1]. Upper human airways consist of nose, mouth, pharynx, larynx and trachea. At the edge of trachea, the structure divides into two branches which called bronchi and lung up until the alveolar.

Tracheal stenosis is a lung disease caused by trauma including accidents, chemical exposure,

and intubation. Stenosis is narrowing the trachea and can obstruct the airflow inside the airways. Symptoms can include, but are not limited to the following: shortness of breathe also known as Dyspnea; wheezing or stridor and also asthma [2]. This airflow problem inside the airways can be understood by using one alternative method: computational fluid dynamics.

Numerous CFD studies exist around the worlds which address the problem of air flow and particle deposition in selected segment in human body. Natalya et al [3] have simulated the airflow and aerosol deposition in human lungs to see the trapping particles on the wall and the locations to be recorded. X.Y Luo et al. [4] used CFD to determine the turbulent/transitional airflow effect in lung airways and have compared the result with the laminar and  $k-\epsilon$  model. Besides, Schroter and Sudlow [5] who have made the earliest experimental study of airflow dynamics within a human respiratory network concluded that the inspiratory flows were independent on either Reynolds number or entry velocity profiles.

Besides, there were others CFD studies exist which address the problem of air flow and particle deposition in selected segments [6-13]. However, most of these studies only focussed on symmetric bifurcation airways, and the effects of obstructive airways on airflow and particle deposition is very rare [14]. This study aims to get the correlations of human airway flow parameters with the tracheal stenosis disease. Pressure distribution and airflow velocity are the significant parameters to analyze during inhalation for both normal and diseased trachea.



## 2. METHODOLOGY

In this study, the commercial 3D modeling Software, Solidworks® (version 2008) and CFD code EFD software (Flomerics, version 2008) were used. This software uses the finite volume analysis to solve the Navier-Stokes and continuity equations on an arbitrary shaped flow with appropriate boundary conditions. This project is seeking to model only part of whole breathing cycle with steady inspiration, as occurs when inhaler is used by an asthmatic patient. There is an experiment that showed steady state flow can ‘accurately mimic’ conditions during inspiration for flow rate up to 150 l/min, [15]. His experiment was agreed by X.Y.Luo et al. [16], in order to solve flow modeling of upper airways during heavy breathing, which produces turbulent features.

### 2.1 The geometric model

The airway model was reconstructed based on same physiological details as Horfield et al. [17]. However the model only consists of the trachea, right and left bronchi. Details of the model dimension are in the Table 1. The top view tube of the airways labeled as shown by figure 1. In this simple airways model, the real shape of trachea like C-shape, D-Shape and others are not considered.

In figure 2, it shows how the trachea is having aiding interpreting process of the plotted results. Note that “left” and “right” refer to the anatomical orientation of human body. Normal asymmetric model without disease was built and validated by the study of Calay et al [1] by comparing both results. Later, the Normal Asymmetric Model reconstructed with the stenosis growth. The modification of the model configurations are for the purpose of studying the flow behavior effect by stenosis.

*Table 1: Geometric details of the model.*

Segment	Diameter (m)	Length (m)	Branching angle (°)
Trachea	0.016	0.1	0
Left	0.012	0.05	73
Right	0.0111	0.022	35

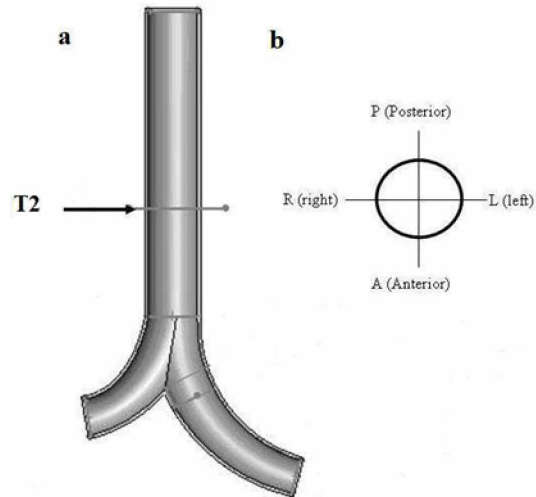


*Figure 1. Reconstruct model of normal trachea and its 1<sup>st</sup> to 2<sup>nd</sup> generations. (a) Normal trachea and main bronchi with the location of stenosis, T2 that would be happen. (b) Cross-sectional of trachea model*

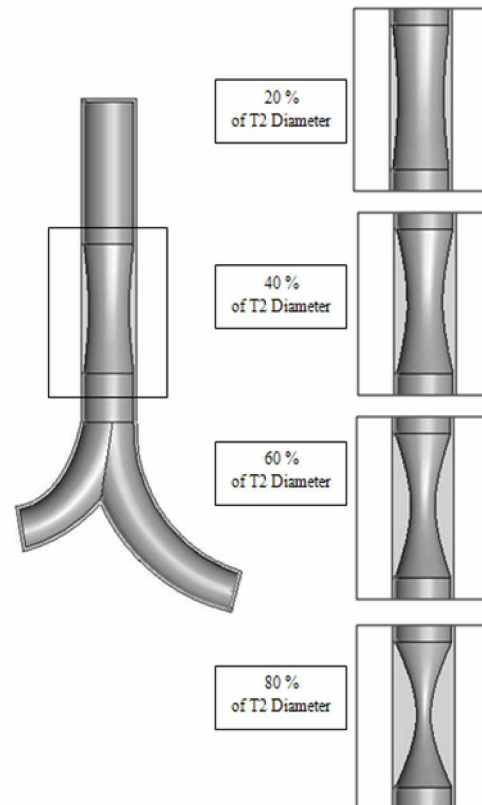


*Figure 2. Size of stenosis growth by diameter percentages at T2. Narrowing of diameter sizes is made from 20 percent up to 80 percent.*

## 2.2 Boundary conditions

Velocity inlet boundary condition at inflow boundary was used. The assumption being made that the volume distal to the respiratory bronchioles is the same through the lung and that the change in volume is the same everywhere. The laminar flow is performed in the inlet trachea area as it is occurs during normal breathing.

The study used the velocity inlet from Calay et al. [1]. The airflow studies as describe in Table 2. A mesh boundary layer was also imposed. The temperature effect was assumed isothermal; steady state condition with constant Reynolds number is used. Incompressible flow is assumed as this flow has low March number. No-slip boundary condition is assumed [18]. The airways walls assume to be a rigid body.

Table 2 .Breathing boundary parameters. Note that high  $Re$  numbers is defined for heavy exercise.

Parameter	Laminar Incompressible flow (Normal)
Reynolds number, $Re$	$1.710 \times 10^3$
Inlet Velocity	$1.5625 \text{ ms}^{-1}$
Pressure outlet	101325 Pa
Density	$1.225 \text{ kg/m}^3$
Viscosity	$1.7894 \times 10^{-5} \text{ kg/ms}^{-1}$
No.of nodes/cell in 3D model	306388/202353

## 2.3 CFD validations

The CFD validity for particle deposition in trachea and primary airways is compared by using the velocity field in an axisymmetric tube by Calay et al.[1] (Figure 3). The velocity profile at the left bronchi has a good agreement with previous study with acceptable skewness shapes. The skewed velocity profile, found toward the inner wall of left bronchi is similar to the validation model due to the secondary flow motion when flow transitions from proximal airway to the distal airway.

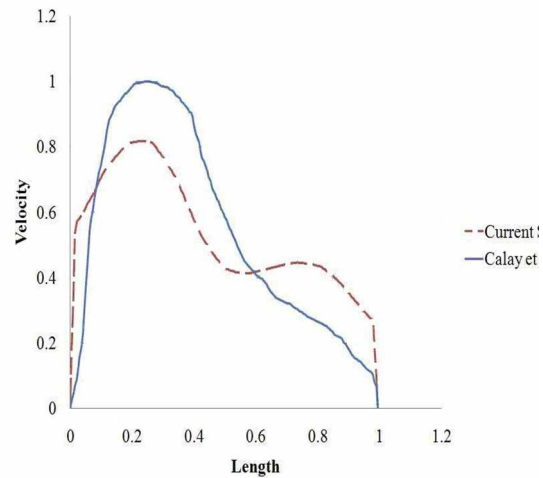


Figure 3: Dimensionless axial velocity profile at left bronchi. This study in red line followed the Calay et al trend (blue line)

## 4. RESULTS

Simulation of airflow inside the normal and stenosis trachea was performed and the results are determined by analyzing the pressure drop and air velocity .

### 4.1 Pressure Distribution

The growth of stenosis alters the pressure gradient and later increases the peak pressure at the bifurcation (refer to figure 4). Normal operating pressure is 101kPa and it consistent until with the 0.4D of stenosis. However, the effect of constriction can be observed significantly when the size of stenosis is above 60 percent of the airway trachea. The highest pressure drop was observed at the downstream 0.8D stenosis and it produced the highest pressure gradient. As the pressure drops in the lung, the driving force for the respiratory system will reduce

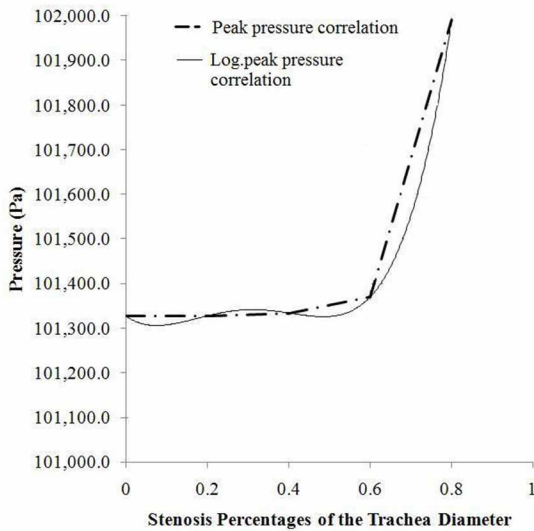


Figure 4: Peak pressure correlation of airflow when pass through stenosis of different size at location T2.

#### 4.2 Velocity profile

Air velocity changed due to the obstruction of stenosis in the trachea. Figure 7 showed the constriction of stenosis at T2 location produced different air velocity flow along the airways.

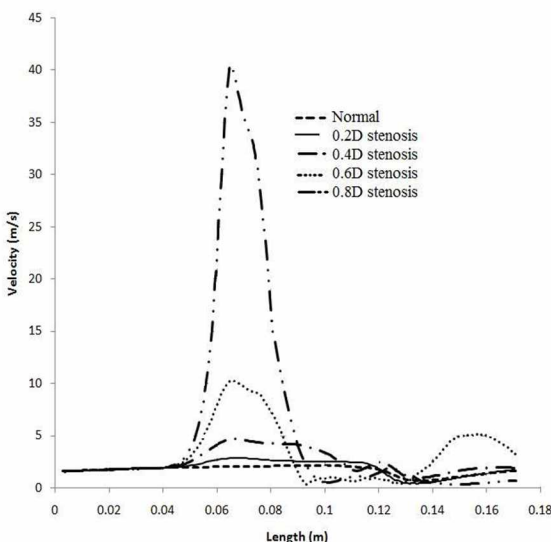


Figure 5: Air velocity at central line along the trachea. Different graph line determined the air velocity at different model of trachea, normal and stenosis structure.

With inlet velocity of  $1.56 \text{ ms}^{-1}$ , it remains stable for upstream and downstream of T2 location inside the normal trachea. Stenosis with the size  $0.8D$  increased the velocity up to  $40 \text{ ms}^{-1}$  compared to only  $2 \text{ ms}^{-1}$  for  $0.2D$  when it flow at T2. Although the growing of diameter is 4 times ( $0.2D$  to  $0.8D$ ), it produce a big different output flow. At extreme velocity,  $40 \text{ ms}^{-1}$  which occurred from  $0.8D$ , it significantly increased 20 times from the flow of  $0.2D$ . It seems like when stenosis increased, it changed the upstream and downstream at location T2 to become stronger.

## 7. CONCLUSION

Finally, this CFD method had solved a fluid dynamics problem inside the human lung and produced the analysis of the effects of obstructed airway narrowing and occlusion on the airstreams. The results showed that stenosis with more than 60 percent diameter, produced significant pressure drop downstream compared to smaller diameter at location T2. The results also showed drastic increased in flow velocity along the centerline. In general, intensive treatment is suggested for stenosis with greater than 60 percent diameter.

## REFERENCES

- [1] Calay R.K, Kurujareon J. and Holdo A.E., "Numerical simulation of respiratory flow patterns within human lung" *Respiratory physiology and neurobiology*, 130,201-221]
- [2] Hermes C. Grillo, "Surgery of Trachea and Bronchi", Harvard University Gazette, 2004].
- [3] Natalya Nowak, Prashant P.Kakade, and Ananth V.Annapragada, "Computational Fluid Dynamics Simulation of Airflow and Aerosol Deposition in Human Lungs" *Annals of Biomedical Engineering*, Vol.31,pp.374-390, 2003.
- [4] X.Y.Luo, J.S.Hinton,T.T.Liew and K.K.Tan, "LES modeling of flow in a simple airway model" *Elsevier Medical Engineering & Physics* 26 , 4003-413, 2004 2]
- [5] Schroeter, R.C., & Sudlow,M.F "Flow patterns in models of human bronchial airways", *Respiration Physiology*, 7, 341-355, 1969
- [6] Balashazy I, Hofmann W, Mortenen TB, "Inspiratory particle deposition in airway bifurcation models", *J Aerosol Sciece*,1991;22:15-30]

- [7] Balashazy I, Hofmann W, "Particle deposition in airway bifurcations", *J. Aerosol Science*, 1993;24:722-45
- [8] Hofmann W, Balashazy I, "Particle deposition within airway bifurcation", *Staub Reinhalt Luft* 1991;33:178-82
- [9] Kim SC, Iglesias JA, "Deposition of inhaled particles in bifurcating airway models: 1. Inspiratory deposition, *J Aerosol Med* 1989;2:1-14
- [10] Kim SC, Fisher DM, Lutz DJ, Gerrity TR, "Particle deposition in bifurcating airway models with varying airway geometry, *J Aerosol Science* 1993;25:567-81
- [11] Koblinger L, Hofmann W, Monte Carlo, "Modelling of aerosol deposition in human lungs. Part 1: simulation of particle transport in stochastic lung structure. *J Aerosol Science* 1990;27:119-38
- [12] Lee JW, Goo JH, "Numerical simulation of airflow and inertial deposition of particles in a bifurcating channel of square cross section, *J Aerosol Med* 1992;5:131-54
- [13] Sclesinger RB, Lippmann M., "Particle deposition in casts of the human upper tracheobronchial tree". *Am Ind Hyg Assoc J* 1972;33:237-51
- [14] Mark B.M., Jayaraju, S.T. Lacor C., Mey JD., Noppen M, Vincken, W. Verbanck, "Tracheal stenosis" A Flow Dynamics Study, *Journal Applied Physiology* 2006.
- [15] Olson DE, Sudlow MF, Horsfield K, Filey GP, "Convective patterns of flow during inspiration", *Arch Int Med* 1973;131:51-7
- [16] J.S. Hinton, T.T. Liew and K.K. Tan, "LES modeling of flow in a simple airway model" *Elsevier Medical Engineering & Physics* 26, 4003-413, 2004
- [17] Horsfield, K. Dart, G. Olson, D.E. Filley, G.F. & Cumming, "Models of the human bronchial tree", *Journal of Applied Physiology*, 31, 207-217
- [18] Yang X.L. and Liu Y., "Simulation of effect of COPD on respiratory flow, Tsinghua University Press & Springer-Verlag, 2006.
- [19] Van Wylen, G.J. and Sonntag, R.E., "Fundamental of Classical Thermodynamics", section 5.9, John Wiley and Sons Inc., New York 1965].

# Study on Characteristics of Briquettes Contain Different Mixing Ratio of EFB Fibre and Mesocarp Fibre

H. M. Faizal, Z. A. Latiff, Mazlan A. Wahid, Darus A. N.

Faculty of Mechanical Engineering  
Universiti Teknologi Malaysia, 81310 UTM Skudai  
Tel: (+60)7-5534657  
E-mail: mfaizal@fkm.utm.my

## ABSTRACT

Based on Malaysia Palm Oil Statistics, the production of palm biomass residues such as shell, mesocarp fibre and empty fruit bunch (EFB) increased significantly from year to year. These residues especially mesocarp fibre and EFB were dumped in areas adjacent to the palm oil mills. Therefore, briquetting technology is expected can improve this waste disposal by converting these residues into solid fuels with higher energy content per unit volume. In this paper, the physical characteristics and combustion properties of briquettes contain new proposed mixture has been investigated. This mixture composed of mesocarp fibre and EFB fibre in different weight ratios. EFB fibre is obtained after drying process by superheated steam with the pressure ranges from 1.0 to 1.5 bar and temperature ranges from 100 to 120°C. Based on several tests done for investigating the capability of new mixture of palm biomass briquettes, it was found that the briquette with weight ratio of 60:40 (EFB fibre: mesocarp fibre) satisfies the minimum requirement for commercial briquette DIN 51731. Besides, this ratio is selected due to the emphasis on the use of large portion of EFB.

## Keywords

Briquetting, briquette, palm biomass, combustion rate, shell, mesocarp fibre, EFB fibre, DIN 51731

## 1. INTRODUCTION

As reported by Malaysia Palm Oil Board (MPOB, 2006), the production of shell, mesocarp fibre and EFB in Malaysia for year 2006 are  $5.20 \times 10^6$  tonne/year,  $9.66 \times 10^6$  tonne/year, and  $17.08 \times 10^6$  tonne/year respectively. Therefore, the utilization of these residues is very important in order to

prevent waste and dumping areas adjacent to the mills.

Conversion of these residues into briquette is one of the methods to improve the properties especially in term of energy content per unit volume. As explained by Bhattacharya et al. (1996), densification (briquetting, pelletizing and baling) is a process that can improve the storage and transportation of biomass fuel.

Chin and Siddiqui (2000) have conducted an experiment to study the combustion rate on various biomass briquettes such as raw husks, sawdust and several others. The compaction pressure was within the range of 1 to 7 MPa. It was found that the burning rate increased as the binder content increased. The binding agents used in their experiment were molasses and starch.

In year 2002, an experiment that was carried out by Husain et al. (2002) explain the physical and combustion characteristics of current local briquettes contain mesocarp fibre and shell in the ratio of 60:40. They used starch as binding agent (10% of the weight of residues) with addition of water (50% of the weight of residues). They found that the combustion of heap of briquettes in the stove releases about 0.5kW, air-fuel ratio was about 10.2 and ash content was 5.8%. Besides, the average compressive strength of about 2.56 MPa is considered as a value for good resistance for disintegration.

Meanwhile, in year 2008, Nasrin et al. (2008) studied the physical and combustion characteristics of palm biomass briquettes containing EFB fibre and palm kernel cake (PKC). The weight ratio for PKC + EFB fibre + sawdust was 30:5:65. In this case, sawdust plays a role as binder. In their study, they found that the strength of briquettes increased when the sawdust was added.



Thus, in this paper, the physical and combustion properties of briquettes contain EFB fibre and mesocarp fibre with different mixing ratios were studied. One ratio then will be selected for further study in the future to investigate the effect of compaction pressure on the combustion characteristics of these briquettes such as combustion rate. The selection of ratio was based on two aspects. The first aspect is minimum requirement of commercial briquette DIN 51731 in term of gross calorific value and moisture content. Meanwhile, the second aspect is the emphasis on the use of EFB.

## 2. METHOD AND PREPARATION

The palm biomass residues (EFB fibre and mesocarp fibre) have been collected and grinded into powder.

For making briquette, EFB fibre powder and mesocarp fibre powder are mixed in weight ratio of 20:80, 40:60, 60:40 and 80:20. As binding agent, starch (20% of weight of residues) and water (80% of weight of residues). After these materials have been mixed homogeneously by using mixer, it is dried under ambient temperature for about 6 hours before pressing process.

For briquetting, constant compaction pressure is used, which was 7 MPa. Figure below shows the experimental setup for briquetting. The setup consists of YASUI hydraulic hand press, die set, load cell and data logger.



Figure 1: Experimental Setup for Briquetting

After briquetting, the briquette produced is removed from the die set and it is dried at room temperature for about 1 week to obtain stability and rigidity.

The relaxed density of briquettes is obtained by determining the volume first using stereometric method. This method has been described by Rabier et al (2006). Stereometric method is based on the measurement of the dimensions such as diameter, length, width and height. The measurement is done by using caliper gauge. By knowing the volume and mass of briquette, the relaxed density is determined by using geometric formulae.

The compressive strength of briquette is investigated by using INSTRON machine. Figure below shows the sample of briquette undergoes the compression test.



Figure 2. Briquette Undergoes Compression Test

Meanwhile, the proximate analysis has been done for raw materials and briquettes produced to investigate the moisture content, volatile matter, fixed carbon and ash content. Table 1 below shows the standard used for this proximate analysis.

Table 1: Standard Used for Proximate Analysis

Properties	Standard Used
Moisture Content	ASTM D3173
Volatile Matter	ASTM D3175
Ash Content	ASTM D3174

Then, the gross calorific value of raw materials and briquettes is investigated by using bomb calorimeter. This value is very important in order to compare with minimum requirement for commercial briquettes stated by DIN 51731

### 3. RESULTS AND DISCUSSION

#### 3.1 For Raw Materials

The result of proximate analysis for raw materials is shown in Table 2 below. It is found that the moisture content for all raw materials are still under the average of current local practiced briquette (12.5%) and also satisfies the minimum requirement of DIN 51731 (<10%).

Table 2. Proximate Analysis for Raw Materials

ITEM	EFB	shell	mesocarp fibre
Fixed Carbon (%)	15.083	15.685	14.889
Moisture Content (%)	7.331	8.528	5.200
Volatile Matter (%)	72.962	73.208	75.111
Ash Content (%)	4.624	2.579	4.800

Meanwhile, the gross calorific value for raw materials is shown in Table 3 below. It is expected that the combination of mesocarp fibre and EFB fibre able to produce the briquette which satisfy the minimum requirement of DIN 51731 (17500 J/g). Therefore, in the following sub section, the result of different mixing ratio of EFB fibre and mesocarp fibre will be discussed.

Table 3. Gross Calorific Value for Raw Materials

Materials	Average Calorific Value (kJ/kg)
Shell	19584
Fibre from mesocarp	18098
EFB fibre	17465

#### 3.2 For Briquettes with Different Mixing Ratio

In this section, the physical characteristics and combustion properties of briquettes with different mixing ratio are discussed. The results from the tests are very useful in order to know the effect of different mixing ratio on durability and potential of briquette to be commercial briquette.

##### 3.2.1 Physical Characteristics

Figure 3 below shows the sample for briquette with mixing ratio 80:20 (EFB fibre: mesocarp fibre)



Figure 3. Image of Briquette with Mixing Ratio 80:20

The density of briquette is very important in showing the energy content per unit volume. Thus, high density is necessary in order to reduce the process of uploading the briquette to boilers.

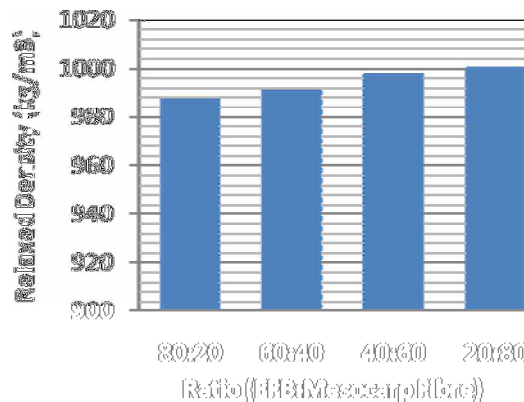


Figure 4. The Relaxed Density of Briquettes Contains Different Mixing Ratio.

As shown in Figure 4 above, there is no significant difference when mixing ratio is changed. The range of density is about 988 kg/m<sup>3</sup> to 1000 kg/m<sup>3</sup>. However, when percentage of mesocarp fibre increased, the relaxed density of briquettes also tends to increase. This is mainly due to the density of mesocarp fibre which slightly higher than the density of EFB fibre.

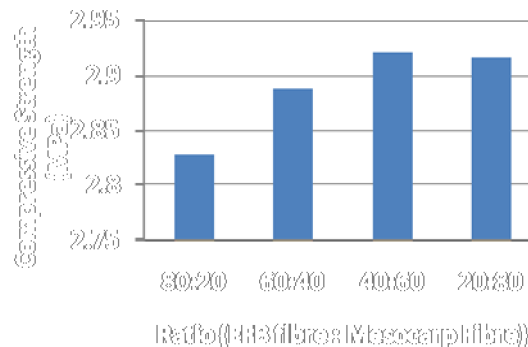


Figure 5. Compressive Strength versus Ratio

During the compression test, the briquettes were pressed until the crack can be observed. Based on Figure 5, it is found that the values of compressive strength are within the range of about 2.83 MPa to 2.92 MPa. There is no significant difference on the values of compressive strength when the weight percentage of EFB fibre increased. All the values obtained already exceeded the minimum value for good resistance to mechanical disintegration of briquette, which is about 2.56 MPa. This limit has been stated by Nor Azmmi, M. et al (2006). Besides, Husain, Z. et al (2002) obtained this value through their compression test on briquette containing mesocarp fibre and shell in the weight ratio of 60:40.

### 3.2.2 Combustion Properties

The tests for determining gross calorific value and proximate analysis have been done on briquettes contain different mixing ratio of EFB fibre and mesocarp fibre. The weight ratios involved are 20:80, 40:60, 60:40 and 80:20.

Gross calorific value for each briquette was obtained by using Bomb Calorimeter. Figure 6 below shows the result of gross calorific value for different weight percentage of EFB fibre in briquette. As shown in Figure 6 below,

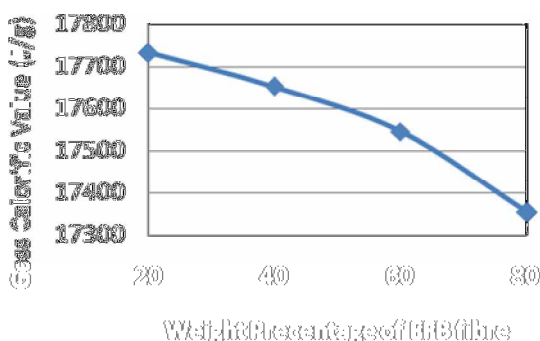


Figure 6. Gross Calorific Value versus Weight Percentage of Fibre

Based on the graph above and the gross calorific value of each raw material, it is found that the existence of mesocarp fibre causes an increase of gross calorific value for briquettes. However, the addition of starch with water has degraded slightly the gross calorific value of briquettes. As reported by Nasrin, A.B. et al (2008), the

minimum gross calorific value for commercial briquette is 17500 kJ/kg or 17500 J/g. This value is a minimum requirement stated by DIN 51731. Based on Figure 6 above, it is found that the briquettes with mixing ratio 60:40, 40:60 and 20:80 satisfy this minimum requirement.

Proximate analysis has been done on the briquettes to investigate the moisture content, volatile matter, fixed carbon and ash content for different mixing ratio of EFB fibre and mesocarp fibre.

Table 4. Proximate Analysis for Briquette with Different Mixing Ratio (EFB fibre: Mesocarp fibre)

	20:80	40:60	60:40	80:20
Ash Content	3.742	3.841	3.777	3.401
Fixed Carbon	13.354	13.502	13.963	15.478
Volatile Matter	72.175	71.935	71.523	71.000
Moisture Content	10.729	10.723	10.737	10.122

The result of proximate analysis as shown in table above shows there is no significant difference between each briquette with different mixing ratio. All the briquettes contain about 10.1 to 10.7% of moisture, 71 to 72% of volatile matter, 13.5 to 15% of fixed carbon and 3.4 to 3.8% of ash. Moisture content is one of important aspects that must be considered to show the quality of briquettes produced. Even though the moisture content of briquettes are slightly higher than DIN 51731's minimum requirement (<10.0%), it is considered still low if compared with moisture content of local practiced palm biomass briquettes (12.5%). This value has been stated by Husain, Z. et al (2002).

### 4. CONCLUSION

Due to the highest production per year of empty fruit bunch (EFB) compared to the production of mesocarp fibre and shell, briquette which contains large portion of EFB fibre is emphasized in this paper. The briquette with ratio 60:40 (EFB fibre: mesocarp fibre) is chosen as this type satisfies the minimum requirement of DIN 51731 and competitive with local practiced briquette. Due to its fibrous structure, this type of briquette will be used for future study. Due to its fibrous structure,

this type of briquette is expected will show good performance of combustion characteristics especially combustion rate and heat release.

## ACKNOWLEDGEMENT

The authors acknowledge the Universiti Teknologi Malaysia for giving cooperation and full of support in this research activity.

## REFERENCES

- [1] Bhattacharya S.C., Augustus Leon M. and Mizanur Rahman M. (1996). A Study on Improved Biomass Briquetting. *Renewable Energy Technologies in Asia*.
- [2] Cattaneo, D. (2003). Briquetting-A Forgotten Opportunity. *Wood Energy*. University of Brescia.
- [3] Chin, O.C., Siddiqui, K. M. (2000). Characteristics of Some Biomass Briquettes Prepared Under Modest Die Pressures. *Biomass and Bioenergy*. 18, 223-228.
- [4] Husain, Z., Zainac, Z., Abdullah, Z. (2002). Briquetting of Palm Fibre and Shell from the Processing of Palm Nuts to Palm Oil. *Biomass and Bioenergy*. 22, 505-509. Pergamon.
- [5] Nasrin, A.B., Ma, A.N., Choo, Y.M., Mohamad, S., Rohaya, M.H., Azali, A. and Zainal, Z. (2008). Oil Palm Biomass as Potential Substitution Raw Materials for Commercial Biomass Briquettes Production. *American Journal of Applied Sciences*. 5 (3), 179-183.
- [6] Nor Azmmi, M., Farid Nasir, A. (2006). *Pressurised Pyrolysis of Rice Husk*. Master Thesis. UTM Skudai.
- [7] Rabier, F., Temmerman, M., Bohm, T., Hartmann, H., Jensen, P. D., Rathbauer, J., Carrasco, J., Fernandez, M. (2006). Particle Density Determination of Pellets and Briquettes. *Biomass and Bioenergy*. 30, 954-963.

# The Flow Modeling of Aneurysm under Physical and Physiological Condition

Ishkrizat Taib<sup>1</sup>, Kahar Osman<sup>2</sup>, Mohammed Rafiq Abd Kadir<sup>3</sup>

<sup>1</sup>Faculty of Mechanical and Manufacturing Engineering  
Universiti Tun Hussein Onn Malaysia,  
Tel : (013) 7270011 ext 51. Fax : (021) 7270077  
E-mail : iszat@uthm.edu.my

<sup>2</sup>Faculty of Mechanical Engineering  
Universiti Teknologi Malaysia  
Tel : (021) 7270011 ext 51. Fax : (021) 7270077  
E-mail : Kahar@fkm.utm.my

## ABSTRACT

*The investigation on the pulsatile flow in an aneurysm can yield unexpected predicament. This study will analyzed the pulsatile flow using numerical modeling for various physical and physiological conditions at peak and late systole times. The results of this study shows the presence of the vortex is observed at aneurysm region for both physical and physiological condition. The presence of the vortex is proportional to the increase of flow activity at the aneurysm. The flow activity is much higher at distal end compared proximal end region. The differnt of flow activity show the different strength of the vortex occurred at the aneurysm bulge. The results also show HBPE peak systole distribute the highest value of the pressure among others condition which is exhibits the high risk of the aneurysm from rupture.*

## Keywords

*Abdominal aortic aneurysm, pulsatile flow, numerical modeling.*

## 1. INTRODUCTION

Aneurysm is focal dilatation of the blood vessel due the weakening of the main aorta which prone to be ruptured if not surgically treated. The physician determines that the possibility of rupture in aneurysm is at the largest diameter [1]. In clinical practice, AAA is considered the surgical treatment after the maximal diameter of aorta exceeds 5-6 cm [2]. The probability of the aneurysm to rupture is high if the diameter of the aneurysm exceed more than 5cm and the aneurysm will be treated using the synthetic graft [1]. R.C. Darling et al reported that the rate of the

aneurysm rupture between 4.1 cm and 7 cm is around 25% while the rupture of the aneurysm less than 4 cm expansion per year is around 9.5% [3]. Rupture of abdominal aortic aneurysm has high morbidity and mortality rates. Many people died before entering the operating room. On that reason, the surgeon has made a difficult decision because of the uncertainty about the risk rupture of abdominal aortic aneurysm. During physiological pulsatile flow, the largest aneurysm demonstrates turbulence rather than in small aneurysm [4]. However, the correlation between the largest of the aneurysm and probability the aneurysm ruptures is still in question mark by many researchers. The expansion of the aneurysm segment eventually increase the risk of the aneurysm rupture [5] although, rupture could occur in a small aneurysm [1]. The aneurysm rupture is a major complication at the disease vessel especially in AAA which lead to 90 percent of the patients died [6]. Hence, the technology will facilitate the medical doctor to make the early prediction of aneurysm rupture on the patient and directly make the decision for endovascular repair (EVAR).

*Pulsatile flow characteristics in AAA have been considered by many researchers [7,8] in which the flow pattern is different from that of steady flow. The hemodynamic stresses are higher in pulsatile flow rather than in steady flow [8] as illustrated in the pulsatile flow behavior which is significant to determine the development of the atherosclerosis and thrombus formation in AAAs. Peattie et al [11] has simulated the resting time in vivo for fusiform model for the pulsatile flow to analyze the flow behavior and shear stress distribution at aneurysm wall. As a result, the flow behavior inside the aneurysm becomes unstable proportional to the increment of the bulge aneurysm size. Egelhoff et al [4] has*



studied both numerically and experimentally, on the effect of the pulsatile flow on the hemodynamic state which may influence the growth of the aneurysm under resting and exercise time. Taylor et al [9] have studied the numerical modeling for physiological lumbar curvature under resting and exercise condition on rigid aneurysm wall. The lower extremity exercise may limit the progression of the AAA and resistive hemodynamic condition [10].

## 2. METHODOLOGY

### 2.1 The geometry of the simplified aneurysm

The simplified 3D model of aneurysm is considered based on the real AAA geometry captured by S.K Badreddin Giama [14]. This model differs from other sinusoidal shape models in the aspect of the overall diameter of the aneurysm. Based on the actual shape, which has a more rounded shape, the current model also maintains the ratio of the diameter of the aneurysm to the ratio of the aorta. The aneurysm has a maximum diameter of  $D$ , length between proximal and distal end of  $L$  and  $d$  for undilated aortic diameter. The current model offers the overall  $D/d$  of the aneurysm to be about 80% of the real shape.

The aneurysm bulge in model A is considered as advanced stage in AAA which may be prone to rupture.

### 2.2 Parameter assumptions and blood properties

There are several assumptions imposed on the model in this study. The assumptions include incompressible flow, homogeneous, Newtonian flow for the rigid axisymmetric wall and the flow is predicted as a laminar flow for the Reynolds number below 2000 and Reynolds number more than 2000 is considered as turbulence flow. Besides that, the effect of Normal Blood Pressure (NBP) and High Blood Pressure (HBP) toward the aneurysm was studied in order to

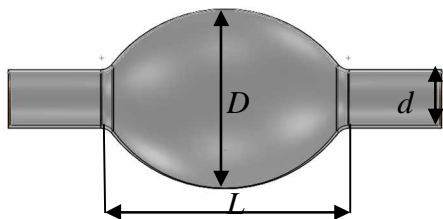


Figure 1: The simplified Abdominal Aortic Aneurysm model.

Table 1: Different of aneurysm diameter used in simulation.

Model	L/d	D/d
A	4	3.3

identify the significant of the NBP and HBP drive the AAA development. Additional to the NBP and HBP flow conditions, this study also include the exercise flow condition to investigate the effect of the combinations of the flow conditions. Resting condition is used as the basis of the comparisons.

Miki Hirabayashi et al [15] reported that the blood exhibit as a non-Newtonian behavior. Other researchers reported that Newtonian liquid is sufficient for the case of large blood vessel. In this study, Newtonian condition is used due to the fact that the artery is large enough for the effect of non-Newtonian to be significant. There is no significant data had confirmed the difference for both non-Newtonian and Newtonian fluid [16] which the researcher found that the non-Newtonian effect was the minimal changes in arterial flow pattern. The Newtonian blood properties can be assumed; blood density is 1050 kg/m<sup>3</sup>, Newtonian reference viscosity is 0.00345 N.s/m<sup>2</sup>, specific heat (Cp) is 4182 J/(kg\*K), Dynamic viscosity is 0.012171 Pa\*s and thermal conductivity is 0.6 W/(m\*K).

### 2.3 Governing equation and boundary conditions

In these simulations, Computational Fluid Dynamic software called Engineering Fluid Dynamic (EFD) was used. Both velocity inlet and pressure outlet are computed to solve the continuity and Navier-Stokes equations. Hence, the physical laws describing the problem of AAA are the conservation of mass and the conservation of momentum. For such a fluid, the continuity and Navier–Stokes equations are as follows:

$$\frac{\partial u_i}{\partial x_i} = 0 \quad (1)$$

$$\rho \left( \frac{\partial u_i}{\partial t} + u_j \frac{\partial u_i}{\partial x_j} \right) = - \frac{\partial P}{\partial x_i} + \mu \frac{\partial^2 u_i}{\partial x_j \partial x_j} + f_i \quad (2)$$

Where  $u_i$  = velocity in the  $i^{\text{th}}$  direction,  
 $P$  = Pressure,  $f_i$  = Body force,  $\rho$  = Density,

$\mu_i$  = Viscosity and  $\delta_{ij}$  = Kronecker delta. The shear stress,  $\tau$  at the wall of aneurysm is calculated based on a function of velocity gradient only:

$$\tau = \mu \frac{\partial u}{\partial y} \quad (3)$$

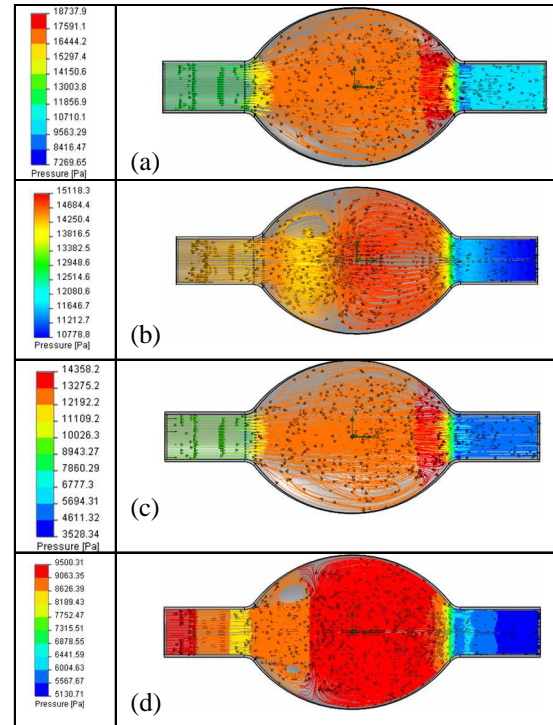
Where  $\partial u/\partial y$  is the velocity gradient along the aneurysmal wall taking into considerations the fluid viscosity. Therefore, the simple viscous fluids considered with linear relationship.

The inlet flow is considered fully developed parabolic flow, with zero radial velocity at the inlet, no slip applied at the wall and zero velocity gradient at the outlet. The inlet boundary condition setting is pulsatile velocity [4] for the resting and exercise condition which whilst the outlet boundary condition setting is pulsatile pressure [13] for time dependent.

### 3. RESULTS AND DISCUSSION

The imbalance flow inside the advanced aneurysm yield unexpected problem. The imbalance flow experiences the presence of the vortex at the aneurysm region. This study discusses the effect of pressure distribution at the aneurysm during physical and physiological condition. The high blood pressure in given more attention since the high possibility of aneurysm rupture is reported in this condition. However, NBP is also taken into consideration as comparison for those HBP results. Flows visualize the presence of vortex for HBPE, HBPR, NBPE and NBPR peak systole at the aneurysm wall as seen in Figure 2. Figure 2 shows the flow pattern for the pressure distribution at the advanced aneurysm wall during exercise and resting time for HBP and NBP. HBPE peak systole flow is shown the dominated vortex which fills the entire bulge of the aneurysm wall. The high pressure distribution exerted at the aneurysm wall will weaken the

Figure 2: Flow pattern for the pressure inside the advanced AAA during the resting time and exercise time waveform for NBP and HBP (a) peak systole exercise time HBP shows the dominated vortex formation inside the aneurysm. (b) peak systole resting time HBP shows the



recirculation flow occur at the proximal end (c) peak systole exercise time NBP shows the vortex formation inside the AAA region (d) peak systole resting time NBP shows the vortex formation at the proximal end.

aneurysm wall. The flow during HBPR peak systole shows the translation and growth of the primary vortex at distal end of the aneurysm. However, the secondary vortex is seen in proximal end of aneurysm. The vortex strength is observed more strong in distal end rather than in proximal end. The investigation on the NBPE peak systole shows the vortex is conquered the entire bulge of the aneurysm when the blood flow travels from proximal end to distal end. NBPR peak systole shows the presence of the vortex only in proximal end which covered roughly one third from the aneurysm area. As summarized, the pressure distribution is shown to be highest during HBPE peak systole compared those others results. Similar phenomenon of vortex formation is seen in HBPE and NBPE peak systole.

Moreover, the investigation on the vortex formation is continued for late systole time for both HBP and NBP during exercise and resting time which is illustrated in Figure 3. The presence of the vortex is seen to dominate the whole region of aneurysm during HBPE late systole as seen in Figure 3(a).

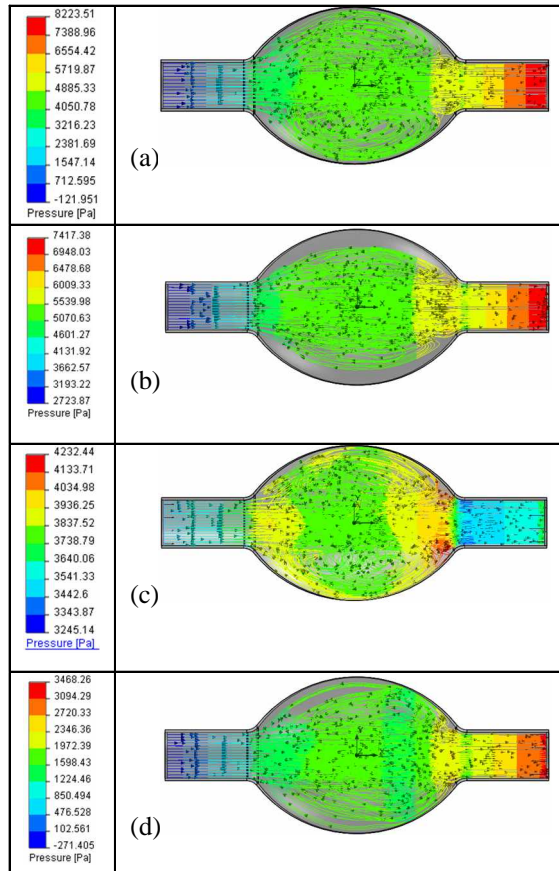


Figure 3: Flow pattern for the pressure inside the advanced AAA during the resting time and exercise time waveform for NBP and HBP (a) late systole exercise time HBP shows the dominated vortex in aneurysm region (b) Late systole resting time HBP shows the formation of vortex at distal end of aneurysm region (c) late systole exercise time NBP shows the vortex formation at the proximal end of AAA region (d) late systole resting time NBP shows the vortex formation at distal end of aneurysm.

The presence of vortex is increased dramatically from proximal end to distal end and finally maximum at proximal end of aneurysm during HBPR late systole. On the other hand, the vortex is observed to be subjugated the whole area of aneurysm during NBPE late systole. During NBPR peak systole, the vortex is formed at the distal end end of aneurysm.

As summary, the pressure distribution is highest at the HBPE late systole which is illustrated in figure 3(a). The vortex is observed to be form at distal end of aneurysm for all condition

which explained the possibility of the aneurysm rupture is high in this location.

## 7. CONCLUSION

This study shows the presence of the vortex is observed at aneurysm region for both physical and physiological condition. The presence of the vortex is proportional with the increase of flow activity at the aneurysm. The flow activity is much higher at distal end compared proximal end region. The different of flow activity shown the different strength of the vortex occurred at the aneurysm bulge. The results also shows HBPE peak systole distributed the highest value of the pressure among others condition which exhibits the high risk of the aneurysm from rupture.

## ACKNOWLEDGMENT

The support-of the University of Teknologi Malaysia, under the Computational Fluid Mechanic Lab Project grant, lead by Dr.Kahar Osman and under grant number 79235 is gratefully acknowledged.

## REFERENCES

- [1] R. Budwig, D. Elger, H. Hooper and J. Slippy, Steady flow in abdominal aortic aneurysm models, *ASME J. Biomech. Eng.* 115 (1993), 419–423.
- [2] Lederle FA, Wilson SE, Johnson GR, Reinke DB, Littooy FN, Acher CW, et al. Immediate repair compared with surveillance of small abdominal aortic aneurysms. *N Engl J Med* 2002;346(19):1437–44.
- [3] R.C. Darling, C.R. Messina, D.C. Brewste and L.W. Ottinger, Autopsy study of unoperated abdominal aortic aneurysms: The case for early detection, *Circulation* 56 (1977), 161–164.
- [4] C.J. Egelhoff, R.S. Budwig, D.F. Elger, T.A. Khraishi and K.H. Johansen, Model studies of the flow in abdominal aortic aneurysms during resting and exercise conditions, *J. Biomech.* 32 (1999), 1319–1329.
- [5] Szilagyi DE, Elliott JP, Smith RF. Clinical fate of the patient with asymptomatic abdominal aortic aneurysm and unfit for surgical treatment. *Arch Surg* 1972;104(4):600–6.
- [6] Khalil M. Khanafer a, Prateek Gadhoke a, Ramon Berguer a,b and Joseph L. Bull a. Modeling pulsatile flow in aortic aneurysms: Effect of non-Newtonian properties of blood. *Biorheology* 43 (2006) 661–679.
- [7] D.F. Elger, J.B. Slippy, R.S. Budwig, T.A. Kraishi and K.H. Johansen, A numerical study of the hemodynamics in a model AAA, *Bio-Med. Fluids Eng.* 212 (1995), 15–22.

- [1] E.A. Finol and C.H. Amon, Blood flow in abdominal aortic aneurysms: Pulsatile flow hemodynamics, *ASME J. Biomech.Eng.* 123 (2001), 474–484.
- [2] Taylor, T.W., Yamaguchi, T., 1994. Three-dimensional simulation of blood flow in an abdominal aortic aneurysm- steady and unsteady flow cases. *ASME Journal of Biomechanical Engineering* 116, 88-97.
- [3] Evangelos Boutsianis, Michele Guala, Ufuk Olgac, Simon Wildermuth, Klaus Hoyer, Yiannis Ventikos, Dimos Poulidakos, " CFD and PTV Steady Flow Investigation in an Anatomically Accurate Abdominal Aortic Aneurysm", *Journal of Biomedical Engineering*.131(2008),2406-2414.
- [4] Peattie, R.A., Schrader, T., Bluth, E.I., Comstock, C.E., 1994. Development of turbulence in steady flow through models of abdominal aortic aneurysms. *Journal of Ultrasound Medicine* 13, 467-472.
- [5] R.A. Peattie, T.J. Riehle and E.I. Bluth, Pulsaile flow in fusiform models of abdominal aortic aneurysms: flow fields, velocity patterns and flow-induced wall stresses, *ASME J. Biomech. Eng.* 126 (2004), 438–446.
- [6] Tayfun E. Tezduyar<sup>1</sup>, Sunil Sathe, Matthew Schwaab and Brian S. Conklin<sup>1</sup>, "Arterial fluid mechanics modeling with the stabilized space-time fluid-structure interaction technique," *International Journal for Numerical Methods in Fluids*, vol. 57, (no. 5), pp. 601-629, 2008.
- [7] Badreddin Giama S.K<sup>1</sup>, Kahar Osman<sup>1</sup> and Mohamed Rafiq Abdul Kadir<sup>1,2</sup>, "Numerical Modeling of Fusiform Aneurysm with High and Normal Blood Pressure".
- [8] Miki Hirabayashi et al, "A lattice Boltzmann study of blood flow in stented aneurism", *Future Generation Computer Systems*, Elsevier B.V, 20 (2004) 925–934.
- [9] K.M. Khanafer et al. "Modeling pulsatile flow in aortic aneurysms: Effect of non-Newtonian properties of blood", *IOS Press, Biorheology* 43 (2006) 661–679.



# Experimental Evaluation of the Effect of Taper Die on Lubricant Performance

Syahrullail, S., Teh, S.C., Najib, Y.M.

*Faculty of Mechanical Engineering, Universiti Teknologi Malaysia,  
81310 UTM, Skudai, Johor, Malaysia.  
Tel : (60) 7-5534-661 Fax : (60) 7-5566-159  
E-mail : syahruls@fkm.utm.my  
E-mail : tsaycheong@hotmail.com  
E-mail : mnajibyahaya@yahoo.com*

## ABSTRACT

In this work, the effects of taper dies on lubricant performance were investigated. The experimental works were done by using cold work plane strain extrusion apparatus. Two types of taper die were prepared. Paraffinic mineral oil and RBD palm stearin were used as test lubricant. The evaluations were focused on the forming load (extrusion load), tool and workpiece surface roughness. From the results, we found that the die shape helps to reduce forming load, which could contribute in minimizing the energy.

## Keywords

*Extrusion, paraffinic mineral oil, palm stearin*

## 1. INTRODUCTION

Forming process is designed to exploit the material property or plasticity, the ability to flow as solids without deterioration of the properties. In other words, it is a permanent deformation of a material under tension, compression, shear or a combination of loads. There are two types of mechanical work where material undergoes plastic deformation which is cold work and hot work. Some example of application of hot and cold working is extrusion, forging and rolling. In this study, we are focusing the cold work forward extrusion.

Extrusion is a compression forming process in which the work metal is forced to flow through a die opening to produce a desired cross-sectional shape. The mechanical extrusion of metals and alloys embraces two methods, that is hot and cold extrusion. In hot extrusion, the operation is performed at a suitable elevated temperature. In

cold extrusion, the billet is placed in the die at room temperature. The advantages of extrusion includes, variety of sections possible (hot extrusion), grain structure and strength enhancement (cold extrusion), close tolerance (cold extrusion), and less or no material wastage. Both methods may be done by the direct and indirect process. Most engineering and structural metals may be extruded either hot or cold.

However, in extrusion process, there are other important factors that are influenced the final product, such as the die shape [1], the properties of the workpiece, workpiece diameter ratio, and the frictional condition at the billet and die interface. Tools and dies play an important role such as to determine the deformation behavior, the plastic flow [2] and the deformation load. The filling of the die cavity of deformed shape in extrusion process is also affected by the die shape. Hence, determining the optimal die angle is crucial part in die making process [3].

## 2. MATERIALS AND METHODS

### 2.1 Experimental apparatus

Figure 1 shows the schematic sketch of plane strain extrusion apparatus used in the experiments. The main components are container wall and taper die, and workpiece (billet). The taper die has two types of die half angle, which are 30° and 60°. The taper die is made from tool steel SKD11 and necessary heat treatment were done before the experiments. The experimental surface of taper dies (surface which contact the billet) were polished with abrasive paper and have surface roughness Ra less than 0.5 micron. The lubricant with specified amount was applied on this surface before the experiments. The other



surfaces of experimental apparatus were applied with same type of test lubricant.

The material of billet is aluminum alloy AA6061. The billets' shape was made by the NC wire cut electric discharge machining device. The surface roughness of experimental surface of billet (surface which contact the taper die) is 0.1 micron.

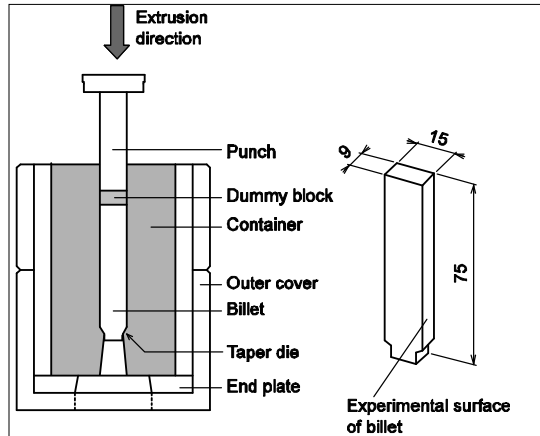


Figure 1 Schematic sketch of cold work plane strain extrusion apparatus and billet.

## 2.1 Taper die

Figure 2 shows the schematic sketch of two types of taper used in the experiments. They have 30° and 60° of die half angle respectively. Test lubricant was applied on this area before the experiment.

## 2.2 Test lubricant

The testing lubricant is RBD palm stearin. RBD is an abbreviation for Refined, Bleached and Deodorized. Palm stearin is the solid fraction obtained by fractionation of palm oil after crystallization at controlled temperature. In this experiments, a standard grade of palm stearin which incorporated in Malaysian Standard MS 815:1991 was used. The results obtained from the experiments used RBD palm stearin were compared with additive free paraffinic mineral oil VG460 (written as paraffin VG460).

## 2.3 Experimental procedure

The plane strain extrusion apparatus was assemble and placed on the press machine. The forming load and displacement data were

recorded by computer. The experiments were carried out at room temperature. Extrusion was stopped at piston stroke of 35 mm. The ram speed is constant to 0.85 mm/s. After the experiment, the partially extruded billets were taken out from the plane strain extrusion apparatus and the combined billets were separated for the surface roughness measurement and metal flow analysis.

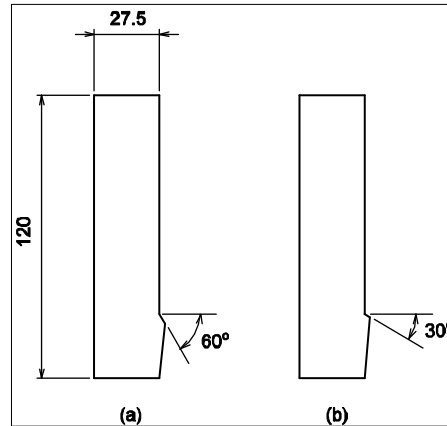


Figure 2 Schematic sketch of taper die with (a) 60° and (b) 30° die half angle.

## 3. RESULTS AND DISCUSSION

### 3.1 Extrusion load

Figure 3 shows the extrusion load – piston stroke curves. The figure shows that the extrusion load in the process reached the steady state condition at the piston stroke 20 mm. From the figure, taper die 60° has lower extrusion load compared to experiment which used taper die 30°. The extrusion load difference is approximately 30 kN. For taper die 60°, there are no obvious difference in extrusion load of RBD palm stearin and paraffinic mineral oil VG460. However, for taper die 30°, RBD palm stearin shows lower extrusion load compared to paraffinic mineral oil VG460. The extrusion load difference is approximately 7 kN.

The increment of die half angle makes the decrement of the shear friction on the material (billet), and decrease the forming load. For taper die 30°, the friction due to the shear friction and sliding friction is greater [4]. The condition between the billet and taper die constituted mixed lubrication condition by a thin lubricant layer and adsorption of fatty acids from the palm oil played role of maintaining the lubricant layer [5] and give low extrusion load compared to paraffinic

mineral oil. Low friction coefficient of palm oil also influenced this result [6].

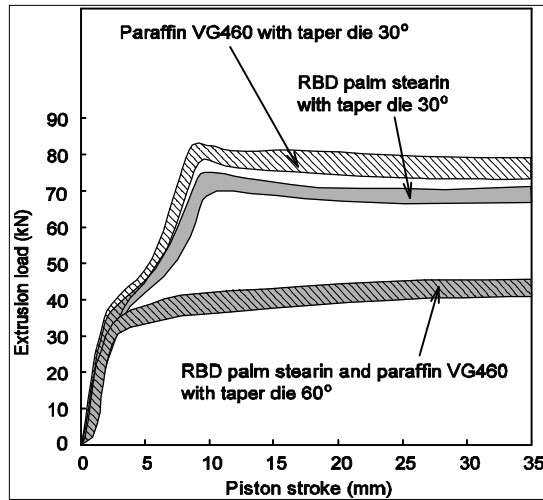


Figure 3 Extrusion load – piston stroke curves.

### 3.1 Surface finish

The distributions of arithmetic mean surface roughness  $R_a$  along on the experimental surface of billet (sliding plane) were measured. The experimental surface of billet is surface of billet which contacts the taper die and container. The measure direction is perpendicular to the extrusion direction. The average value of the arithmetic mean surface roughness  $R_a$  is shown in Table 1. From the figure, the surface roughness  $R_a$  for product area of billet which extruded with RBD palm stearin is greater compare to those extruded with paraffinic mineral oil VG460 for taper die 30°. This shows that RBD palm stearin, which is in semi-gel condition (due to its high melting point), creates thick lubricant layer. It condition could reduce the metal-to-metal contact and reduce the extrusion load.

The CCD pictures of billet experimental surface at product area for all experimental condition are shown in Figure 4. There are no severe wear were found.

Table 1 The average value of the arithmetic mean surface roughness of the experimental surface of billet.

	Taper die 30°	Taper die 60°
RBD palm stearin	0.50 $\mu\text{m}$	0.45 $\mu\text{m}$
Paraffinic mineral	0.44 $\mu\text{m}$	0.43 $\mu\text{m}$

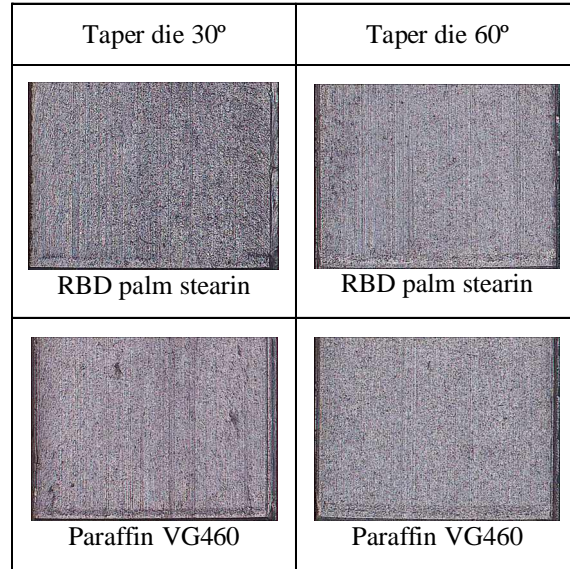


Figure 4 CCD pictures of experimental surface of billet at product area (5 $\times$  magnification)

## 4. CONCLUSION

The effects of taper die on lubricant performance were investigated by using cold work plane strain extrusion apparatus. Test lubricant was RBD palm stearin and additive free paraffinic mineral oil VG460. The experimental results show that the increment of taper die half angle could reduce the forming load; however, this will eliminate the ability of RBD palm stearin to reduce the forming load. There are no obvious differences in product (billet) surface quality after the forming process.

## ACKNOWLEDGMENT

The author would like to thank Faculty of Mechanical Engineering, Universiti Teknologi Malaysia and IRGS research grant No. 77024 for their cooperation on this research.

## REFERENCES

- [1] S.Y.Lim, F.C.Lin, "Influences of the Geometrical Conditions of Die and Workpiece on the Barreling Formation during Forging-Extrusion Process", *Journal of Material Processing Technology*, vol.144, pp.54-58, 2003.

- [1] J.W.Pilarczyk, J.Markowski, "FEM Analysis of Effect of Die Angle on Strain and Stress State in Process of Drawing of Steel for Prestressed Concrete", *Metalurgija*, vol.44, no.3, pp.227-330, 2005.
- [2] S.Z.Qamar, "FEM Study of Extrusion Complexity and Dead Metal Zone", *Archives of Materials Science and Engineering*, vol.36, no.2, pp.110-117, 2009.
- [3] J.A.Schey, "Tribology in Metal Forming", ASME, U.S., 1983.
- [4] F.P. Bowden and D. Tabor, "The Friction and Lubrication of Solids", Oxford University Press, U.K., 1986.
- [5] B.L. Abdulquadir and M.B. Adeyemi, "Evaluations of Vegetable Oil-based as Lubricants for Metal-forming Process", *Industrial Lubrication and Tribology*, Emerald, volume 65, no.5, pp. 242-248, 2008.

# Unsteady Flow Analysis for Trachea and Main Bronchi for Various Reynolds Number

Mohd Zamani Ngali, Kahar Osman

Faculty of Mechanical Engineering,  
Universiti Teknologi Malaysia,  
81310, Skudai, Johor, Malaysia.  
E-mail : zamani@uthm.edu.my, kahar@fkm.utm.my

## ABSTRACT

*The inspiratory flow characteristics in a three-generation lung airway were numerically investigated using a finite difference method for fully two-dimensional laminar Navier–Stokes equations. The three-generation simplified airway geometry was extracted from previous works. Particular attention was paid to establishing relations between the increase in inlet flow Reynolds number and the overall flow characteristics, including flow patterns, vortex developments and pressure distributions. The streamline patterns for inlet flow Reynolds number 1000, 2000 and 3000 showed that as the Reynolds number increased, the flow became unsmooth and vortices developed whenever high enough flow velocity encountered stiff changes in directions. The correlations between flow speed, change in directions and vortex developments in this study suggested that in order to assure the maximum amount of inhaled particles progress deep in the airways, inhaled aerosol should be taken with deep and slow breaths rather than fast and short breaths.*

## Keywords

*Three-generation lung airway, Navier-Stokes equation, simplified geometry.*

## 1. INTRODUCTION

The respiratory diseases such as asthma, emphysema and bronchitis are connected with the air pollution in the nowadays-urban environment and the number of these diseases tends to increase. The therapy of respiratory diseases mostly uses pharmaceuticals in the form of aerosol delivered into the lungs. The efficiency and efficacy of the therapy are also dependent on

the size of the drugs particles, their transport and deposition in the lungs.

Very little information on the pattern of the particle deposition or the effectiveness of the aerosol treatment is available and this forms an effective area of clinical respiratory research. However, knowledge of the airflow mechanism within the airway is the first step in the understanding of the movement of the particles and their deposition in the respiratory airflow network. The objective of understanding the airflow characteristics can be approached either using physical modeling or numerical modeling of the respiratory airflow network.

The airways network has quite small dimension and the smaller airways deep down into the lungs are inaccessible. It is difficult to simulate the highly asymmetric branching structure together with curvatures of the bifurcation in physical models. Research on scale models shows that it is not easy to retain dynamic similarity to the physical model. Therefore, most experimental and simulation techniques for the study of physical scale models of the airflow in the lung are limited up to the third generations only.

Several studies of respiratory airflow dynamics have been performed until now. An extensive literature search is provided in Kurujareon [1]. Schroter and Sudlow [2] made the earliest experimental study of airflow dynamics within a human respiratory network. Their test model was of a single symmetric bifurcation and flow was at Reynolds numbers ranging from 50 to 4500. They concluded that the inspiratory flows were independent on either Reynolds number or entry velocity profiles. Other experimental studies of the respiratory airflow dynamics also concluded that the respiratory flow patterns were

likely dependent on the airway geometry (Chang and El Masry, [3]; Isabay and Chang, [4]; Pedley, [5]). There also have been a number of studies using CFD in both two- and three-dimensional bifurcating tube models. A significant difference was found in between the flow patterns predicted by the symmetric and the asymmetric models and also between two- and three-dimensional models.

The respiratory flow is more dependent on oscillatory time dependent flow and the onset of turbulence is likely within the central airway region. Although there are few studies using a realistic model of the central airway, including asymmetric bifurcation and multiple generations of the branching (Gatlin et al., [6]; Wilquem and Degrez, [7]), the results are based on the assumption of the steady flow. The aim of this study is to numerically simulate the time dependent flow phenomenon within a symmetric bifurcation model of the central airway at different breathing conditions.

## 2. NUMERICAL MODELLING

The simplified airway geometry in this study was extracted from previous works by T. W. H. Sheu et al. [8] and Y. Liu et al. [9]. The problem, known as the Weibel model of the human central airway, has been considered by Wilquem and Degrez [7]. The domain, schematically shown in Fig. 1, involves a mother branch and a set of symmetrically configured lateral and medial branches. Downstream of the mother branch, there exist two bifurcation points which are symmetric to the mother branch centerline.

The principal dimensions and the turning angles for this test model are also shown in the schematic diagram. In this study, the full domain was computed in order to avoid the Coanda effect present even in a symmetric configuration. Three inhalation flow inlet with Reynolds number of 1000, 2000 and 3000 were studied. The airway wall surface was assumed to be in no-slip condition. The air flow was modeled using Navier-Stokes with Splitting Method finite difference solution approach.

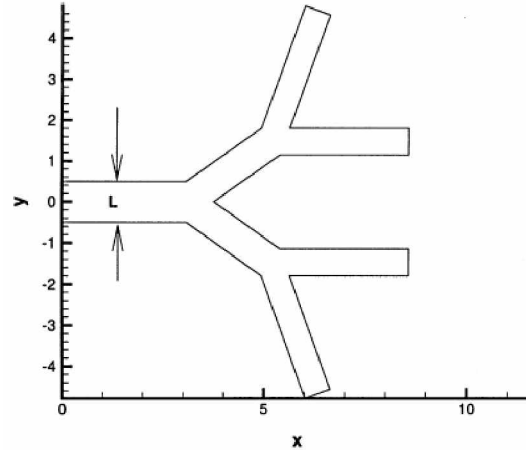


Figure 1: The outline of the airways under the present investigation, T. W. H. Sheu et al. [8].

The temporal integration of the Navier-Stokes system is achieved using a semi-implicit splitting method, similar to the method of Karniadakis et. al [2] and others. Consider the Navier-Stokes expression below

$$\frac{\partial v^0}{\partial t} + N(v^0) = -\nabla p + \frac{1}{R_e} L(v^0), \quad (1)$$

where  $L$  is the linear viscous term and  $N$  is the non-linear advective term,

$$\begin{aligned} L(v^0) &= \nabla^2 v^0, \\ N(v^0) &= v^0 \cdot \nabla v^0. \end{aligned} \quad (2)$$

Integrate the above equation over one time step,  $\Delta t$ ,

$$\int_{t_k}^{t_{k+1}} \frac{\partial v^0}{\partial t} dt + \int_{t_k}^{t_{k+1}} N(v^0) dt = - \int_{t_k}^{t_{k+1}} \nabla p dt + \int_{t_k}^{t_{k+1}} \frac{1}{R_e} L(v^0) dt, \quad (3)$$

where  $k$  is the time step.

The first term is easily evaluated without approximation,

$$\int_{t_k}^{t_{k+1}} \frac{\partial v^0}{\partial t} dt = v^0_{k+1} - v^0_k. \quad (4)$$

A semi-implicit method treats linear terms implicitly for stability, and non-linear term is



achieved with the second-order Adams-Bashforth method,

$$\int_{t_k}^{t_{k+1}} N(v) dt = \left[ \frac{3}{2} N(v^k) - \frac{1}{2} N(v^{k-1}) \right] \Delta t \quad (5)$$

The explicit treatment of the nonlinear term avoids sampling  $\bar{N}$  at the leading time step, which would result in nonlinear algebraic equations, requiring further iteration. The pressure term is treated by reversing the order of integration and differentiation, then introducing time-averaged pressure,

$$\int_{t_k}^{t_{k+1}} \nabla p dt = \nabla \left[ \int_{t_k}^{t_{k+1}} p dt \right] = \nabla \bar{p}^{k+1} \Delta t. \quad (6)$$

Implicit treatment of the linear viscous term is achieved with the second-order Crank-Nicholson method,

$$\int_{t_k}^{t_{k+1}} L(v) dt = \frac{1}{2} \left[ \nabla^2 v^{k+1} + \nabla^2 v^k \right] \Delta t. \quad (7)$$

The combined difference equation is now,

$$\begin{aligned} v^{k+1} - v^k + \left[ \frac{3}{2} N(v^k) - \frac{1}{2} N(v^{k-1}) \right] \Delta t = \\ -\nabla \bar{p}^{k+1} \Delta t + \frac{1}{2R_e} \left[ \nabla^2 v^{k+1} + \nabla^2 v^k \right] \Delta t \end{aligned} \quad (7)$$

The continuity equation is imposed at the leading time step,

$$\nabla \cdot v^{k+1} = 0. \quad (8)$$

In splitting method, (7) is integrated numerically in three for each time step, each stage addressing the three terms independently. Two intermediate

velocity fields,  $v^{\circ}$  and  $v^{\bullet}$ , are introduced in order to achieve this. The three stages are,

$$v^{\circ} - v^k = \left[ \frac{3}{2} N(v^k) - \frac{1}{2} N(v^{k-1}) \right] \Delta t,$$

$$v^{\bullet} - v^{\circ} = -\nabla \bar{p}^{k+1} \Delta t,$$

$$v^{k+1} - v^{\bullet} = \frac{1}{2R_e} \left[ \nabla^2 v^{\bullet} + \nabla^2 v^{\circ} \right] \Delta t. \quad (9)$$

In order to process the second step, the average pressure,  $\bar{p}$ , must be determined. The pressure is not needed for the first step, and therefore can be determined after  $v^{\bullet}$ . take divergence of (7) and use the continuity equation to obtain the Poisson's equation for pressure,

$$\nabla^2 \bar{p}^{k+1} = \nabla \cdot \left( \frac{v^{\bullet}}{\Delta t} \right) \quad (10)$$

where the nonlinear term is neglected.

All variables require boundary conditions, including  $v^{k+1}$ ,  $v^{\bullet}$ ,  $v^{\circ}$  and  $\bar{p}$ . The boundary conditions on  $v^{k+1}$  are the natural boundary conditions, which must be enforced at the final stage if the splitting method. Boundary conditions on  $v^{\bullet}$  and  $v^{\circ}$  can be chosen to enhance the numerical aspect of the method. Hence,

$$v^{\bullet} \cdot k = v^{\circ} \cdot k = 0 \quad (11)$$

on all boundaries.

Finally, there are no natural boundary conditions on the pressure since the value of pressure at the boundary depends on the velocity field in the neighborhood of the boundary.

Pressure boundary conditions must be approximated from the governing equations. Take the normal component of (7) to get,

$$\begin{aligned} k \cdot \nabla \bar{p}^{k+1} = k \cdot v^{\bullet} - k \cdot v^{k+1} - k \cdot \left[ \frac{3}{2} N(v^k) - \frac{1}{2} N(v^{k-1}) \right] \Delta t + \\ \frac{1}{2R_e} k \cdot \left[ \nabla^2 v^{\bullet} + \nabla^2 v^{\circ} \right] \Delta t \end{aligned} \quad (12)$$

Karniadakis [2] has shown that all the right hand side terms of above equation can be neglected for large Reynolds number, leaving,

$$n \cdot \nabla \bar{p}^{k+1} = 0. \quad (13)$$

For that reason, Karniadakis [10] recommends higher order boundary conditions for a better

approximation, especially for low Reynolds number flow.

### 3. RESULTS AND DISCUSSIONS

Streamline patterns throughout the airways for three different inlet Reynolds numbers of 1000, 2000 and 3000 will be first discussed in this chapter. Variations of flow intensity, flow directions, vortex formations throughout the period will be scrutinized.

The streamline figure will then further magnified on the most critical locations for the vorticity analysis. The analysis will be based on vortex locations, strengths and its effects.

The last section will briefly discuss the pressure drop difference along the airways for each Reynolds number. Highlight will be taken for Reynolds number 3000 since many vortices variants were found along the airways.

#### 3.1 Streamline Pattern Analysis

Three different Reynolds numbers were selected for the trachea inlet flow, representing three dissimilar breathing conditions in physical means. Figure 2 shows the streamline pattern for the inlet flow Reynolds number of 1000. The streamlines were captured for the time equals to 0.2, 0.4, 0.6 and 0.8 respectively.

Throughout the observation period, The streamline for this particular Reynolds number showed very little variations where there were very minimum change in flow directions in all locations. Eventhough the forcing function effect from the airway inlet were gradually transferred deeper by the time increment, these changes were not strong enough to form any vortex on the airway. However, there were still divergence effects observed for streamlines close to the airway walls.

Flow development throughout the analyzed airway for inlet flow Reynolds number of 2000 can be viewed in Figure 3 below. Unlike the previous forcing function strength, Reynolds number of 2000 was observed to give significant transient variation on the streamline pattern.

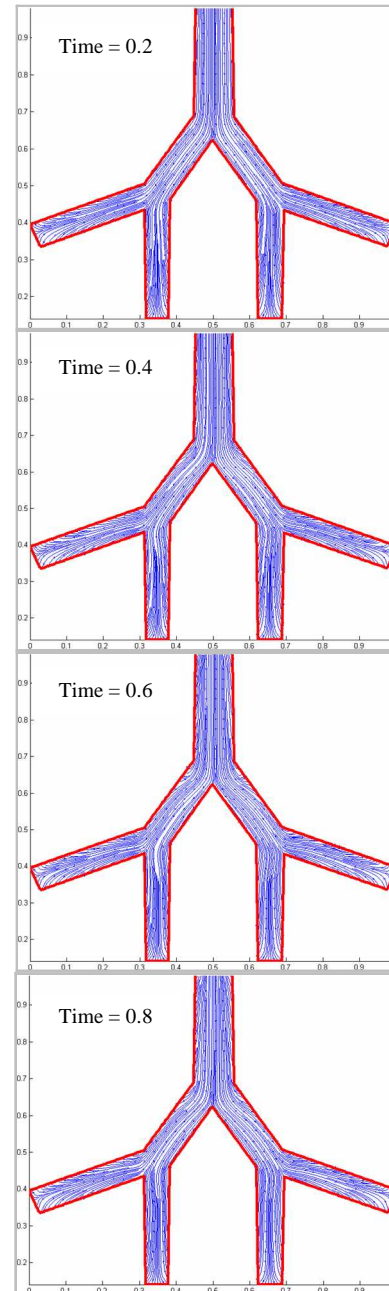


Figure 2: Streamline pattern for inlet flow Reynolds number of 1000.

At the time of 0.2, the flow was seemed to be very smooth but started to form weak vortices in few locations.

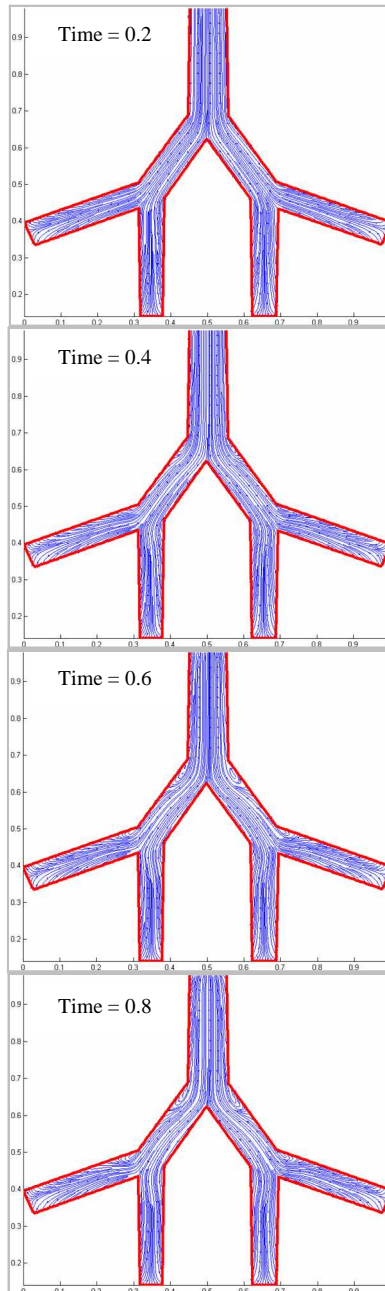


Figure 3: Streamline pattern for inlet flow Reynolds number of 2000.

Figure 4 gives the most interesting streamline patterns among the three Reynolds numbers. Strong vortex formations can be monitored at four locations where abrupt change in flow directions found. The flow changes very fast with vortices started to form as early as time equals to 0.4. Due to the formation of these strong vortices, the clearance where flow can go through seems to be reduced and the flow path become more groovy towards deeper regions.

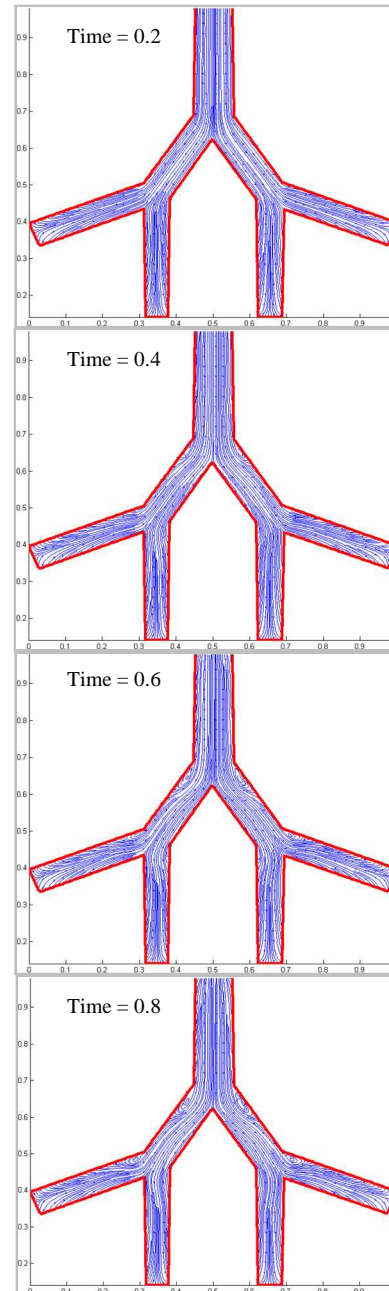


Figure 4: Streamline pattern for inlet flow Reynolds number of 3000.

## 2.1 Vortex Growth Analysis

Last section had shown that as the inlet flow Reynolds number increased, the more vortices could take place. These vortices did not propagate randomly but started where the flow encounter abrupt change of directions. At the location between the trachea and the main bronchi, the

flow bifurcated and yielded equally hurried change of flow angles. Since the location was very much close to the forcing function, vortices formed strongly at both joints.

Vortices were also observed at the joints between the main bronchi and the second bronchi but not at all joints. Vortices were only occurred at the joints with relatively huge angle differences. As in Figure 5 where the flow with Reynolds number of 3000 were magnified, joints between the main bronchi with the outer secondary bronchi with higher angle difference were shown having weak vortices while the others were not.

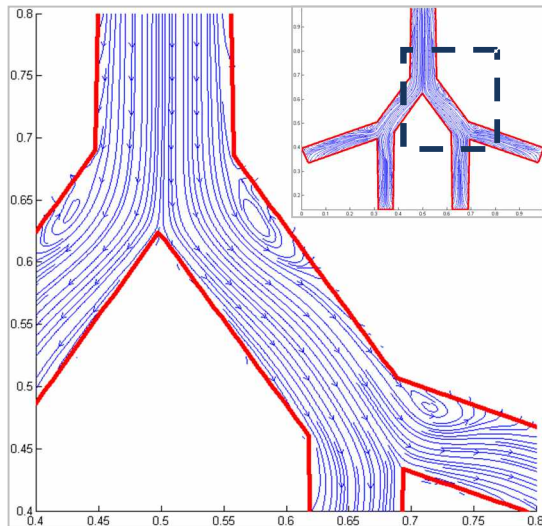


Figure 5: Magnified streamline pattern for inlet flow Reynolds number of 3000.

### 2.1 Pressure Distributions Analysis

Pressure distribution along human airways has been an important issue in medical studies especially when we deal with asthmatic problems. Figure 6 shows how pressure behaves along human airways when we increase the inlet flow Reynolds number from 1000 to 3000. The pressures at the centre points of airways at location 1 to 6 in the figure were recorded and the values were distributed for all three Reynolds number.

The initial pressures at the inlet were found to be higher for higher Reynolds number but the increments were not linear. All three cases show that the pressure increases as the flow go deeper in the airways where the velocity is slower. The

pressure gradients along the airways were found to be higher for higher inlet flow Reynolds number.

The figure shows that for Reynolds number 1000, the pressure range was between 2.95 to 3.00 only while for Reynolds number 2000, the range is bigger from 3.20 to 3.30. However, this relationship was also not linear where for Reynolds number 3000, the range is between 3.38 and 3.49 only.

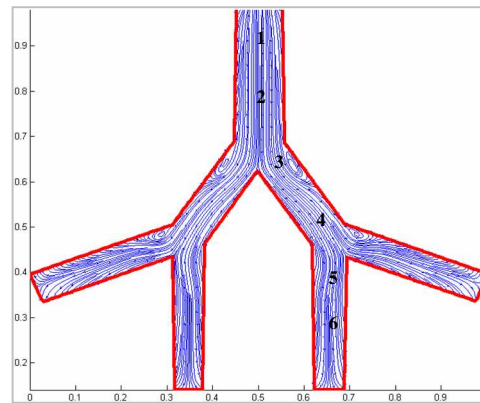
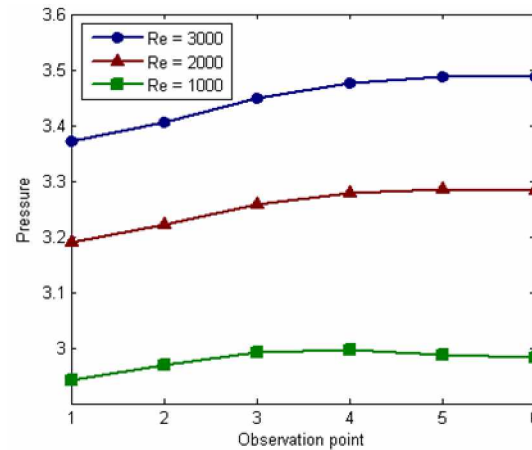


Figure 6: Pressure distributions along human airways from point 1 to 6.

### 4. CONCLUSION

The streamline patterns for inlet flow Reynolds number 1000, 2000 and 3000 show that as the Reynolds number increased, the flow became unsmooth and vortices developed whenever high enough flow velocity encountered stiff changes in directions. Eventhough joints between generations were having the same flow velocity and pressure, joints with abrupt change in

directions showed the development on vortexes.

Higher Reynolds number for the inlet flow could result in more chaotic and unsmooth flow throughout the airways. Vortex developments and changes in flow directions are major factors that could reduce the amount of drug delivery in asthmatic cases. This study suggests that in order to assure the maximum amount of inhaled particles go deep in the airways, patient whenever they use the inhaler should take their breaths slowly but deeply rather than fast and short breaths.

## 5. REFERENCES

- [1] Kurujareon, J., 2000. Simulations of Airflow in the human tracheobronchial network, Ph.D. Thesis, University of Hertfordshire, UK.
- [2] Schroter, R.C., Sudlow, M.F., 1969. Flow patterns in model of the human bronchial airways. *Respir. Physiol.* 7, 341–355.
- [3] Chang, H.K., El Masry, O.A., 1982. A model study of flow dynamics in human central airways. Part 1 axial velocity profiles. *Respir. Physiol.* 49, 75–95.
- [4] Isabey, D., Chang, H.K., 1982. A model study of flow dynamics in human central airways. Part II: secondary flow velocities. *Respir. Physiol.* 49, 97–113.
- [5] Pedley, T.J., 1977. Pulmonary fluid dynamics. *Ann. Rev. Fluid Mech.* 9, 229–274.
- [6] Gatlin, B., Cuicchi, C., Hammersley, J., Olson, D.E., Reddy, R., Burnside, G., 1995. Computational simulation of steady and oscillating flow in branching tubes. *ASME Bio-Medical Fluids. Engineering.* FED 212, 1–8.
- [7] Wilquem, F., Degrez, G., 1997. Numerical modeling of steady inspiratory airflow through three-generation model of the human central airways. *ASME J. Biomech. Engg.* 119, 59–65.
- [8] T. W. H. Sheu, S. K. Wang and S. F. Tsai, Finite element analysis of particle motion in steady inspiratory airflow, *Computer Methods in Applied Mechanics and Engineering*, Volume 191, Issues 25-26, 12 April 2002, Pages 2681-2698
- [9] Y. Liu, R.M.C. Soa, C.H. Zhang, *Journal of Biomechanics* 35 (2002) 465–473
- [10] G. Karniadakis, M. Israeli, and S. Orszag, 1991, “High-order splitting methods for the incompressible Navier-Stokes equations,” *Journal of Computational Physics*, 97, pp. 414-443.



# Thermally-Induced Strain in FCBGA Microelectronics Package Subjected to Transient Temperature Loading

Nazri Bin Kamsah<sup>a</sup>, Nurul Nadiah Bt Mohd Top

<sup>a</sup>Faculty of Mechanical Engineering  
Universiti Teknologi Malaysia  
81310 Skudai  
Johor, Malaysia  
nazrikh@fkm.utm.my

## ABSTRACT

About 65% of failure of microelectronic packages is caused by the heat generated by the silicon chip. The failure is primarily due to thermally-induced strain in the second-level solder balls interconnection resulting from the mismatch of coefficient of thermal expansion (CTE) of the various materials making up the package. This paper reports a study on the use of finite element method for estimating the thermally-induced strains in solder balls interconnection of a Flip Chip Ball Grid Array (FCBGA) microelectronics package when the package is subjected to a transient heating. Commercial finite element software is used to develop a quarter model of the package and to perform a transient thermal simulation during which the temperature of the package is raised 25°C to 100°C. This temperature range represents a temperature rise experienced by the package during service. The effect of different substrate material on the thermally-induced strains developed in the solder ball interconnections is also studied.

## Keywords

*Microelectronics Package Thermal Strain, Finite Element Method, Transient Temperature Loading, CTE Mismatch.*

## 1. INTRODUCTION

The performance of the computer systems nowadays has been vastly improved and much of the improvement is by reduction in feature sizes. The present new technology produces more advanced silicon devices with increased processing speed, higher device density and also greater power dissipation. Microelectronics package contains the silicon die (chip), which is the brain of any electronic products, attached to a substrate material through a first-level solder balls interconnection. An underfill

material is added to this interconnection to reduce the possibility of solder balls failure during service. The silicon-substrate assembly is then attached onto a printed-circuit board (PCB) through a second-level solder balls interconnection. Advances in electronics technology have resulted in chips that are smaller and have higher density integrated circuits, faster processing speed and more functions. As a consequence, the rate of heat dissipation also increases and it becomes more complicated to manage. The excessive heat generation has been identified as one of the causes of failures of microelectronics packages, which results in thermally-induced strain in the solder balls in the second-level interconnection. The primary cause of this problem is the mismatch in the coefficient of thermal expansion (CTE) of the various components making up the package [1]. Figure 1 illustrates a cross-section of a typical flip chip ball grid array (FCBGA) microelectronics package, which is one of the most popular packaging technologies used by many microelectronics industries [2]. The mechanical and thermal properties of the materials making up the package are tabulated in Table 1.

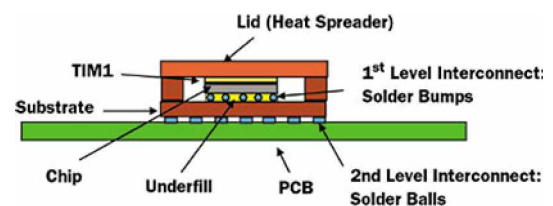


Figure 1 Schematic cross-section of a typical FCBGA package [1]

Table 1 Properties of various material of the FCBGA package [3,4]

Material	E (Gpa)	CTE (ppm/K)	$\nu$
Silicon	131	2.5	0.28
Epoxy	14.5	20	0.28
Copper Pad	69	17	0.34
Solder Ball	26	25	0.36
PCB	22	17	0.28

This paper reports on the use of finite element method to estimate the magnitude of thermally-induced strains in the second-level solder balls interconnection of the FCBGA package as it is subjected to a temperature rise from 25°C to 100°C. Commercial finite element software is employed to develop the simplified model of the FCBA package and to simulate the heating process of the package. Due to the symmetry in the geometry of the package and the thermal loading, only a quarter section model of the package is employed in the analysis. The effect of different substrate material on the thermally-induced strains in the solder balls interconnection is also evaluated.

## 2. FINITE ELEMENT IMPLEMENTATION

Figure 2 shows the finite element (FE) model of a quarter section of the FCBA package. For simplicity, the first-level solder balls interconnection is assumed to be made up of an underfill material only. This simplification is acceptable since the solder balls in the first-level interconnection are very small and are difficult to model. The entire model is discretized using hexahedral elements since they can produce more precise results. The front left and right edges of the model represent the symmetrical cutting surfaces. The thermal and mechanical properties are assigned to the respective materials, as tabulated in Table 1. All materials are assumed to behave in a linear elastic manner. Mechanical constraints are applied on the left surface such that there will be no translation in the 1-direction and rotations about the 3-axis. The right surface is constrained from translation in the 2-direction and rotations about the 3-axis. An initial temperature of 25°C is prescribed to the entire model. During the transient thermal simulation, the temperature of the model is then raised from 25°C to 100°C in

several time steps. In addition, convection heat loss from the top surface of the silicon chip and the exposed surfaces of the substrate and the printed circuit board by prescribing convective heat transfer coefficient of 25 W/m<sup>2</sup>K and the ambient air temperature of 25°C. Also, the symmetrical cutting surfaces are assumed to be adiabatic. To investigate the effect of substrate material on the thermally-induced strains, two substrate materials are considered in the study. The mechanical and thermal properties of these materials are shown in Table 2.

Table 2 Properties of substrate materials [3][4]

Material	E (Gpa)	CTE (ppm/K)	$\nu$
Alumina	275	6.7	0.21
Copper	117	17	0.35

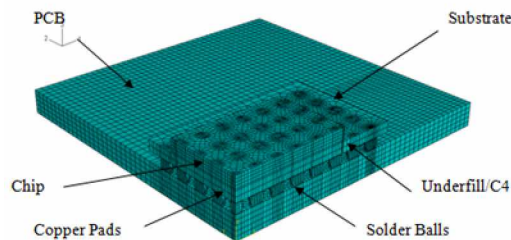


Figure 2 FE model of the FCBGA microelectronic package

## 3. RESULTS

Figure 3 shows the deformed shape of the package with copper substrate material when its temperature reaches 100°C. The contour of total displacement (in m) within the package is shown. It can be observed that the silicon die deforms in a convex direction because it is stretched in both the  $x$ - and  $y$ -direction, by the substrate and the PCB that have much higher CTE. The out-of-plane deformation of the substrate and the PCB underneath the silicon is also in tandem with that of the silicon. As a result, the solder balls interconnections in this region are in the state of compression.

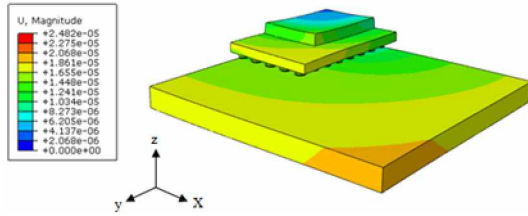


Figure 3 Deformation of the package with copper substrate at 100°C.

It is also seen that the out-of-plane deformation of both the substrate and the PCB continue to increase further away from the silicon die. The highest out-of-plane displacement of the substrate and the PCB is about  $1.8 \times 10^{-5}$  m and  $2 \times 10^{-5}$  m, respectively and these occur at the corner of both materials. Figure 4 shows the deformed shape of the package with an alumina substrate at 100°C.

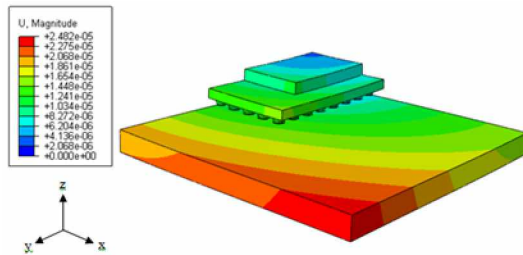


Figure 4 Deformation of the package with alumina substrate at 100°C.

In this case, the silicon die appears to have deformed in similar fashion as in the previous model but the magnitude of the out-of-plane deformation is much greater than the package with copper substrate. This is because the solder balls interconnection which has much higher CTE dictate the out-of-plane deformation. The solder balls interconnection are in the state of compression as their expansion is constrained by the substrate above them. The out-of-plane displacement at the tip of PCB is about  $2.48 \times 10^{-5}$  m, which is almost 25% greater than that in the package with copper substrate.

The state of thermally-induced maximum principal strain in the second-level solder balls interconnection for the package with copper substrate is shown in Figure 5. It can be observed from this figure that the highest strain occurs on the top edge of the solder balls located directly underneath the silicon die, along the outer edge of the die. The largest strain is about  $6.766 \times 10^{-3}$ . The

solder balls located along the left edge of the copper substrate also appear to be highly strained, on their upper edges that are facing in the  $x$ -direction.

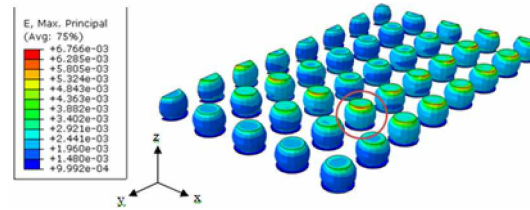


Figure 5 Maximum principal strains in solder balls for copper substrate

The state of strain in the second-level solder balls interconnection for the package with alumina substrate is shown in Figure 6.

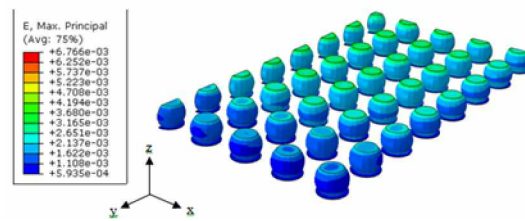
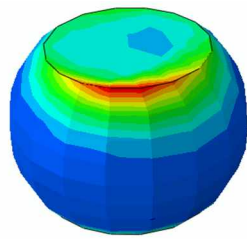


Figure 6 State of strains in solder balls for alumina substrate

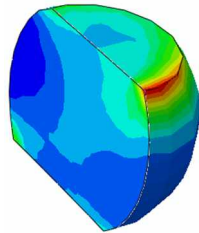
It can be seen that, in contrast to the package with the copper substrate, the solder balls located directly underneath the silicon die are less strained. Also, almost all the solder balls experience somewhat similar level of principal strain of about  $3.68 \times 10^{-3}$ , on their upper faces. The solder balls along the left edge of the alumina substrate are also less strained compared to the same solder balls for copper substrate.

Figure 7(a) shows the most critically strained solder ball in the package with copper substrate. This solder ball is located at the corner of the silicon die, underneath the substrate (enclosed in a circle in Figure 5). Clearly, the upper region of this solder ball is much higher strained as compared to the bottom region. Figure 7(b) shows a half-section of the critical solder ball and it illustrates the state of the maximum principal strain inside the critical solder ball. It is seen that the strain penetrates into the solder ball from both the upper and bottom surfaces, but the penetration

from the top surface goes much deeper into the solder ball.



(a)



(b)

Figure 7 (a) The most critically strained solder ball; (b) The state of inner strain the critical solder ball.

## CONCLUSION

When an FCBGA electronics package is subjected to a transient temperature rise from 25°C to 100°C, thermally-induced strains are developed in the solder balls in the second-level interconnection. This is due to the CTE mismatch between the various materials making up the package. The solder balls that are located at underneath the silicon die, along the edge of the die experience higher strains at their upper faces. The principal strain in these solder balls are higher when copper is used as substrate material compared to alumina. The solder ball located underneath the corner of the silicon die experiences the highest principal strain when the substrate material is copper. The principal strain penetrates into the solder ball from both upper and lower faces of the solder ball but the penetration is a lot deeper from the upper face due to the higher strain on the upper face.

## REFERENCES

- [1] Guatao Wang, Jie-Hua Zhao, Min ding, Paul S. Ho (2002). Thermal Deformation Analysis on Flip-Chip packages using High Resolution Moire Interferometry. Austin: pp 869-875.
- [2] Yuko Sawada, Kozo Harada and Hirofumi Fujioka (2003). Study of Package Warp Behavior for High-Performance Flip-Chip BGA. Microelectronics Reliability. Science Direct Journal, 43(3): 465-471.
- [3] G.Q. Zhang, W.D van Driel, and X.J. Fan (2006). Mechanics of Microelectronics Handbook. Netherlands: 169-263.
- [4] S. B. Park, Rahul Joshi, and Bahgat Sammakia (2005). Thermomechanical Behavior of Organic and Ceramic Flip Chip BGA Packages Under Power Cycling. 21<sup>st</sup> Semiconductor Thermal Measurement and Management Symposium. March 15-17. San Jose, CA, USA: IEEE, 214-222.

# A REVIEW – THERMAL LOAD ANALYSIS OF PASSENGER COMPARTMENT

Haslinda Mohamed Kamar<sup>a</sup>, Mohd Yusoff Senawi<sup>b</sup>

<sup>a</sup>*Department of Thermo-Fluids  
Faculty of Mechanical Engineering,  
Universiti Teknologi Malaysia,  
81310 Skudai, Johor Bahru, Malaysia  
Tel : (006) 075534656  
E-mail : haslinda@fkm.utm.my*

<sup>b</sup>*Department of Thermo-Fluids  
Faculty of Mechanical Engineering,  
Universiti Teknologi Malaysia,  
81310 Skudai, Johor Bahru, Malaysia  
Tel : (006) 075534747  
E-mail : myusoff@fkm.utm.my*

## ABSTRACT

The thermal environments in a passenger compartment are created according to the performance of its air conditioning system. Basically, there are two main aspects that need to be considered to develop a comprehensive and accurate passenger compartment thermal simulation program. The first aspect is load analysis in the passenger cabin. Via load analysis, the thermal behavior in the passenger compartment under the influence of the outside environment, over a wide temperature range and under various air-conditioning (A/C) operating conditions can be described. The second aspect is the characteristics of the air-conditioner evaporator coil. In this respect, the transient air temperature and humidity in the passenger compartment are dependent on the temperature and humidity of the discharged air. The discharged air conditions affect the thermal behavior inside the passenger cabin. As a result, two selected topics are reviewed in this paper. The pertinent topics are: thermal load analysis in the passenger compartment, and the linkage between the passenger compartment thermal load model and the A/C system.

## Keywords

*Thermal load simulation, passenger compartment, automotive air conditioning system*

## 1. INTRODUCTION

The required capacity of cooling systems that can maintain the required conditions in the conditioned passenger compartment can be estimated by carrying thermal load analysis. The total passenger compartment load consists of external and internal loads. The external loads consist of heat transfer by conduction through the cabin walls, roof, floor, doors etc, and heat transfer by radiation through glass windows. The internal loads consist of sensible and latent heat transfer due to occupants and appliances.

Generally, thermal load calculations involve a systematic procedure by taking into account all the space energy flows. In practice, a variety of methods ranging from simple rules-of-thumb to complex Transfer Function Methods are used to arrive at the space loads. Accurate analysis of space loads is important in air-conditioning load calculations when predicting the peak design day load for equipment sizing. It is also valuable in obtaining the space envelope temperatures when performing thermal comfort studies. Furthermore, the rising demand of energy conservation, more and more attentions are given on the studies of thermally non-uniform and dynamic environments [1].

## 2. A REVIEW

Several thermal load models have appeared in the open literature. In a study by Ingersoll et al [2], the authors developed a passenger compartment thermal comfort model to predict human comfort



for various environmental conditions, vehicle design, and Heating, Ventilation, and Air Conditioning (HVAC) system operating conditions. The thermal load model reflects on the geometrical configuration of the passenger compartment including glazing surfaces; the pertinent physical and thermal properties of the enclosure; the environment conditions; the direct and diffuse incident solar radiation through the glass areas; the inlet air parameters as specified from the HVAC system; and the conduction, convection, mass flow, and radiation heat transfer modes. The model outputs are interior air temperatures, surface temperatures, air velocities and air relative humidity. The passenger compartment and mass flow in the passenger compartment are modeled as lumped parameter networks. The conduction heat gain through the passenger compartment was calculated based on steady-state assumption and the method to connect the thermal load system and its A/C system was not clarified.

Lin et al [3] simulated a steady-state cooling process in a simplified GM-10 passenger compartment to evaluate passenger thermal comfort. Four design parameters were studied, specifically, conditioned air flow rate, A/C outlet location, body vent location and glass properties. Three dimensional air flow and temperature distributions were obtained using CFD approach specifically, the flow and convection solver VINE3D, which solves a set of partial differential equations, namely, governing mass, momentum and energy balance. The outputs of the numerical simulation model are air flow and temperature distributions. However, there is no analysis on the physical link between the A/C system performance and the corresponding passenger compartment model, but the effect of A/C outlet flow rate was examined by varying the flow rates at various magnitudes. Stancato and Onusic [4] developed a simulation model to calculate steady-state cooling loads in a cab compartment. They incorporate various sources of heat loads into the model specifically: conduction heat gain through opaque walls and glasses; solar radiation through glasses; conduction heat gain through motor compartment panels; heat gain from people and infiltration. However, the thermal storage effects due to the heat capacity of the interior mass and body wall were excluded in the analysis. The model is a stand-alone model, since the variations of air temperature inside the cabin are not coupled to the air-conditioner evaporator inlet conditions.

The A/C discharge air temperature was determined experimentally.

Currle et al. [5] investigated the air flow through the complete HVAC system together with the flow field in the passenger compartment using CFD approach. The HVAC system includes all parts of air handling system such as inlet plenum chamber, fan, filters, air distribution chamber with evaporator, air ducts and vents. The passenger compartment model includes a detailed description of the passenger compartment occupied by four occupants. However, the calculation of the temperature field including all relevant thermal effects such as free convection, conduction and radiation was not performed in the study. Currle and Jurgen Maue [6] extended the previous computational model, by expanding their study to investigate the effects of relevant flow and geometrical parameters on the microclimate and the thermal comfort of the occupants inside the passenger compartment. The model consists of three programs which are coupled together. The first program is used to calculate the flow and temperature distribution inside the passenger compartment using CFD code. The program represents the convective heat load inside the passenger compartment. The second program simulates the passenger compartment heat load. This program signifies the radiative heat load inside the cabin. The third program is used to compute the thermal state and sensation of the occupants under a given load. However, in this study, they did not investigate the effects of the A/C system performance (specifically at the evaporator inlet air conditions) with regard to the transient behavior inside the passenger compartment. The inlet conditions at the vents are manually specified as inlet conditions of the computational model. Due to this absence, the model is developed based on the theoretical simulation only without appreciating the realities of A/C system as a whole. The study also include the conduction heat transfer through cabin walls, solar and thermal radiation, into the passenger compartment thermal load model however, the method is unclear. Furthermore, both studies [5] and [6] are based on steady-state analyses.

Huang [7] built a dynamic computer simulation model to calculate temperature and humidity variations inside a passenger compartment while simulating the performance of the A/C system. The vehicle is divided into two linked modules representing the A/C network and

the passenger compartment climate. The A/C network consists of the evaporator, compressor, condenser, orifice, air handling system, and the connecting hoses. Pressure drop and thermal capacity of the evaporator, condenser and the connecting ducts/hoses are also included in the A/C system model. The passenger compartment climate was simulated using lumped capacitance method. In this scheme, the temperature and humidity inside the passenger compartment are assumed spatially uniform at any time during the simulation. A lumped analysis of the interior masses such as seats, instrument panel and floor console are also incorporated. The transient cabin average air temperature, seat average temperature and cabin average air humidity were modeled using three non-linear ordinary differential equations based on mass balance and energy balance. Those equations were solved via a fourth-order Runge-Kutta method. A relationship between the A/C system characteristics and the passenger compartment load model is linked up via simulation model. The conduction heat gain through opaque walls is assumed as one-dimensional transient heat conduction. For a composite wall analysis, the thermal properties and temperature within each individual layer are assumed uniform.

A similar study has been carried out by Khamsi and Petitjean [8]. They developed simulation software of a car cabin and its A/C system. The car cabin thermal simulation was modeled based on dynamic and stationary conditions. This model is meant for computing the cooling or heating capacities required to compensate the effect of different heat loads inside the car cabin and obtaining the required comfort conditions inside the cabin. The outputs of the cabin thermal model are surface temperature of various elements, the air temperature and relative humidity in various zones and the instantaneous cooling or heating capacities required to reach the optimum conditions of comfort in the cabin. However, the technique to develop the car cabin thermal load model was not described. The link between the car cabin model and the A/C model was established via model correlation.

Akihiro Fujita et al [9] developed a numerical simulation to predict steady-state internal thermal environment specifically air velocity and space temperature in a passenger cabin. The coupled analysis of solar radiation, long-wave radiation,

conduction heat gain through the materials and CFD was used in this method. The heat conduction through the materials is based on a steady-state analysis. The effects of ventilation inside the instrument panel and air leaks from the gaps of interior parts were incorporated into the model but excluded the effect of latent heat and humidity. Furthermore, no occupants are assumed to be present in the cabin. The study did not portray the effects of A/C load towards its corresponding cabin model. However, the A/C discharge air temperature was determined experimentally.

Ali Heydani and Saeed Jani [10] have developed an integrated computer simulation model which consists of three mathematical models, specifically, the compression A/C system, air handling system and the passenger cabin model to predict the transient performance of an automobile HVAC system. The A/C system model is developed based on a steady-state mathematical model to simulate the performance of major components of the A/C system. The air handling simulation model is used to describe the process of heating and cooling of fresh or re-circulated air, fan performance along with associated losses due to movement of air through the ducts and the air distribution registers. The passenger thermal model is developed using a one-dimensional thermal resistance scheme, which is used to predict the heat load and temperature distribution inside the passenger compartment. The A/C model and the passenger thermal model are physically linked through the air-conditioner evaporator via a correlation model. The thermal model inside the passenger cabin is established using a three-dimensional transient heat transfer model (which is belonged to lumped system approach). Each sub-region is assumed to be at a uniform temperature under a given thermal load. The thermal model includes the effects of conduction, convection, radiation, energy interaction between interior components, energy flow between sub-regions, energy infiltration into the passenger compartment and heat released due to human loads.

You Ding and Robert Zito [11] developed a numerical model using lumped analysis technique to investigate the effects of passenger compartment heat load, discharge panel temperature and discharge volumetric air flow in relation to the average air temperature. The study did not physically couple the passenger cabin

model with its A/C performance. Roy et al [12] as well have developed a comparable model of passenger compartment to calculate surface temperatures, air temperature at different levels and cooling loads. They used a zonal approach method to model the cabin thermal. The cabin was divided into several sets of components geometrically, specifically the external walls (including floor, roof, doors, dashboard, rear shelf and glasses); the internal solid components (seats, and steering wheel) and the internal air. All major elements of heat loads including steady-state conduction through opaque materials; radiation due to temperature difference between the cabin components as well as direct and diffused solar radiation; convection (natural and forced); and convection and radiation due to outside environment are incorporated into the model. The A/C model, particularly its mass flow rate was determined using CFD analysis.

P+Z Engineering [13] have developed an interface to the two commercial software products with the aim to directly connecting the numerical calculation of the refrigerant circuit with a transient cabin simulation. One of the software is used to calculate the transient temperature behavior of a cabin. The passenger compartment model is developed using lumped system approach.

Rugh [14] on the other hand, has used an integrated modeling approach composed of CAD model, computational fluid dynamics (CFD), cabin thermal model and vehicle simulation tools to assess thermal comfort, fuel economy, and emissions. The CAD is used to define vehicle interior geometry and to morph a generic vehicle to the appropriate dimensions and generate a mesh in preparation for cabin thermal/fluid modeling using CFD software. The CFD software in conjunction with a solar radiation model and vehicle solar load tool is used to provide solar boundary conditions for the cabin thermal/fluid model. The cabin thermal/fluid model predicts the flow field inside the passenger compartment, as well as the surface temperatures and temperature and humidity of the air. A transient air-conditioning (A/C) model provides air flow boundary conditions specifically the airflow rates, humidity, and temperatures for the CFD analysis inside the passenger cabin. A comparable study has also been done by Todd et al [15].

Jonas Jonsson [16] has developed a numerical model using CFD analysis (specifically FLUENT software) that integrates solar load when computing the 3-D temperature distribution in a passenger compartment. Three cases were simulated throughout the study: a steady state, a transient soaking and a transient cooling. As well as Huajun Zhang et al [17] they also used FLUENT software to simulate the 3-D transient temperature and air-flow field inside the passenger compartment with or without passengers. The A/C discharge air temperature was determined experimentally. The numerical model has been validated using the experimental data to investigate the influence of different factors on the thermal comfort and the energy consumption. The test conditions and the numerical models are described in details. In the following paper, Huajun Zhang et al [18] presented the simulated results. Several findings have been obtained, among them are, to reduce the cooling load in the passenger compartment is by increasing the inlet air temperature, without reducing the volume flow rate of the inlet air and the thermal comfort in a compartment with given conditions depends on the number of occupants in it.

Farzaneh and Tootoonchi [19] have developed a fuzzy controller to control automobile thermal comfort. In their study, Fanger's predicted mean value (PMV) index is used as controller feedback such as, temperature, relative humidity, air velocity, environment radiation, activity level and cloths insulation. To clearly show the effect of control parameters on occupant thermal comfort a simulation model of passenger cabin and the HVAC system has been developed by the authors. This model includes blower, evaporator, heater core as well as the impact of important thermal loads such as sun radiation, outside air temperature and passengers on climate control of cabin. The thermal loads generated by solar radiation, outside air and cabin temperature difference as well as assumption of four people in cabin have been estimated by using empirical formula for Peugeot 206 automobile.

### 3. CONCLUSION

From the reviews discussed above, much useful information in the areas of occupant comfort, cabin heat load, heat transfer and A/C system modeling are described. Most of the studies used computational fluid dynamics (CFD) technique

and numerical simulation to achieve their objectives. Generally, CFD solves the conservation equations for mass, momentum, and thermal energy for all nodes of a two- or three-dimensional grid inside or around the object under investigation. In theory, the CFD approach is applicable to any thermo-fluid phenomenon. However, in practice, and in the passenger compartment physics domain in particular, there are several problematic issues, of which the amount of necessary computing power, the nature of the flow fields, and the assessment of the complex occupant-dependent boundary conditions are the most problematic [20]. This has often led to CFD applications being restricted to steady-state cases or very short simulation periods. A lumped parameter approach which belongs to the numerical methods, model the continuous physical domain of a thermal system as a network of discrete points, where the unknowns are sought only at those points rather than everywhere in the domain [21, 22 and 23]. Specifically, the node points are centered within the lumps, and temperatures at the nodes are considered uniform throughout the lump. Due to that reason, the most critical aspect of the lumped parameter approach is to determine the lump size. Although there are methods for optimizing the lump size of any given physical system, they usually involve more analytical efforts and computer time than the original problem [2].

In the preceding reviews, there are several studies that [7, 8, 10 and 14] have coupled the A/C system analysis with the passenger compartment model. This approach is unique, since it provides a means for an optimized design of passenger compartment climate control system derived from realistic and accurate behavior of the automotive A/C system. It also portrays the mutual effect between the A/C system and the passenger compartment. Furthermore, it offers a better understanding of the synergistic impact of the various parameters in the design of the vehicle that can affect comfort and the possible tradeoffs between such parameters.

From the thermal load model point of views, nearly all studies presented above disregard the effect of thermal storage of the interior mass and neglect interior air humidity analysis. The thermal storage effect is due to the heat storage of the interior seats, panels, and vehicle materials. Only Huang [7] considered thermal storage effects and variation of interior air humidity.

## ACKNOWLEDEMENT

The authors would like to express their appreciation to Universiti Teknologi Malaysia for funding this study.

## REFERENCES

- [1] Zhang Y. and Zhao R. (2008). Relationship Between Thermal Sensation and Comfort in Non-uniform and Dynamic Environments. *Building and Environment*. doi:10.1016/j.buildenv.2008.04.006.
- [2] Ingersoll, J. G., Thomas, G. K., Maxwell, L. M. and Niemeck, R. J. (1992). Automobile Passenger Compartment Thermal Comfort Model – Part 1: Compartment Cool-Down / Warm-Up Calculation. *Society of Automotive Engineers (SAE) Technical Paper Series*. Paper No. 920265: 232 – 242.
- [3] Lin, C. H., Han, T. and Koromilas, C. A. (1992). Effects of HVAC Design Parameters on Passenger Thermal Comfort. *SAE Transactions*. Paper No. 920264.
- [4] Stancato Fernando, Onusic Helcio (1997). Road Bus Heat Loads Numerical and Experimental Evaluation. *Society of Automotive Engineers (SAE) Technical Paper Series*. Paper No. 971825.
- [5] Currel, J., Harper, M., Ross and F., Heid, T. (1997). Evaluation of HVAC System of Passenger Cars and Prediction of The Microclimate in The Passenger Compartment by Application of Numerical Flow Analysis. *Society of Automotive Engineers (SAE) Technical Paper Series*. Paper No. 971788.
- [6] Currel, J. and Jurgen Maue (2000). Numerical Study of The Influence of Air Vent Area And Air Mass Flux of The Thermal Comfort of Car Occupants. *Society of Automotive Engineers (SAE) Technical Paper Series*. Paper No. 2000-01-0980.
- [7] Huang Chi-Chang Daniel (1998). *A Dynamic Computer Simulation Model For Automobile Passenger Compartment Climate Control and Evaluation*. Michigan Technological University: Ph.D. Thesis.
- [8] Khamsi, Y. and Petitjean, C. (2000). Dynamic Simulation of Automotive Passenger Compartment And It's Air Conditioning System. *Society of Automotive Engineers (SAE) Technical Paper Series*. Paper No. 2000-01-0982.
- [9] Akihiro Fujita, Jun-ichi Kanemaru, Hiroshi Nakagawa and Yoshiichi Ozeki (2001). Numerical Simulation Method To Predict The Thermal Environment Inside A Car Cabin. *Society of Automotive Engineers of Japan (JSAE)*,\_22: 39 – 47.
- [10] Ali Heydani and Saeed Jani (2001). Entropy-Minimized Optimization of an Automotive Air-conditioning and HVAC System. *Society of Automotive Engineers (SAE) Technical Paper Series*. Paper No. 2001-01-0592.
- [11] You Ding and Robert Zito (2001). Cabin Heat Transfer And Air Conditioning Capacity. *Society*



- of *Automotive Engineers (SAE) Technical Paper Series*. Paper No. 2001-01-0284.
- [12] Roy, D. El-Khoury, K. Clodic, D. and Petitjean, C. (2001). Modeling of In-Vehicle Heat Transfer Using Zonal Approach. *Society of Automotive Engineers (SAE) Technical Paper Series*. Paper No. 2001-01-1333.
- [13] P+Z Engineering GmbH (2002). Simulation of an Air Conditioning System and the Vehicle Interior. *ATZ Worldwide 2/2002*. Volume 104.
- [14] Rugh, J. P. and Hendricks, T. J. (2001). Effect of Solar Reflective Glazing on Ford Explorer Climate Control, Fuel Economy, and Emissions. *Society of Automotive Engineers (SAE) Technical Paper Series*. Paper No. 2001-01-3077.
- [15] Todd, M. T., Balaji Maniam, Milind Mahajan, Gaurav Anand and Nagendra Jain (2004). e-Thermal: A Vehicle-Level HVAC/PTC Simulation Tool. *Society of Automotive Engineers (SAE) Technical Paper Series*. Paper No. 2004-01-1510.
- [16] Jonas Jonsson (2007). Including Solar Load in CFD Analysis of Temperature Distribution in a Car Passenger Compartment. Luleå University of Technology, Sweden: Master Thesis.
- [17] Huajun Zhang, L. Dai, G. Xu, Y. Li, W. Chen, W-Q. Tao (2009). Studies of Air-flow and Temperature Fields Inside a Passenger Compartment for Improving Thermal Comfort and Saving Energy: Part I Test/Numerical Model and Validation. *Applied Thermal Engineering*. 29: 2022–2027.
- [18] Huajun Zhang, L. Dai, G. Xu, Y. Li, W. Chen, W-Q. Tao (2009). Studies of Air-flow and Temperature Fields Inside a Passenger Compartment for Improving Thermal Comfort and Saving Energy: Part II Test/Numerical Model and Validation. *Applied Thermal Engineering*. 29: 2028–2036.
- [19] Farzaneh, Y. and Tootoonchi, A. A. (2008). Controlling Automobile Thermal Comfort Using Optimized Fuzzy Controller. *Applied Thermal Engineering*. 28 : 1906–1917.
- [20] Hensen, J., Bartak, M. and Drkal, F. (2002). Modeling and Simulation of a Double-Skin Facade System. *ASHRAE Transactions*. 108 (2) : 1251-1259.
- [21] Schneider, P. J. (1955). *Conduction Heat Transfer*. Reading, Massachusetts: Addison-Wesley Publishing Company Advanced Book Program.
- [22] Holman, J. P. (1981). *Heat Transfer*. 5<sup>th</sup> ed. Auckland: McGraw-Hill International Book Company.
- [23] Shih, T. M. (1984). *Numerical Heat Transfer*. New York : Springer-Verlag.



# Utilization of Waste Cooking Oil as Diesel Fuel and Improvement in Combustion and Emission

Wira Jazair, Mohd Norhisyam

Faculty of Mechanical Engineering, Universiti Teknologi Malaysia  
81310 UTM Skudai, Johor, Malaysia  
Tel : 6(019) 7326919  
E-mail : wira@fkm.utm.my

## ABSTRACT

Due to high price of Straight Vegetable Oil (SVO) for bio-diesel production, the use of Waste Cooking Oil (WCO) will be cost effective. Furthermore, utilization of WCO will refrain waterways pollution and endanger ecosystem. In Malaysia, more than 50-tone of WCO from various sources was produced everyday. This study evaluates combustion performance and exhaust emission characteristics of several WCOs with different sources. Modification on fuel properties has been done to improve the combustion and exhaust emission of using WCO as diesel fuel. Regular diesel fuel also has been used for comparison in the test. A 0.6 liter, single-cylinder, air-cooled direct injection diesel engine was used to perform this experiment. Experiment was done at variable engine loads at constant speed.

## Keywords

Waste Cooking Oil, Diesel Engine, Emission

## 1. INTRODUCTION

Energy reserves in the world (Deiterium, Uranium, Coal, Crude oil, Natural gas) only can support the user only less than thirty years based on present consumption. If the consumption rate increases, the reserve energy might only enough not less than twenty years [1]. In addition, high uses of petroleum fuel around the world resulted in increasing the air pollution cause by the burning of the petroleum fuel. On top of that, in 2007, crude oil reaches the maximum price over 100 dollar US per barrel surpass the price during Oil Crisis around 1980's [2]. This makes some

alternative diesel fuel particularly bio-diesel become popular in a growing number of countries around the world. Bio-diesel can be defined as mono alkyl ester of long chain fatty acids derived from renewable lipid sources. Bio-diesel can be produced from some type of renewable lipid sources such as vegetable oil and animal fat [3]. Bio-diesel is uses seriously in developed country such as United State, France, Germany and others. In Malaysia, bio-diesel becomes more popular due to the prices and also due to these countries vehicle's regulation and law. As palm oil is a main source of fat in Malaysia, production of bio-diesel from palm oil will affect the price of product based on fat, such as food and others. By producing bio-diesel from palm oil (commercial production), there will increase price of crude palm oil. As alternative, Waste Cooking Oil (WCO) has been chosen to be investigating in this research. Beside the price factor, re-used of WCO can solve the water pollution that caused by WCO.

## 2. TEST FUEL

In this research, there are three types of WCO sources used. This three test fuel are named A, B and C. The sources of these fuels are shown in Table 1. These three types of WCO have different fuel properties due to different cooking style and duration. WCO B and WCO C were used for many times (more than 5 times) and the color of the cooking oil changed to become dark brown. In contrast, for WCO A is only being used two or three times before it will be drained.

Table 1: Test Fuel Sources

Test Fuel	Source	Freq. Use
WCOME A	House Kitchen	< 3 times
WCOME B	Cafeteria Kitchen	> 5 times
WCOME C	Indian Muslim Restaurant	> 5 times

These three test fuels have been transformed into waste cooking oil methyl ester (WCOME) through transesterification process. This process needed waste cooking oil (triglyceride) as main substance, methanol as converter of main substance, and with the present of potassium hydroxide as reaction accelerator (catalyst). As the result of this process, two separate layers are produced after being left about 12 hours. The upper layer is WCOME or bio-diesel and the bottom layer is glycerin. In order to have clean bio-diesel, the WCOME layer was rinsed with distilled hot water (70 – 80 °C). This washing process is to make sure remaining methanol or other sustains removed from WCOME.

Table 2 shows the fuel properties of all test fuels. It can be seen that all WCOME has higher kinematic viscosity and density compared with diesel fuel. Compared with diesel fuel, WCOME A has 9.1%, WCOME B 13.2% and WCOME C 38.6% higher kinematic viscosity. WCOME C has highest and WCOME A has lowest kinematic viscosity and density among WCOMES. The kinematic viscosity and density of WCOME might closely relate to the frequent and duration usage of WCOME sources.

Table 2 : Fuel Properties

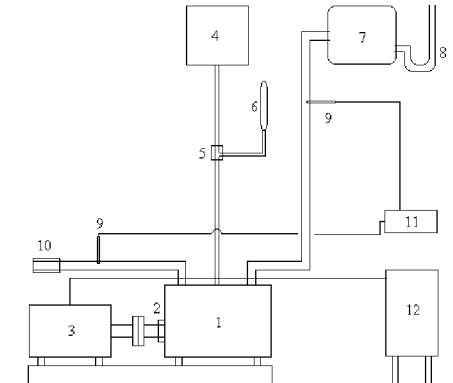
Test Fuel	Kinematic Viscosity (mm <sup>2</sup> /s)	Density (g/ml)
Diesel Fuel	3.918	825
WCOME A	4.274	836
WCOME B	4.437	844
WCOME C	5.431	852

### 3. EXPERIMENTAL SETUP

The test engine is a four-stroke single cylinder naturally aspirated direct-injection diesel engine (Lister ST1). Base engine specifications are given in Table 3. The engine is 94.8mm cylinder diameter and 90.0mm stroke. The compression ratio is 16. Standard mechanical injection pump is used. Figure 1 shows the schematic diagram of experimental apparatus. Engine performance and exhaust emissions data are obtained under stable operating conditions at engine speed of 1500rpm. Smoke density is measured with a Bosch smoke meter.

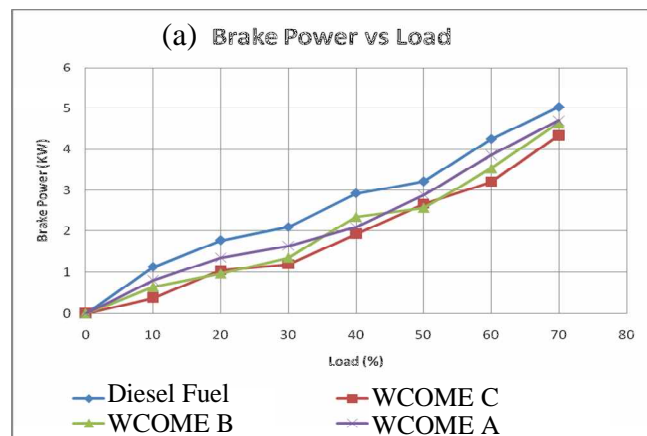
Table 3 : Engine Specification

Engine Type	Diesel
Model	Lister ST 1
Power Output	10.5 bhp
Maximum Speed	3000 rpm
Compression Ratio	16
Displacement	600 cc
Bore	94.8 mm
Stroke	90.0 mm



1. Engine
2. Tachometer
3. Dynamometer
4. Fuel tank
5. Three way valve
6. Venture meter
7. Surge tank
8. Manometer
9. Thermocouple
10. Smoke meter
11. Thermocouple display unit
12. Dynamometer control unit

### 4. RESULTS AND DISCUSSION



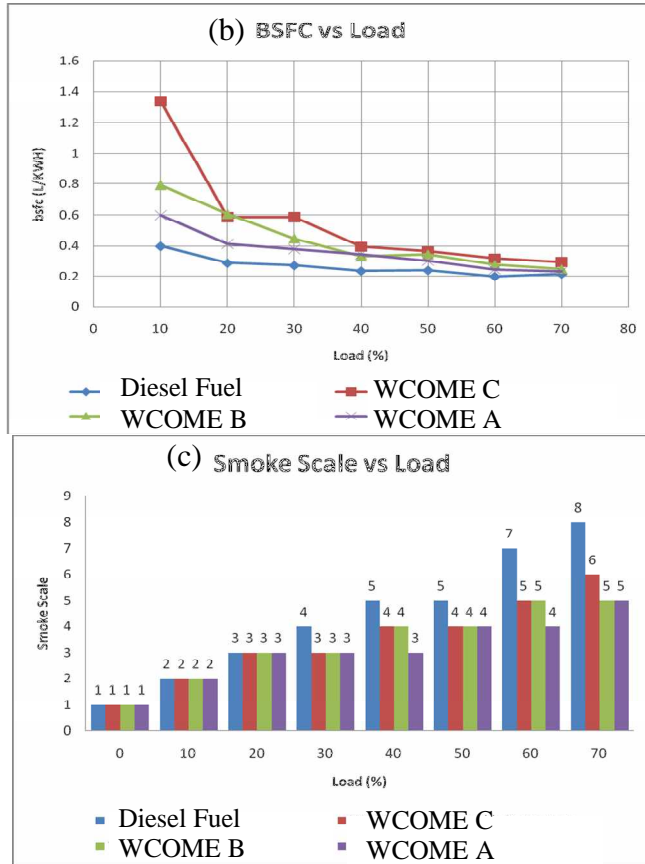


Figure 2. Effect of WCOME on (a) Brake Power, (b) Brake Specific Fuel Consumption (bsfc), (c) Smoke

Figure 2(a) shows the brake power versus load for each test fuel. From the figure, it can be seen the brake power increased with increasing of engine load. At all loads, diesel fuel gives higher brake power than other test fuels. This is due to higher calorific value of diesel fuel around 45 – 47 MJ/kg compared with WCOMES has calorific value about 34-38 MJ/Kg [4-5]. Between WCOME; WCOME A has higher brake power, followed by WCOME B. WCOME C produces the lowest brake power.

Figure 2(b) shows the brake specific fuel consumption (bsfc) versus engine load. From the figure, as the load increase, the bsfc for each fuel decrease. Diesel fuel shows the lowest bsfc than other fuel at all loads. WCOME A has the lowest bsfc while WCOME C show the highest bsfc. All WCOME show significant higher bsfc at low load particularly WCOME C with 3.25 times higher than diesel fuel. This is due to higher kinematic

viscosity and density of WCOME. High kinematic viscosity can cause reduction of fuel atomization when injected into combustion cylinder. High density can increase momentum of fuel droplets that will lead to longer travel distance of fuel droplets. High-density fuel droplets may reach and hit cylinder wall and retrenched. It becomes worse with low in-cylinder temperature at low load that lead to low vaporization of injected fuel. These can increase unburned WCOME and bsfc. High emission of unburned hydrocarbon and carbon monoxide can be predicted at low load engine condition.

Figure 2(c) shows the smoke number versus engine load for all test fuels. Generally, the graph shows increment of smoke number with increasing of engine load for each fuel. At low load, smoke number are at the same level for all fuels. However, at high load diesel fuel shows the significant higher smoke number than WCOMES. At high load, high amount of fuel injected into the combustion cylinder need high amount of oxygen for combustion reaction. However, at some stratified fuel rich region, lack of oxygen will cause the formation of soot that will finally emit as smoke. WCOME are oxygenated fuel that carrying oxygen in the fuel itself and solve some oxygen lack problem at stratified fuel rich region. Therefore, WCOME emit lower smoke than diesel fuel. Between the WCOME, it can be seen that WCOME A give the lower smoke number in all load engine condition. This result might be affected by the low frequent and short duration usage of the WCO. High frequent and long duration use of WCOME B and WCOME C sources may contaminate the fuel with fine particle of foods. This additional particle might emit as smoke and increase smoke reading of WCOME B and WCOME C.

### 5. IMPROVEMENT OF FUEL PROPERTIES

Compared with diesel fuel, WCOMES show comparable combustion performance and improved smoke emission at high engine loads. However, at low engine loads, WCOMES need some properties modification in order to reduce unburned fuel and improve combustion performance as well as exhaust emissions.

As mention in the previous subtopic, the main cause of this unwanted result at low load engine

condition is due to high kinematic viscosity and density of WCOME. In this study, WCOME C has been blended with 30% kerosene. Kerosene has lower kinematic viscosity and density than WCOME and diesel fuel so that smaller amount of blending percentage will give significant reduction of WCOME's kinematic viscosity and density. 30% blend of kerosene had reduced WCOME C kinematic viscosity by 25% and become closer to kinematic viscosity of diesel fuel as shown in Table 4.

Table 4 : Fuel Properties

Test Fuel	Kinematic Viscosity (mm <sup>2</sup> /s)	Density (g/ml)
Diesel Fuel	3.918	825
WCOME C	5.431	852
WCOME C + 30% Kerosene	4.067	839.3

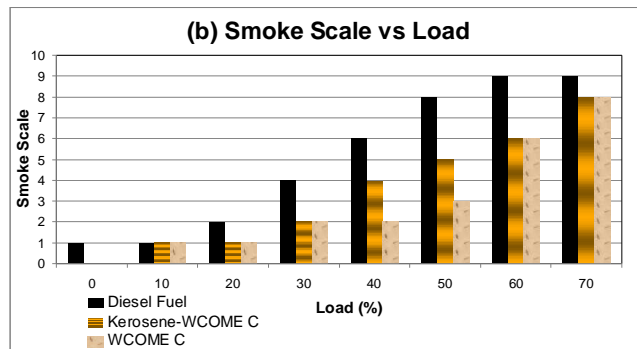
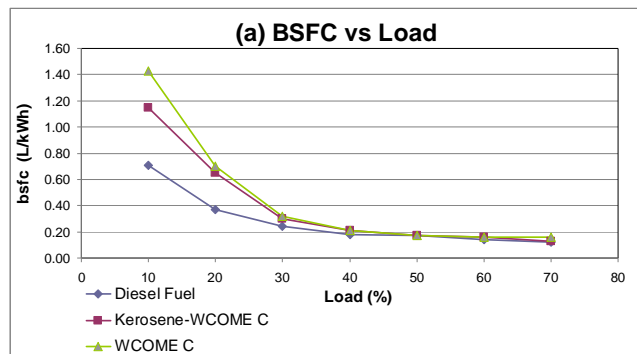


Figure 3. Effect of Kerosene-WCOME C on  
 (a) Brake Specific Fuel Consumption (bsfc),  
 (b) Smoke

Figure 3(a) and 3(b) show bsfc versus load and smoke versus load respectively. It can be seen in figure 3(b) that Kerosene-WCOME C blend remain same level of smoke emission with WCOME C at high load. In figure 3(a), bsfc of Kerosene-WCOME C is improved by 20% than WCOME C at low load engine condition. This indicates that bsfc of WCOME at low loads engine condition can be improved by blending some amount of kerosene without effecting low emission obtained at high loads. However, the bsfc improvement by blending 30% kerosene into WCOME C is not close enough to the bsfc obtained by diesel fuel. This might due to the density of Kerosene-WCOME C is still high compared with diesel fuel. Upon this matter, the author will further investigate on affect of further reduction of WCOME's fuel density in order to utilize WCO as diesel fuel.

## 7. CONCLUSION

1. Diesel fuel produced higher brake power than Waste Cooking Oil Methyl Ester (WCOME). This is due to higher calorific value of diesel fuel.
2. All WCOMES have lower smoke emission at high load compared with diesel fuel. This is because WCOMES are oxygenated fuel that can promote combustion at stratified fuel rich region.
3. WCOME has higher bsfc than diesel fuel at low loads due to higher kinematic viscosity and density of the fuel.
4. Bsfc of WCOME at low loads can be improved by blending some amount of kerosene to reduce kinematic viscosity of WCOME.
5. The affects of further reduction of WCOME's density need to be studied.

## REFERENCES

- [1] Aysel Hilal Demirbas, Imren Demirbas, Importance Of Rural Bioenergy For Developing Countries, Energy Conversion And Management, 2007, 48 (2007) : 2386 – 2398.
- [2] Naruse, S., "Japan's Policy toward Energy Security", 2007 JSAE/SAE International Fuels and Lubricants Meeting, 2007.
- [3] Wang, Shiyi Ou, Pengzhan Liu, Feng Xue And Shuze Tang, Comparison Of Two Different Processes To Synthesize Biodiesel By Waste Cooking Oil, Journal of Molecular Catalysis a

Chemical, 2007, Volume 252, Issues 1-2 : 107 - 112.

- [4] Hamasaki, K., Kinoshita, E., Tajima, H., Takasaki, K., Combustion Characteristics of Diesel Engines with Waste Vegetable Oil Methyl Ester, JSAE Jurnal, (01-204) pp.55 20010701.
- [5] Wira, J., Harada, T., Kubo, S., Kidoguchi, Y., Miwa, K., Improvement of Emissions in a DI Diesel Engine Fuelled by Bio-Diesel Fuel and Waste Cooking Oil, SAE 2007-01-2029.